NASA/CR—1998-207928 AlliedSignal Engines 21–9835

TMC Behavior Modeling and Life Prediction Under Multiaxial Stresses

H.F. Merrick
AlliedSignal Engines, Phoenix, Arizona

S.Z. Aksoy and M. Costen
Aerospace Structural Research Corp., Milford, Connecticut

J. Ahmad
Research Applications, Inc., San Diego, California

Prepared under Contract NAS3–27027

National Aeronautics and
Space Administration

Lewis Research Center

September 1998

Available from

NASA Center for Aerospace Information
7121 Standard Drive
Hanover, MD 21076
Price Code: A10

National Technical Information Service
5287 Port Royal Road
Springfield, VA 22100
Price Code: A10

TABLE OF CONTENTS

LIST OF FIGURES

TMC BEHAVIOR MODELING AND LIFE PREDICTION UNDER MULTIAXIAL STRESSES

NASA CONTRACT NAS3-27027

SUMMARY

The goal of this program was to manufacture and burst test small diameter SCS-6/Ti-6Al-4V composite rings for use in the design of an advanced titanium matrix composite (TMC) impeller. The Textron Specialty Metals grooved foil-fiber process was successfully used to make high quality TMC rings. A novel spin test arbor with "soft touch" fingers to retain the TMC ring was designed and manufactured. The design of the arbor took into account its use for cyclic experiments as well as ring burst tests. Spin testing of the instrumented ring was performed at ambient, 149C (300F), and 316C (600F) temperatures. Assembly vibration was encountered during spin testing but this was overcome through simple modification of the arbor. A spin-to-burst test was successfully completed at 316C (600F). The rotational speed of the TMC ring at burst was close to that predicted.

In addition to the spin test program, a number of SCS-6/Ti-6Al-4V test panels were made. Neat Ti-6Al-4V panels also were made.

TMC BEHAVIOR MODELING AND LIFE PREDICTION UNDER MULTIAXIAL STRESSES

1. INTRODUCTION

The aggressive goals of the IHPTET (Integrated High Performance Turbine Engine Technology) initiative require the development of high performance turbine engine components of advanced design. For the turboshaft/turboprop engine, one of the key components is the centrifugal compressor, or impeller, which is required to operate at high tip speeds and metal temperatures in order to achieve the high overall pressure ratio of an advanced compressor. An example of an advanced impeller design is shown in Figure 1.

Impellers in current engines are made either of nickel base alloys, e.g., alloy 718, or high-strength titanium alloys such as Ti-6-2-4-6. The titanium alloys have the advantage of lower density than nickel alloys and can operate at higher tip speeds. The nickel alloys have the advantage of being able to operate at higher compressor exit temperatures. Neither system of monolithic alloys has the capability of meeting the requirements of an advanced impeller to meet the Phase II IHPTET goals for the turboshaft/turboprop gas generator.

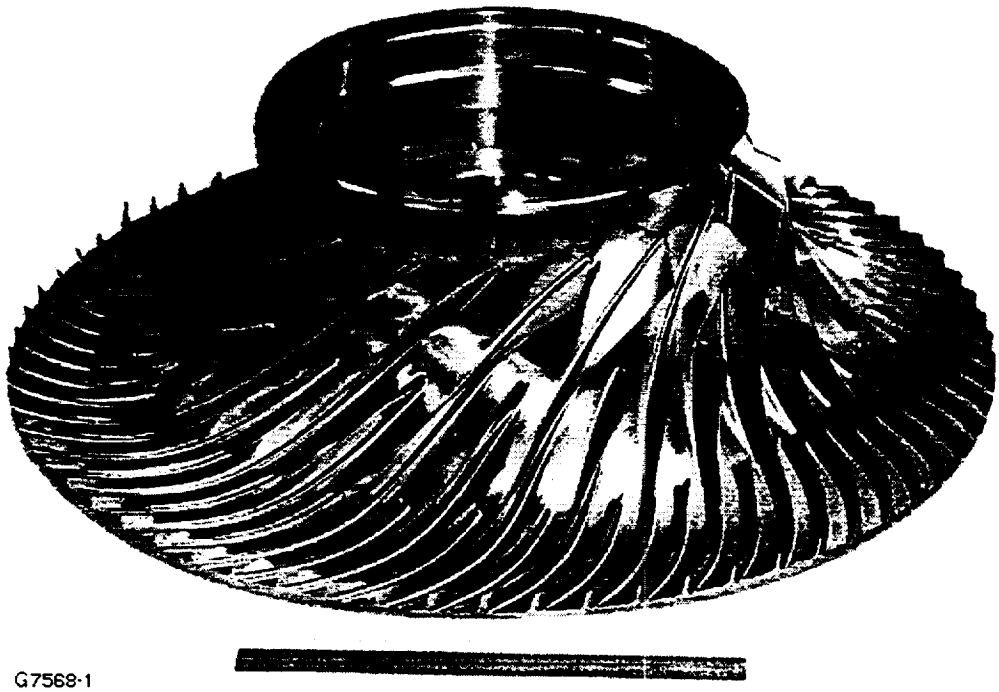

Figure 1. Finished Machined Titanium Advanced Impeller Design Showing Splittered Airfoils.

As a consequence, radically new materials technologies are required to provide the necessary strength at the operating temperatures of an advanced impeller. An attractive new technology for meeting the strength requirements is titanium metal matrix composites (TMC) in which continuous fibers of silicon carbide are dispersed in a titanium alloy matrix. A commonly used silicon carbide fiber is the Textron Specialty Metals fiber SCS-6 with a strength of 550 ksi at room temperature and a modulus of 60 Msi (413 GPa). A higher strength fiber, Ultra SCS, is now also available from Textron Specialty Materials. A number of titanium alloy matrices have been evaluated for the SCS-6 fiber, e.g., Ti-6Al-4V, Beta 21S and Ti-15-3. In this program we chose the SCS-6/Ti-6-4 system. Considerable property data exists for this system. It is being used as a standard by the Titanium MMC Life Prediction Cooperative.

It must be appreciated that unidirectional layups of the silicon carbide fiber/titanium alloy matrix provide, as a consequence, a highly anisotropic system. In the longitudinal or [0] direction, the system possesses very high specific strength and modulus and the properties are controlled by the fiber. In the transverse or [90] direction, the properties are significantly lower as a function of the titanium alloy matrix, the fiber/matrix interface, and the fiber volume fraction. Recognition of the anisotropy of the TMC is necessary in the design of a rotating turbine component such as the impeller if the strengthening potential of the composite is to be successfully used as a reinforcing ring or more complex structure bonded within the body of the component.

The implementation of a TMC reinforcing structure for an advanced turbine engine requires development activity in several areas, including:

a. Materials and Processing
b. Component Design
c. Component Fabrication
d. Life Prediction.

The sound design and manufacture of a TMC reinforced component is predicated on a complete understanding of deformation under static and dynamic loading that occurs under the multiaxial stress state engendered by component rotation.

The objective of this program, initially, was to predict and verify the monotonic and low-cycle fatigue response of a titanium composite ring, which would serve as an insert in a centrifugal compressor component, using the NASA developed Differential Continuum Damage Mechanics Model. Ti-6-4/SCS-6 rings would be fabricated using Textron Specialty Materials grooved foil-fiber process and subjected to internal pressurization tests. These tests would be performed to burst and separate rings would be tested cyclically.

As will be described, difficulties were experienced in performing fluid internal pressurization at the required test temperature. As a result, the program was redirected to the design and fabrication of a test arbor for spin testing and the subsequent spin to burst of a test TMC ring.

Additionally, several Ti-6-4 neat and Ti-6-4/SCS-6 TMC panels were made and forwarded to NASA Lewis Research Center (LeRC) for use in the MMC Life Prediction Cooperative test program.

2. PROCEDURES

2.1 TMC Ring Design and Manufacture

The TMC ring used in this study comprised 35 volume percent SCS-6 silicon carbide fibers in a Ti-6Al-4V matrix. The nominal ring dimensions were 102 mm (4.0 inch) ID by 181 mm (7.125 inch) OD by 6.6 mm (0.26 inch) thick. The TMC core had dimensions of 127 mm (5.0 inch) ID by 178 mm (7.0 inch) OD by 6.4 mm (0.25 inch) thick. A section diagram of the ring is given in Figure 2. The original outer diameter of the ring was to be 203 mm (8.0 inch) but this was reduced to 181 mm (7.125 inch) in order that flatness could be maintained during the hot pressing operation.

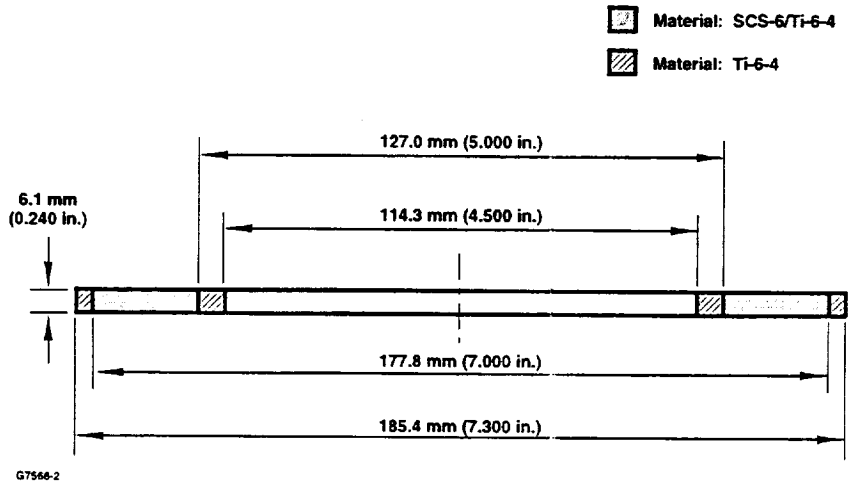

Figure 2. Dimensions of the SCS-6/Ti-6Al-4V TMC Ring.

The spiral grooved-foil preform process (ref. 1) developed by Textron Specialty Materials (TSM), Lowell, MA, was used to make the TMC rings. The significant attributes of this innovative approach to the manufacture of TMC ring structures are that it allows the precise location and spacing of the silicon carbide fiber, as well as control of the width, thickness, and shape of the reinforced region.

This is particularly important for the case of the turbine centrifugal impeller which has a generic triangular shape in cross-section. Additionally, the grooved-foil preform process allows a variation in fiber volume fraction to be employed simply by changing the spacing of the grooves. This can be an advantage in component reinforcement design where radial loads in the component need to be managed.

The grooved-foil preform process makes use of photolithography and photoetching to precisely locate the spiral groove in the surface of the titanium foil, in this case Ti-6Al-4V foil having a thickness of about 0.13 mm (5 mils). The photoetched grooves are typically 0.09 to 0.10 mm (3.5 to 4.0 mils) deep. Both single-sided etched grooves or double-sided etched grooves can be used for making TMC rings. The ring used for this program employed the double-sided etching method. The grooves were displaced so that a triangular array of the SCS-6 fibers resulted upon consolidation. It should be noted that other geometric arrays of fibers, e.g., square,

are also possible using the grooved-foil preform process. Figure 3 shows diagramatically the steps involved in making the fiber arrangement for the ring used in this study. A micrograph of the microstructure that typifies the precision layup afforded by this process is shown in Figure 4.

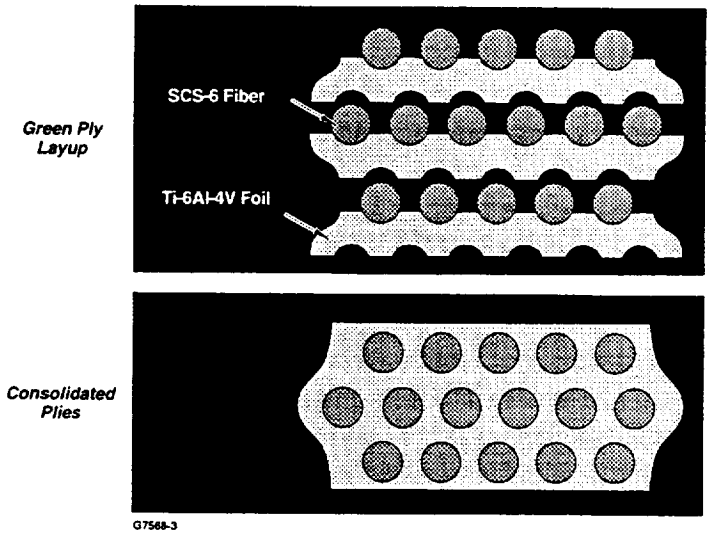

Figure 3. Schematic of the TSM Double-Sided, Grooved-Foil Process Used to Make the TMC Ring.

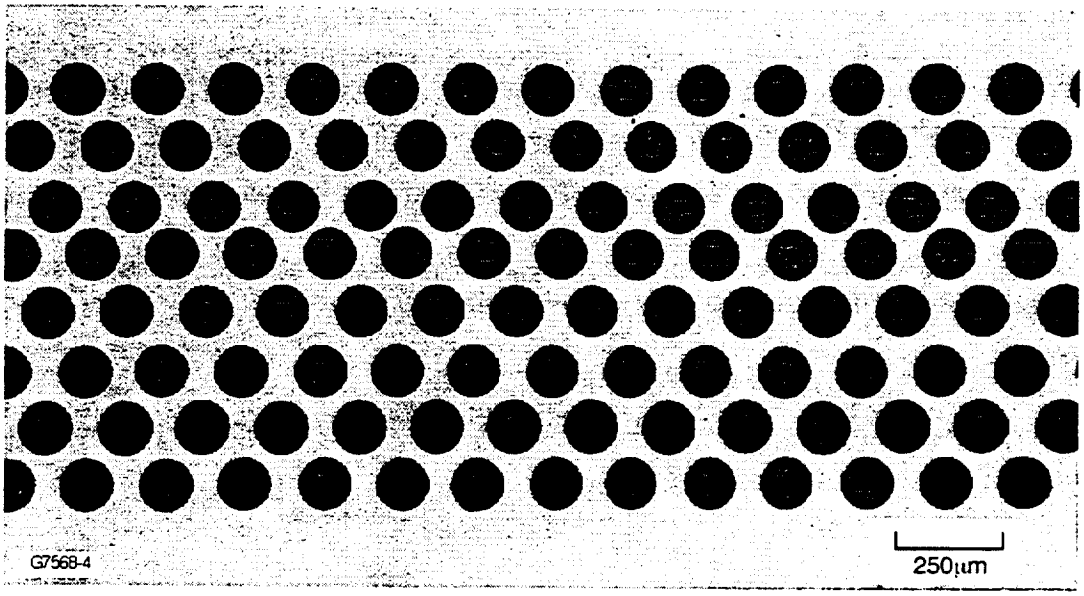

Figure 4. Micrograph Illustrating the Precise Layup Afforded by the Textron Specialty Materials Grooved-Foil Process.

TSM's initial trial to fabricate the TMC ring was not wholly a success. Visual examination of the outer diameter of the fiber zone indicated that buckling of the fibers had occurred. The ring was submitted for ultrasonic nondestructive testing. This test confirmed that buckling of the fibers had indeed occurred at discrete locations.

A reduction in defect state was achieved in a second ring. However, rather than proceed with further empirical ring fabrication trials, NASA felt that the fabrication process should be modeled to provide information that might pinpoint the cause of fiber buckling. NASA conducted a number of concentric cylinder elastic and elastic-plastic creep analyses of the disk manufacturing process. Several trends were noted, the most important being that the tooling must be taken into account in order to arrive at realistic stress states and that the inner tooling must have a low coefficient of thermal expansion (CTE). Consequently it was recommended that TSM increase the CTE of inner tooling so that it exceeded that of the Ti-6Al-4V clad material of the TMC ring. In this way the inner tooling would provide radial pressure during heat-up and hold time during the consolidation process, but would allow release during cooldown to minimize residual stress within the disk. The stress state from the NASA analysis were then used for a buckling analysis to investigate whether sufficient hoop and radial stresses would be induced by the non-optimal tooling configuration which caused the fiber buckling.

The buckling modeling work was conducted by Dr. Jalees Ahmad at AdTech Systems Research, Inc., Dayton, Ohio. In the model, consideration was given to consolidation induced residual stresses and to the thermal and mechanical applied loads. Details of the analysis are given in Appendix 1 of this report. It was concluded that a net compressive radial force acting on a partially bonded or unbonded fiber segment could result in fiber buckling and even breakage.

Based on the NASA recommendations, remedial fabrication steps were undertaken by TSM. This included the deployment of a graphite cylinder at the inner diameter of the TMC ring as well as at the outer diameter. Experiments on larger diameter TMC rings had provided some measure of success with this tooling setup.

The third ring manufactured was a success. Visual examination indicated no obvious flaws and subsequent x-ray and CT-scan evaluation showed no evidence of delamination, poor bonding of the Ti-6-4 with the SiC fiber, or buckling. An x-ray photograph of this ring in comparison with a ring made by the original TSM procedure is shown in Figure 5.

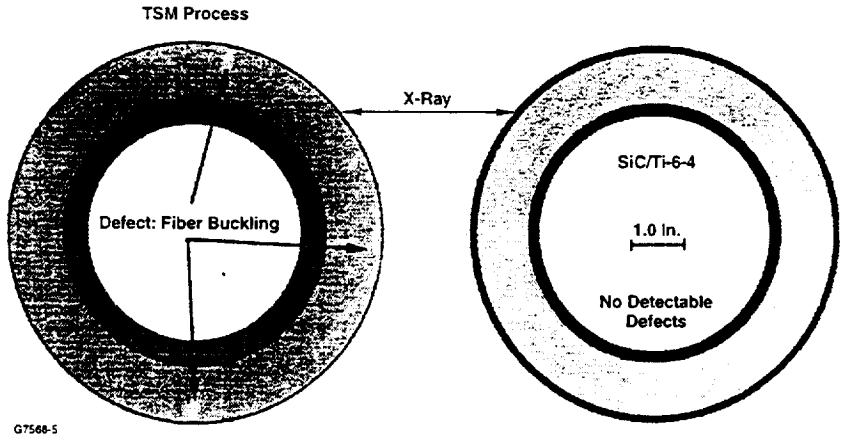

Figure 5. X-ray Photographs of Subsequent TMC Rings Made.
Left: Fiber Buckling Defects are Present in Ring
Made by Original TSM Procedure
Right: Defect-Free Ring Made after Change in Tooling

2.2 Test Fixture Design and Manufacture

2.2.1 Internal Pressurization

Initially it was proposed that a fluid internal pressurization method be used for burst and cyclic testing. This method to test the TMC ring was chosen since it was a logical follow-on to the previous work undertaken in a NASA-Pratt & Whitney cooperative program. There were several advantages associated with this method of testing. First, it allowed the accurate measurement of strain during monotonic burst and cyclic fatigue testing and thus the assessment of damage accumulation in the TMC ring that would be used for lifing. Second, it is a low cost test method. The disadvantage, of course, is that such a test method does not truly define the stress state in a rotating body.

Despite this disadvantage it was decided to proceed with this test method. The National Technical Systems, Saugus Division, California, was engaged for the design and fabrication of an apparatus which would be used for testing.

An analysis to predict the burst pressure for the TMC ring geometry to be tested was performed by Dr. Jalees Ahmad and Dr. Iftikhar Haq of AdTech Systems Research, Inc. This work is included as Attachment 1, "Report on MMC Behavior Modeling Under Multiaxial Stresses for MMC Ring Reinforced Impeller, Phase 1." The approach employed a nonlinear, finite element analysis based micro-mechanics model, generating the unidirectional composites global stress-strain response under biaxial (combined 0 and 90 degree) loading.

A literature search was undertaken to generate mechanical properties data for the SCS-6/Ti-6-4 composite system. A listing of these references is given in Attachment 1, Appendices A and B. Attachment 1, Appendix C, "Metal Matrix Composite Response Under Biaxial Loading," contains details of the analytical procedure and the specific results for this TMC ring. The burst pressure of the ring at room temperature was predicted to be 770 MPa (112 ksi).

Figure 6 shows a longitudinal section drawing of the test assembly. It consisted of a mandrel (drawing part 3) which is connected to a pump system. The pump is used to supply the active light fluid, kerosene/oil, to the internal diameter of the test article, the TMC ring, by locally expanding a metallic sleeve or bladder (drawing part 4). This sleeve is backed up by a metallic spacer (drawing part 5).

The kerosene/oil fluid is contained by a pair of O-ring seals (drawing part 9). The test article is positioned by a shrink disk (drawing part 7). The pressurized fluid locally expands the metallic bladder, which is in contact with the TMC ring, and thus applies an internal pressure to the ring.

In order to check out the internal pressurization method, tests were performed at 21C (70F) using a Maraging steel ring of the same dimensions as the TMC ring. The Maraging steel ring was instrumented with strain gauges. Three pairs of strain gauges were affixed to the Maraging steel ring. No difficulties were experienced in applying the internal pressure in the ambient temperature check of the test apparatus. The test was stopped after the internal pressure reached 64,700 psi to avoid possible yielding of the ring. The test demonstrated that the apparatus would operate effectively at 21C (70F).

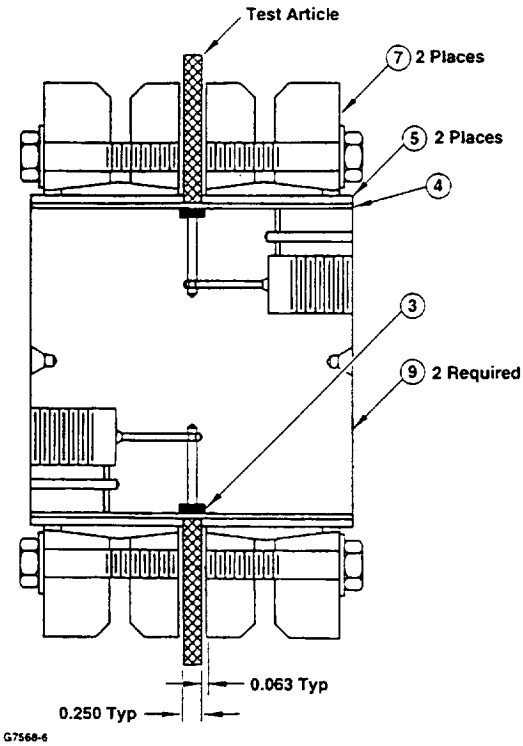

Figure 6. Schematic of Internal Pressurization Test Apparatus Designed for Burst Test.

However, problems surfaced during testing at 316C (600F). In this test of the apparatus, leakage of the 90 percent kerosene - 10 percent oil fluid was experienced when the applied pump pressure reached 11,000 psi corresponding to an effective applied stress to the ring of 5,700 psi. The maximum pressure that would be needed to burst the Ti-6-4/SCS-6 could not be reached. O-rings of another polymer were installed and the test repeated. Again fluid leakage occurred and the test discontinued. In a third test, the test apparatus was heated to 93C (200F) and the shrink disks bolts retorqued at temperature in an attempt to tighten the system at temperature. However, fluid leakage was again experienced.

In a final attempt to qualify the system, a modified mandrel with internal cartridge heaters and a revised seal configuration was installed. The new seals consisted of a pair of teflon encapsulated, stainless steel spring O-rings in combination with a pair of backup polyetheretherketone (PEEK) polymer O-rings. Despite this effort leakage was again encountered.

At this point it was decided that a solution to the leakage problem would not be found and that an alternate method to test the TMC ring should be undertaken. In consultation with NASA it was decided that spin testing should be employed. This required a significant effort since a suitable test arbor needed to be designed. Spin testing, however, would have direct relevance to the stresses experienced by a component in a gas generator or engine test.

2.2.2 Spin Test Arbor

The spin test arbor was designed by Mr. Sait Aksoy of Textron Lycoming, and later of Aerospace Structural Research Corporation, Milford, CT. The arbor was designed so that the ratio of the polar and transverse moments of inertia would be 1.04. For the arbor/TMC ring assembly this ratio rises to 1.32, comfortably above the dynamically unstable value of 1.0.

A diagram of the spin test arbor is shown in Figure 7. The arbor consists of a central shaft and two support disks with "soft touch" fingers to hold the TMC ring in position (ref. 2).

The clamping pressure, applied through a torque nut and locking washer, is transmitted to the support disks by two "arm" disks. Minimal clamping pressure is applied to the TMC ring so as not to interfere with the motion of the TMC ring as it expands during the spin test. A hollow spindle connects the arbor to the drive motor.

In a photograph of the arbor and ring assembly (Figure 8), the castellated "soft touch" fingers of the support disk are clearly visible. A cutaway, computer-generated picture of the assembly is shown in Figure 9.

Prior to assembling the TMC ring into the arbor for the spin test, the ring was outfitted with tangential and radial high-temperature strain gauges. Details of the positioning of the strain gauges and the access ports for the lead wires is shown in Figure 10. The strain gauges were mounted 90 degrees apart. At each location a tangential or hoop gauge was mounted at the inner diameter of the SCS-6/Ti-6-4 composite zone and another at the outer diameter of the composite zone. A radial gauge was located at the mid-radius of the composite zone. Since the radial strains would be small, it was reasoned that the positioning of the radial gauge should be at the location where the maximum radial strain would be expected. This configuration was arrived at after discussion with NASA.

Mounting of the strain gauges was performed by HITEC Corp., Westford, MA. These were FSM-06-3585 type sensors which would operate at the test temperature of 316C (600F). Epoxy was used for the mounting medium and an epoxylite protective coating applied to the Constantan lead wires. All splices were either tweezer welded or silver brazed. The strain gauge lead wires were routed along the axis of the arbor shaft and joined to a slip ring assembly which in turn connected to the strain data recorders. Approximately two feet of lead wire exited the shaft via the hollow spindle.

Type K thermocouples were also attached to the TMC disk. Figure 11 shows a photograph of the attached thermocouples as well as one set of strain gauges.

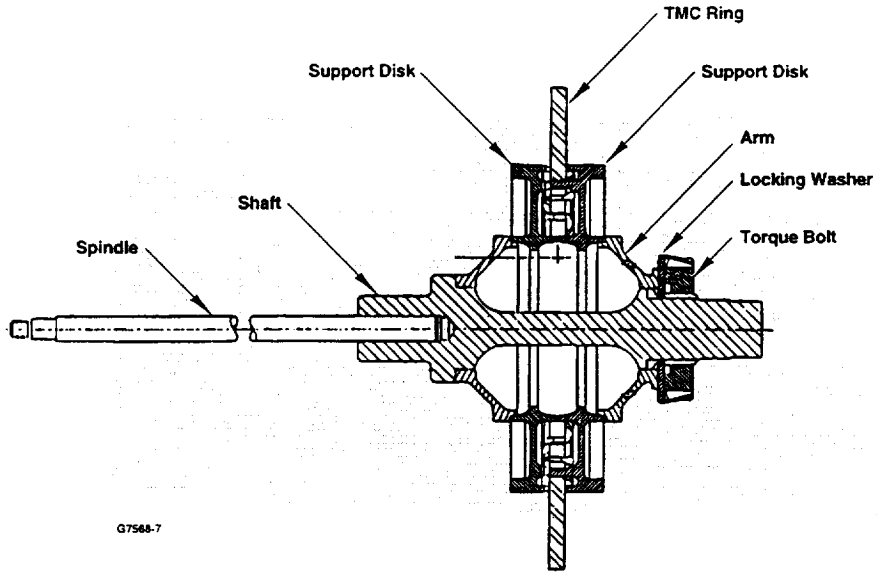

Figure 7. Cross-section Diagram of the Spin Test Arbor and TMC Ring Assembly.

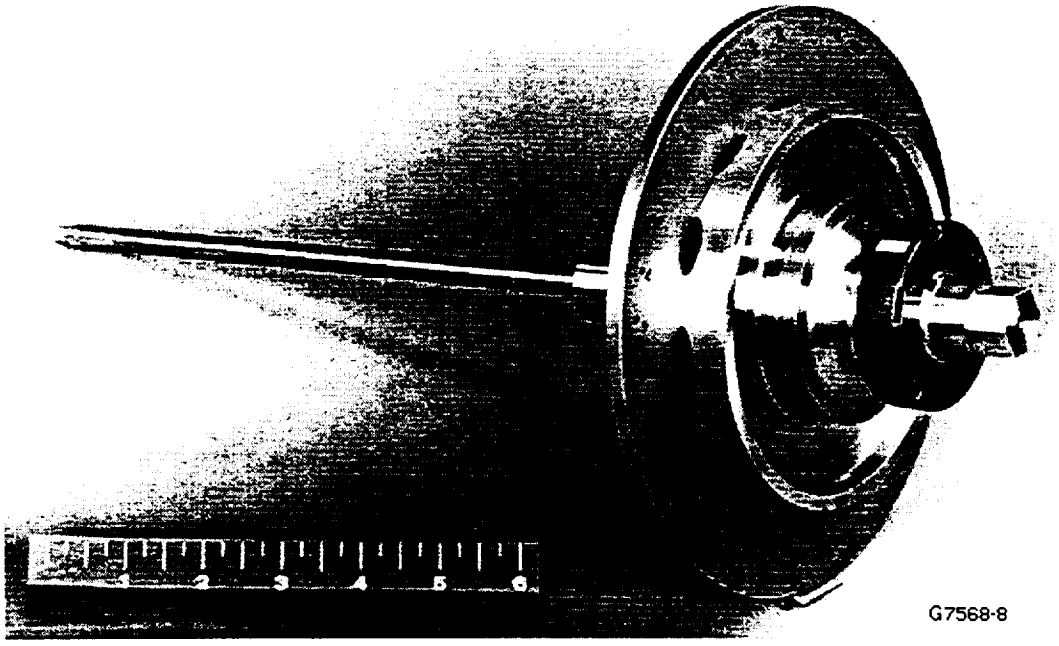

Figure 8. Photograph of Arbor and TMC Ring Assembly. Note the Castellated "Soft Touch" Fingers of the Support Disk.

Figure 9. Computer-Generated Picture of the Arbor and TMC Ring Assembly with Cutaway.

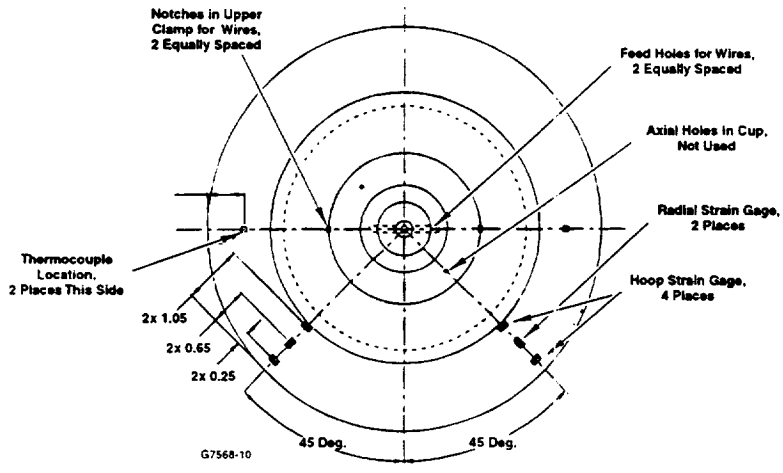

Figure 10. Diagram Showing Location of the Instrumentation (Strain Gauges and Thermocouples) on the TMC Ring. View is from the Spindle Side.

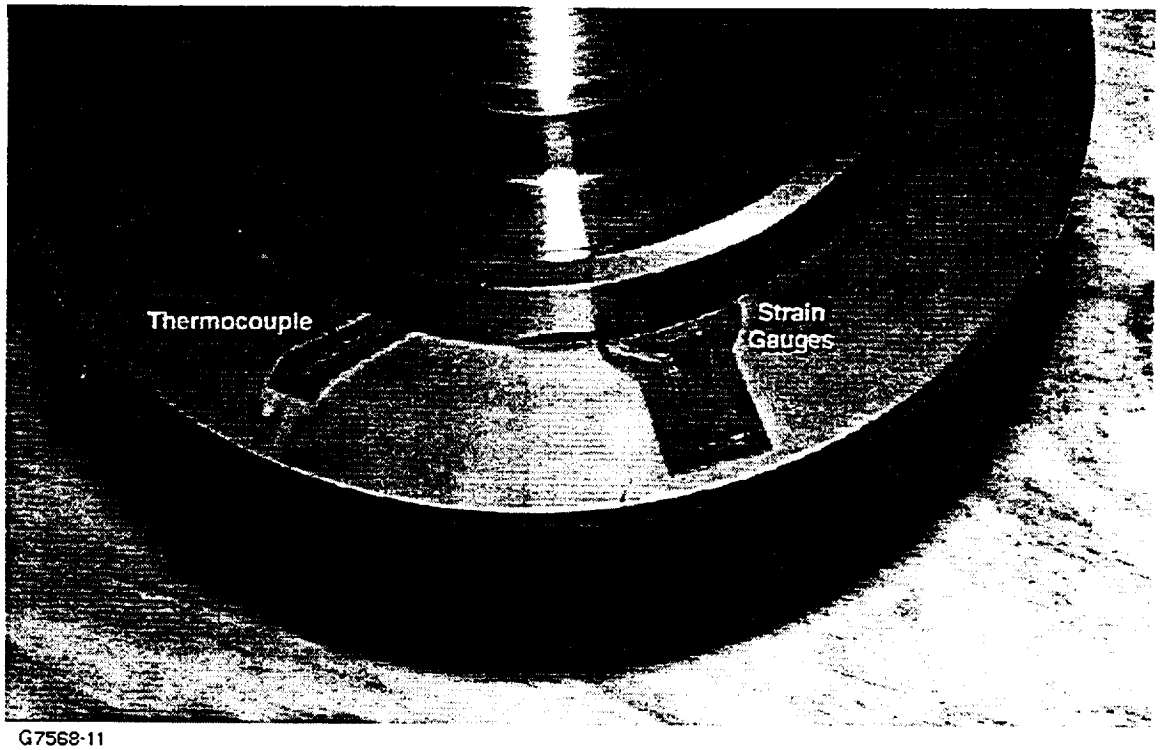

Figure 11. Photograph of the Assembled Strain Gauges (One Set) and the Thermocouple.

3. RESULTS AND DISCUSSION

3.1 MMC Ring Spin Testing

Prior to spin testing an analysis was performed to predict the burst speed. This was necessary since the arbor design must meet the burst speed as a minimum requirement.

3.1.1 Burst Speed Analysis

The three-dimensional, finite element model chosen for the TMC ring burst speed analysis consisted of a twenty-noded brick mesh. A perfect bond was assumed between the Ti-6Al-4V matrix and the fibers, as well as between the clad and TMC core. The ABACUS code was used to calculate the burst speed based on the material properties for SCS-6/Ti-6Al-4V given in Figure 12. A maximum stress in the hoop direction was used as the failure criterion for the TMC ring.

Temp., C (F)	E (l) GPa (msi)	E (t) GPa (msi)	UTS (l) MPa (ksi)	UTS (t) MPa (ksi)	v (l)	v (t)	CTE (l) (10^{-6})	CTE (l) (10^{-6})
21 (70)	214 (31)	132 (19)	1770 (257)	453 (66)	0.28 (0.28)	0.28 (0.28)	1.94 (1.94)	2.89 (2.89)
316 (600)	200 (29)	130 (19)	1540 (244)	296 (43)	0.28 (0.28)	0.28 (0.28)	2.33 (2.33)	2.99 (2.99)

G7568-12

Figure 12. Material Properties for SCS-6/Ti-6Al-4V.

Figure 13 shows the radial and hoop stress distribution in the composite zone at a speed corresponding to that of the hoop stress attaining the ultimate tensile stress of the composite in the [0]. At a rotational speed of 64,000 rpm the maximum hoop stress is 1,517 MPa (220 ksi), a value close to the ultimate tensile strength of the composite in the [0].

The maximum radial stress at this speed is 77 MPa (11 ksi). This value is below the fiber/matrix debond stress.

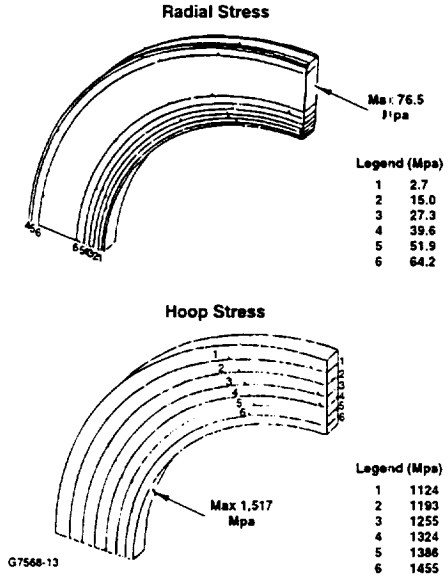

Figure 13. Radial and Hoop Stress Distribution in the Composite Corresponding to a Rotational Speed of 64,000 rpm.

3.1.2 Spin Test Results

The spin testing was performed at Test Devices, Hudson, MA. It was agreed with NASA that the test should be performed in three steps as follows:

a. Spin to 30,000 rpm at room temperature (duplicate runs)

b. Under vacuum, heat test chamber to 149C (300F) and again spin to 30,000 rpm (again duplicate runs)

c. Heat the test chamber, again under vacuum, to 316C (600F) and spin to burst

The ambient temperature test to 30,000 rpm proceeded without incident. Strain data were recorded at intervals of 10,000 rpm. Readings were obtained from all gauges except the Number 4 hoop. Adherence of the strain gauges to the TMC disk was good so this failure to record data was attributed to the slip ring assembly. Recordings from the Number 1 hoop gauge were not obtained after the 10,000 rpm mark. The data recorded are shown in Figure 14.

Test data for the 149C (300F) runs are shown in Figure 15. Again, not all strain gauges provided recordings. No data were recorded for the two hoop gauges. Adherence of the strain gauges themselves remained sound, so again the failure to record data was assumed associated with the slip rings. Excellent data correspondence was obtained for the two outer diameter strain gauges, Numbers 3 and 6.

Limited data obtained for the test at 316C (600F) are given in Figure 16. The Number 1 hoop gauge provided data at the 10,000 rpm mark, but thereafter no strain readings were obtained. The fact that the Number 1 hoop gauge provided data in this run indicated proof that failure to record was solely due to the slip ring assembly.

Strain data were obtained to a speed of 40,000 rpm when vibration problems with the arbor and TMC ring assembly began. When a speed of 42,000 rpm was reached a decision was made to stop the test because the vibration was excessive.

An analysis of the cause of vibration included the positioning of the strain gauges on the TMC ring and the arbor itself. The possibility existed that the strain gauges could cause vibration at the high rotational speeds because they were located in one quadrant of the TMC ring. Because the strain gauges/slip ring assembly/recorder system were not functioning as had been planned, it was decided to remove the strain gauges from the TMC ring and to rebalance the ring/arbor assembly. Minor adjustments were also made to the arbor.

A second test at 316C (600F) was then performed. In this run a speed of 60,800 rpm was achieved before the onset of excessive system vibration. A reassessment of the arbor revealed that a 229 mm (9.0 in.) spindle had been used. This was shorter than had been specified since rotor dynamics analysis showed that with a spindle of this length the critical speed would be 58,000 rpm, too close to the anticipated burst speed (ref. 3). For the final run to burst, the arbor was fitted with a longer spindle, 289 mm (11.375 in.). This moved the critical speed to 33,000 rpm. Figure 17 shows the rotor dynamics model used to determine the critical speeds for the longer spindle.

This final test run was completely successful with burst of the TMC ring occurring at a speed of 61,200 rpm. This speed was only just below the predicted one of 64,000 rpm.

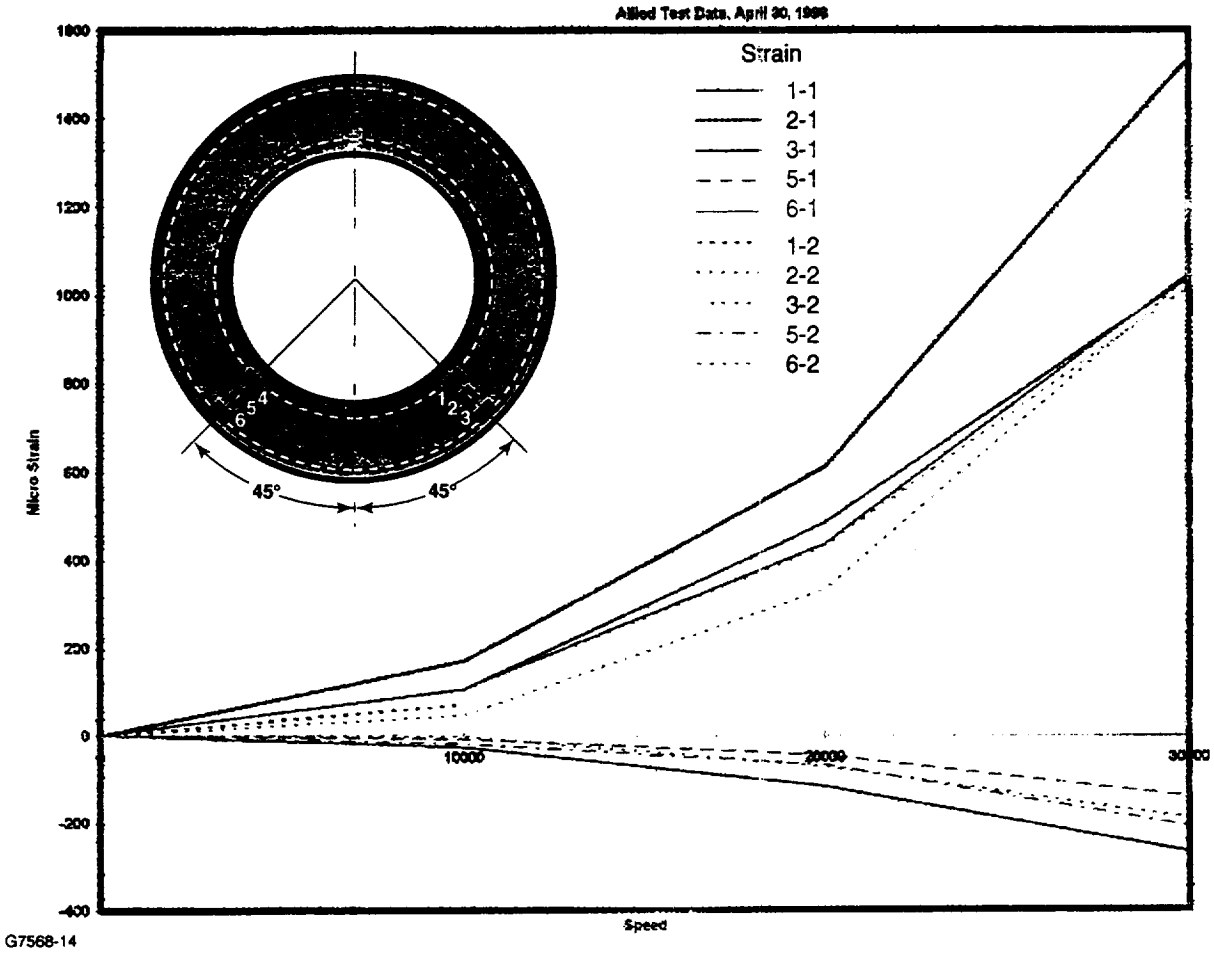

Figure 14. Strain Gauge Data for the 21C (70F) Spin Test.

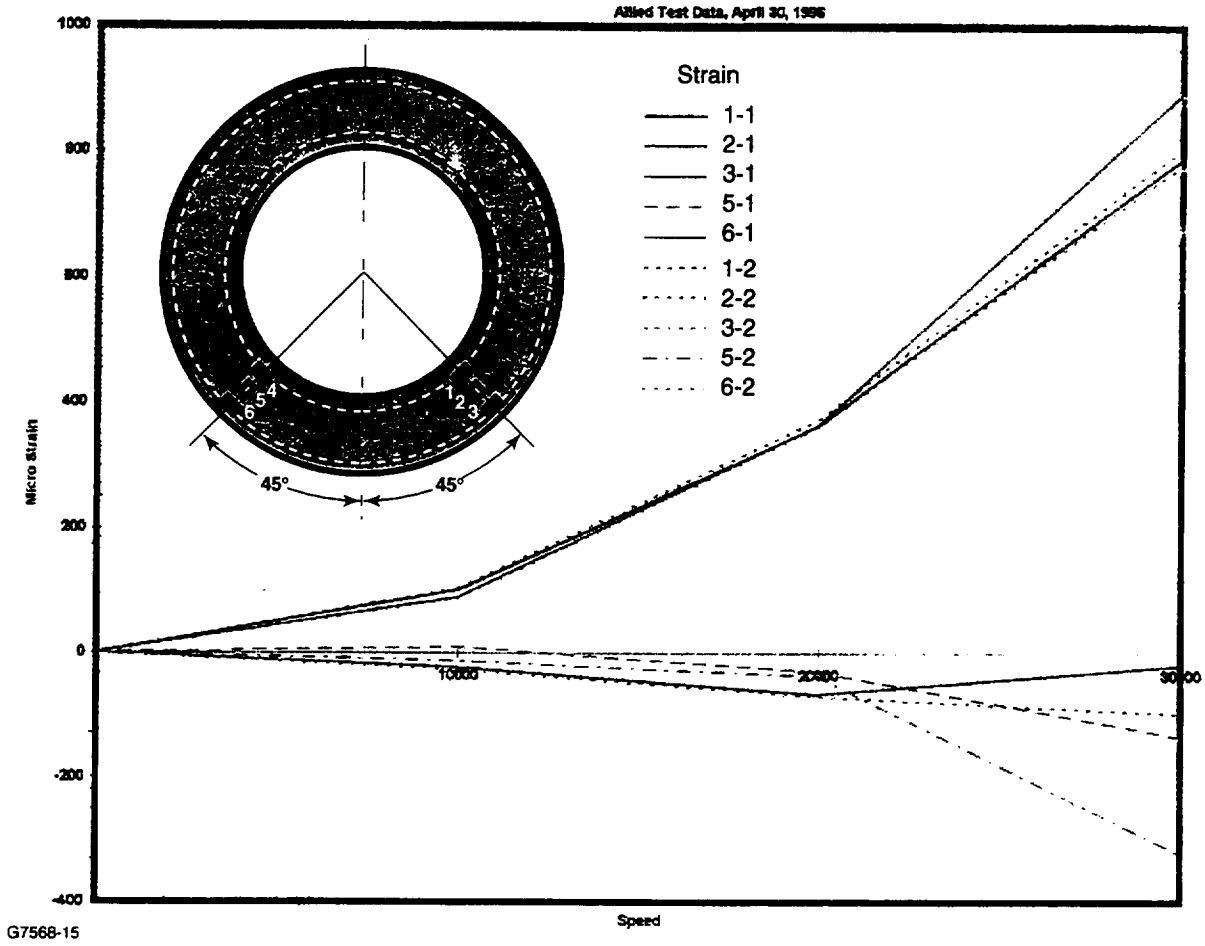

Figure 15. Strain Gauge Data for the 149C (300F) Spin Test.

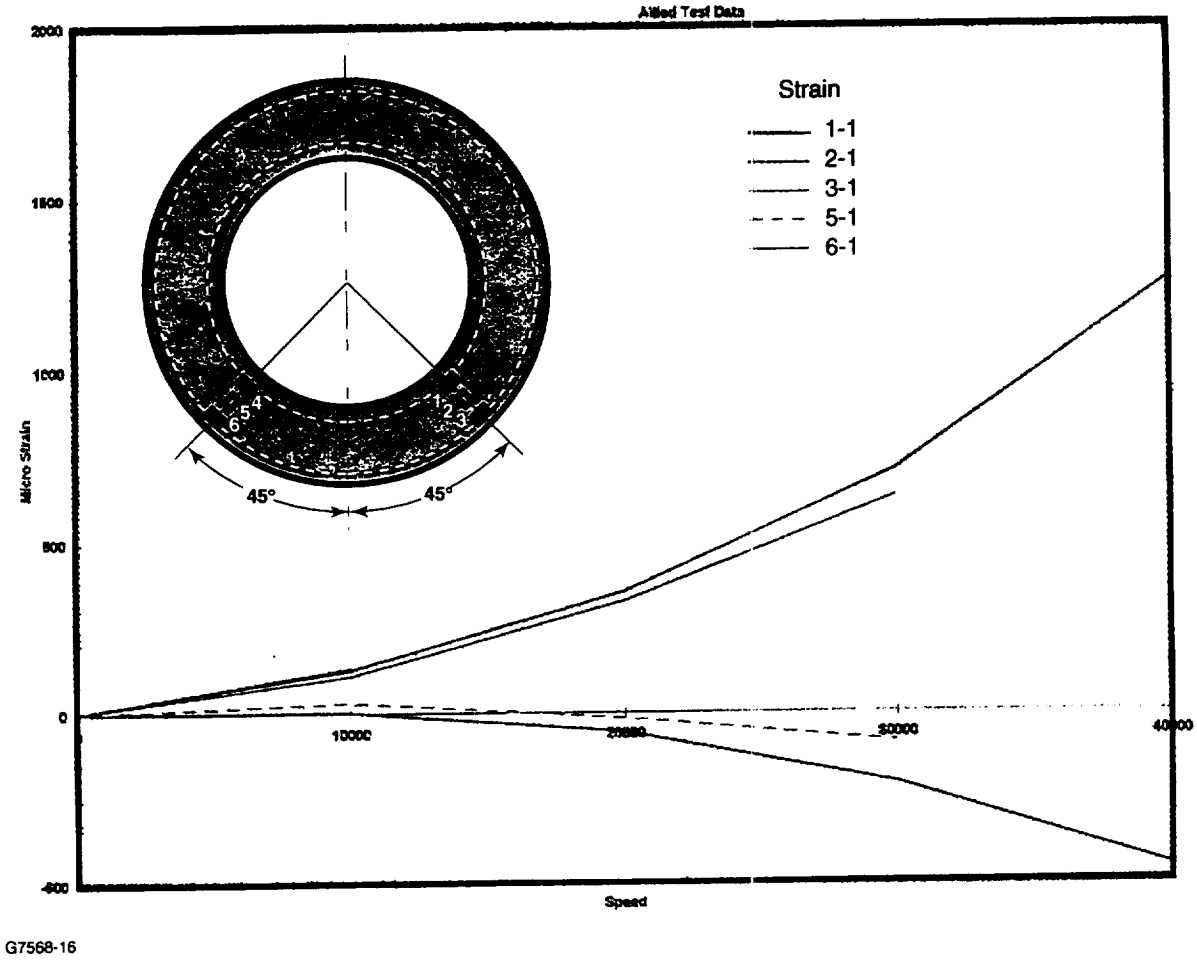

Figure 16. Strain Gauge Data for the 316C (600F) Spin Test.

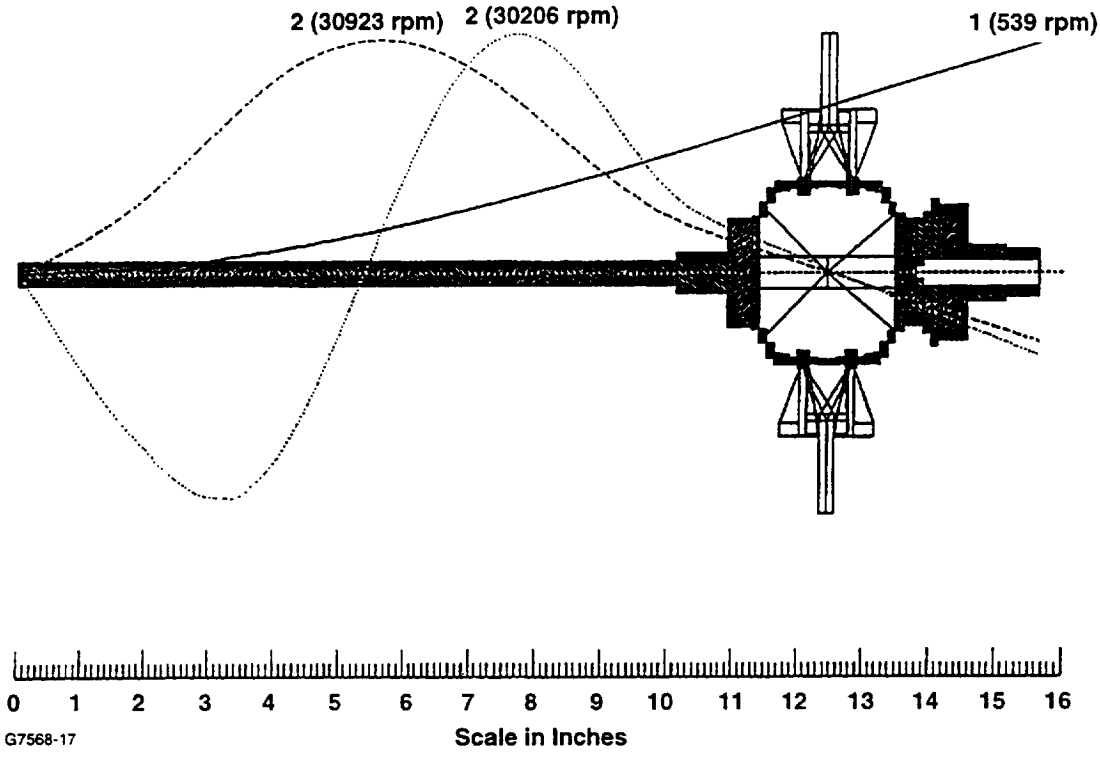

Figure 17. Rotor Dynamics Model for a 289mm (11.375 inch) Spindle Length.

3.2 Nondestructive Evaluation (NDE)

3.2.1 Pretest Evaluation

Pretest NDE evaluation was performed by NASA before and after heat treatment of the ring to assess quality. Tests were performed using x-radiography, computerized tomography (CT) and pulse-echo ultrasonic scans.

The x-ray NDE showed the fiber distribution to be well maintained during the consolidation procedure, as would be expected for the grooved foil-fiber process, although the x-ray photographs hinted at the presence of possible defects.

The CT slices were taken at the locations where the x-radiography indicated soundness as well as the regions where possible defects were present. However, the CT analysis revealed no major differences between the regions.

The pulse-echo ultrasonic scans also indicated that the ring was essentially free of significant defects, although small differences in thickness of the clad over the composite region and that in the unclad zones at the inner and outer diameter of the ring were revealed.

3.2.2 NDE Evaluation After Interrupted Spin Testing to 60,800 RPM

No major changes in ring integrity were observed using radiographic examination (Figure 18), although possible weaker interface regions were suggested. CT analysis was unable to confirm such a change. However, the pulse-echo ultrasonic examination detected a flaw located at 15 degrees from the zero fiduciary point and at the interface between the cladding on the inner diameter and the composite. This is shown in Figure 19. A more detailed analysis is given in reference 3.

3.2.3 Post Burst Test Evaluation

The TMC ring fractured into multiple pieces. With the help of liquid penetrants and optical observations the pieces were repositioned by Dr. G. Baaklini of NASA. A photograph of the reconstructed assembly is shown in Figure 20. Since the test vessel was not furnished with "soft landing" protection for the burst ring, considerable damage to the ring occurred during its collision with the test vessel and the safety pit in which the test was conducted. Nevertheless, careful examination of the parts (ref. 3) indicated that the region of primary failure occurred within an angular domain of 0 to 110 degrees wherein three major cracks were visible. The first crack was between 0 and 20 degrees, the second at about 70 degrees, and the third at the 100 degree mark. The region of most damage was diametrically opposite the region of primary failure, i.e., pieces 5, 6, 7, and 8, shown in Figure 20.

Despite the large scale damage to the ring it was concluded that failure was due to tensile fiber overload with some shear.

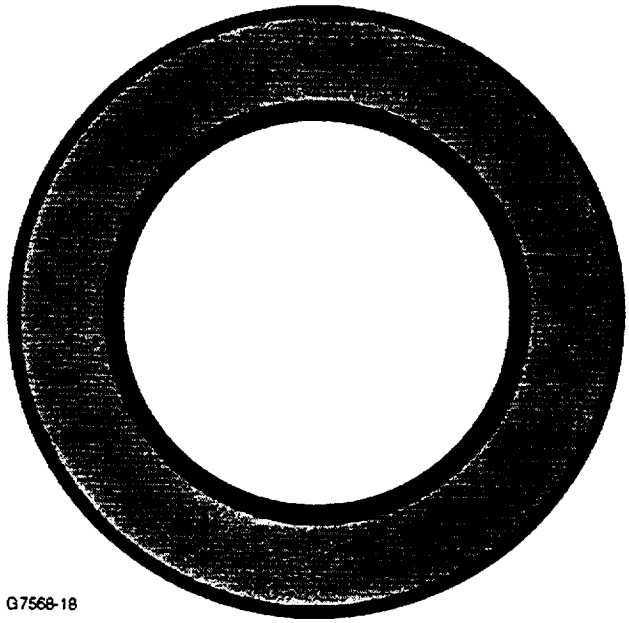

Figure 18. X-radiograph of TMC after Spin Testing to 60,800 rpm at 316C (600F) and before Final Burst.

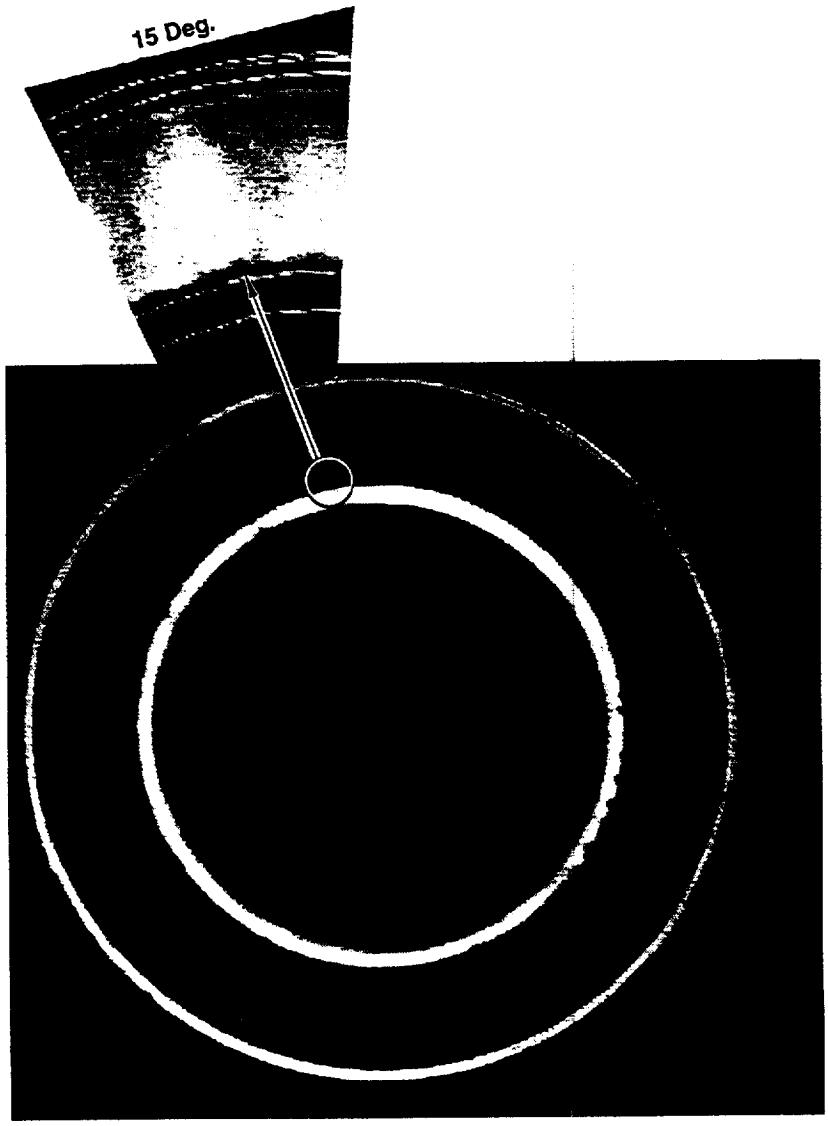

Figure 19. Pulse-echo Ultrasonic image of TMC after Spin Testing to 60,800 rpm at 316C and before Final Burst.

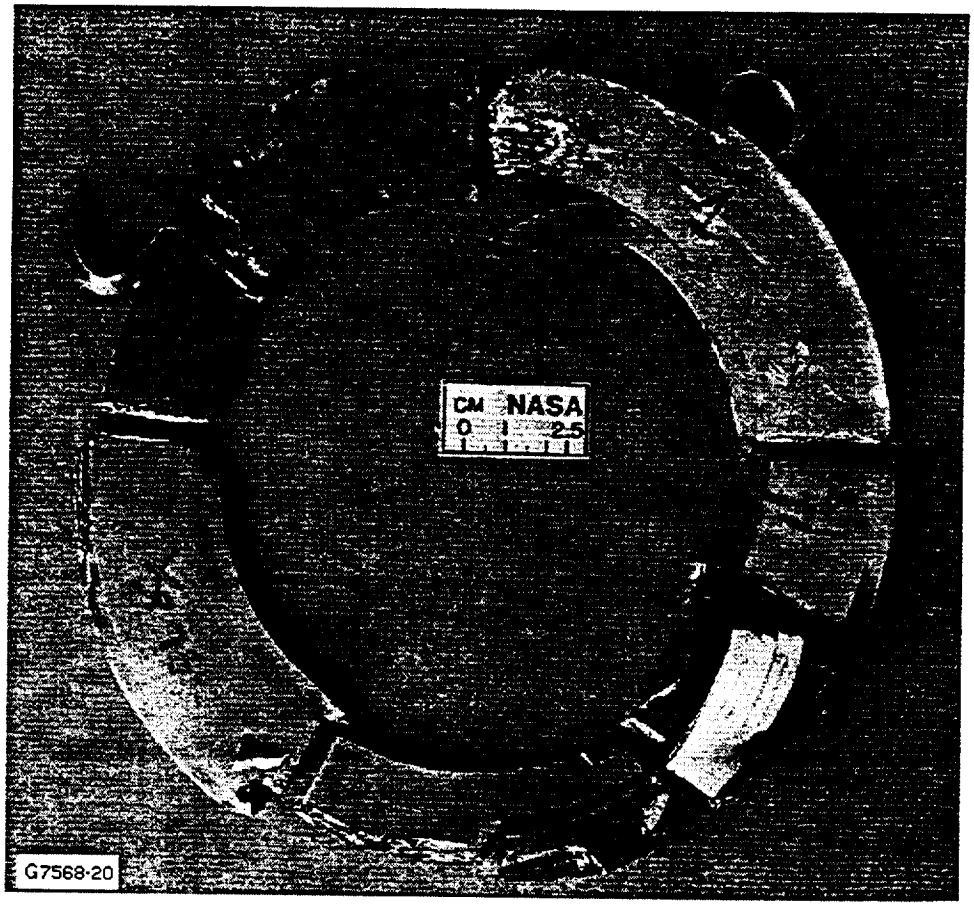

Figure 20. Photograph of Reconstructed TMC after Burst at 316C (600F).

3.3 Strain Data Analysis

Limited analysis of the strain data was performed. A comparison of the hoop strain recordings with the finite element model analysis for the 21C (70F) test run is given in Figures 21 and 22. The ANSYS code was used to convert the rotational speed to stress valves using the materials property data in Figure 12 and the specific ring geometry used in the test.

The correlation with the first run is good, indicating that the recording system, while not perfect, was reasonable. Simple analysis shows the hoop elastic modulus to be about 207 GPa (30 msi).

It is clear that the correlation with the second run is not as good. Poorer correlation was obtained for the elevated temperature test runs, with the strain data indicating a stiffening of the TMC. These data could not be rationalized since such behavior would not be expected. Some change in composite modulus could possibly arise because of the nature of the test program in that the TMC ring was subjected cyclic testing, although only a few cycles were imposed. The effect of cyclic stress on the mechanical behavior of the composite was beyond the scope of this revised program.

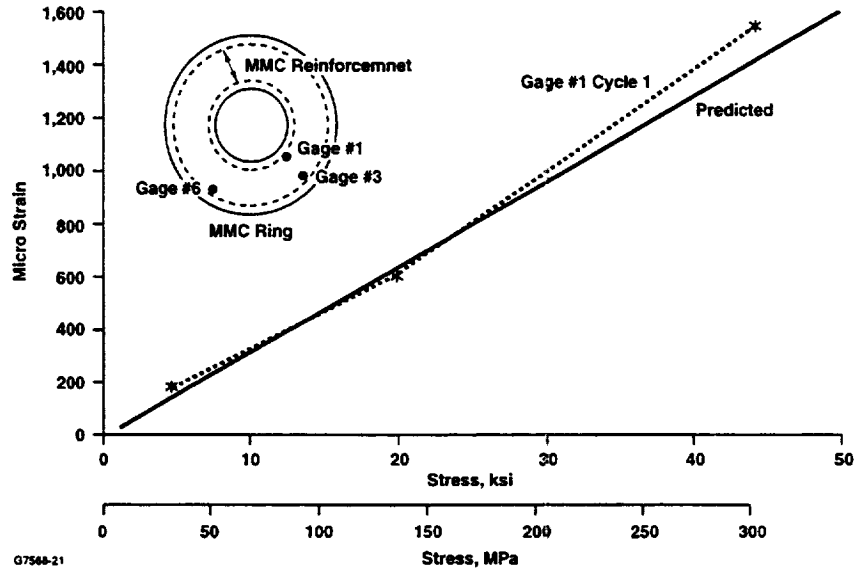

Figure 21. Comparison of Strain Gauge Data with FEM Calculation. 21C (70F) Spin Test, Gauge 1.

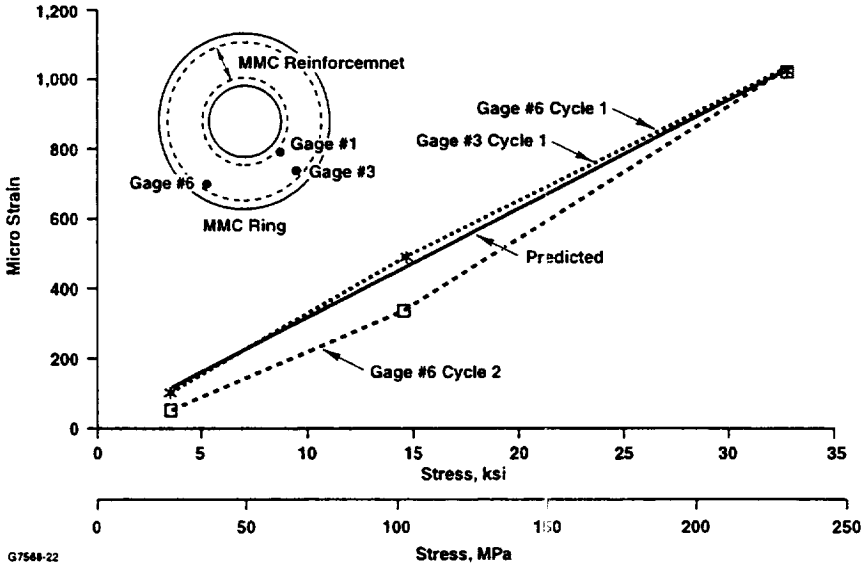

Figure 22. Comparison of Strain Gauge Data with FEM Calculation. 21C (70F) Spin Test, Gauges 3 and 6.

4. CONCLUSIONS

(1) Defect-free, small diameter, SCS-6/Ti-6Al-4V TMC rings were successfully made using a NASA modified approach to the Textron Specialty Materials grooved foil-fiber process.

(2) A spin test arbor employing "soft touch" fingers was designed having TMC ring burst and low-cycle fatigue capability. The arbor performed as designed in the burst test and this design is now being used by NASA for fatigue spin tests in other programs.

(3) Spin tests were successfully conducted on an instrumented TMC ring at temperatures to 316C (600F).

(4) The TMC ring burst at 316C (600F) occurred at a speed of 61,200 rpm, a value close to the predicted speed of 64,000 rpm.

(5) An internal pressurization test apparatus for ring burst was designed and constructed. While suitable for ambient temperature testing, the apparatus failed to reach the required pressure for ring burst at 316C(600F) due to leakage of fluid around seals. Despite a number of remedial steps this problem could not be overcome.

5. REFERENCES

1. Lewis, R.C. and Nagy, P.: " MMC Ring Fabrication with Grooved Foil Preforms," Proceedings of the Titanium Metal Matrix Composite II Workshop, LaJolla, CA, 2-4 June, 1993; WL-TR-93-4105, pp 131-157.

2. Merrick, H.F.; Aksoy, S.Z.; Costen, M.; Ahmad, J.; and Arnold, S.M.: "Multi-Axial Deformation of an SCS-6/Ti-6Al-4V Composite Ring," HITEMP Review 1995: Advanced High Temperature Engines Materials Technology Program, NASA CP-10178, 1995, pp 35-1 to 35-9.

3. Merrick, H.F.; Aksoy, S.Z.; Costen, M.; Arnold, S.M.; and Baaklini, G: "Spin Testing of SCS-6 Fiber Reinforced Ti-6Al-4V Disks," HITEMP Review 1997: Advanced High Temperature Engines Materials Technology Program, NASA CP-10192 1997, pp 40-1 to 40-9.

4. Baaklini, G.Y., Roth, D.J. and Kautz, H.E.: "Structural Characterization of Metal Matrix Composites Using NDE Data," HITEMP Review 1997: Advanced High Temperature Engines Materials Technology Program, NASA CP-10192, 1997, pp 41-1 to 41-15.

APPENDIX I

A MODEL TO PREDICT BUCKLING OF A SINGLE FIBER IN HOOP REINFORCED COMPOSITE RINGS

by Jalees Ahmad

(17 pages)

1.0 Introduction

Due to consolidation process induced residual stresses and/or due to thermal and mechanical applied loads, the fibers in a uniformly reinforced composite ring may be susceptible to elastic instability. For example, Figure 1 shows schematic view of a metal matrix composite (MMC) ring insert surrounded by metal on its inner and outer perimeters. The MMC insert has continuous circumferential fibers. The configuration schematically shown in Figure 1 is under consideration for providing a basis for the design of high performance rotors in advanced aircraft engines.

During the cool down portion of the consolidation process, the MMC and, therefore, the fibers can experience considerable amount of hoop compression because the coefficient of thermal expansion (CTE) of the fiber material (such as silicon carbide) is much smaller than that of the matrix material (such as a titanium alloy or intermetallic) and of the metal surrounding the MMC insert. A fiber may also be subjected to either tensile or compressive radial stress (depending on a fiber's location within the insert).

In the present work a model is developed which can be used to investigate possible buckling of a single fiber subjected to the combined action of hoop and radial stresses.

2.0 Fiber Microbuckling Under Combined Hoop and Radial Stresses

In this section we first present the mathematical model of a single fiber under combined action of hoop and radial stresses. The derivation of the mathematical model is followed by some parametric results relevant to an MMC reinforced metal ring.

2.1 Mathematical Model

Consider a circular arc of length $2\alpha R$ of a single fiber subjected to hoop force P_h, and uniform radial force per unit length, p_r, as shown in Figure 2. The fiber is located at a radial distance R from the ring center, which is large compared to the fiber radius (r). The fiber in Figure 2 can be considered to be a curved beam-column, thus allowing the use of the simple beam theory in its analysis.

With reference to Figure 2, the governing equation for fiber deflection can be expressed as follows:

$$\frac{d^2y}{dx^2} + a^2y + b^2x - c + \frac{1}{\sqrt{R^2 - x^2}}\left(1 + \frac{x^2}{R^2 - x^2}\right) = 0 \ , \qquad (1)$$

where,

$$a^2 = \lambda^2 \cos\alpha - \eta^2(1 - \cos\alpha), \qquad (2)$$

$$b^2 = \eta^2 \sin\alpha, \qquad (3)$$

$$c = \eta^2\left[R\cos\alpha(1 - \cos\alpha) - R\sin^2\alpha\right] , \qquad (4)$$

$$\lambda^2 = \frac{P_h}{EI} \ , \qquad (5)$$

$$P_h = \sigma_H \pi r^2,$$

$$\eta^2 = \frac{Rp_r}{EI}, \qquad (6)$$

$$p_r = 2\sigma_r rR \ ,$$

σ_H = Hoop stress in the fiber (positive when tensile),
σ_r = Radial stress in the fiber (positive when tensile),
E = Young's Modulus of the fiber material, and
I = Moment of inertia of the fiber cross-section .

The general solution of equation (1) is as follows:

$$y(x) = \left(\int \left(1 + x^2 R\left(\frac{-3}{2}\right)^2 \sqrt{R^2 - x^2} + b^2 x\sqrt{R^2 - x^2} - c\sqrt{R^2 - x^2} - x^2 x\left(\frac{-3}{2}\right)^2 \sqrt{R^2 - x^2} \right) \right.$$

$$\sin(a\,x) \Big/ \sqrt{R^2 - x^2}\, dx \cos(a\,x) - \int \cos(a\,x)$$

$$\left(1 + x^2 R\left(\frac{-3}{2}\right)^2 \sqrt{R^2 - x^2} + b^2 x\sqrt{R^2 - x^2} - c\sqrt{R^2 - x^2} - x^2 x\left(\frac{-3}{2}\right)^2 \sqrt{R^2 - x^2} \right) \Big/$$

$$\left. \sqrt{R^2 - x^2}\, dx \sin(a\,x) + \_C1 \cos(a\,x)\, a + \_C2 \sin(a\,x)\, a \right) \Big/ a \qquad (7)$$

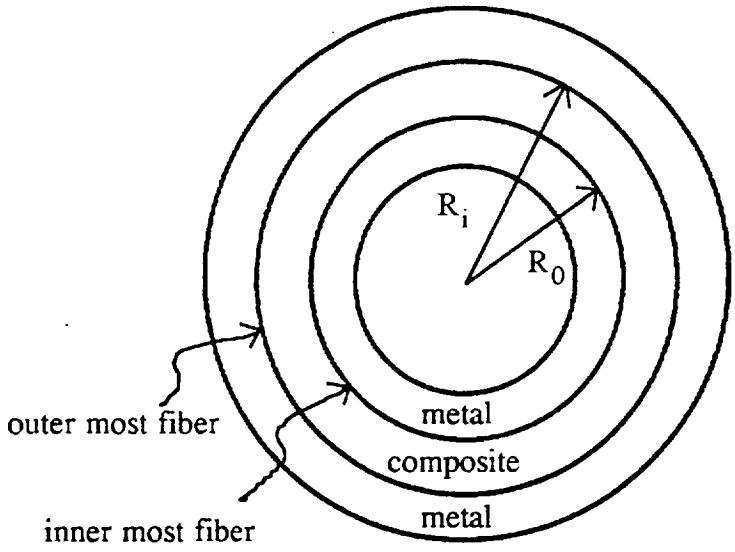

Figure 1: Metal Ring With MMC Hoop Insert

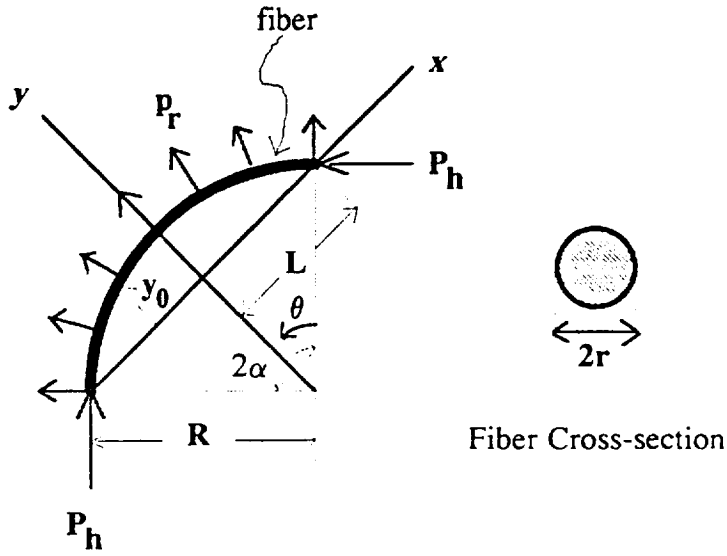

Figure 2: Arc Segment of a Single Fiber Under Radial and Hoop Forces

where C1 and C2 are arbitrary constants to be evaluated using specific boundary conditions. The solution is simplified somewhat when it is assumed that R>>L, so that in equation (1), (R^2-x^2) can be replaced by R^2. Then,

$$y(x) = -\frac{-a^2 R^3 c + a^2 R^2 - 2 + b^2 x a^2 R^3 + x^2 a^2}{a^4 R^3} + \_C1 \cos(a x) + \_C2 \sin(a x) \tag{8}$$

For the case when both ends of the fiber segment in Figure 1 are pinned, displacement (y) is zero at $x = \pm L$. Then, the constants C1 and C2 of equation (8) are as follows:

$$C1 := -\frac{R^3 a^2 c - R^2 a^2 + 2 - L^2 a^2}{\cos(a L) R^3 a^4}$$

$$C2 := \frac{b^2 L}{\sin(a L) a^2} \tag{9}$$

Equations (8) and (9) provide the complete solution for the fiber pinned at both ends. For non-zero a and L, the solution becomes unbounded when $a = \pi/2L$. This provides the following condition for the first buckling mode to occur when:

$$\lambda^2 \cos\alpha - \eta^2 (1 - \cos\alpha) = \frac{\pi^2}{4L^2} \tag{10}$$

In the special case of $\eta = 0$ and $\alpha = 0$, equation (10) becomes the same as Euler's buckling equation for a column of length 2L. In general, equations (5) and (6) together with equation (10) provide the following expressions for normalized critical hoop and radial stresses:

$$\bar{\sigma}_{HC} = -\left[\left(\frac{\pi r}{4 \sin\alpha}\right)^2 + \frac{2R}{\pi r}(1 - \cos\alpha)\bar{\sigma}_r\right] \sec\alpha \tag{11}$$

$$\bar{\sigma}_{rC} = -\left[\left(\frac{\pi r}{4 \sin\alpha}\right)^2 + \bar{\sigma}_H \cos\alpha\right] \frac{\pi r}{2R}(1 - \cos\alpha)^{-1} \tag{12}$$

Note that in the above equations, $L = R \sin\alpha$ and

$$\bar{\sigma}_{HC} = \sigma_{HC}/E \;,\; \bar{\sigma}_{rC} = \sigma_{rC}/E \;,\; \bar{\sigma}_H = \sigma_H/E \text{ and } \bar{\sigma}_r = \sigma_r/E$$

2.1 Parametric Results

The model presented in the foregoing section can be employed to study the behavior of an arc segment of a fiber which (over a length of $2\alpha R$) has either somehow debonded from, or remained unbonded with the surrounding matrix.

Consider a fiber whose axis is at radial distance R from the ring center (Figure 1). If a fiber segment has totally debonded from the matrix on both sides (i.e. along R+r and R-r), then there is no net radial force acting on the fiber segment. Thus, $P_h \neq 0$ and $p_r = 0$. On the other hand, if the fiber segment is detached from the matrix only on one side, there is a net radial stress on the fiber segment, i.e. $P_h \neq 0$ and $p_r \neq 0$. In order to employ the model of the previous section to the case of $p_r \neq 0$, it must be assumed that the net radial force remains unchanged while the fiber segment deforms. This implies that the matrix material on either side of the fiber segment offers no resistance to deformation. In the following we present results of the above two cases.

2.1.1 Case 1: $P_h \neq 0$ and $p_r = 0$

Figures 3(a, b, c and d) show the deflection behavior of a fiber segment subjected to increasingly compressive value of hoop stress. In these figures, the hoop stress is indicated as 'sh', the vertical axis shows deflection in inches, and the distance x see (Figure 2) is in inches. In all cases, the deflection profile (which is indicative of buckling mode shape) is the same. In the plots, the following numerical values for the various parameters in equations (8) and (9) were used:

fiber diameter (2r)=0.00551 inch,
fiber material's Young's Modulus (E)=58000 Ksi, and
fiber location (R)=3.5 inch in Figures 3(a, b and c) and 4.0 inch in Figure 3(d).

The plots in Figure 3(a, b and c) were obtained for increasing value of the half subtended angle α from 1.0 degree to 10.0 degrees. The figures show a strong effect of α on the hoop stress at which deflections begin to grow indefinitely. As seen, this value of hoop stress varies from approximately 70 Ksi for $\alpha=1.0$ degree to approximately 2.5 Ksi for $\alpha=5.0$ degrees and less than 7.5 Ksi for $\alpha=10.0$ degrees. For a given α, the effect of changing fiber location within the ring has a relatively small effect on the hoop stress close to instability. This is seen by comparing Figures 3(b) and 3(d) which both correspond to $\alpha=5.0$ degrees, but to R=3.5 inch and R=4.0 inch, respectively.

Figure 4 shows the critical hoop stress values in Ksi (vertical axis) for various α and R combinations. As noticed in Figure 3, the critical hoop stress value falls rapidly with α and reaches less than 10 Ksi for $\alpha>2.5$. This is more clearly seen in Figure 5 which shows the critical hoop stress values for a fiber segment located at R=3.5 inches.

2.1.2 Case 2: $P_h \neq 0$ and $p_r \neq 0$

In this case we consider the combined effect of hoop and radial forces acting on the fiber segment. But before investigating the combined effect it is instructive to look at the deflected shape of the fiber segment in Figure 6 only under the action of a uniform radial stress directed toward the center of the ring. In the particular case shown in Figure 6, hoop stress=0.0, α=5 degrees and R=3.5 inches. It is seen that the fiber deflection is in the opposite direction than that due to compressive hoop stress (Figure 3). Figures 7 and 8 show the same result when a compressive hoop stress of 1.0 Ksi and 2.0 Ksi, respectively, is present. In Figure 8, the deflection shape is seen to change as increasingly compressive radial stress is applied.

Figure 9 shows critical hoop stress value in Ksi as a function of α and compressive radial stress. It is interesting to note that a positive buckling hoop stress can occur if a sufficiently large compressive radial stress is present.

Figure 10 shows critical radial stress value in Ksi as a function of α and compressive hoop stress. Again it is seen that a positive buckling radial stress can occur if a sufficiently large compressive hoop stress is present.

3.0 Conclusions

The model developed in the present work can be effectively used to investigate microbuckling of individual fibers during the consolidation of an MMC reinforced rotor. The parametric analyses performed using the model indicate that a net compressive radial force acting on a partially unbonded (or debonded) fiber segment can result in the mode of fiber break sometimes observed in MMC reinforced rings. In this mode the broken fiber ends are found to point radially inward toward the center of the ring. The parametric studies show that this mode is possible with or without the presence of hoop stress in the fiber segment. A plausible explanation for the observed fiber breaks is that at certain locations of outer fibers in the ring, lack of bond or debond occurs on either side of the fiber (i.e. at R+r or R-r) resulting on a net negative radial force acting on the fiber segment. This force in conjunction with hoop stress causes inward buckling of the fiber segment. Detailed stress analyses of the MMC ring consolidation process are needed to determine whether the quantitative values of critical hoop and radial stress values estimated in the present work are indeed possible.

Deflection

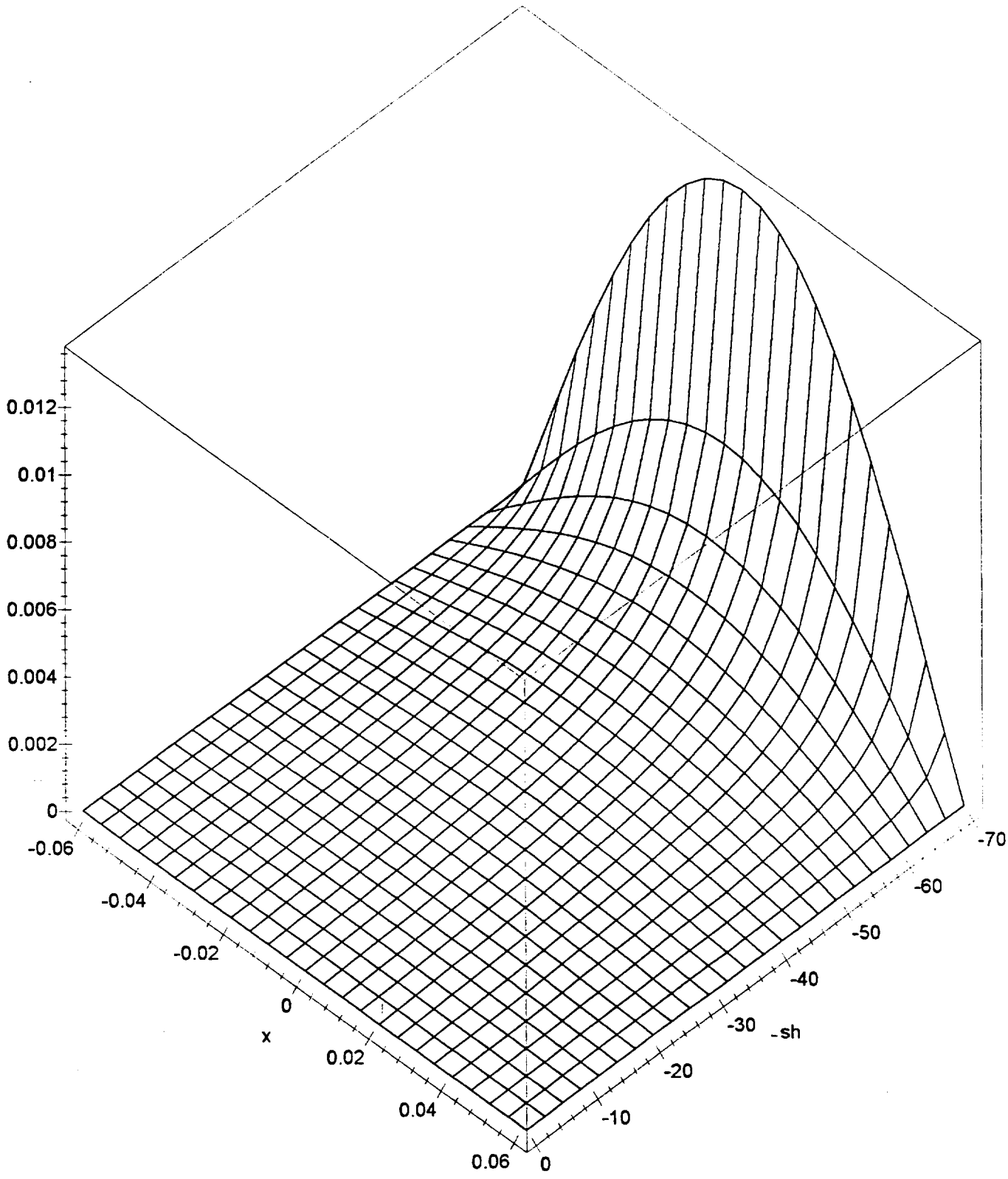

Figure 3(a): Deflection of fiber segment (vertical axis in inches) subjected to increasing compressive hoop stress 'sh' (in Ksi). The fiber segment length is along the x axis (in inches), R=3.5 inches, α=1.0 degree.

Deflection

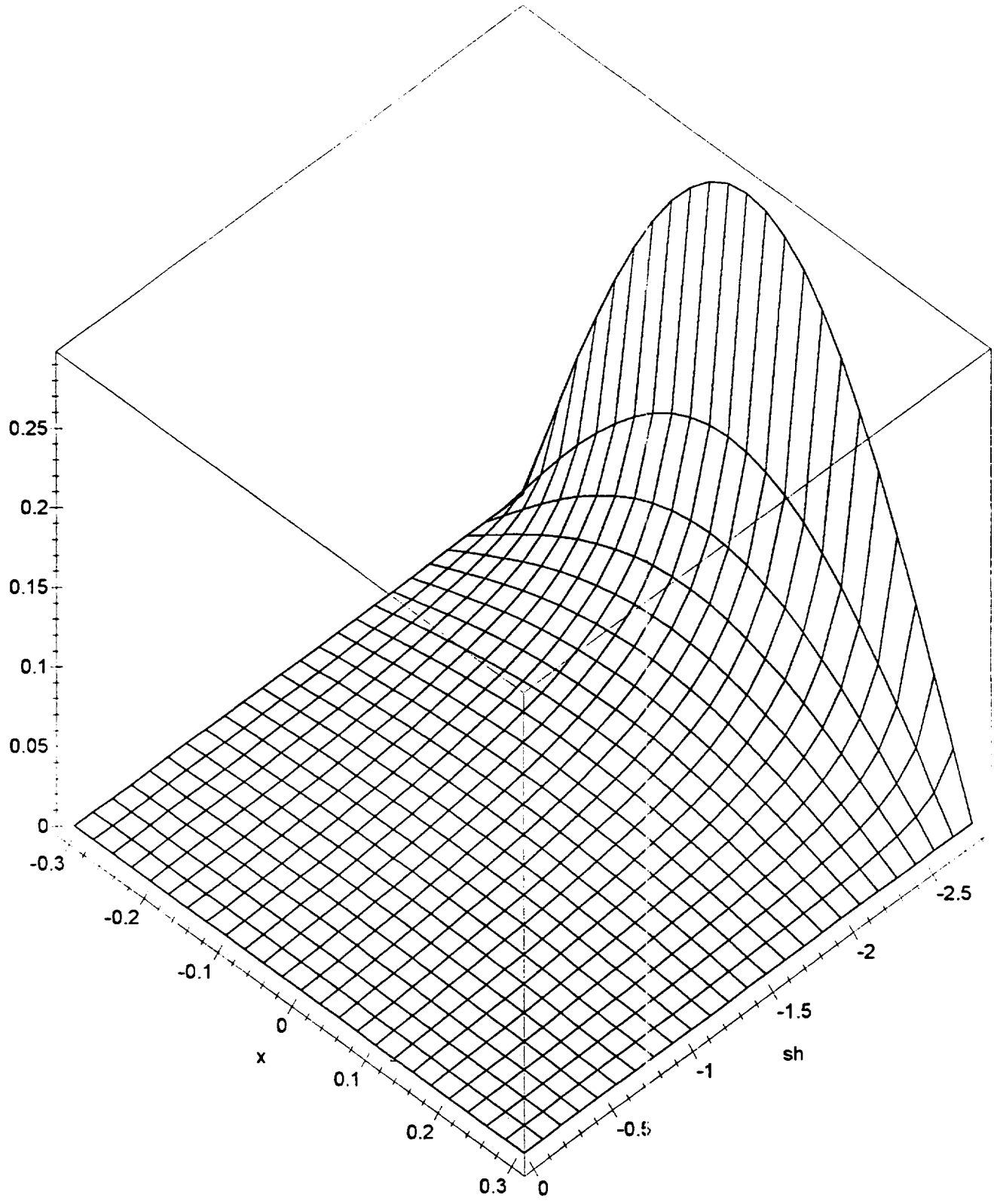

Figure 3(b): Deflection of fiber segment (vertical axis in inches) subjected to increasing compressive hoop stress 'sh' (in Ksi). The fiber segment length is along the x axis (in inches), R=3.5 inches, α=5.0 degrees.

Deflection

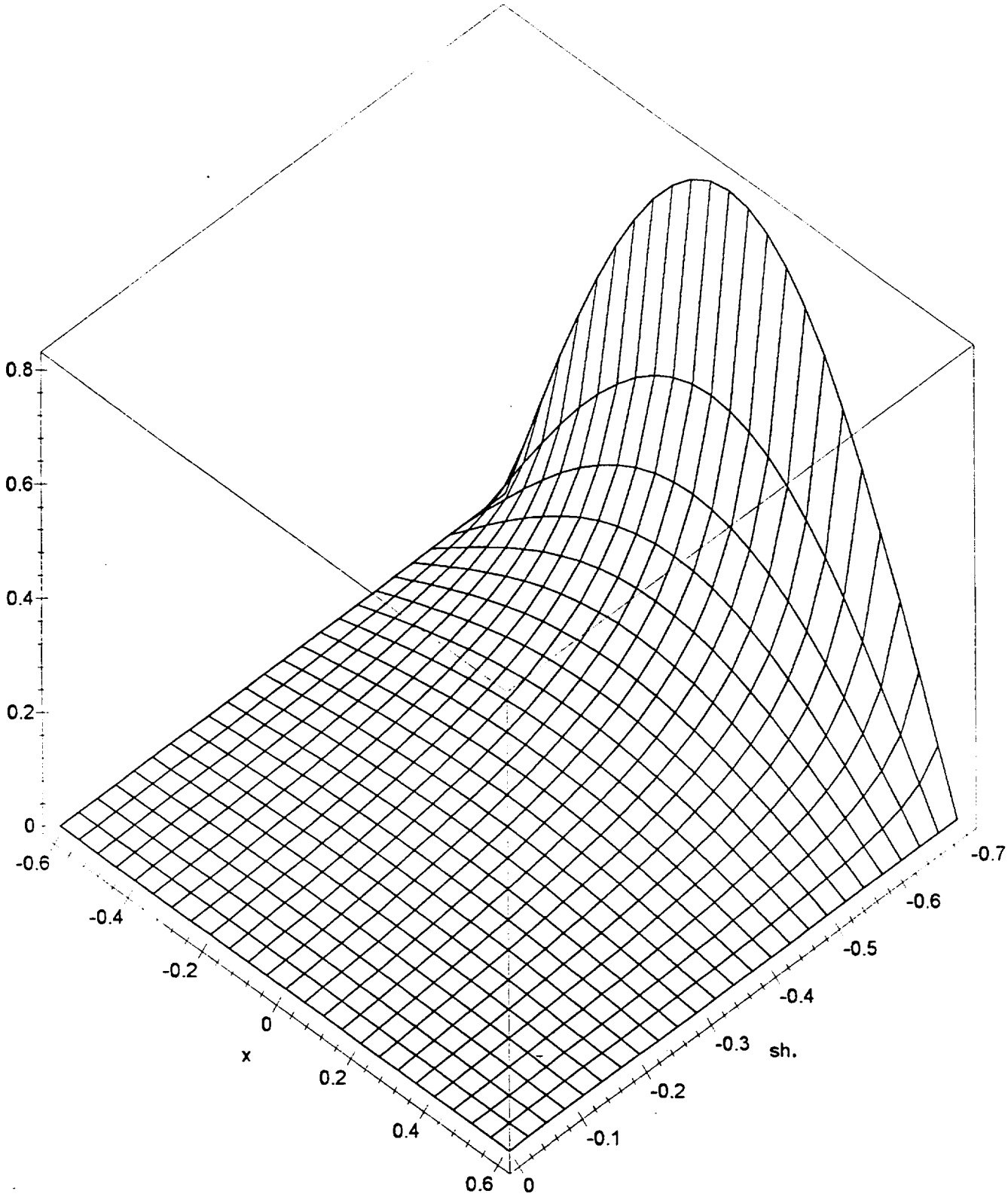

Figure 3(c): Deflection of fiber segment (vertical axis in inches) subjected to increasing compressive hoop stress 'sh' (in Ksi). The fiber segment length is along the x axis (in inches), R=3.5 inches, α=10.0 degrees.

Deflection

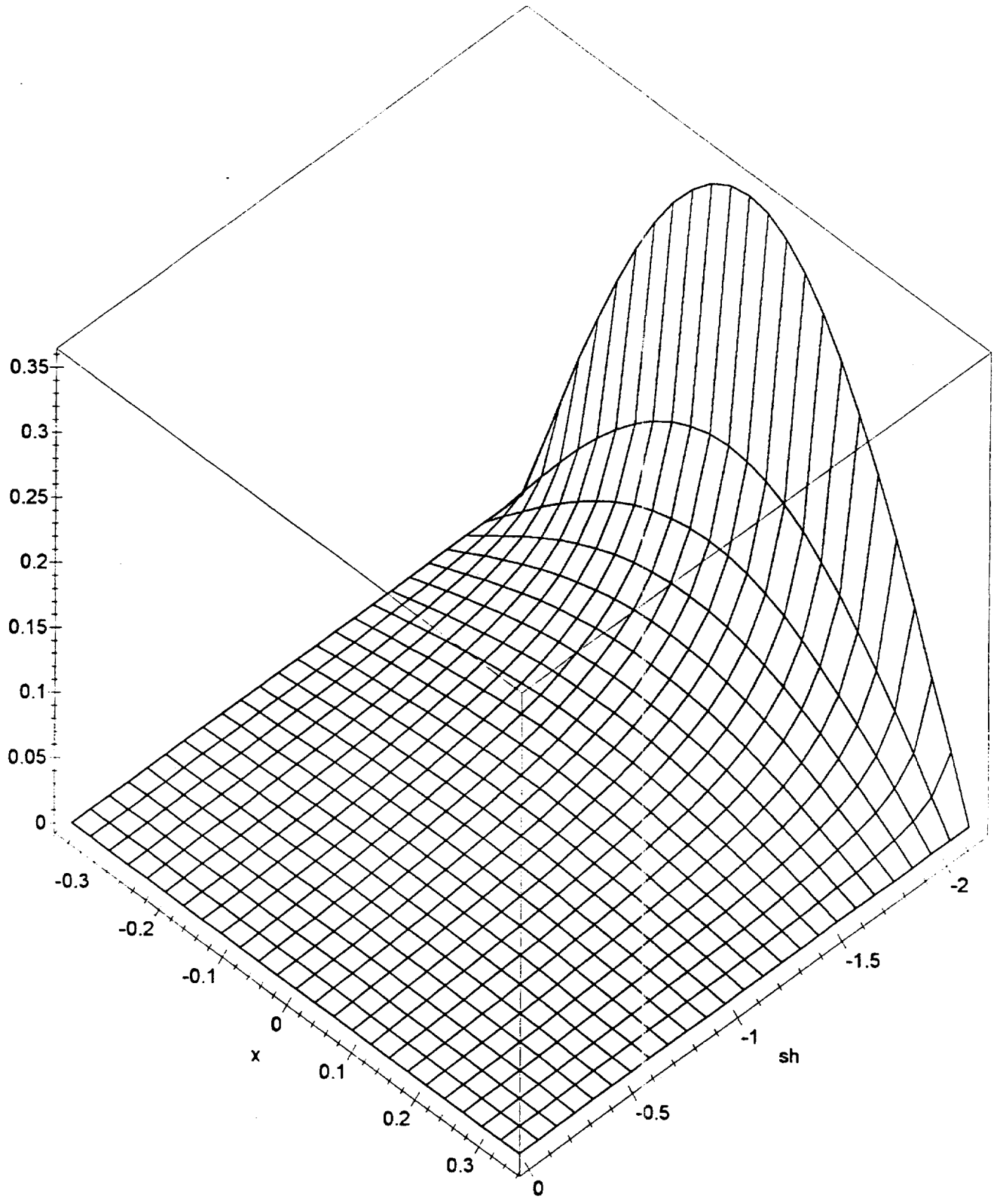

Figure 3(d): Deflection of fiber segment (vertical axis in inches) subjected to increasing compressive hoop stress 'sh' (in Ksi). The fiber segment length is along the x axis (in inches), R=4.0 inches, α=5.0 degrees.

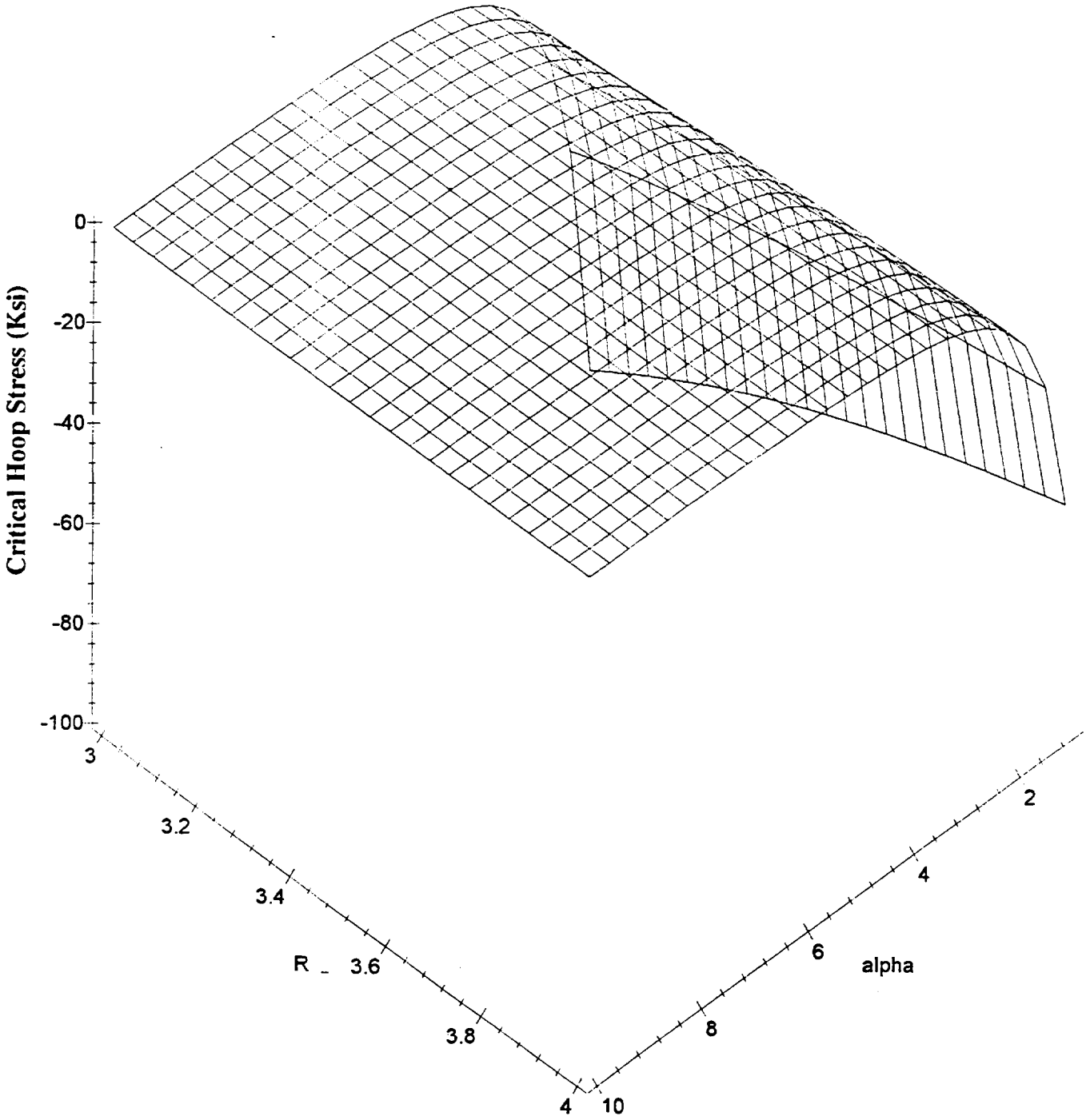

Figure 4: Critical Hoop stress for Case 1 as a function of half the arc angle (α) and fiber location within the ring.

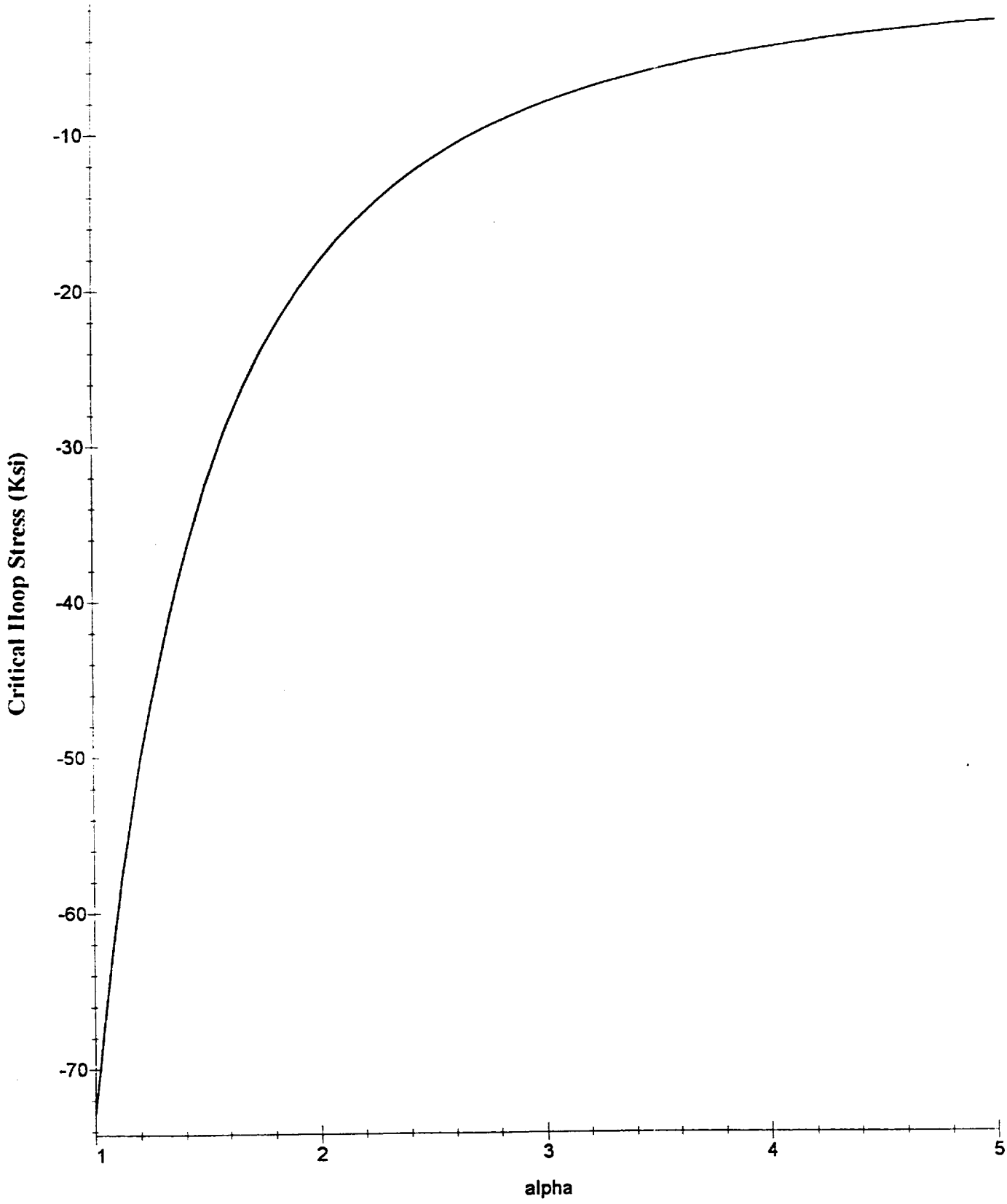

Figure 5: Critical Hoop stress for Case 1 as a function of half the arc angle (α) for R=3.5 inches.

Deflection

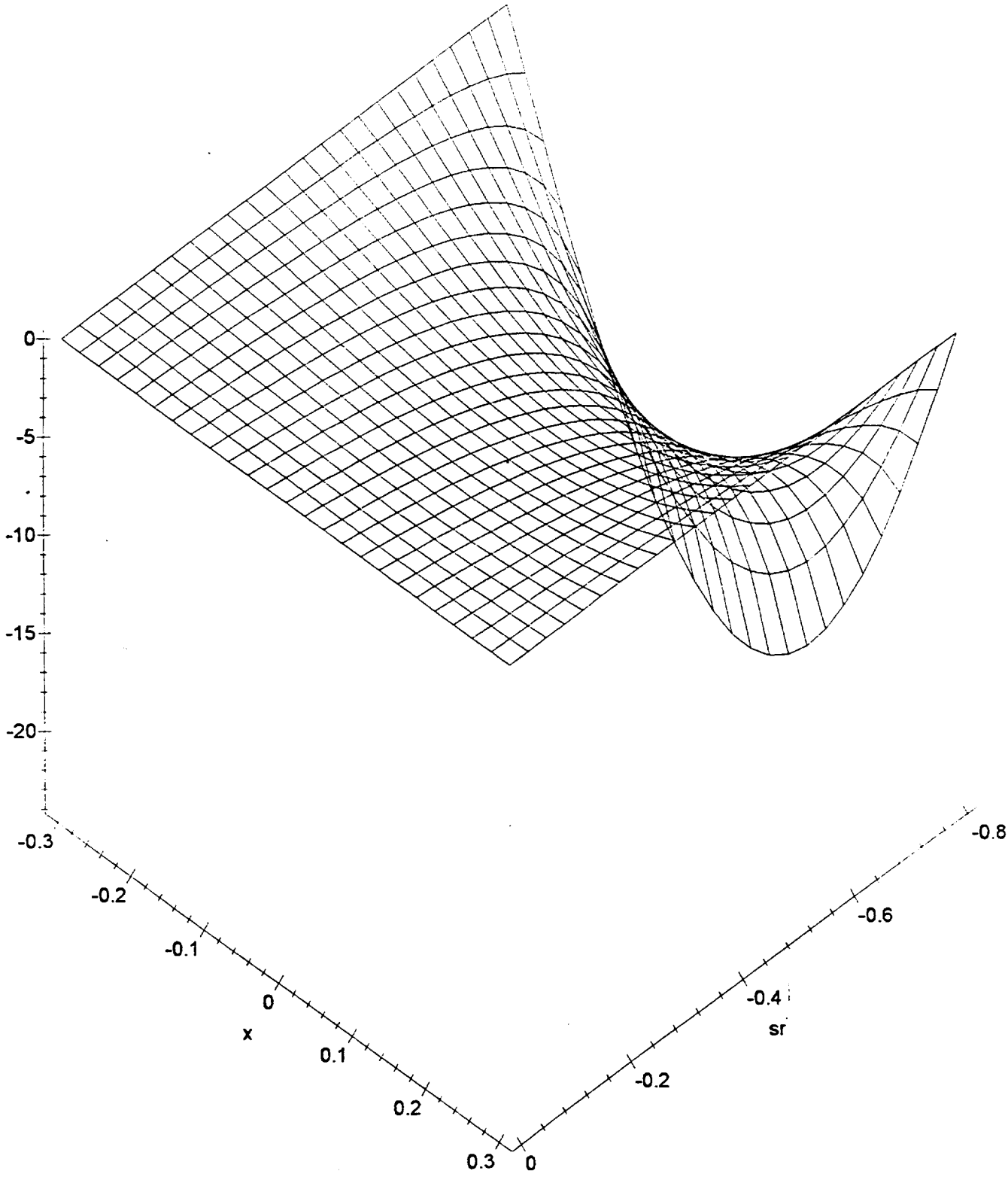

Figure 6: Deflection of fiber segment (α=5.0 degrees) in inches at R=3.5 inch and hoop stress=0.0 Ksi.

Deflection

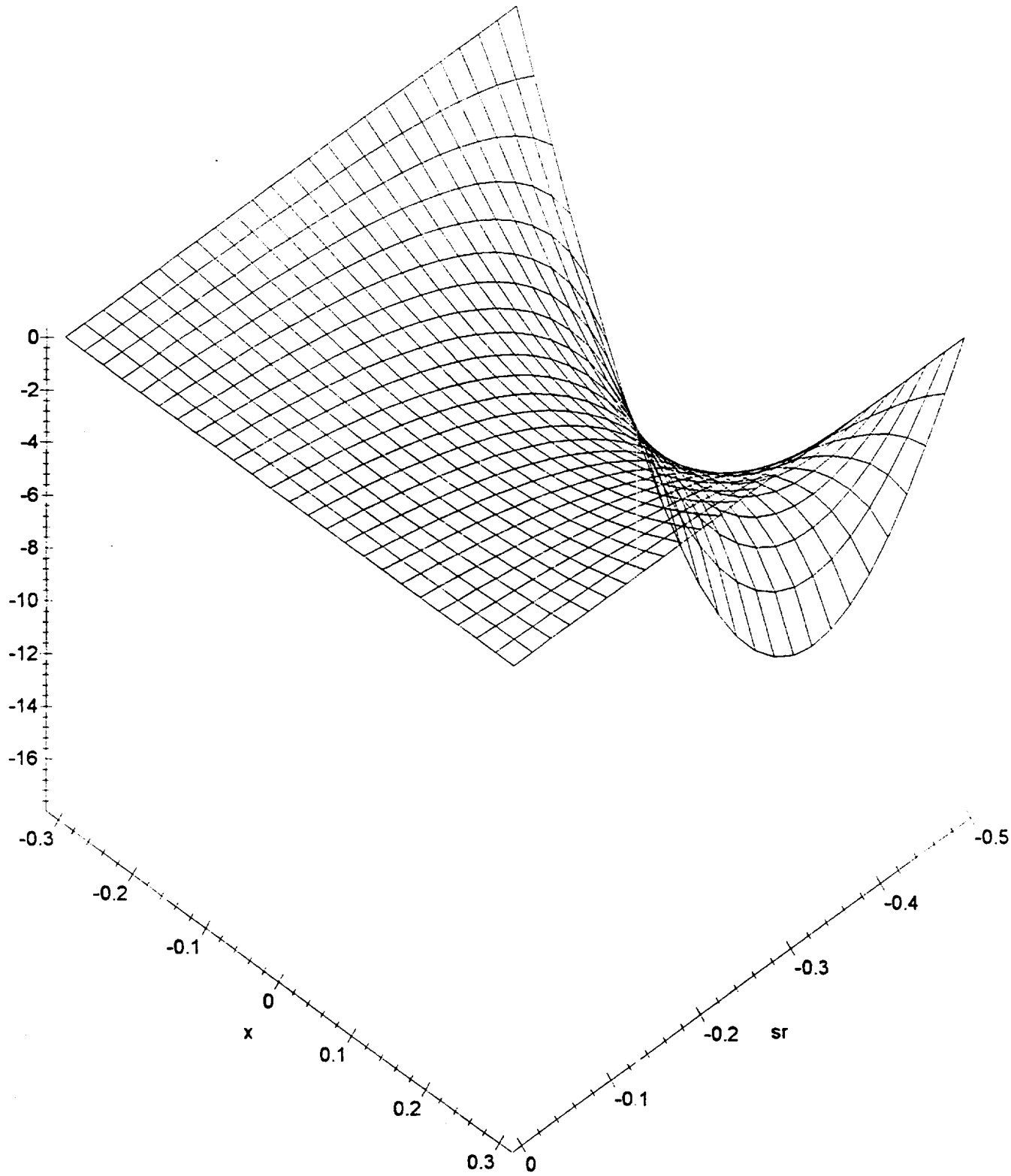

Figure 7: Deflection of fiber segment (α=5.0 degrees) in inches at R=3.5 inch and hoop stress=-1.0 Ksi.

Deflection

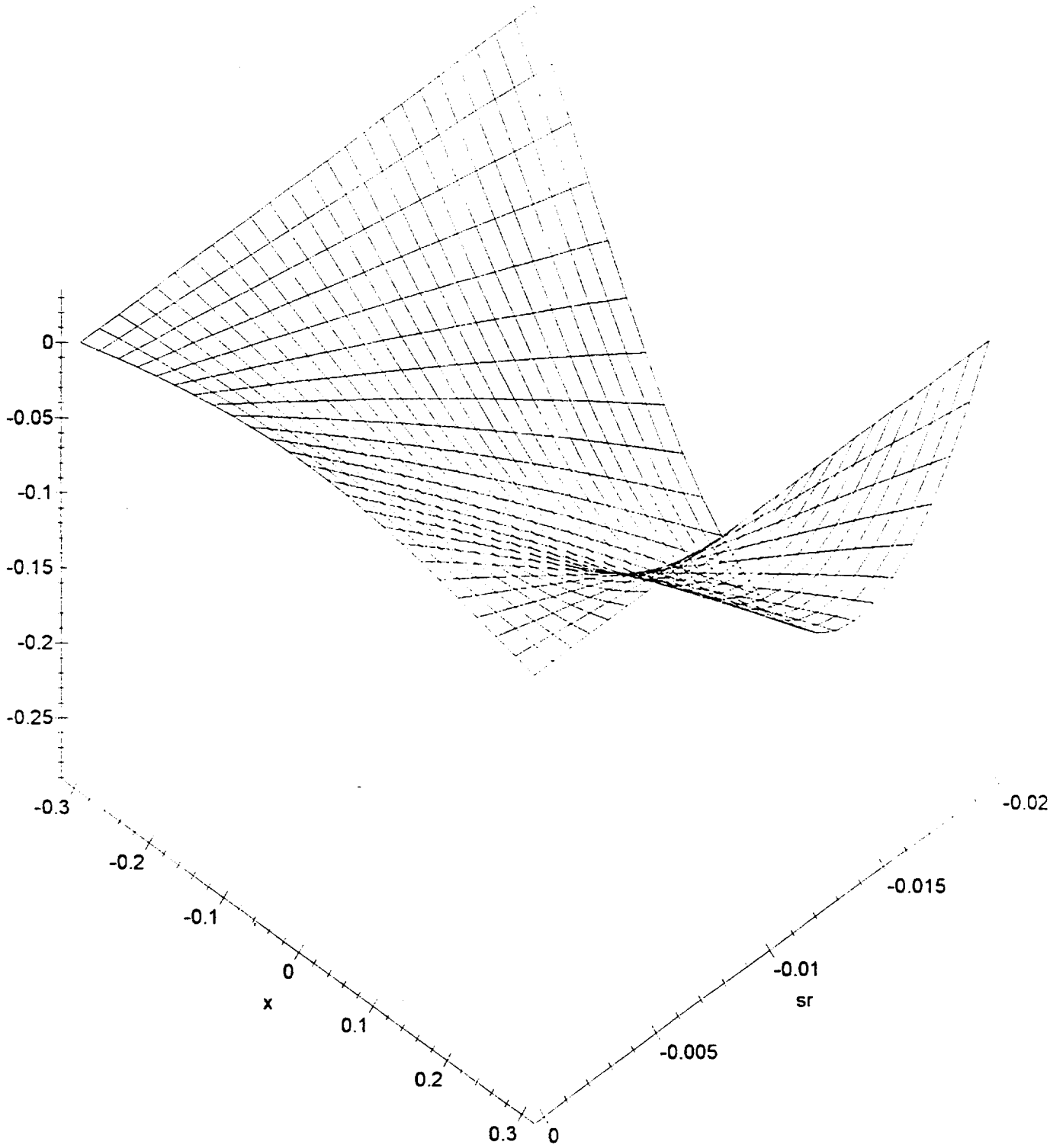

Figure 8: Deflection of fiber segment (α=5.0 degrees) in inches at R=3.5 inch and hoop stress=-2.0 Ksi.

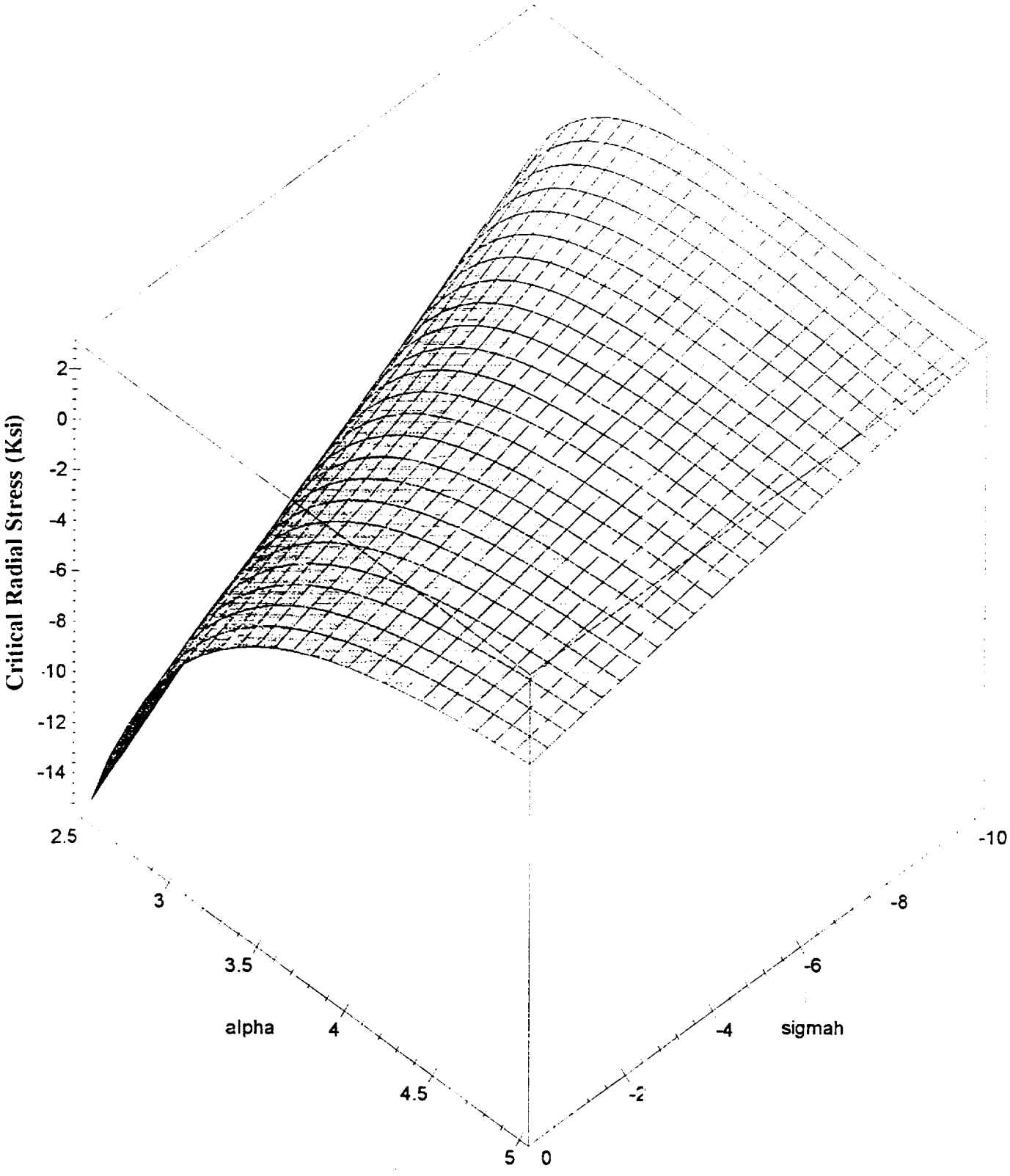

Figure 9: Critical Hoop Stress (Ksi) for Case 2 as a function of α and radial stress in the fiber at R=3.5 inches.

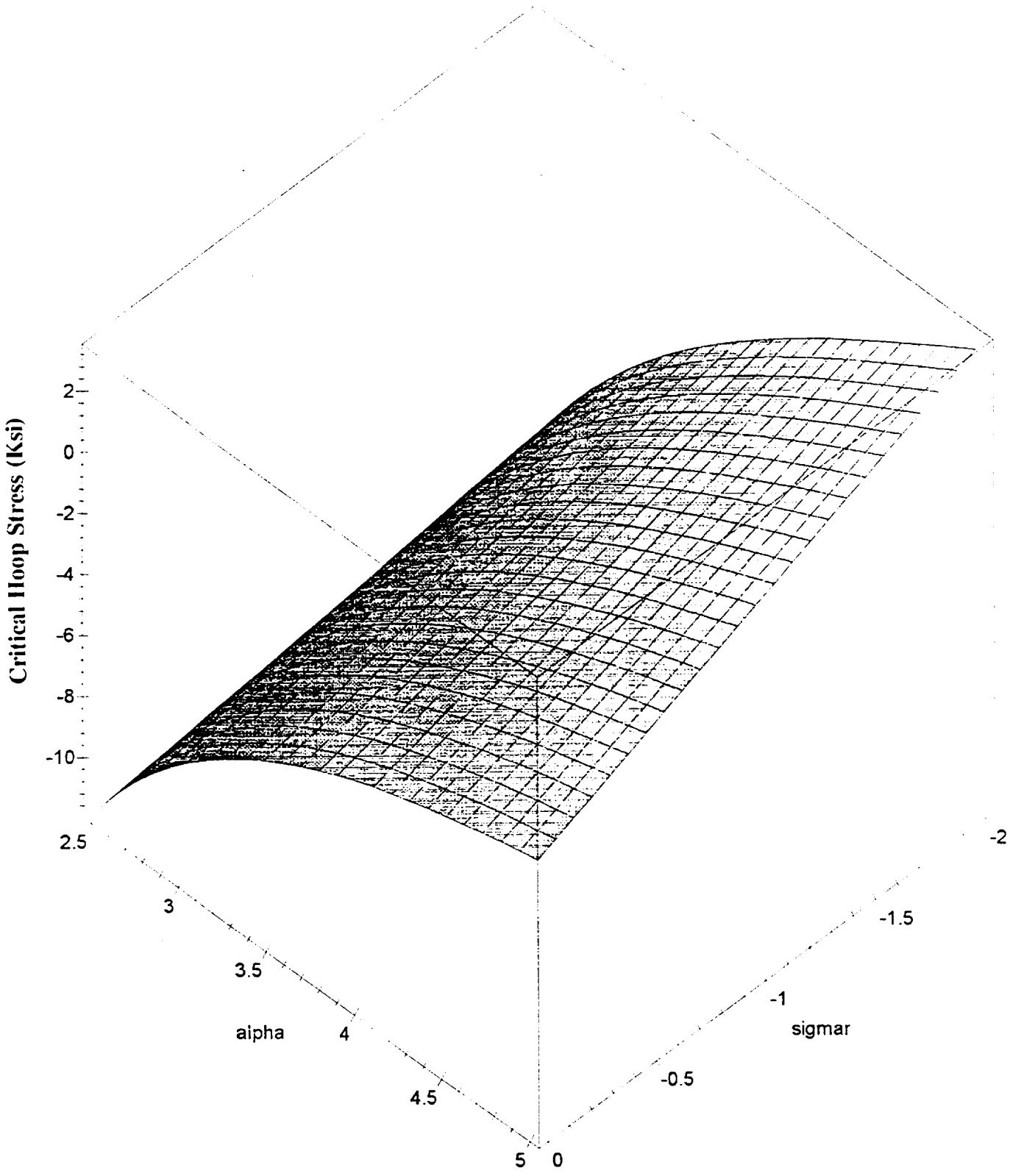

Figure 10: Critical Radial Stress (Ksi) for Case 2 as a function of α and hoop stress in the fiber at R=3.5 inches.

ATTACHMENT 1

REPORT ON MMC BEHAVIOR MODELING UNDER MULTIAXIAL STRESSES FOR MMC RING REINFORCED IMPELLER

(152 pages)

Report on

MMC Behavior Modeling Under Multiaxial Stresses

for

MMC Ring Reinforced Impeller

PHASE I

to

Textron Lycoming

by

Jalees Ahmad
and
Iftikhar Haq

AdTech Systems Research, Inc.
1342 N. Fairfield Road
Beavercreek OH 45432

Introduction

AdTech Systems Research, Inc. is pleased to submit this report on the Phase I effort under Contract No. NAS3-27027. The Phase I Statement of Work (entitled "Analytical Verification) required AdTech to perform the following two activities:

(1) Perform a literature search to obtain mechanical and physical property data on Ti-6Al-4V/SiC continuous fiber composites.

(2) Utilize collected data and selected analytical models to predict deformation response and burst pressure in an MMC ring to be tested by Textron Lycoming.

Both the above activities have been completed. The results are given in the following paragraphs.

Results of Literature Survey

The following two methods were used to conduct the search for data on Ti-6-4/SiC composites:

(1) Contact key technical personnel at main engine manufacturing companies.

(2) Computerized search

The first method resulted in acquiring a GE Aircraft Engines (GEAE) document entitled "Survey of Available Literature: Mechanical Properties of Ti-6Al-4V/SCS-6 and Ti-14Al-21Nb/SCS-6 Metal matrix Composites", prepared by G. A. Smith on March 29, 1990. This document provided extensive amount of data and important references on the composite of interest. A copy of this document was given to Dr. Steve Arnold of NASA Lewis Research Center on November 2, 1993 as instructed by Dr. Tapas Mukherji of Textron Lycoming. It is not clear if AdTech can provide a copy directly to Textron Lycoming as part of the present document.

The computerized search resulted in identification of a number of documents listed in Appendix A. The most relevant of these documents are described in Appendix B. Appendices A and B do not contain Textron Lycoming data which was provided to NASA LeRC as part of a bimonthly report.

Burst Test Analysis

The analysis approach followed in predicting the deformation behavior and burst pressure in a MMC ring (to be tested by Textron Lycoming) consisted of the following two steps:

(1) Using a nonlinear finite element analysis based micromechanics model, generate the unidirection composites global stress-strain response under biaxial (combined 0 and 90 degree) loading. This procedure is described in detail in Appendix C. Figure 1 (a-e) shows predicted global stress-strain response at room temperature under selected combinations of 0 degree (z-direction) and 90 degree (x-direction) loading.

The predicted composite stress-strain curves as well as Ti6-4 stress-strain curve were used as part of the input to an axisymmetric finite element analysis of the MMC ring (Figures 2 and 3) subjected to uniform internal pressure. The elastic constants for the composite were found using the micromechanics approach in the ASCA computer code. These constants are shown in Table 1. Figure 4 shows the result of finite element analysis in the elastic range in terms of stresses along a ring radius. The Hill's criterion was used to model yielding of the composite and isotropic hardening was assumed. The Ti6-4 layers were assumed to be isotropic. Figures 5(a) and 5(b) show the elastic-plastic analysis results at strain gage location 1 which is at the inside boundary of the MMC insert and experiences the highest stress.

Room temperature data on Ti6-4/SCS-6 panels suggests that 0 degree composite (or in-situ fiber) strain at failure to be approximately 1.0 percent. In the form of a ring, the fibers may have up to 0.11 percent initial strain. Assuming no significant processing related differences between composite panels and rings, we choose the strain of failure to be 0.89 percent. Then, using Figures 5 (a and b), the burst pressure for the ring is estimated to be 770 MPa.

Table 1. Constituent and Composite Elastic Constants

Fiber: $E = 392$ GPa, $\upsilon = 0.25$
Matrix: $E = 110$ GPa, $\upsilon = 0.30$
Composite ($\upsilon_f = 0.35$, unidirectional):
$E_{11} = 211.7$ GPa
$E_{22} = E_{33} = 169.6$ GPa
$\upsilon_{12} = 0.3$
$\upsilon_{13} = \upsilon_{23} = 0.22$

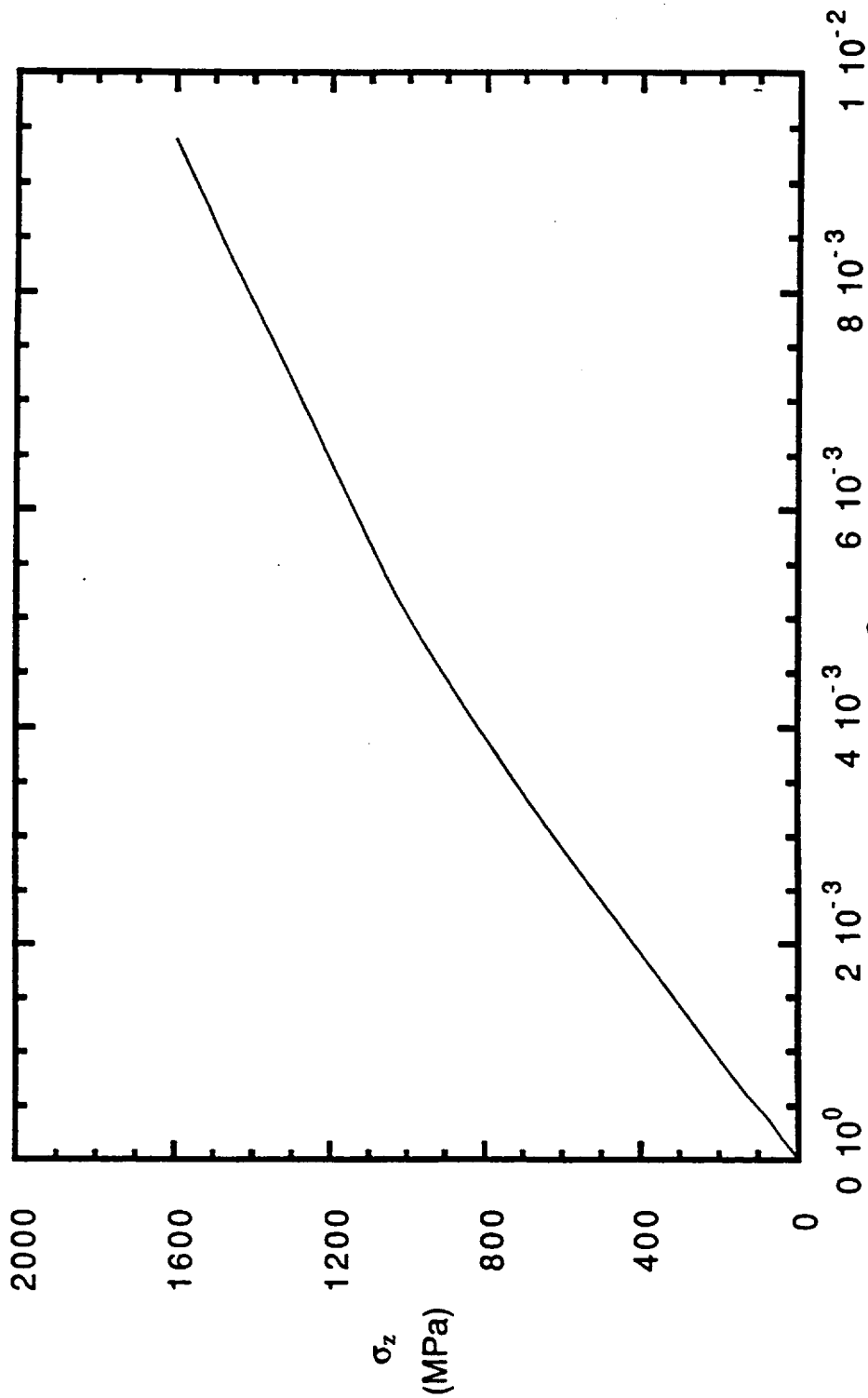

Figure 1(a). Predicted 0 degree tensile response.

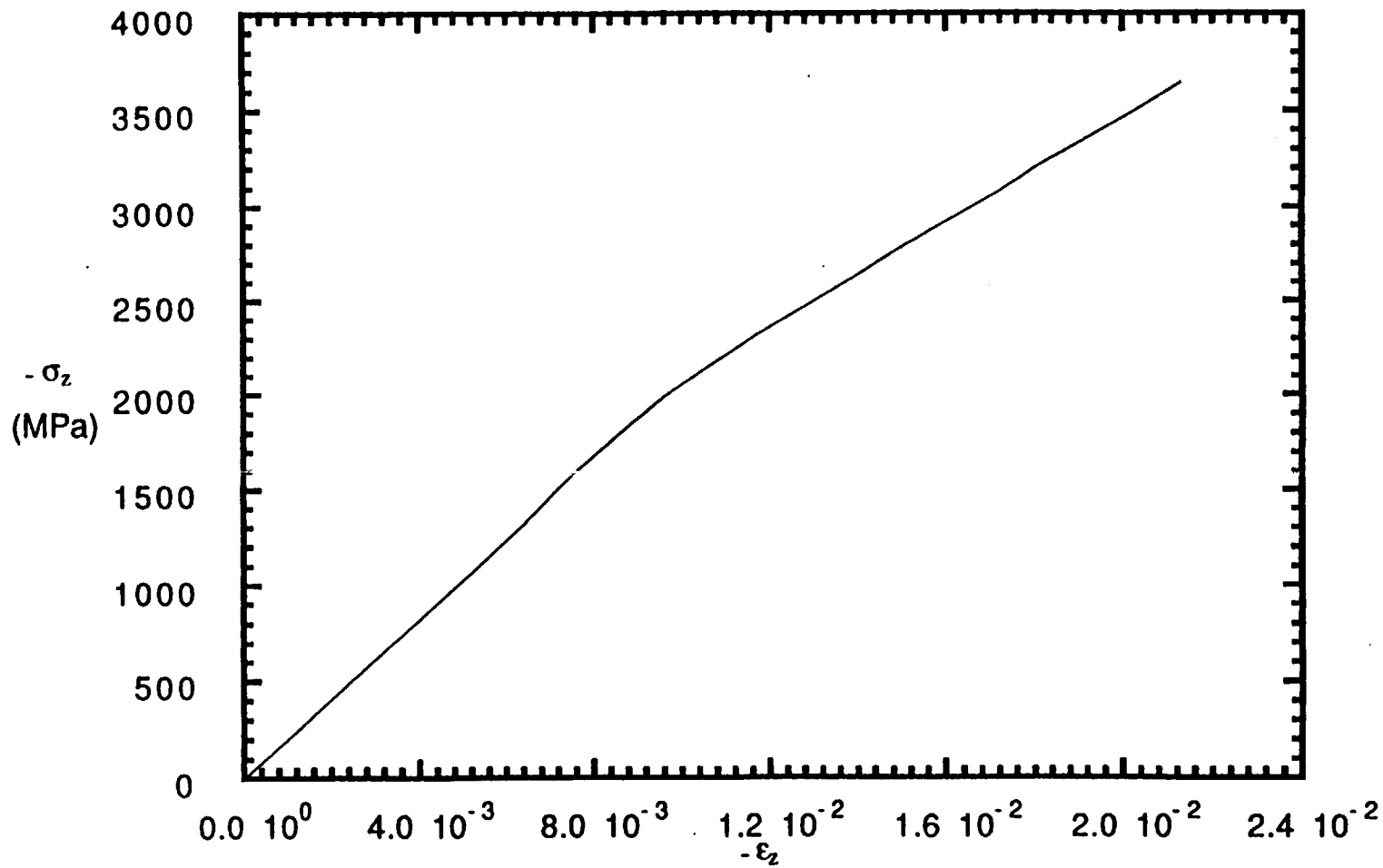

Figure 1(b). Predicted 0 degree compressive response.

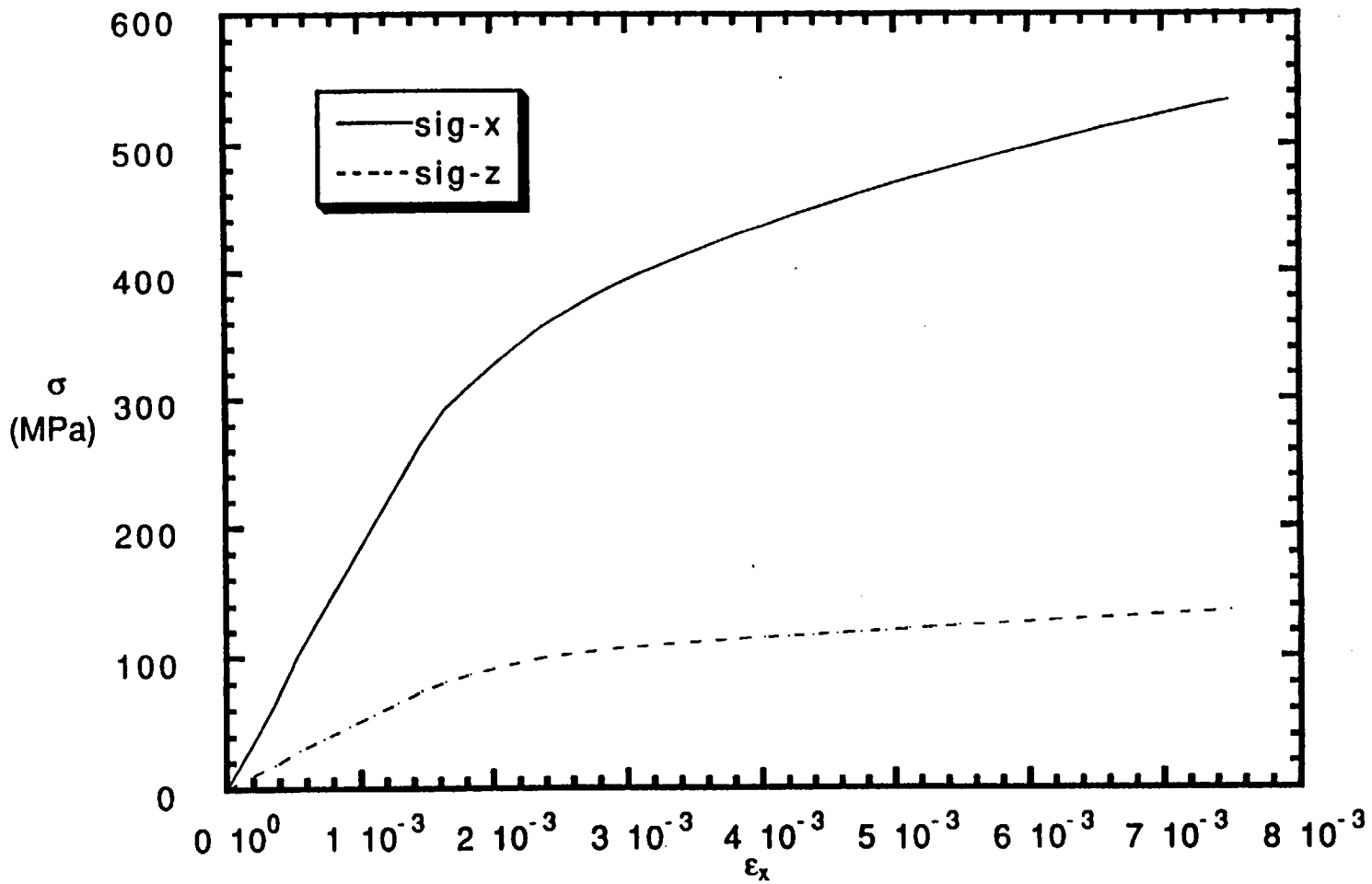

Figure 1(c). Predicted 90° tensile response.

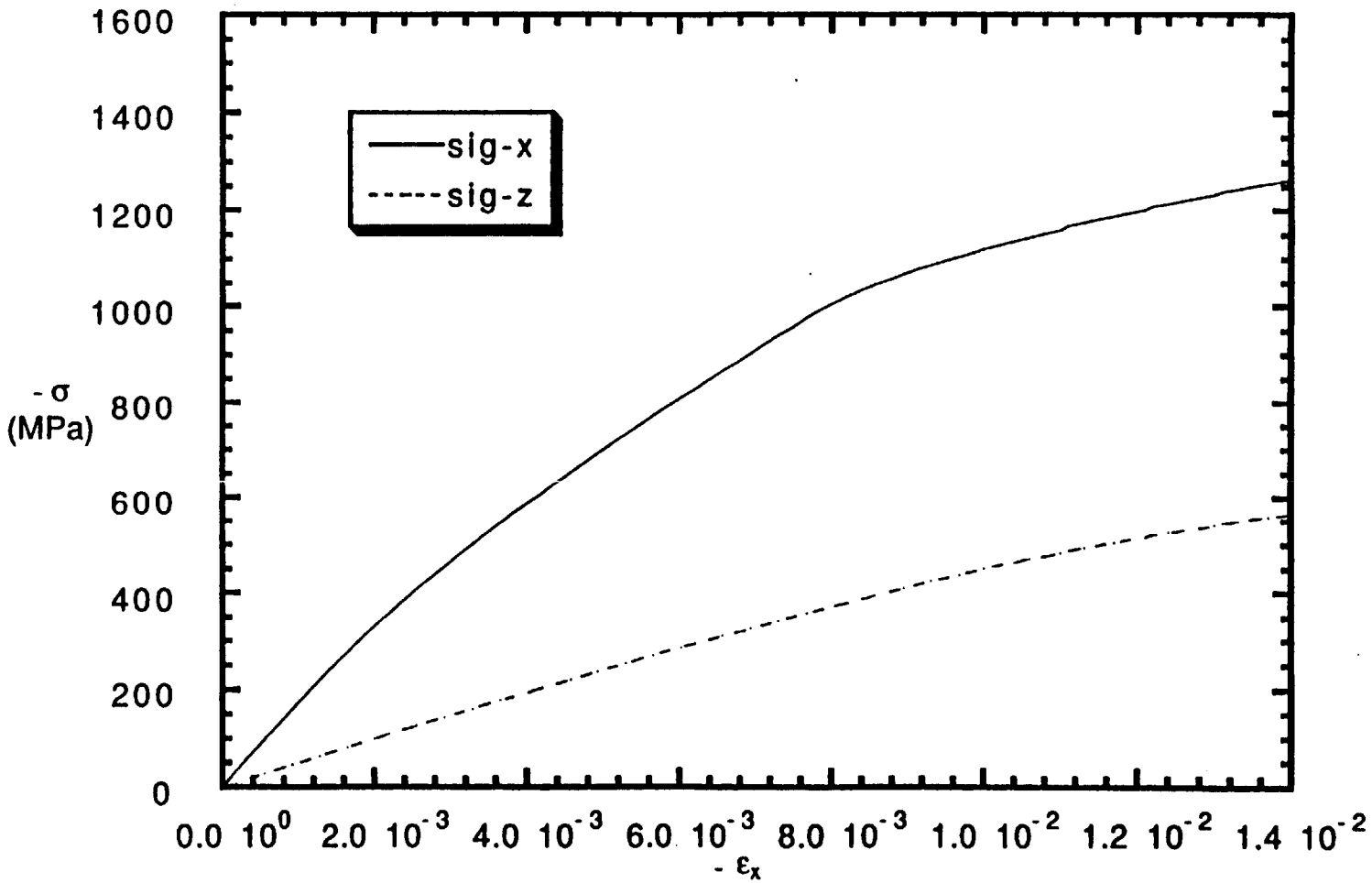

Figure 1(d). Predicted 90° compressive response.

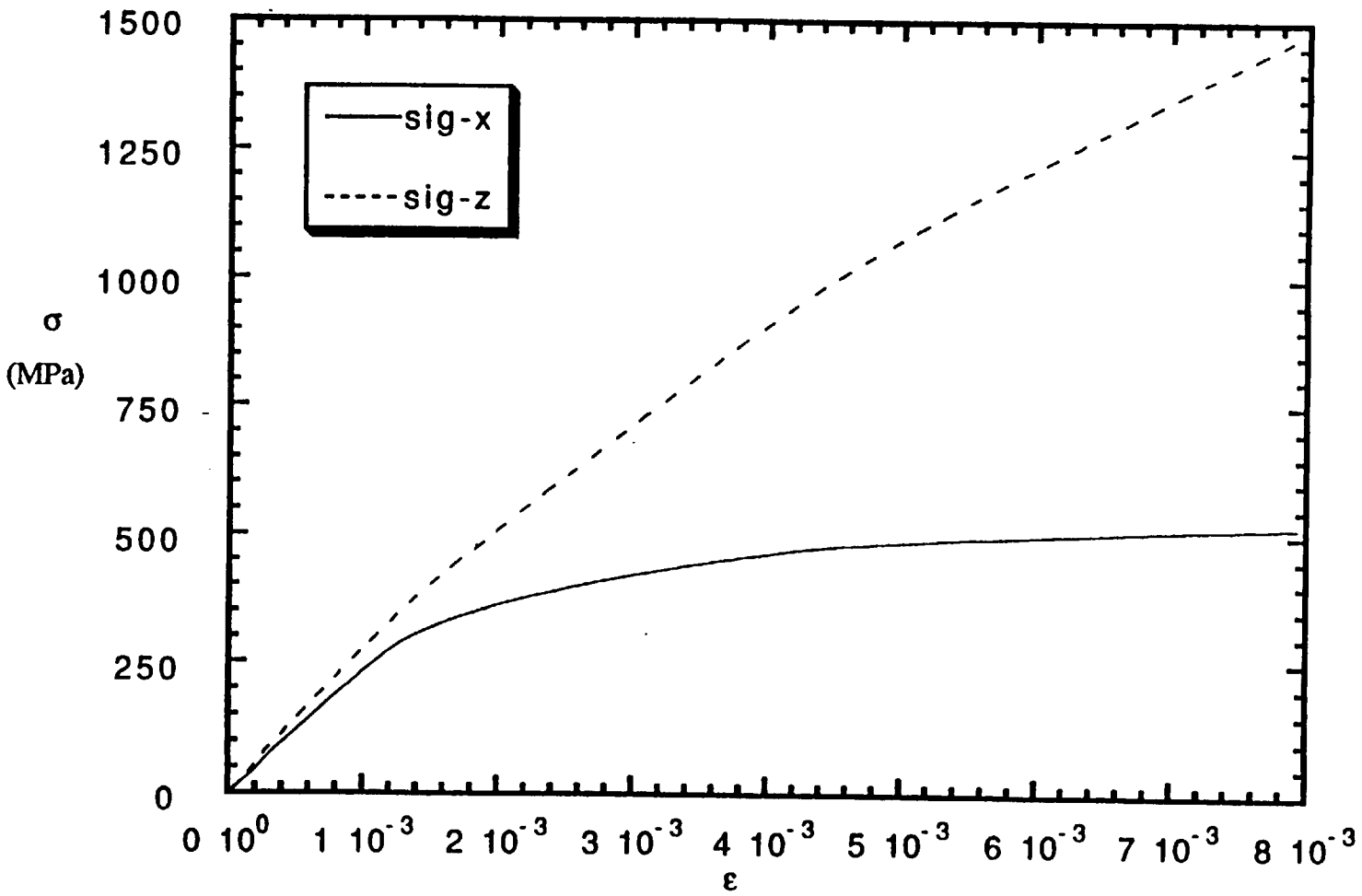

Figure 1(e). Predicted biaxial tensile response.

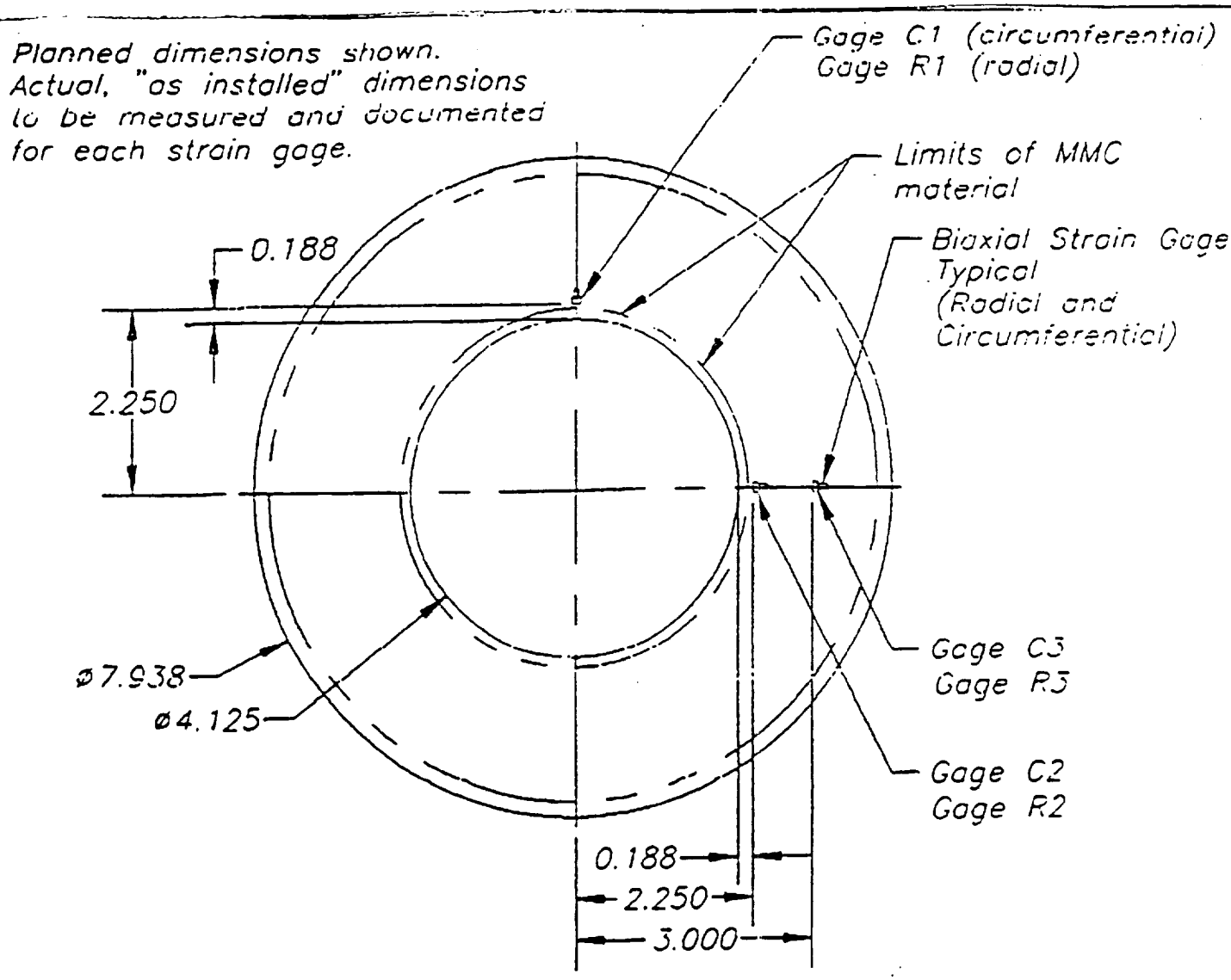

Figure 2. The MMC Ring Configuration Supplied by Textron Lycoming.

SIZE	CODE IDENT NO.	DRAWING NO.
A	1N643	
SCALE 1/2		SHEET OF

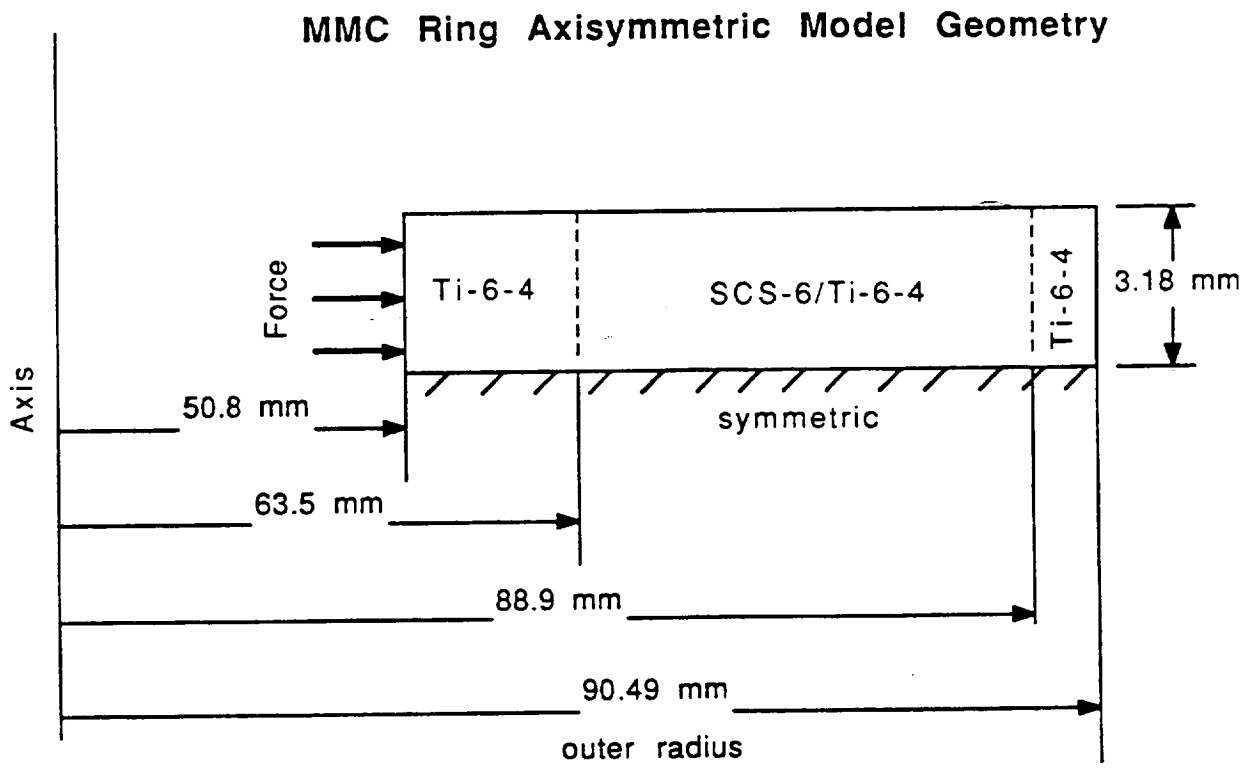

Figure 3. Ring cross-section using dimensions provided by Textron Lycoming.

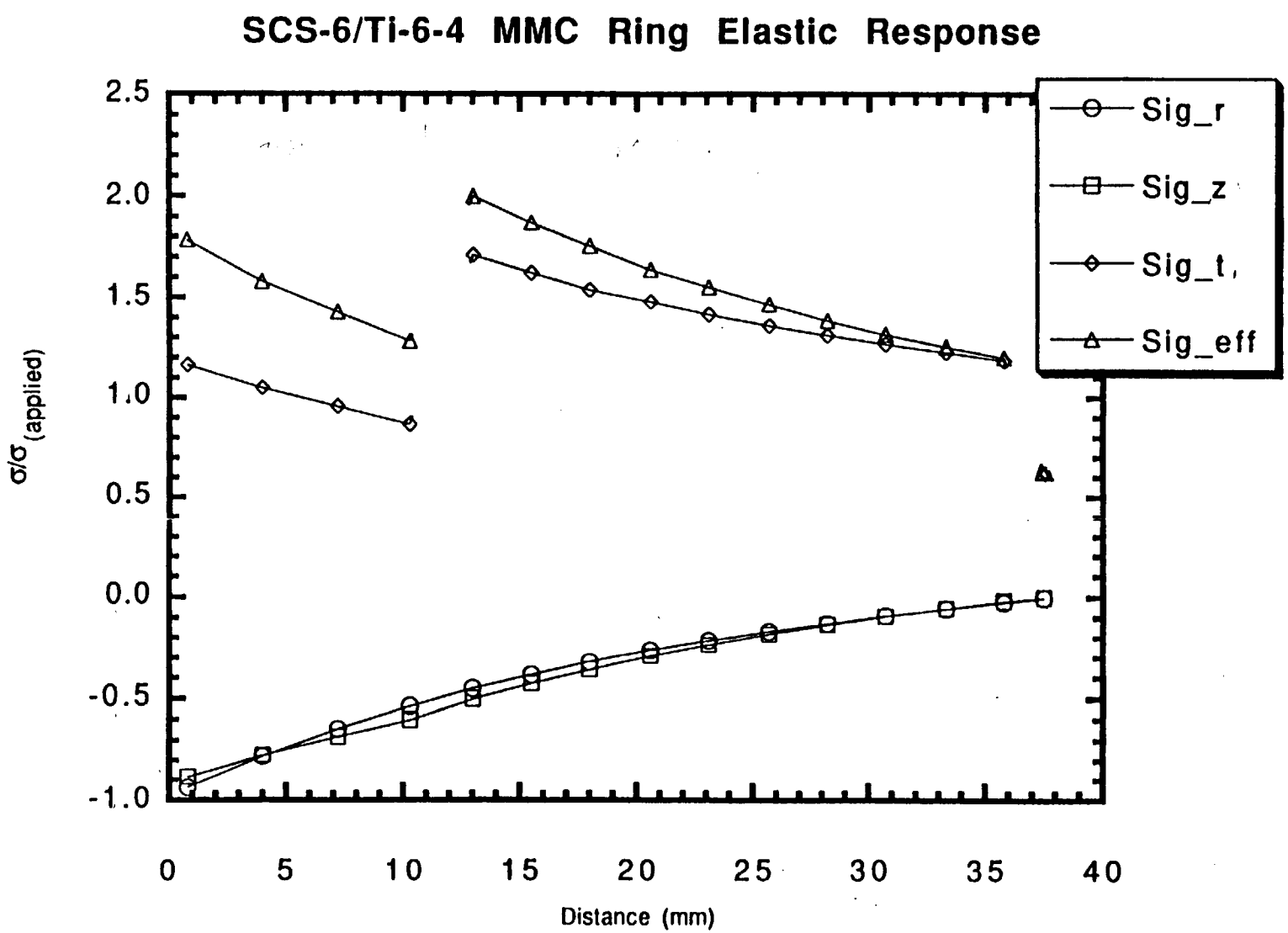

Figure 4. Elastic stress analysis of ring. The stresses are normalized by applied internal pressure.

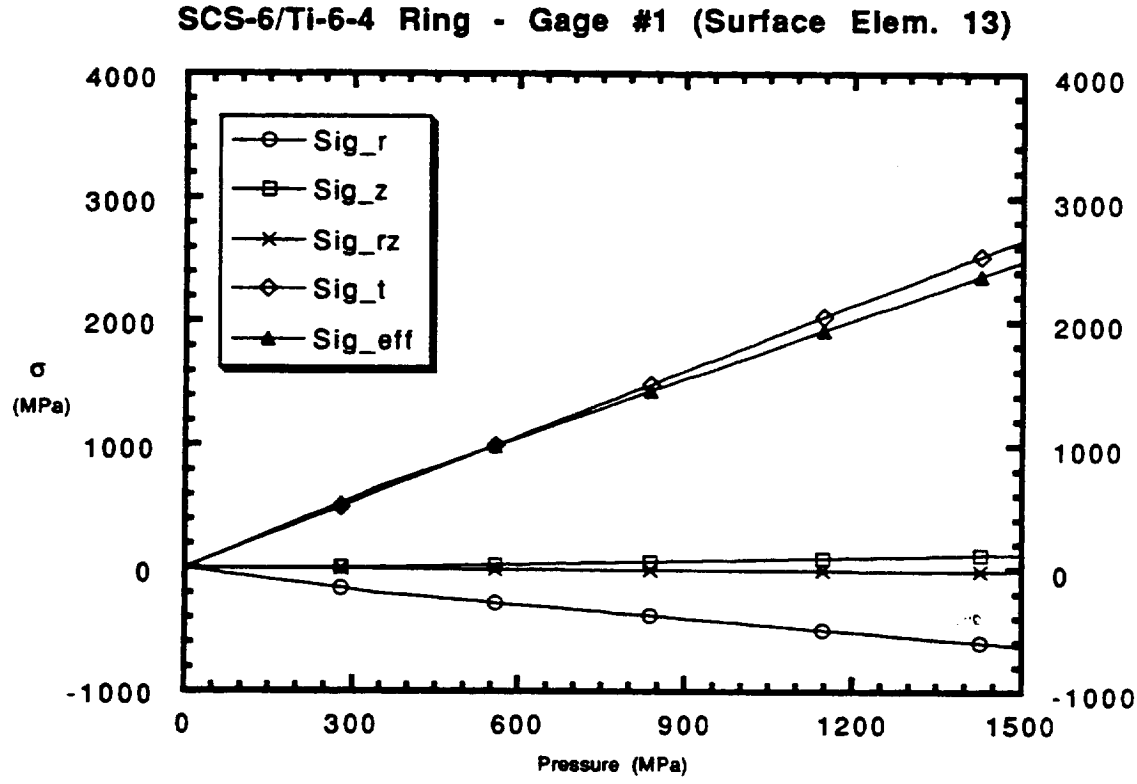

Figure 5(a). Stresses at the inside radius of the MMC insert.

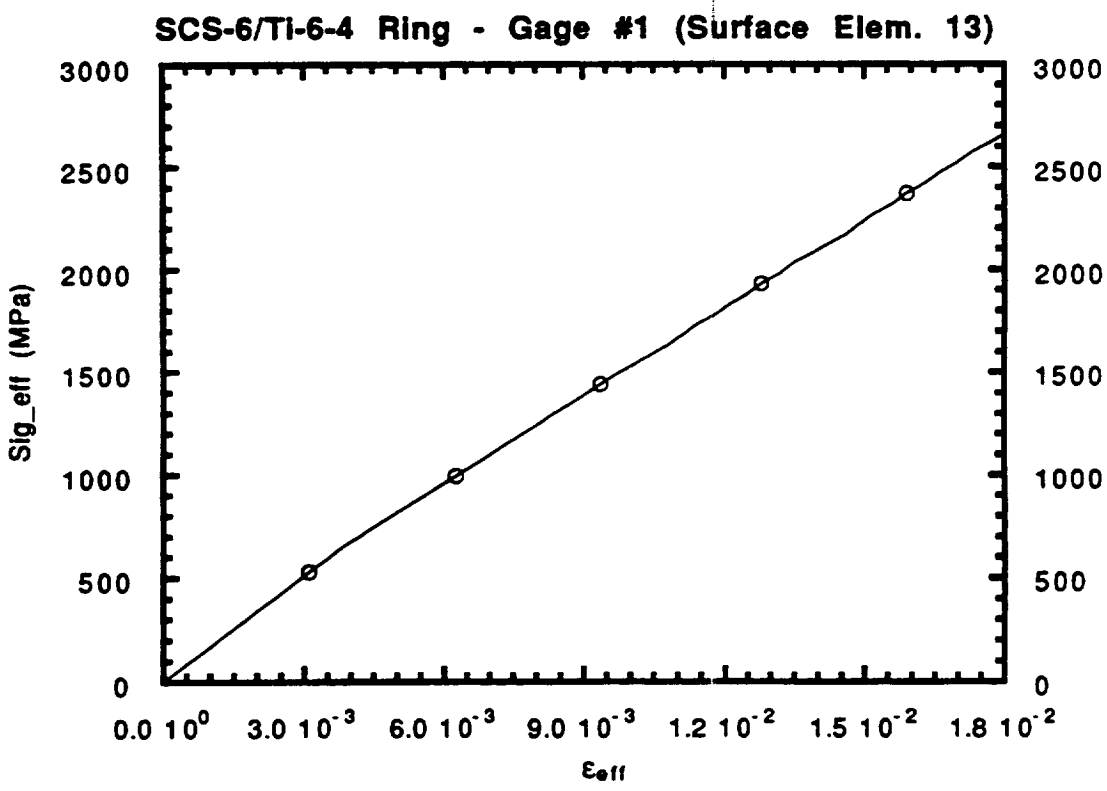

Figure 5(b). Effective stress-strain response at the inside radius of the MMC insert.

APPENDIX A

References and Abstracts

References and Abstracts

(1) Bandyopadhyay, S, **Mechanical and Fracture Properties of Metal Matrix Composites,** Conference: Materials Processing and Performance, Melbourne, Victoria, Australia, 2-5 Sept. 1991, p. 187-190

Abstract: A brief overview of the mechanical and fracture properties of metal matrix composites (MMCs), in particular discontinuously reinforced Al alloys, is presented. Mechanical properties discussed include uniaxial tensile strength, modulus of elasticity, longitudinal and transverse strength and stiffness. Properties of B/Al, SiC/Al, SiC/Ti- 6Al- 4V and 6061 Al are shown. Factors contributing to yield and tensile strength of particulate SiC/Al composites are discussed. Matrix materials and content and type of reinforcement have been shown to be important parameters. Extensive work on fracture properties of MMCs is also reported. Graphs. 7 ref.

(2) Wright, P K ; Nimmer, R ; Smith, G ; Sensmeier, M ; Brun, M, **The Influence of the Interface on Mechanical Behavior of Ti- 6Al- 4V/SCS-6 Composites.,** GE Aircraft Engines, General Electric Corporate Research and Development, Conference: Interfaces in Metal-Ceramics Composites, Anaheim, California, 18-22 Feb. 1990, p. 559-581.

Abstract: The mechanical properties of Ti- 6Al- 4V/SCS-6 composites are influenced in various degrees by the nature of the interfacial bonding between the fiber and the matrix. A combination of experimental and analytical evidence is presented which identifies the interface bonding as weak (in comparison to matrix yield strength) with interfacial strength primarily controlled by thermal residual clamping stresses. Loading the composite under various stress states produces various sensitivities of behavior to the interface; the component of tensile loading perpendicular to the fiber appears to be the key factor governing response, with greater amounts of transverse tension promoting interface separation. Thermal treatments to change the interface character influenced some properties but not others, depending on the sensitivity of the property to interfacial strength. Graphs, Photomicrographs. 14 ref.

(3) IMAI, YOSHIO; SHINOHARA, YOSHIKAZU; IKENO, SUSUMU; SHIOTA, ICHIRO, **The relationship between interfacial reaction and tensile strength of SiC filament reinforced Ti alloy composites,** Proceedings of the 5th Japan-U.S. Conference on Composite Materials, Tokyo, Japan, June 24-27, 1990, p. 347-354.

Abstract: Ti-alloy-matrix composites are fabricated by means of diffusion bonding and heat-treated, and an investigation is undertaken of the reaction products and their effects on the composites' strengths. The Ti alloys include Ti-6Al-4V and Ti-8Mo/Ti-6Al-4V and are reinforced with SiC filaments and heat-treated at 1023-1123 K for 32.4-360 ks. The strength of the Ti matrices is found to decrease by up to 60 percent at the higher-temperature longer-duration treatments. The reaction products include TiC on the filament surfaces and a layer of Ti5Si3 on the TiC surface, and the reaction-rate constants and activation energies are given. The results suggest that the alloying elements effectively inhibit the interface reaction but that defects in the reaction products causes a significant decrease in composite strength.

(4) MIYASE, A.; WANG, S. S. (Illinois, University, Urbana), **Shear creep deformation of SCS6/Ti-6Al-4V metal matrix composite at elevated temperatures,** Proceedings of the 5th Japan-U.S. Conference on Composite Materials, Tokyo, Japan, June 24-27, 1990 , p. 283-291.

Abstract: Monotonic shear and shear creep experiments are conducted on SCS6/Ti-6Al-4V metal matrix composite using an Iosipescu-type shear test method at room and elevated temperatures. First, a brief description is given on the MMC material and the specimen design for the experiments. Also, detailed experimental procedures for the monotonic shear and shear creep tests are described. Discussion is made on the shear creep constitutive relationships, shear creep deformation and failure modes as well as the effects of the applied shear stress levels on shear creep rates.

(5) Jeng, S. M.; Yang, J. -M.; Yang, C. J., **Fracture mechanisms of fiber-reinforced titanium alloy matrix composites. Part II. Tensile behavior,** Materials Science & Engineering A: Structural Materials: Properties, Microstructure and Processing v A138 n 2 Jun 15 1991 p 169-180

Abstract: The mechanical properties and deformation mechanisms of several unidirectional SCS-6 fiber-reinforced titaniurn alloy matrix composites under tensile loading were studied. Three different titanium alloys were used as matrix materials: Ti-6Al-4V, Ti-15V-3Al-3Cr-3Sn and Ti-25Al-10Nb. The key microstructural parameters which dominate the stress-strain response, damage initiation, damage growth and fracture behavior of the composites were identified. The strength and Weibull modulus of the interfacial reaction layer as a function of its thickness were also quantified. Finally, the tensile fracture mechanisms near the interface region were classified on the basis of

the ratio of fiber strength (sigma //f) to interfacial shear strength (tau //i) vs. matrix toughness. 20 Refs.

(6) Curtin, W A, **Ultimate Strengths of Fibre-Reinforced Ceramics and Metals,** BP Research Centre, Conference on Fatigue and Fracture of Inorganic Composites, Cambridge, UK, 31 Mar.-2 Apr. 1992, Composites, 24,(2), p. 98-102

Abstract: A theory to predict the ultimate tensile strength of fibre-reinforced ceramics (CMCs), i.e. Nicalon/LAS, SCS-6/LAS, Nicalon/Soda line, Nicalon/carbon, and Nicalon/CAS is presented. The theory incorporates the statistical nature of the fibre strength and the presence of fibre/matrix sliding, the latter allowing broken fibres to retain some load-carrying capacity, and yields a simple analytic expression for the strength. Comparisons with measurements on a wide range of CMCs indicate that the theory improves considerably on rule-of-mixtures estimates. An extension of the concepts used for CMCs to metal-matrix composites (MMCs) with weak, sliding fibre/matrix interfaces is then proposed, and the resultant predictions for MMC strengths agree well with data on SCS-6/titanium-alloy (Ti- 6AL-4V, Ti- 24Al- 11Nb) materials. Graphs. 15 ref.

(7) Arsenault, R J, **Tensile and Compressive Properties of Metal Matrix Composites,** University of Maryland, Publ: Academic Press, Inc., 1250 Sixth Ave., San Diego, California 92101, USA, 1991, Metal Matrix Composites: Mechanisms and Properties, p. 133-167

Abstract: The tensile and compressive properties of discontinuous (DMMC) and continuous (CMMC) composites are discussed. The discussion is almost exclusively in terms of tensile properties with some discussion of compressive properties and of the mechanisms of strengthening. The section on DMMCs focuses on SiC/Al composites. Matrix alloys considered include 1100, 2024, 2124, 5083, 6061, and 7075. The section dealing with CMMCs is divided into five parts: rule of mixtures (ROM); CMMCs that follow ROM predictions; CMMCs that do not follow the predictions of ROM; a comparison of the longitudinal and transverse properties; and compression vs. tensile strengths. Data is included in this section for Al sub 2 O sub 3 /5056 Al, C/Al, SiC/Ti-6Al- 4V, Borsic/Ti- 6Al- 4V, and SCS-6/Ti- 6Al- 4V CMMCs. Graphs. 42 ref.

(8) Yang, C. J.; Jeng, S. M.; Yang, J. M., **Interfacial properties measurement for SiC fiber-reinforced titanium alloy composites,** Scripta Metallurgica et Materialia v 24 n 3 Mar 1990 p 469-474

Abstract: The purpose of this work was to use an indentation technique to measure the interfacial debond strength and frictional stress for various fiber reinforced titanium alloy matrix composites. The quantitative interfacial mechanical properties will be useful for understanding the failure behavior and deformation mechanisms of these composites. The composites used in this study were SiC fiber (SCS-6) reinforced alpha //2-titanium aluminides. Ti-at% 25 Al-10 at% V-3at% Al-3at% Cr-3at% Sn (Ti-15-3 3) and Ti-6at% Al-4at% V (Ti-6-4). Ti-25-10 alloy contains both alpha //2 and beta phase, and the presence of beta -phase is due to the addition of beta -stabilizing elements such as Nb, Mo and V. Ti-6-4 is an alpha plus beta alloy and Ti-15-3 is a metastable beta titanium alloy. A B//4C coated B fiber-reinforced Ti-6-4 composite was also used to asses the effect of fiber surface chemistry on the interfacial properties. The unidirectional composite panels were consolidated by the vacuum diffusion bonding technique. The fiber/matrix interfacial debond strength was measured by a Vickers microhardness indentator. 12 Refs.

(9) Watson, M C ; Clyne, T W, **The Tensioned Push-Out Test for Fibre/Matrix Interface Characterisation Under Mixed Mode Loading,** Materials Science and Engineering A A160, (1), 1-5 15 Jan. 1993

Abstract: A novel test procedure is suggested for the exploration of interfacial mechanical properties in fibre-reinforced composites. This is based on the established single fibre push-out test, which has the advantage of being applicable to specimens which can be routinely produced from normal unidirectional long fibre composite material. The suggested modification involves the application of equal biaxial in-plane tension while the push-out testing is carried out. This allows the interface to be subjected to various combinations of mode I and mode II loading, ranging from pure opening to pure shear. Hence, it should be possible to obtain data characterising the resistance to interfacial debonding and disengagement over all of this range. Illustrative data are presented here for titanium-based composites, in the form of measured critical shear stresses for various applied normal stresses at the interface. Graphs. 32 ref.

(10) Nimmer, Ronald P.; Bankert, R. J.; Russell, Edward S.; Smith, Gary A.; Wright, P. Kennard, **Micromechanical modeling of fiber/matrix interface effects in transversely loaded SiC/Ti-6-4 metal matrix composites,** Journal of Composites Technology & Research v 13 n 1 Spring 1991, p 3-13

Abstract: The transverse tensile behavior of a composite composed of unidirectional silicon-carbide fiber (Textron SCS-6) in a Ti-6Al-4V matrix is examined with emphasis on the effects of fiber-matrix interface strength. The residual stresses as a result of a mismatch in the coefficients of thermal expansion of silicon carbide and titanium are estimated analytically and compared with measurements made using X-ray diffraction techniques. Idealizing the composite as a regular rectangular array of fibers in an elastoplastic matrix, the transverse tensile stress-strain behavior is predicted under the assumptions of an infinitely strong interface as well as an interface without tensile strength. These results are compared with experiments conducted at three different temperatures. The agreement between experiment and predictions based on an interface without tensile strength is extremely close. The modeled stress-strain curves predict a well-defined knee in the transverse tensile stress-strain curve associated with the separation of fiber and matrix at their interface. The same stress-strain behavior is observed experimentally. Results of edge replica experiments and mechanical unloading from stress levels above the knee are also presented as additional evidence of the association of fiber-matrix separation with the knee in the transverse tensile stress-strain curve. (Author abstract) 17 Refs.

(11) Brayshaw, J B ; Pindera, M -J, **The Effect of the Matrix Constitutive Model on Residual Thermal Stresses in MMC.,** Conference: Mechanics of Composites at Elevated and Cryogenic Temperatures, Columbus, Ohio, USA, 16-19 June 1991, p. 23-38

Abstract: A thermomechanical analysis of advanced composites (B/Al, Gr/Al, SiC/Ti), in a wide temperature range is presented. This analysis is based on the micromechanics method of cells. An incremental formulation of the micromechanics model is developed to facilitate the use of various inelastic constitutive theories. These theories incorporate time-dependent and temperature-dependent features for modeling different types of metal matrices (e.g. Al 2024). The constitutive models include the Bodner- Partom unified theory of viscoplasticity, the incremental plasticity model, and a power-law creep model. The effect of the cooling rate, taking into account temperature-dependent matrix properties, on residual thermal stresses is subsequently investigated for a SiC/Ti (Ti- 6Al- 4V) composite using the different models for the matrix phases. Predictions generated using the micromechanics method are compared with available results of finite-element analysis. Graphs. 8 ref.

(12) Sun, C T ; Chen, J L ; Sha, G T ; Koop, W E, **Mechanical Characterization of SCS-6/Ti-6-4 Metal Matrix Composite,** Purdue

University, General Motors, Air Force Wright Aeronautical Laboratories, Journal of Composite Materials 24, (10), Oct. 1990, p. 1029-1059.

Abstract: Off-axis tension tests were performed on SCS-6/Ti-6-4 metal matrix composite. A one-parameter plasticity model was used to characterize the elastic- plastic properties. In addition, a micromechanical model was developed, assuming elastic fiber and elastic- plastic matrix properties. This model was employed to relate the apparent yielding with the fiber/matrix separation in the MMC. From the micromechanical model, the fiber/matrix interfacial bond strength was estimated and, with the aid of a damage model, the nonlinear off-axis stress- strain curves were accurately predicted. Graphs. 16 ref.

(13) Eggleston, M. R.; Krempl, E., **Modeling the transverse creep of titanium-based metal matrix composites,** Damage Mechanics in Composites American Society of Mechanical Engineers, Applied Mechanics Division, AMD v 150. ASME, New York, NY, USA. p 313-326, 1992

Abstract: The creep deformation of continuous fiber, titanium-based metal matrix composites in the transverse orientation was modeled. Creep tests were performed on a composite of SCS-6 silicon carbide fibers in a matrix of Ti-6Al-4V with a nominal fiber volume fraction of 28%. Tests were performed at 480 degree C (900 degree F) in an air environment. The creep of the transverse composites was generally faster than that of the monolithic matrix material. The unified viscoplasticity theory based on overstress (VBO) was used to model the matrix in a finite element analysis. The VBO theory was able to model most of the observed matrix behavior. Composite models were created with both strong and weak bonding between the fiber and matrix. The composite creep tests possessed a creep rate that was between the behavior of the pure matrix and that of the weakly bonded interface model. SEM analysis of the failed specimens supported the conclusion that debonding of the fiber and matrix occurs in the test, and is a source of an increased creep rate. Additional improvements in the modeling of the fiber-matrix interface are required for more accurate prediction of the composite's creep behavior.

(14) Schwenker, S.W., Roman, I., and Eylon, D., **Creep Behavior of SCS 6Ti-6Al-4V Unidirectional Composites,** Proceedings of the International Conference on Advanced Composites 1993, University of Woolongong, Australia, Feb. 15-19, 1993.

(15) Ahmad, U. Santhosh and I.U. Haq, **ON TIME DEPENDENT DEFORMATION MODELING OF METAL MATRIX COMPOSITES,** ASME Winter Annual Meeting, Nov 27-Dec 02, New Orleans, Louisiana.

Abstract: A simple engineering model is presented to predict time dependent response of unidirectional metal matrix composites (MMCs) under sustained loading in the fiber direction. The model takes into account the effect of matrix creep and consolidation process induced residual stresses. Model predictions are compared with experimental data on SCS-6/Ti-6Al-4V composite and with nonlinear finite element analyses. Also, a simple modeling approach is presented to assess the effect of possible fiber fractures on the composites global strain-time response.

(16) El-Soudani, S M ; Gambone, M L, **Strain-Controlled Fatigue Testing of SCS-6/Ti- 6Al- 4V Metal-Matrix Composite,** Rockwell International, General Motors, Conference: Fundamental Relationships Between Microstructures and Mechanical Properties of Metal Matrix Composites, Indianapolis, Indiana, 1-5 Oct. 1989, p. 669-704

Abstract: A high sensitivity method is developed for strain-controlled fatigue testing of Ti- 6Al- 4V/SiC at room and elevated temperature in air environment and is shown to provide much better insight, by comparison with load-controlled tests, into the mechanisms of damage growth and gradual degradation of metal-matrix composites. The fatigue behavior of Ti matrix composite is characterized by three basic regimes of damage development corresponding to three distinctive regions of the strain- life curve, respectively. Early fatigue damage was found to take place on the first few cycles in the transverse test orientation. The low transverse strength and the brittle nature of the fiber/matrix interface are the two prime contributors to the low strain- life behavior of the Ti metal-matrix composite loaded normal to the fiber direction. Graphs, Photomicrographs. 5 ref.

(17) Lawrence, C.W.; Briggs, G.A.D.; Scruby, C.B., **Acoustic microscopy of ceramic-fibre composites. Part III. Metal-matrix composites,** Journa of Materials Science v 28 n 13 Jul 1 1993. p 3653-3660

Abstract: Scanning acoustic microscopy (SAM) has been used to study metal matrix composites (MMCs) reinforced with silicon-carbide monofilaments. For most of the specimens the matrix was Ti-6Al-4V, but Ti//3Al and 6061 Al

matrices were also examined. The titanium-matrix specimens were subjected to a range of thermal ageing treatments to investigate potential in-service degradation. The main effect was progressive deterioration of the fibre-matrix interface. In the as-received material the carbon-rich coating protected the SiC by forming a reaction layer with the titanium. As a result of ageing, the reaction layer was penetrated adjacent to the beta -phase titanium grains. More extensive ageing caused the carbon-rich coating to degrade and eventually disappear. The final stage of deterioration was direct attack on the SiC. Cracks and porosity between fibres were observed in some specimens, probably due to poor diffusion bonding during fabrication. Fine radial microcracks were observed in an annular region inside the mid-radius of some fibres; they are believed to be a consequence of stress relief during thermal ageing. These cracks could not be observed optically. The extra sensitivity of acoustic microscopy is due to the reflection of Rayleigh waves by tight closed cracks. 14 Refs.

(18) Karpur, P.; Matikas, T.; Krishnamurthy, S., **Matrix-fiber interface characterization in metal matrix composites using ultrasonic imaging of fiber fragmentation,** Proceedings of the 7th Technical Conference of the American Society for Composites, 1992

Abstract: This paper presents an ultrasonic method of imaging used in conjunction with the fiber fragmentation test of a model composite sample made of a single SCS-6 or SIGMA fiber embedded in matrix of Ti-6Al-4V or Ti-14Al-21Nb. The imaging technique is very useful for the estimation of the fiber fragmentation size which is an indicator of the mechanical properties of the interface between the matrix and the fiber. Other applications of ultrasound for the characterization of the composite system will be presented and the future directions of research will be discussed. (Author abstract) 7 Refs.

(19) Ferraris, M.; Badini, C.; Marino, F.; Marchetti, F.; Girardi, S., **Interfacial reactions in a Ti-6Al-4V based composite: Role of the TiB//2 coating,** Journal of Materials Science v 28 n 7 Apr 1 1993. p 1983-1987

Abstract: The characterization of TiB//2/C-coated SiC fibres and their interface region in a Ti-6Al-4V based composite has been performed by using scanning electron microscopy (SEM), energy-dispersion X-rays (EDX) and Auger electron spectroscopy (AES). The features of the as-received fibre and the reactivity between fibre and matrix occurring during preparation of the composite have been studied in this paper. The interaction of the TiB//2 external coating of the fibre with both the adjacent carbon layer and the

titanium-based matrix is already appreciable in the as-received composite: TiB needles grow from TiB//2 towards the matrix and a new layer containing C, Ti and B appears between TiB//2 and C. The thicknesses of the original carbon and TiB//2 fibre coatings decrease in the composite from 1000 nm to 400 and 800 nm, respectively. The TiB//2 inhibits the reaction between SiC and Ti: there is no evidence of Si//xTi//y brittle phases. (Author abstract) 24 Refs.

(20) Hirose, A.; Matsuhiro, Y.; Kotoh, M.; Fukumoto, S.; Kobayashi, K.F., **Laser-beam welding of SiC fibre-reinforced Ti-6Al-4V composite,** Journal of Materials Science v 28 n 2 Jan 15 1993. p 349-355

Abstract: Three- and ten-ply SiC fibre-reinforced Ti-6Al-4V composites were jointed using a laser beam. With a 300 mu m thick Ti-6Al-4V filler metal, fully penetrated welds without apparent fibre damage, could be obtained in welding directions both parallel and transverse to the fibre direction by controlling the welding heat input. Excess heat input resulted in the decomposition of SiC and subsequent TiC formation, and also caused degradation of joint strength. The welding of the three-ply composite in which full penetration was achieved at lower laser power, exhibited higher flexibility in heat input than that of the ten-ply composite. Heat treatment at 1173 K after welding improved the joint strength because of the homogenization of the weld metal and decomposition of TiC. The strengths of the transverse weld joints after the heat treatment were approximately 650 and 550 MPa for the three- and ten-ply composites, respectively. With the welding direction parallel to the fibre direction, the strengths both parallel and transverse to the weld joint were equivalent to those of the base plate. (Author abstract) 6 Refs.

(21) Chan, K.S., **Effects of interface degradation on fiber bridging of composite fatigue cracks,** Acta Metallurgica et Materialia v 41 n 3 Mar 1993. p 761-768

Abstract: This paper presents a theoretical analysis that examines the effects of cyclic degradation of interface on fiber bridging of fatigue cracks in metal-matrix or intermetallic-matrix composites. Using fiber bridging models and crack-tip micromechanics results available in the literature, the frictional stresses on individual fiber/matrix interfaces located within the bridging zone in the wake of a fatigue crack in a SCS-6/Ti-6Al-4V composite are calculated. The results are used to demonstrate that a reduction of the interface friction stress by fatigue can lead to a decrease of the fiber bridging stress, and an increase in the near-tip stress intensity range. The consequence is that the

near-tip stress intensity range and, thus, the crack growth of a bridged fatigue crack are sensitive to cyclic interface degradation and the distribution of the frictional stress within the bridged zone. (Author abstract) 24 Refs.

(22) Hirose, A.; Kotoh, M.; Fukumoto, S.; Kobayashi, K. F., **Diffusion bonding of SiC fibre reinforced Ti-6Al-4V alloy.,** Materials Science and Technology v 8 n 9 Sep 1992 p 811-815

Abstract: A continuous SiC fibre reinforced Ti-6Al-4V composite was diffusion bonded to itself. Incorporation of a Ti-6Al-4V interlayer and use of an etching treatment to smooth the faying surface improved the diffusion bondability of the composite. The bond strength increased with bonding time up to 10.8 ks under 10 MN m** minus **2 pressure at 1173 K, at which time, after reaching the maximum value of approximately 700 MN m** minus **2, the strength was saturated Corresponding to this behaviour, the bonding between the interlayer and the composite matrix was completed after a bonding time of 10.8 ks. Bonding between the fibre and the interlayer was considered not to contribute to the joint strength on the basis of observation of the fracture surfaces. The bond strength therefore seems to be controlled by the bonding of the interlayer and the composite matrix. (Author abstract) 7 Refs.

(23) Stock, Stuart R.; Breunig, Thomas M.; Guvenilir, Abbas; Kinney, John H.; Nichols, Monte C., **Nondestructive X-ray tomographic microscopy of damage in various continuous-fiber metal matrix composites.,** ASTM Special Technical Publication n 1128., p 25-34, 1992.

Abstract: X-ray tomographic microscopy (XTM), a high resolution variant of industrial computed tomography, provides nondestructive, high-resolution 'sectioning' of samples and allows three-dimensional mapping of X-ray absorptivity multiple times during an in-situ experiment on a single msample. The capabilities of XTM for damage accumulation studies in composites are described in this paper, with emphasis on what can be accomplished using monochromatic synchrotron radiation. Results are shown for five continuous-fiber metal matrix composites (MMC) (aligned SiC/Al, left bracket 0//2/ plus or minus 45 right bracket //s SiC/Al, aligned SiC/Ti//3Al, aligned SiC/Ti-6Al-4V, and aligned Al//2O//3/NiAl). The samples' cross-sectional dimensions are approximately 1.5 by 1.5 mm or smaller, and the variation of X-ray absorptivity is measured within each (5.6- mu m)**3 volume element of the volume studied. An experimental approach for nondestructively quantifying damage evolution with XTM is outlined, and preliminary results are presented for the aligned-fiber SiC/Al MMC. Also

discussed are the prospects for improved spatial resolution with XTM and for examining specimens under applied loads and/or with dimensions larger than the current 2 or 3 mm. 18 Refs.

(24) Jeng, S. M.; Yang, J. -M.; Aksoy, S., **Damage mechanisms of SCS-6/Ti-6Al-4V composites under thermal-mechanical fatigue.,** Materials Science & Engineering A: Structural Materials: Properties, Microstructure and Processing v A156 n 2 Aug 15 1992 p 117-124.

Abstract: The damage mechanisms of the unidirectional SCS-6/Ti-6Al-4V composites under thermal-mechanical fatigue loading and high temperature isothermal fatigue were studied. The maximum cyclic temperature varied from 370 to 650 degree C and maximum applied stresses ranged from 828 to 1180 MPa. The resulting thermal-mechanical fatigue life for each condition was plotted against the maximum stress in the matrix. The crack initiation and propagation mechanisms were identified. It was found that matrix cracking with unbroken fiber bridging is the major damage mode for the composites under thermal-mechanical fatigue and isothermal fatigue loading. Furthermore, oxidation-assisted matrix cracking and oxidation pitting on the fiber surface are the major damage mechanisms for high temperature oxidizing environments. 9 Refs.

(25) Grady, Joseph E.; Lerch, Bradley A., **Effect of heat treatment on stiffness and damping of Sic/Ti-15-3,** SAMPE Quarterly v 23 n 2 Jan 1992 p 11-16

Abstract: The effect of heat treatment on material properties of Sic/Ti-15-3 was measured by vibration tests. Heat treatment changes the microstructure, which stiffens the matrix and reduces its damping capacity. Test results illustrate how the changes in matrix material affect the stiffness and damping properties of the composite. Damping was found to be more sensitive than stiffness to microstructural changes in the matrix. Effects of heat treatment temperature and exposure time are presented.12 Refs.

(26) Zedalis, M. S.; Bryant, J. D.; Gilman, P. S.; Das, S. K., **High-temperature discontinuously reinforced aluminum,** JOM v 43 n 8 Aug 1991 p 29-31

Abstract: High-temperature discontinuously reinforced aluminum (HTDRA) composites have been developed for elevated-temperature applications by incorporating SiC particulate reinforcement into a rapidly solidified, high-temperature Al-Fe-V-Si (alloy 8009) matrix. HTDRA combines the superior

elevated-temperature strength, stability and corrosion resistance of the 8009 matrix with the excellent specific stiffness and abrasion resistance of the discontinuous SiC particulate reinforcement. On a specific stiffness basis, HTDRA is competitive with Ti-6Al-4V and 17-4 PH stainless steel to temperatures approaching 480 degree C. Potential aerospace applications being considered for HTDRA include aircraft wing skins, missile bodies, and miscellaneous engine, spacecraft and hypersonic vehicle components. 37 Refs.

(27) Hunt, Margaret, **Aerospace composites,** Materials Engineering (Cleveland) v 108 n 6 Jun 1991 p 27-30

Abstract: Though considered impossible just a few years ago, entire families of lightweight composites are either available now or hovering on the brink of commercialization. For example, a high-temperature creep-resistant titanium alloy has been developed as matrix material for the National Aerospace Plant by Timet for McDonnell Douglas. Titanium alloy Ti-6Al-4V, reinforced with continuous silicon carbide filaments, is hot isostatically pressed by Textron for turbine engine shafts. A powder metallurgy titanium composite from Alloy Technology features titanium carbide particles for long wear and improved hardness in moving parts. A new beryllium composite for avionics from Brush Wellman has density of only 2.2 g/cm**3, as well as excellent thermal properties. Aluminum-lithium structural composites from BP are lightweight yet stiff enough for aircraft module doors, with other applications imminent. Magnesium composites for structural and thermal applications from Martin Marietta, Lanxide, Cordec, ACMC, Dow, and other manufacturers are fabricated by powder metallurgy, casting, layup, and in situ techniques.

(28) Wei, W., **Effect of long term thermal exposure on the interface chemistry and mechanical properties of metal matrix composites,** Werkstoffe und Korrosion v 41 n 12 Dec 1990 p 751-752

Abstract: The reinforcement of high temperature metals with lightweight ceramic fibers provides the designer and manufacturer of high temperature components materials with increased strength and stiffness, and a significant reduction in weight. A recently published study on the SiC continuous fiber reinforced Ti-6Al-4V system has shown that long term exposure of the MMC to operating conditions leads to oxidation of the interfaces and a subsequent reduction in low cycle fatigue life. 6 Refs.

(29) Johnson, W. S.; Lubowinski, S. J.; Highsmith, Alton L., **Mechanical characterization of unnotched SCS//6/Ti-15-3 metal matrix**

composites at room temperature, ASTM Special Technical Publication v STP n 1080

Abstract: Ti-15V-3Cr-3Al-3Sn is a new metastable beta strip alloy used where cold formability and high strength are desired. Ti-15-3 metal matrix composites containing silicon-carbide (SCS//6) fibers in five different lay-ups have been tested at room temperature to determine static strengths and mechanical properties. Experimental data and predicted values of the laminate properties and strengths showed good correlation. The off-axis laminate plies (that is 90 degree and 45 degree) suffered fiber/matrix interface failures at stress levels as low as 20 ksi, thus significantly affecting the mechanical properties. Microscopic examinations determined that the fiber/matrix failures were occurring in the titanium/silicon reaction layer. Fatigue tests were performed on unnotched specimens to determine the number of cycles to failure versus cyclic stress level. The stress in the 0 degree fiber could be used to correlate the fatigue life of different laminates containing 0 degree plies. 12 Refs.

(30) Loretto, M. H.; Konitzer, D. G., **Effect of matrix reinforcement reaction on fracture in Ti-6Al-4V-base composites,** Metallurgical Transactions A (Physical Metallurgy and Materials Science) v 21a n 6 Jun 1990. p 1579-1587

Abstract: Samples of Ti-6Al-4V containing 10 vol pct of either TiC or SiC have been tested in tension at temperatures up to 760 degree C, and the mechanical properties have been compared with those of the unreinforced matrix alloy. The yield and tensile strength of the TiC-containing composite are superior to those of the SiC composite at room temperature, but that this behavior is reversed at the higher temperatures. The ductility of the TiC composite is about 2 pct at room temperature and increases with increase of temperature. No ductility is found for the SiC composite at room temperature, but some ductility is observed at higher temperatures. These observations are interpreted in terms of the extent and nature of the reaction zones between the matrix alloy and the reinforcement and in terms of the failure mechanisms observed using scanning (SEM) and transmission electron microscopy (TEM). 20 Refs.

(31) Jones, C.; Kiely, C. J.; Wang, S. S., **Effect of temperature on the chemistry and morphology of the interphase in an SCS6/Ti-6Al-4V metal matrix composite.,** Journal of Materials Research v 5 n 7 Jul 1990 p 1435-1442

Abstract: The changes in the chemistry and morphology within the interphase region of an SCS6/Ti-6Al-4V metal matrix composite upon exposing the samples to varying heat treatments have been studied using Auger electron spectroscopy, TEM and convergent beam diffraction techniques. These changes, such as the formation of small TiC particles at one interface and the narrowing of a protective pyrocarbon layer at another, induce fracture to occur at different places within the interphase upon heating. The reasons for this are explained. Evidence for a change in phase of a Ti//xSi//y(C) layer to the more thermodynamically stable Ti//5Si//3 is also given. 7 Refs.

(32) Fukumoto, S.; Hirose, A.; Kobayashi, K.F., **Diffusion bonding of SiC/Ti-6Al-4V composite to Ti-6Al-4V alloy and fracture behaviour of joint,** Materials Science and Technology, vol.9, no.6, p.520-7

Abstract: Continuous SiC fibre reinforced Ti-6Al-4V composites were diffusion bonded to Ti-6Al-4V alloy. Bondability and the fracture mechanism of the joint were investigated. The joint strength increased with bonding time, and was a maximum at 850 MN m/sup -2/ for V/sub f/= 30% composite and 650 MN m/sup -2/ for V/sub f/= 45% composite. The bonding was completed sooner for V/sub f/= 30% composite than for V/sub f/=45% composite. In V/sub f/= 30% composite, the maximum joint strength was about 85% of the tensile strength of Ti-6Al-4V. The void ratio at the interface between matrix and Ti-6Al-4V alloy decreased as bonding time increased. The joint strength was controlled by the bonding between the composite matrix and the Ti-6Al-4V alloy. The maximum joint strength was 100-150 MN m/sup -2/ higher than the strength simply calculated from the area fraction of the bonded matrix/Ti-6Al-4V interface. Fibres were debonded from the matrix and the defects were produced around fibres, so the state of stress at the bond interface is triaxial owing to the defects and/or restraint of fibres. This may be the reason for the higher measured strength. 9 Refs

(33) Fukumoto, S.; Hirose, A.; Kobayashi, K.F.,**Application of laser beam welding to joining of continuous fibre reinforced composite to metal,** Materials Science and Technology, vol.9, no.3, p.264-71

Abstract: Laser beam welding was applied to the joining of SiC fibre reinforced Ti-6Al-4V composite to Ti-6Al-4V alloy. The weldability obtained for a wide bead (900 mu m width) is superior to that for a narrow bead (400 mu m width), the maximum joint strength of 991 MN m/sup -2/ being obtained at the optimum laser beam position for the wide bead. When the beam position was closer to the composite than the optimum range, the SiC

fibres were damaged and segregation of carbon and silicon occurred near the damaged fibres. This caused a deterioration of joint strength. When the laser beam position was further from the composite than the optimum range, the joint strength was reduced by incomplete welding and/or formation of grain boundaries between the composite matrix and the Ti-6Al-4V plate. Heat treatment at 1173 K for 3.6 ks improved the joints that were welded using unfavourable laser beam positions. Therefore, heat treatment extended the range of suitable beam positions, thereby facilitating control of the laser beam. 9 Refs.

(34) Briggs, G.A.D.; Lawrence, C.W.; Scruby, C.B., **Acoustic microscopy of ceramic-fibre composites,** Journal of Microscopy vol.169, pt.2, p.139-53

Abstract: A variety of ceramic-fibre composites has been studied by acoustic microscopy at 1.9 GHz with a resolution of 0.8 mu m. The material studied were Nicalon-reinforced borosilicate glass, SiC fibres in a magnesium-aluminosilicate matrix and a calcium-aluminosilicate matrix, and SiC monofilaments in a Ti-6Al-4V matrix. In all the specimens the contrast was dominated by strong excitation of Rayleigh waves in the surface. This gave strong contrast from different phases, and revealed interfaces and cracks by characteristic crack patterns. Quantitative agreement between observed and calculated fringe patterns was found, and values of shear and Young's modulus were measured. In the SiC monofilament specimens, various stages of progressive deterioration as a result of thermal ageing treatments were observed. 13 Refs

(35) Choy, K.L.; Derby, B., **The compatibility of TiB/sub 2/ protective coatings with SiC fibre and Ti-6Al-4V,** Journal of Microscopy, vol.169, pt.2, p.289-95

Abstract: TiB/sub 2 /coatings have been studied as prospective protective layers to inhibit the interfacial reaction between SiC fibres and Ti-alloy matrices. This protective coating has been deposited onto SiC monofilament fibres using a chemical vapour deposition (CVD) technique. The fibre-matrix compatibility of these TiB/sub 2/-coated SiC fibres in Ti-6Al-4V composites was evaluated by incorporating the coated fibres into Ti-6Al-4V using a diffusion bonding technique. The interfaces of this composite were characterised by scanning electron microscopy (SEM), transmission electron microscopy (TEM) and electron probe microanalysis, to evaluate the interfacial microstructures, chemical stability and the efficiency of TiB/sub 2/ as a protective coating for SiC fibres in Ti-alloy matrices, and to study the effects of deposition temperature on the interface of the coated fibre. Results

show that stoichiometric TiB/sub 2/ coatings are stable chemically to both SiC fibres and Ti-6Al-4V and hinder the deleterious fibre-matrix reactions effectively. Boron-rich TiB/sub 2/coatings should be avoided, as they lead to the formation of a needle-like TiB phase at the fibre-matrix interface. These findings provide promising evidence for the value of further exploration of the use of stoichiometric TiB/sub 2/ as a protective coating for SiC fibre in Ti-based composites. 15 Refs

(36) .Guo, Z.X.; Derby, B.; Cantor, B., **Comparison of interfaces in Ti composites reinforced with uncoated and TiB/sub 2//C-coated SiC fibres,** Journal of Microscopy, vol.169, pt.2, p.279-87

Abstract: Interfaces play an important role in determining the mechanical properties of composite materials. The interfaces established between a titanium-alloy matrix (Ti-6Al-4V) and uncoated and TiB/sub 2//C-coated SiC fibres are analysed by scanning electron microscopy, transmission electron microscopy and X-ray techniques. Emphasis is placed upon the interfacial morphology and microstructure, identification of reaction products, and the stability of the coating layer. Complex multi-reaction layers are observed frequently in the interfacial zones. Previous, often contradictory, reports about the interlayers are reviewed. Experimental observation demonstrates that the type and distribution of interlayers vary in a given system, due to prolonged treatment of the samples at temperature. The formation and distribution of the interlayers are discussed further, with respect to these and previous findings. Methods of reducing interfacial reactivity are discussed. 16 Refs

(37) Guo, Z.X.; Derby, B., **Microstructural characterization in diffusion-bonded SiC/Ti-6Al-4V composites,** Journal of Microscopy, vol.169, pt.2, p.269-77, Feb. 1993

Abstract: The microstructural evolution during the diffusion bonding consolidation of a Ti-6Al-4V/SiC fibre composite was investigated by optical, scanning and transmission electron microscopy. The effects of processing parameters, particularly temperature, on the microstructures of the matrix and the fibre and their bonding were considered. Processing at too high a temperature can result in growth of SiC crystals in the fibre in addition to rapid interfacial reaction, while interfacial bonding cannot be established if the temperature is too low. Various defects can be caused by inadequate fabrication practices. These include micro-pores, matrix-cracking, cracking, bending and impingement of fibres, and heterogeneous fibre distribution. Methods for avoiding these are discussed. A defect-free and uniformly

distributed fibre composite can only be achieved by optimizing the processing parameters (such as temperature, pressure, time and cooling rate) and adequately combining fibre spacing and matrix thickness with accurate fibre alignment. 10 Refs

(38) Zhao, Y.Y.; Grant, P.S.; Cantor, B., **The microstructure of spray-formed Ti-6Al-4V/SiC/sub f/metal-matrix composites,** Journal of Microscopy, vol.169, pt.2, p.263-7, Feb. 1993

Abstract: Spray-forming is a possible manufacturing route for the fabrication of Ti alloy fibre-reinforced metal-matrix composites (MMCs) because high rates of alloy-droplet cooling on impact with the fibres prevent excessive fibre-matrix reaction. Ti-6Al-4V matrix MMC monotapes containing TiB/sub 2/-coated SiC fibres have been manufactured by electric-arc spray-forming, and the key MMC microstructural characteristics in the as-sprayed monotapes have been investigated by optical and scanning electron microscopy. Fibre infiltration increases with decreasing spraying distance, decreasing atomizing gas pressure and increasing arc current, because of higher temperatures in the Ti alloy spray droplets on impact with the fibres. Too much binder in the fibre preform leads to poor fibre-matrix contact, while removing the binder leads to the fibres becoming misaligned during spraying. 10 Refs.

(39) Ibbotson, A.R.; Beevers, C.J.; Bowen, P., Composites, vol.24, no.3, p.241-7, 1993

Abstract: The fatigue response of a continuous silicon carbide (SCS-6) fibre-reinforced Ti-6Al-4V metal-matrix composite in the presence of a sharp precrack has been studied in single-edge notched test-pieces in bending. Crack growth rates have been measured for different values of span-to-width ratio (s/W) at ambient temperature and at a test temperature of 550 degrees C in air by the use of a direct current potential difference technique. It was found that in most cases the observed crack growth rates initially decreased with increasing crack length (and hence increasing nominal applied stress intensity range). Effects of frequency on fatigue crack growth rates at 550 degrees C in air have also been identified. In general, crack growth rates are increased at 550 degrees C only at low frequencies, relative to the crack growth rates measured at ambient temperature. Based on observations to date it has been shown that fatigue cracks grown at a large span-to-width ratio propagate to failure more rapidly than cracks grown at small span-to-width ratios for equivalent initial nominal stress intensity ranges. Metallographic sections through the composite indicate that the improved

fatigue life observed at low values of s/W ratio may be attributable to debonding at the fibre/matrix interface, which is deduced to delay the onset of fibre failure. (21 Refs)

(40) Barney, C.; Beevers, C.J.; Bowen, P., **Fatigue crack propagation in SiC continuous fibre-reinforced ,Ti-6Al-4V alloy metal-matrix composites,** Composites, vol.24, no.3, p.229-34, 1993

Abstract: Fatigue crack growth from a through-thickness cut notch has been studied at ambient temperature in a Ti-6Al-4V alloy matrix reinforced with Sigma (SiC) fibres. All tests have been carried out in three-point bending, and localized dominant cracks have been produced in all cases. In these composites such dominant cracks often grow off-axis, and marked effects of stress ratio on crack growth rates have been measured. At low stress ratio, the composites exhibit outstanding crack growth resistance. It has been possible to observe fatigue striations within the matrix alloy and these observations allow local crack growth rates (and hence local effective stress intensity ranges) to be determined. The implications of such studies for defect tolerance and usable stress ranges for these composites have been considered. (17 Refs)

(41) Watson, M.C.; Clyne, T.W., **Reaction-induced changes in interfacial and macroscopic mechanical properties of SiC monofilament-reinforced titanium,**

Abstract: Results are presented from single fibre push-out testing, simple tension and impact three-point bending of SiC/Ti composites based on Ti-6Al-4V alloy reinforced with W-cored monofilaments having duplex C/TiB/sub 2/ coatings. Specimens were tested after various heat treatments and it is shown that a progressive increase in the interfacial shear stress for frictional sliding is observed as reaction proceeds. This increase in the resistance to frictional sliding can be correlated with a decrease in the thickness of the graphitic layer. Testing of composites subjected to the same heat treatments also revealed progressive reduction in tensile strength with increased reaction layer thickness. Monitoring of Poisson's ratios during testing was used to confirm that matrix plasticity occurred during axial loading, but inelastic behaviour was due to interfacial damage under transverse load. Consistent with this, impact energies were found to be higher under axial loading. Although some fibre pull-out was observed for axially loaded specimens without thick reaction layers, it is suggested that neither this nor any other interfacial process was contributing significantly to the work associated with impact loadings. (32 Refs)

(42) Yang, K.; Guo, Z.X.; Edmonds, D.V., **Processing of titanium matrix composites with hydrogen as a temporary alloying element,** Scripta Metallurgica et Materialia, vol.27, no.12, p., 1695-700,1992

Abstract: The fabrication temperature for Ti-1100 and Ti-6Al-4V matrices composites can evidently be lowered by the addition of hydrogen as a temporary alloying element to the matrices before fabrication, owing to the beta-stabilizing effect of hydrogen which enhances the hot-deformability of the matrices. Through this processing method the thickness of the interfacial reaction layer for the Ti-1100 matrix composite has been significantly reduced and the bonding of fibre/matrix for the Ti-6Al-4V improved. Additionally, the matrix microstructure for the Ti-6Al-4V composite was also found to be refined. It is expected that the fabrication temperature might be further lowered if the fabrication conditions are optimized further. (10 Refs)

(43) Davidson, D.L., **The micromechanics of fatigue crack growth at 25 degrees C in Ti-6Al-4V reinforced with SCS-6 fibers,** Metallurgical Transactions A (Physical Metallurgy and Materials Science), vol.23A, no.3, p.865-79,March 1992

Abstract: Micromechanics parameters for fatigue cracks growing perpendicular to fibers were measured for the center-notched specimen geometry. Fiber displacements, measured through small port holes in the matrix made by electropolishing, were used to determine fiber stresses, which raged from 1.1 to 4 GPa. Crack opening displacements at maximum load and residual crack opening displacements at minimum load were measured. Matrix was removed along the crack flanks after completion of the tests to reveal the extent and nature of the fiber damage. Analyses were made of these parameters, and it was found possible to link the extent of fiber debonding to residual COD and the shear stress for fiber sliding to COD. Measured experimental parameters were used to compute crack growth rates using a well-known fracture mechanics model for fiber bridging tailored to these experiments. (25 Refs)

(44) Morel, D.E., **Reaction kinetics in continuous silicon carbide reinforced titanium15V-3Cr-3Al-3Sn,** Journal of Materials Engineering, vol.13, no.4, p.251-5, Dec. 1991

Abstract: The reaction kinetics of a silicon carbide (SCS-6) reinforced titanium 15V-3Cr-3Al-3Sn composite have been characterized using a

combination of phase contrast optical microscopy and scanning electron microscopy. The matrix is an all beta alloy that is a potential substitute for the more commonly used Ti-6Al-4V because it can be cold rolled into thin foils without expensive intermediate anneals. The composite panel was fabricated via diffusion bonding and was composed of eight plies (0 degrees)/sub 8/. Samples were annealed under vacuum at temperatures ranging from 600 degrees C to 950 degrees C for periods of 4 to 96 hr. For a given temperature, the zone thickness was observed to increase linearly as a function of the square root of time. The data fit an Arrhenius type relationship where the slope of the ln k versus 1/T curve represents the activation energy for the process. Values for the activation energy, Q, are presented and compared for the 15-3 alloy, 6Al-4V, and other titanium matrix alloys. (13 Refs)

(45)..Watson, M.C.; Clyne, T.W., **The use of single fibre pushout testing to explore interfacial mechanics in SiC monofilament-reinforced Ti II. Application of the test to composite material,** Acta Metallurgica et Materialia, vol.40, no.1, p.141-8, 1992

Abstract: For pt.I see ibid., vol.40, no.1, p.131-9 (1992). Single fibre pushout testing has been used to measure the load needed to displace a fibre, as a function of its aspect ratio. This has been done for SiC monofilaments, having duplex carbon/TiB/sub 2/ coatings, embedded in a matrix of Ti-6Al-4V. Wedge-specimens have been used, allowing pushout of fibres with a range of aspect ratios from a single specimen. Partially pushed-out fibres have also been pushed back into the matrix. Specimens have been examined in the as-fabricated form and also after subsequent heat treatments. Analysis of the results indicates that in all cases it was the resistance to the onset of frictional sliding which was determining the pushout load. Values of the interfacial shear stress necessary for frictional sliding, tau /sub 0/ have been established, although it was not possible to measure separately the coefficient of static friction or the residual radial compressive stress. (21 Refs)

(46) Choy, K.-L.; Derby, B., **The CVD of TiB/sub 2/ protective coating on SiC monofilament fibres,** Journal de Physique IV (Colloque), vol.1, no.C2, p.697-703, Sept. 1991

Abstract: TiB/sub 2/ protective coatings have been deposited on SiC monofilament by a CVD technique. The CVD coating process studied involved the formation of TiB/sub 2/ on resistively heated SiC fibres from the chemical reaction of TiCl/sub 4/, BCl/sub 3/, H/sub 2/ at reduced pressure in a cold wall reactor. The effects of temperature, pressure and input reactant gas

ratio on the morphology and nature of the coatings were investigated. The efficiency of chemically vapour deposited TiB/sub 2/ as protective coating to inhibit the fibre-matrix interaction in titanium metal matrix composites was also evaluated by incorporating coated fibres in Ti-6Al-4V using diffusion bonding. (6 Refs)

(47) Lancin, M., **Title: Relationship between the microstructure of th interface and the mechanical behaviour of composites materials,** Journal de Physique III (Applied Physics, Materials Science, Fluids, Plasma and Instrumentation), vol.1, no.6, p.1141-66, June 1991

Abstract: The mechanical behaviour of glass, ceramic or metal matrix composites reinforced by long fibers depend on any parameters. The most important are the fiber strength and the resistance to debonding and/or to sliding at the interfaces. The aim of the tailoring of the interfaces, whose principle is briefly described, is to control these parameters. To predict its efficiency is till uncertain. Coupled microstructural and mechanical characterizations of the composites, but also of their constituents, have to be performed to reach a better understanding of the mechanical behaviour of these complex materials. The efficiency of such an approach is demonstrated by the studies of the SiC Nicalon fiber/LAS glass matrix and the SCS-6 fiber/Ti-6Al-4V matrix composites described. From the comparison of these studies to those previously performed in glass or ceramic glass matrix composites, it is possible to discuss the interest of a key point in the tailoring of the interfaces: the introduction of a carbon interphase by fiber-matrix reaction or by fiber coating before the process. (40 Refs)

(48) Leucht, R.; Dudek, H.J.; Ziegler, G., **Laboratory scale processing of SiC-Ti6Al4V composites,** Proceedings of the Institution of Mechanical Engineers Fourth International Conference. FRC '90 Fibre Reinforced Composites, 27-29 March 1990, Liverpool, UK, p. 279-82

Abstract: Using continuous SiC fibres for the reinforcement of the Ti6Al4V alloy and applying different processing routes, laboratory-scale processing of the composites is discussed. Plate samples with one or a few layers of fibres have been processed using hot pressing, cylindrical samples have been obtained using hot isostatic pressing. Fibre volume fractions of about 20 to 40% have been achieved resulting in an essential improvement of mechanical properties. Problems arising during processing, such as fracturing of fibres, fibre alignment and envelopment as well as the microstructure of the fibre-matrix interface are indicated. Examples of processing parts of different shapes are given. (11 Refs)

(49) Ferraris, M ; Badini, C ; Marino, F ; Marchetti, F ; Girardi, S, **Interfacial Reactions in a Ti- 6Al- 4V Based Composite: Role of the TiB sub 2 Coating,** Journal of Materials Science 28, (7), 1983-1987, 1 Apr. 1993

Abstract: The characterization of TiB sub 2 /C-coated SiC fibres and their interface region in a Ti-6Al-4V based composite has been performed by using scanning electron microscopy (SEM), energy-dispersion X-rays (EDX) and Auger electron spectroscopy (AES). The features of the as-received fibre and the reactivity between fibre and matrix occurring during preparation of the composite have been studied. The interaction of the TiB sub 2 external coating of the fibre with both the adjacent carbon layer and the titanium-based matrix is already appreciable in the as-received composite: TiB needles grow from TiB sub 2 towards the matrix and a new layer containing C, Ti and boron appears between TiB sub 2 and C. The thicknesses of the original C and TiB sub 2 fibre coatings decrease in the composite from 1000-400 and 800 nm, respectively. The TiB sub 2 inhibits the reaction between SiC and Ti: there is no evidence of Si sub x Ti sub y brittle phases. Graphs; Photomicrographs. 24 ref.

(50) Fukuhara, M ; Sanpei, A, **Elastic Moduli and Internal Friction of Low Carbon and Stainless Steels as a Function of Temperature,** ISIJ International 33, (4), 508-512 1993

Abstract: Elastic (Young, shear and bulk moduli, Poisson's ratio and Lame parameter), longitudinal and transverse internal friction values for low carbon steel (S10C) and stainless steel (304) were simultaneously measured over a temperature range 300-1500K, by an ultrasonic pulse sing-around method. These elastic moduli decrease and Poisson's ratio increases with increasing temperature, suggesting activation of shear mode in a high temperature region. Longitudinal and transverse internal frictions are sensitive to recrystallization, and to alpha (ferritic)/ gamma (austenitic) phase transition and solution of precipitated carbide phases into the austenitic matrix, respectively. A relaxation peak with an apparent activation energy of 0.97 eV was observed at approx 610K for the C steel. Comparisons are made to alumina, TZP, beta -sialon, SiC, Inconel 718, and Ti-6Al-4V. Graphs. 32 ref.

(51) Zhao, Y Y ; Grant, P S ; Cantor, B, **The Microstructure of Spray-Formed Ti-6Al-4V/SiC sub f Metal-Matrix Composites,** Journal of Microscopy 169, (2), 263-267 Feb. 1993

Abstract: Spray-forming is a possible manufacturing route for the fabrication of titanium alloy fibre-reinforced metal-matrix composites (MMCs) because high rates of alloy-droplet cooling on impact with the fibres prevent excessive fibrer-matrix reaction. Ti-6Al-4V matrix MMC monotapes containing TiB sub 2 -coated SiC fibres have been manufactured by electric-arc spray-forming, and the key MMC microstructural characteristics in the as-sprayed monotapes have been investigated by optical and scanning electron microscopy. Fibre infiltration increases with decreasing spraying distance, decreasing atomizing gas pressure and increasing arc current, because of higher temperatures in the Ti alloy spray droplets on impact with the fibres. Too much binder in the fibre preform leads to poor fibrer-matrix contact, while removing the binder leads to the fibres becoming misaligned during spraying. Photomicrographs; Graphs; Diffraction patterns. 10 ref.

(52) Warrier, S G ; Lin, R Y, **Using Rapid Infrared Forming to Control Interfaces in Titanium-Matrix Composites.**, JOM 45, (3), 24-27 Mar. 1993

Abstract: Control of the fiber-matrix reaction during composite fabrication is commonly achieved by shortening the processing time, coating the reinforcement with relatively inert materials, or adding alloying elements to retard the reaction. To minimize the processing time, a rapid infrared forming (RIF) technique for metal-matrix composite fabrication has been developed. Experiments have shown that the RIF technique is a quick, simple, and low-cost process to fabricate titanium-alloy (Ti80, Ti85, Ti- 6Al- 4V, Ti- 15V- 3Cr- 3Al- 3Sn, Ti- 24Al- 11Nb, Ti- 15Mo- 2.7Nb- 3Al- 0.2Si) matrix composites reinforced with either silicon carbide or carbon fibers. Due to short processing times, typically on the order of 1-2 min in an inert atmosphere for composites with up to eight-ply reinforcements, the interfacial reaction is limited and well controlled. Composites fabricated by this technique have mechanical properties that are either comparable to or, in several cases, superior to those made with conventional diffusion-bonding techniques. Graphs; Photomicrographs. 21 ref.

(53) Nicolaou, P D ; Piehler, H R ; Saigal, S, **Finite Element Analysis of the Consolidation Behavior of Composite Materials Using the Foil/Fiber/Foil Technique,** Conference: Concurrent Engineering Approach to Materials Processing, Chicago, Illinois, USA, 1-5 Nov. 1992, p. 247-260

Abstract: Finite element simulation was used to model the consolidation of metal matrix composites fabricated by the foil/fiber/foil technique. Material data were used for Ti- 6Al- 4V matrix and SCS-6 silicon carbide 142 mu m

diameter fibers and the temperature was kept constant at 875 deg C. The process parameters that were varied to characterize the consolidation behavior were applied stress level, and fiber spacing. Foil deformation occurred primarily by time dependent creep processes. Densification maps, which can be used to select the consolidation parameters, were constructed. A delay was observed in the densification in the latter stages of pore closure after the two neighboring foils have established contact with one another. This delay is attributed to the low stresses acting on the foil in the vicinity of the void. Fiber spacing is important in determining the time required to reach full density because higher strains must be imposed on the foils for smaller fiber spacings than for larger spacings. The simulation results presented are in very good agreement with experimental results reported earlier in the literature. Graphs; Photomicrographs. 11 ref.

(54) Bowen, P ; Ibbotson, A R ; Beevers, C J, **Characterisation of Crack Growth in Continuous Fibre Reinforced Titanium Based Composites Under Cyclic Loading,** Conference: Fatigue of Advanced Materials, Santa Barbara, California, USA, 13-18 Jan. 1991, p. 379-393

Abstract: Crack growth resistance has been studied under cyclic loading in continuous fibre (SiC) reinforced titanium alloy (Ti- 6Al- 4V) composites at ambient temperature. Single dominant cracks are formed, and they dictate the crack growth resistance of the composite. The mechanism of crack growth is characterised by initial matrix crack growth alone which results in fibres bridging the crack surfaces. The incidence of fibre failure then controls both the local value of da/dN and ultimately the onset of final catastrophic failure. Inevitably, this results in a crack size dependent crack growth resistance and toughness. Crack growth rates decrease in general with increased matrix fatigue crack length, but extreme care is required to predict stable/unstable transitions. Indeed, subtle effects of stress ratio are observed, but fibre failure appears to depend primarily on the cyclic load range. Graphs; Photomicrographs. 9 ref.

(55) Cox, B N, **Fatigue and Fracture of Brittle Fibrous Composites,** Conference: Fatigue of Advanced Materials, Santa Barbara, California, USA, 13-18 Jan. 1991, p. 53-65

Abstract: Theoretical aspects of fatigue and fracture in brittle fibrous composites, referring to prior observations of different failure modes in several such materials, are reviewed. Materials discussed include composites with ceramic and intermetallic matrices (Ti-25Al-10Nb-3V-1Mo/SCS-6, Ti-6Al-4V/SCS-6, LAS/SiC, Al sub 2 O sub 3 /Cu). The micromechanical

(intrinsic) and geometrical (extrinsic) factors that determine the mode of failure are discussed. Most of these considerations are based on detailed descriptions of matrix crack growth normal to aligned fibers under both monotonic and cyclic loading that have been developed over the last five years. The connection of micromechanical composite properties and macroscopic fracture and fatigue characteristics is highlighted. Graphs. 27 ref.

(56) Nicolaou, P D ; Piehler, H R ; Saigal, S, **Finite Element Simulations of the Consolidation of Continuous Fiber Reinforced Composites,** Conference: Computer Applications in Shaping & Forming of Materials, Denver, Colorado, USA, 21-25 Feb. 1993, p. 117-135

Abstract: The foil/fiber/foil process is one of the most common techniques used to fabricate continuous fiber reinforced composite. In composites consisting of several layers of foils and fibers, some of the fibers form a triangular arrangement, while others are arranged in a square pattern. Finite element analysis using the commercial code ABAQUS has been employed in order to determine which of these fiber arrangements densify at a lower rate, and hence, controls the densification process. The simulation results, based on composites comprised of Ti- 6Al- 4V foils and SCS-6 silicon carbide fibers showed that the triangular arrangement densifies much faster than the square. Foils comprising the square order to produce a fully densified composite. A slowing of the densification was observed in the latter stages of pore closure after the two neighboring foils have established contact with each other. This slowing may be attributed to both low stress levels and strain increases in the pore vicinity. Densification maps showing the change of density with time for a range of processing temperatures and applied stresses were also constructed. These maps can be used to select the consolidation parameters designed to minimize reaction zone formation at the matrix/ reinforcement interface, residual stresses, etc. Graphs; Photomicrographs. 12 ref.

(57) James, N A, **Small Coupon Tensile Tests for Ranking Monofilament-Reinforced Titanium MMC's,** Conference: Test Techniques for Metal Matrix Composites, London, UK, 20 Nov. 1990, p. 40-54

Abstract: BP Metal Composites is developing the technology required for the production of monofilament-reinforced composites. A range of fabrication methods are being studied. Development is taking place at the BP Research Centre, and at the recently-acquired subsidiary, DWA Composite Specialties in the USA. To assess the quality of MMC's produced by vacuum hot pressing at the BP Research Centre, a tensile ranking test has been developed. The test

provides a rapid assessment of the relative quality of small MMC coupons. The net-shape coupons are fabricated by vacuum-hot pressing in a Nimonic die. The samples are then tabbed and strain gauges applied to prepare them for testing. The details of fabrication and preparation are described. Composites have been produced using uncoated BP Sigma SiC monofilament and the recently-developed duplex coated BP Sigma monofilament in Ti- 6Al-4V. The test data from these composites are presented, and the importance of these data to the development of a successful fabrication process is indicated. Graphs; Photomicrographs. 3 ref.

(58) Bowen, P ; Cotterill, P J ; Ibbotson, A R, **Fatigue Crack Growth in Continuous Fibre Reinforced Metal Matrix Composites,** Conference: Test Techniques for Metal Matrix Composites, London, UK, 20 Nov. 1990, p. 82-97

Abstract: A unique relationship between the crack growth rate per cycle, da/dN, and the applied alternating stress intensity range, Delta K, does not exist in continuous fibre reinforced titanium (Ti-15V-3Cr-3Al-3Sn, Ti-6Al-4V) based metal matrix composites because crack growth resistance depends critically on fatigue crack length. This is a direct consequence of crack bridging by intact fibres which causes a marked reduction in the value of stress intensity range local to the growing crack-tip. Nevertheless, if a single dominant crack dictates the crack growth resistance of the composite, then it appears that fracture mechanics parameters may be of use in predicting crack growth rates. They also have potential for estimating lifetimes provided that effective crack-tip stress intensities can be modelled accurately. The use of the direct current potential drop technique is considered in detail. Care must be taken to ensure that standard calibration curves that relate changes in potential to changes in crack length are applicable to the small scale testpieces under study. Most importantly, the technique shows some promise in detecting individual fibre failures. Graphs. 13 ref.

(59) Roman, I ; Jero, P D, **Interfacial Shear Behavior of Two Titanium-Based SCS-6 Model Composites,** Conference: Intermetallic Matrix Composites II, San Francisco, California, USA, 27-30 Apr. 1992, p. 337-342

Abstract: Single fiber push-out and push-back tests combined with acoustic response monitoring were used to examine the interfacial behavior in two Ti alloy-SiC fiber comosites. Distinctly different behaviors were observed in the two systems. The differences were attributed to the formation of a substantial interfacial reaction layer in one of the composites which changed the interfacial chemistry and the resulting debond topography. The reaction layer

caused an increase in the interfacial bond strength and in the roughness of the debonded interface. The latter resulted in substantially increased sliding friction. Although both composite interfaces exhibited some roughness, only one showed a seating drop during fiber push-back. This is related to the fact that the reaction layer which formed in one of the composites was severely degraded during fiber push-out. Although this interface was still rough, the roughness correspondence between fiber and matrix was destroyed during sliding, such that seating was no longer possible. Graphs; Photomicrographs. 20 ref.

(60) Bowen, P ; Ibbotson, A R ; Beevers, C J, **Fatigue Crack Growth in Continuous Fibre Reinforced Titanium Alloy Metal Matrix Composites,** Conference: Mechanical Behaviour of Materials- VI. Vol. 3, Kyoto, Japan, 29 July-2 Aug. 1991,p. 107-112

Abstract: Crack growth rate/cycle, da/dN, does not have an unique relationship with the applied alternating stress intensity range, Delta K, in continuous SiC fibre reinforced Ti based metal matrix composites. This is a direct consequence of crack bridging by intact fibres which results in crack size dependent crack growth resistance. In the testpiece geometry considered, a single dominant crack develops and grows through matrix regions first, leaving fibres bridging in the crack wake. This results in decreased crack growth rates as the crack grows. The onset of first fibre failure appears to be controlled by the applied stress intensity range, but care is needed to define stable/unstable crack transition. The number of intact fibres bridging the crack is of paramount importance in determining the onset of catastrophic failure. Graphs; Photomicrographs. 9 ref.

(61) Iamai, Y ; Shinohara, Y ; Ikeno, S ; Shiota, I, **Deterioration Factor of SiC/Ti Alloy Composite After Heat Treatment,** ISIJ International 32, (8), Aug. 1992, p. 917-922

Abstract: Reaction is caused at the interface between fiber and metal-matrix in a composite at an elevated temperature. The reaction greatly affects the strength of the composite. SiC-fiber reinforced Ti-alloy composites were fabricated by diffusion bonding. The reaction products were examined after heat-treatment of the composites. Effect of the reaction products on the strength of the composites was studied. SiC fiber was used as the reinforcement material. Titanium, Ti- 6Al- 4V or Ti- 8Mo/Ti- 6Al- 4V was used as the matrix. The heat-treatment was carried out at a temperature of 1073 or 1123K for 32.4-360 ks. The strengths of heat-treated composites were measured at room temperature. In the case of Ti matrix, the strength of

composites decreased to 60% with increasing temperature and time of the heat-treatment. The decreasing of the strength of composites was little in the cases of the alloy matrices except at 1123K for 360ks. The reaction products were TiC and Ti sub 5 Si sub 3 in every matrix studied. TiC was formed on the surface of the SiC fiber and Ti sub 5 Si sub 3 was formed outward of TiC. From these results, the alloying elements were effective to decrease the reaction at the interface. The abrupt decrease of the strength of the composites was due to increasing of defects between SiC and the reaction products. A small pit was often observed at the periphery of the fiber in fracture surface. The morphology of the fracture surface showed the pit was the initiation of the crack propagation. This means the deterioration of the fiber depends not on the thickness of the reaction zone but on the pit, especially in the case of serious degradation. Then the deterioration of the fiber was often rather serious even though the thickness of the reaction zone was small. Graphs; Photomicrographs. 7 ref.

(62) Jeng, S M ; Yang, J -M ; Rosenthal, D G ; Aksoy, S, **Mechanical Behaviour of SiC Fibre-Reinforced Titanium/Titanium Aluminide Hybrid Composites,** Journal of Materials Science 27, (19), 5357-5364, Oct. 1992

Abstract: The viability of developing an SiC fibre-reinforced Ti/titanium aluminide hybrid matrix composite was explored. The hybrid composites are expected to be used at temperatures beyond those attainable in conventional Ti matrix composites while improving the damage tolerance of the titanium aluminide matrix composites. The room-temperature mechanical characteristics studied were tensile strength, fracture toughness, low-cycle fatigue life and fatigue crack growth rate. The mechanisms of damage initiation and propagation under various loading conditions were also characterized. The directions for developing a satisfactory composite with hybrid Ti/titanium aluminide (Ti- 6Al- 4V, Ti- 25Al- 10Nb- 3V- 1Mo) matrix are also addressed. Photomicrographs; Graphs. 12 ref.

(63) Jeng, S M ; Alassoeur, P ; Yang, J -M, **Fracture Mechanisms of Fiber-Reinforced Titanium Alloy Matrix Composites,** Materials Science and Engineering A A154, (1), 11-19, June 1992

Abstract: The fatigue crack propagation behavior of several SCS-6 fiber-reinforced Ti alloy matrix composites (Ti- 6Al- 4V, Ti-15-3, Ti-25-10) at room temperature was studied. The testing was conducted in a tension-tension mode on specimens with a chevron notch perpendicular to the fiber direction. The maximum applied stress intensity ranged from 25-50 MPa m

exp 1/2 . The fatigue crack growth rates at different applied stress intensity levels were measured. The fatigue damage mechanisms at each testing condition were also identified. Several damage mechanisms were observed at the crack tip including matrix cracking, fiber bridging, crack splitting and crack deflection. The loading conditions, fiber/matrix interfacial shear strength and matrix cracking stress under cyclic loading were the major microstructural parameters controlling the fatigue crack growth behavior. A modified frictional slip model was also used to predict the fatigue crack propagation behavior and correlated with experimental results. Graphs; Photomicrographs. 18 ref.

(64) Ibbotson, A R ; Beevers, C J ; Bowen, P, **Fatigue Crack Growth in Fibre Reinforced Metal Matrix Composites.,** Conference: Euromat 91. Vol. II. Advanced Structural Materials, Cambridge, UK, 22-24 July 1991 p. 469-478

Abstract: Studies are presented in which composite systems (Ti-15.3/SiC and Ti- 6Al- 4V/SiC) displayed good crack growth resistance even though dominant cracks are produced. In particular, fatigue crack growth rates do not increase significantly with increased nominal applied stress intensity range, and in many instances decreases in crack growth rates are observed with fatigue crack length increase. This is explained by a reduction in effective stress intensity range by fibre bridging in the crack wake, and stable/unstable crack growth transitions are considered. Similar behaviour is seen in general at elevated temperature (550 deg C) although crack growth rates are higher; and crack growth occurs off-axis, consistent with a decrease in the effective fibre-matrix interface strength. Graphs; Photomicrographs. 17 ref.

(65) Bowen, P ; Cardona, D C ; Ibbotson, A R, **Micromodelling of Crack Growth in Fibre Reinforced Composites,** Conference: Second International ASM Conference on High Temperature Aluminides and Intermetallics. II, San Diego, California, Sept. 16-19,1991, p. 628-634

Abstract: Rudimentary modelling based on point-loading (weight function) methods has been used to assess the crack growth resistance of fibre reinforced composite materials (Ti- 6Al- 4V matrix, SiC fibers). Many trends in observed crack growth resistance behaviour in the presence of crack bridging can be predicted qualitatively. For the case of single dominant cracks the application of fracture mechanics parameters to characterize crack growth appears to be justified. Graphs; Photomicrographs. 8 ref

(66) Jeng, S, **Fracture Mechanisms of the SCS-6 Fiber-Reinforced Titanium Alloy Matrix Composites,** University of California (Los Angeles), Dissertation, p 198 June 1992

Abstract: The mechanical properties and failure mechanisms of several SCS-6/Ti alloy matrix composites have been studied. Tensile, notched three-point bending, low cycle fatigue and fatigue crack propagation tests were conducted at room temperature on the unidirectional SiC fiber-reinforced Ti-15V-3Cr-3Al- 3Sn, Ti-6Al-4V and Ti-25Al-10Nb-3V -1Mo composites. Microstructural parameters controlling the deformation, damage initiation and growth of the composites were investigated using metallographic technique and fractographic analysis. These parameters include interfacial reaction between fiber and matrix, interfacial mechanical properties, matrix toughness, fiber strength and loading conditions. The resulting deformation and fracture mechanisms of these composites under quasi-static and notched three-point bend loading were classified on the basis of the ratio of the fiber strength (sigma sub f): interfacial shear strength (tau sub i) vs. matrix toughness. These failure mechanisms provide a scientific basis for the development of an analytical model to predict the micro- and macro-fracture processes of fiber-reinforced metal matrix composites. Furthermore, the low cycle fatigue damage diagram was constructed using the maximum stress in the fiber vs. fatigue life. Depending on the stress levels applied, the fatigue damage of the composites can be classified into three regions: fiber breakage dominated; interfacial cracking, matrix cracking and fiber breakage dominated (progressive); and matrix cracking dominated. Matrix cracking with bridging fibers in the wake of the crack tip was the major mechanism for the fatigue crack propagation behavior of the composites. The transition from the noncatastrophic to catastrophic mode I failure was controlled by the fiber breakage in the wake of crack. A micromechanical model was also proposed to predict the fatigue crack propagation behavior of the composites. These results can be used as guidelines for the selection of processing parameters, fiber coating, and matrix modification to develop high-performance metal matrix composites.

(67) Bakarinova, V I, **Interphase Interaction in Composite Materials Based on Titanium,** Conference: MICC 90: Moscow International Composites Conference 1990, Moscow, USSR, 14-16 Nov. 1990, p. 445-453

Abstract: A characteristic feature of the fibrous composite materials (FCM) is that their ceramic fibers and matrix are mutually active, the resultant reaction being responsible, in most cases, for the formation of chemical compounds. The boundary conditions can be improved by selecting a matrix alloy and strengthener which are less likely to interact with one another, and

by applying barrier coats to the fibers. The nature and rate of the physicochemical interaction at the fiber-matrix boundary were estimated by analyzing the results of comparing the thickness values of the zones formed in various temperature and time conditions of annealing the FCM produced by means of diffusion welding. The investigation of the FCM reinforced by ceramic fibers showed that the rate of forming the interaction zones when using the matrixes made of high alloys was lower than that in the case of pure Ti. The thermal stability of the silicon carbide fibers proved to be greater than that of the boron fibers in several Ti alloys. The study of the effects of the silicon carbide, boron carbide and boron nitride barrier coats of the B fibers has revealed a difference in the nature and degree of efficiency of the coats on the interphase surface while confirming that much could be expected as a result of further study. Graphs; Photomicrographs. 3 ref.

(68) Kahveci, A I ; Cook, C R ; Auhl, J R ; Meyer, T N, **Processing and Properties of SiC Fiber Reinforced Aluminum and Titanium Alloy Composites,** Conference: Thermal Spray Coatings: Properties, Processes and Applications, Pittsburgh, Pennsylvania, USA, 4-10 May 1991, p. 357-362

Abstract: A summary of research on the processing of SiC fiber reinforced metal matrix composites is presented. Composites were fabricated by thermal spraying of Al and Ti alloys. As-sprayed and consolidated composites were evaluated by optical and SEM techniques. Fiber damage during thermal deposition and the effect of various coatings on fiber damage were studied. Mechanical properties of some consolidated composites were determined at room temperature. The matrix materials are conventional high temperature 2319 Al alloys, very high temperature Al- Fe- Ce alloys (CZ42-[Al- 7Fe- 6Ce] and CU78-[Al- 8.3Fe- 4Ce]), Ti- 6Al- 4V, and Ti- 14Al- 21Nb alloys. Photomicrographs; Graphs. 18 ref.

(69) Wei, W, **Interfacial Properties of a SiC Fibre-Reinforce Titanium Alloy After Long-Term High-Temperature Exposur** Journal of Materials Science 27, (7), Apr.1992, p.1801-1810

Abstract: The effect of long-term high-temperature exposure on the interfacial properties of a typical SiC continuous fibre-reinforced Ti alloy was investigated. Specimens were annealed in air and in vacuum under simulated operating conditions using temperatures up to 500 deg C for times up to 700 h. The interfacial chemistry and fracture morphology of the specimens were determined using Auger and scanning electron microscopy. It was shown that high-temperature long-term exposure to air resulted in embrittlement of the fibre/matrix interface through combined oxidation and attack of the Ti

matrix on the fibres and fibre coating. Exposure to operating temperatures in vacuum did not lead to a significant degradation of the interfaces. The degradation of the interfaces in high temperature service can lead to a reduction of the service life of components made of reactive system metal-matrix composites such as SiC-reinforced Ti alloys (e.g. Ti- 6Al- 4V). Spectra; Photomicrographs; Graphs. 15 ref.

(70) Saigal, A ; Kupperman, D S ; Majumdar, S, **Residual Strains in Titanium Matrix High-Temperature Composites**, Materials Science and Engineering A A150, (1), 20 Feb. 1992, p. 59-65.

Abstract: Residual thermal strains and stresses that developed during cooling of a silicon-carbide-fiber-reinforced Ti matrix high-temperature composite were determined by an experimental neutron diffraction technique. The results were compared with those obtained by finite element analysis. The study was conducted over the temperature range 20-950 deg C. As a result of thermal expansion mismatch, compressive residual strains and stresses were generated in the fibers during cool-down. The axial residual strains and stresses were highly tensile in the matrix, and the matrix underwent plastic deformation. Average transverse residual strains in the matrix were compressive. The measured data compare fairly well with finite element method predictions. The effects of fabrication procedures and thermal processing, such as liquid nitrogen dipping and thermal cycling, on the residual strains were also studied. Graphs 14 ref.

(71) Masuda, C ; Tanaka, Y ; Shiota, I ; Imai, Y ; Furubayashi, E ; Usami, K ; Hirano, T ; Iwasaki, H, **Nondestructive Evaluation of Fibers or Defects in Metal Matrix Composites by X-Ray Computed Tomography Using Synchrotron Radiation**, Conference: Structural Composites: Design and Processing Technologies, Publ: ASM International, Materials Park, Ohio 44073-0002, USA, 1990, p. 179-186

Abstract: Boron or silicon carbide fiber reinforced Al or Al alloys (6061) matrix composites and silicon carbide reinforced Ti alloy (Ti- 6Al- 4V) matrix composite were used for the observation of inner fibers contained in the composites by X-ray computed tomography (CT) using synchrotron radiation in the photon factory in National Laboratory for High Energy Physics (KEK) in Japan. The energies were selected to 21 and 29 keV for Al alloy and Ti matrix composites on the basis of the X-ray absorption coefficients of the included elements in composites, respectively. The inner fibers and debonding part of the interface between fiber and matrix were clearly observed for composites used. In the case of the silicon carbide reinforced Al composites, the core

carbon fibers of 30 mu m in diameter were also observed. It is considered that the resolution of X-ray CT scanner used was approx 10 mu m. The three-dimensional images were reconstructed from several CT images. It is pointed out that the three-dimensional images visually displayed inner structures and it is very useful to discuss the model of the fracture process of the fiber contained in the metal matrix composites. Graphs; Photomicrographs. 9 ref.

(72) Davidson, D L, **The Micromechanics of Fatigue Crack Growth at 2: deg C in Ti- 6Al- 4V Reinforced With SCS-6 Fibers,** Southwest Research Institute (US), Metallurgical Transactions A 23A, (3), Mar. 1992 , p. 865-879.

Abstract: Micromechanics parameters for fatigue cracks growing perpendicular to fibers were measured for the center-notched specimen geometry. Fiber displacements, measured through small port holes in the matrix made by electropolishing, were used to determine fiber stresses, which ranged from 1.1-4 Gpa. Crack opening displacements at maximum load and residual crack opening displacements at minimum load were measured. Matrix was removed along the crack flanks after completion of the tests to reveal the extent and nature of the fiber damage. Analyses were made of these parameters, and it was found possible to link the extent of fiber debonding to residual COD and the shear stress for fiber sliding to COD. Measured experimental parameters were used to compute crack growth rates using a well-known fracture mechanics model for fiber bridging tailored to these experiments. Graphs; Photomicrographs. 25 ref.

(73) Bashyam, M, **Ultrasonic NDE for Ceramic- and Metal-Matrix Composite Material Characterization,** General Electric Aircraft Engines, Conference: Review of Progress in Quantitative Nondestructive Evaluation. Vol. 10B, La Jolla, California, USA, 15-20 July 1990, p. 1423-1430

Abstract: A theoretical model to calculate elastic properties and ultrasonic velocities for a variety of materials was developed. This model has proven suitable for parametric studies to examine effect of varying fiber volume fractions and porosity, among other things. The materials used in experiments (Ti- 6Al- 4V/silicon carbide, calcium aluminum silicate/silicon carbide, and calcium aluminum silicate/nicalon) seem to be mildly anisotropic in contrast with graphite- epoxy composites. The low attenuation properties of the metal matrix composite (MMC) and ceramic matrix composite (CMC) materials make it practical to measure sound velocities. It was also noted that the velocity transverse to the fibers is a useful indicator of the fiber volume fraction. The measurement of frequency-dependent attenuation has proven

to be very useful to classify defects. A practical method to acquire and process signals was used and results indicate that this method has the potential to distinguish between porosity and planar type defects. For large scale operations, it would be necessary to optimize this inspection procedure. One rewarding approach could be the use of real-time DSP filtering techniques to extract two or three frequencies of interest instead of analyzing the entire waveform and spectrum. Polar backscatter technique was used to analyze fiber orientation and other fiber related defects. The backscatter technique has contributed to improving the sensitivity of porosity detection for the MMC and CMC materials. It was demonstrated that low frequency SAW has the potential to detect sub-surface defects, porosity, and material inhomogeneity. Photomicrographs; Graphs. 7 ref.

(74) Murthy, P L N ; Chamis, C C, **Computational Simulation of High Temperature Metal Matrix Composite Behavior.,** NASA Lewis Research Center NASA. Technical Memorandum Pp 18 1991. Report No.: NASA TM-104377.

Abstract: Computational procedures are described to simulate the thermal and mechanical behavior of high temperature metal matrix composite (HT-MMC) in the following four broad areas: (1) behavior of HT-MMC from micromechanics to laminate; (2) HT-MMC structural response for simple and complex structural components; (3) HT-MMC microfracture; and (4) tailoring of HT-MMC behavior for optimum specific performance. Representative results from each area are presented to illustrate the effectiveness of the computational simulation procedures. Relevant reports are referenced for extended discussion regarding the specific area. (SiC/Ti-6-4 is used as an example). Graphs. 15 ref.

(75) Paley, M ; Aboudi, J, **Inelastic Thermal Buckling of Metal Matrix Laminated Plates,** Tel-Aviv University, Journal of Thermal Stresses 14, (4), Oct.-Dec. 1991, p.479-497

Abstract: A method is proposed for determining the critical temperature changes that cause inelastic thermal bifurcation buckling of metal matrix composite plates (SiC/Ti- 6Al- 4V). The inelastic behavior of the metallic matrix is described by an elastic- viscoplastic temperature-dependent constitutive law; the fibers are allowed to be either elastic or elastic-viscoplastic material. The approach is based on the applied thermal load and the history-dependent instantaneous effective thermomechanical properties of metal matrix composites, which are established by a micromechanical analysis. The method is illustrated by the prediction of the inelastic thermal

buckling of SiC/Ti metal matrix angle-ply laminated plates by employing the classical and first-order shear deformable laminated plate theories. Graphs. 15 ref.

(76) Jeng, S M ; Alassoeur, P ; Yang, J -M ; Aksoy, S, **Fracture Mechanisms of Fiber-Reinforced Titanium Alloy Matrix Composites.IV. Low Cycle Fatigue,** University of California (Los Angeles), Materials Science and Engineering A A148, (1), 30 Nov. 1991, p. 67-77

Abstract: The low cycle fatigue behavior and mechanisms of fatigue damage initiation and propagation of several SCS-6 fiber-reinforced Ti alloy composites (Ti- 6Al- 4V, Ti- 15V- 3Cr- 3Al- 3Sn, Ti- 25Al- 10Nb- 3V- 1Mo) at room temperature were investigated. The fatigue damage diagram was constructed using the maximum stress in the fiber vs. fatigue life. Depending on the stress levels applied, the fatigue damage of the composites can be classified into three regions; (1) fiber breakage dominated; (2) interfacial cracking, matrix cracking, and fiber breakage dominated (progressive); and (3) matrix cracking dominated. The microstructural parameters which affect the low cycle fatigue behavior of these composites are also discussed. Graphs; Photomicrographs. 16 ref.

(77) Stock, S R ; Breunig, T M ; Guvenilir, A ; Kinney, J H ; Nichols, M C, **Damage in Metal Matrix Composites and Crack Face Interactions During In Situ Loading of Al- Li Alloy 2090 Studied by X-Ray Tomographic Microscopy,** Georgia Institute of Technology, Conference: 1991 Industrial Computed Tomography II Topical Conference, San Diego, California, USA, 20-24 May 1991, p. 158-162.

Abstract: Results of quantitative damage accumulation studies in a continuous, aligned-fiber SiC/Al metal matrix composite and observations of internal crack geometry in samples of Al- Li alloy 2090 are summarized for synchrotron and laboratory XTM. A small, portable load frame for in situ XTM is described and is used to observe fatigue crack face interactions as a function of applied load in the Al- Li alloy. Data for SiC/Ti- 6Al- 4V composites illustrate what can be accomplished with wiggler radiation at energies as low as 30 keV. Future applications of XTM to mechanical properties studies are suggested, and the corresponding experimental requirements are discussed. Photomicrographs.

(78) Ko, W L ; Jackson, R H, **Combined-Load Buckling Behavior of Metal-Matrix Composite Sandwich Panels Under Different Thermal**

Environments. (Report), NASA Dryden Flight Research Center, NASA. Technical Memorandum Pp 28 1991, Report No.: NASA TM-4321.

Abstract: Combined compressive and shear buckling analysis was conducted on flat rectangular sandwich panels with the consideration of transverse shear effects of the core. The sandwich panel is fabricatd with Ti honeycomb core (e.g. Ti- 6Al- 4V) and laminated metal-matrix composite (e.g. Ti- 15V- 3Cr- 3Al/SiC sub F) face sheets. The results show that the square panel has the highest combined-load buckling strength, and that the buckling strength decreases sharply with the increases of both temperature and panel aspect ratio. The effect of layup (fiber orientation) on the buckling strength of the panels was investigated in detail. The metal-matrix composite sandwich panel was much more efficient than the sandwich panel with nonreinforced face sheets and had the same specific weight. Graphs. 8 ref.

(79) Gigerenzer, H ; Kumnick, A J, **Low Pressure Induction Plasma Spraying of Titanium Metal Matrix Composites SCS-6/Ti6Al- 4V and SCS-6/Ti6Al- 2Sn- 4Zr- 2Mo,** Textron Specialty Materials, Conference: Plasma Processing and Synthesis of Materials. III, San Francisco, California, USA, 17-19 Apr. 1990, p. 29-37.

Abstract: Two Ti metal matrix composites (MMCs) have been successfully fabricated from low pressure induction plasma sprayed monotape and their mechanical behavior has been characterized. Powders of Ti6Al- 4V (Ti6-4) and Ti6Al- 2Sn- 4Zr- 2Mo (Ti6-2-4-2) were used as matrix sources and the reinforcement was Textron Specialty Materials (TSM) SCS-6 silicon carbide fiber. The importance of process control to minimize interstitial (O, nitrogen, hydrogen, and carbon) contamination effects is discussed. Oxygen m pick-ups were reduced to typicaly < 200 ppm and total interstitial pick-up levels were in the range of 200-500 ppm. Uniaxially reinforced composite panels of four-ply construction were fabricated from these monotape materials by the HIP process and tension tests in the fiber direction were performed. Tensile strengths and elastic moduli averaged 1565 MPa (227 ksi) and 182 GPa (26.4 MSI) for the SCS-6/Ti6-4; and 1531 MPa (222 ksi) and 184 GPa (26.7 MSI) for the SCS-6/Ti6-2-4-2 for composite fiber volume fractions of 0.27-0.28 and 0.29-0.30, respectively. The results compared favorably with other fabrication approaches for these composite systems and with rule-of-mixture (ROM) predictions. It was concluded that SCS-6/Ti composites fabricated from plasma sprayed monotapes exhibit properties consistent with state-of-the-art MMC fabrication technology. Graphs, Photomicrographs. 6 ref.

(80) Jeng, S M ; Yang, J -M ; Yang, C J, **Fracture Mechanisms of Fiber-Reinforced Titanium Alloy Matrix Composites.III. Toughening Behavior,** University of California (Los Angeles), Materials Science and Engineering A A138, (2), 15 June 1991, p. 181-190

Abstract: The damage mechanisms of several notched unidirectional SCS-6 fiber-reinforced Ti alloy (Ti- 6Al- 4V, Ti- 15V- 3Al- 3Cr- 3Sn, Ti sub 3 Al) matrix composites tested under three-point bending are evaluated. The key microstructure parameters which dominate the load- deflection curve, crack tip initiation, crack tip damage growth and fracture behavior of these composites are discussed. The role of the fiber/matrix interface in crack initiation and propagation is also examined. Results indicate that the crack initiation energy is affected by the fiber strength, matrix yield strength or shear strength. The crack propagation energy is controlled by matrix phase deformation, multiple fiber fracture and fiber pull-out. Graphs, Photomicrographs. 9 ref.

(81) Yang, J -M ; Jeng, S M ; Yang, C J, **Fracture Mechanisms of Fiber-Reinforced Titanium Alloy Matrix Composites.I. Interfacial Behavior,** University of California (Los Angeles), Materials Science and Engineering A A138, (2), 15 June 1991, p. 155-167

Abstract: Interfacial shear strength and frictional stress of SiC, boron, Al sub 2 O sub 3 fiber-reinforced Ti alloy (Ti- 6Al- 4V, Ti- 15V- 3Al- 3Cr- 3Sn, Ti sub 3 Al) matrix composites were determined using indentation and fragmentation tests. The influences of fiber surface chemistry, matrix alloy comopsition, microstructure and prolonged thermal exposure on the interfacial properties were invstigated. The interface failure resulting from indentation loading was characterized using scanning electron microscopy. Also, the influence of interfacial reaction on the strength of the fiber was determined. Results indicate that the mechanical properties and failure characteristics of the interfacial region depend on fiber surface chemistry, matrix microstructure, and residual stresses at the interface. Graphs, Photomicrographs. 25 ref.

(82) Cornie, J A ; Argon, A S ; Gupta, V, **Designing Interfaces in Inorganic Matrix Composites,** MRS Bulletin 16, (4), Apr. 1991, p. 32-38.

Abstract: The conditions for engineering interfaces between P-55 (10 mu m diameter graphite fiber) and an Al matrix to provide mechanical fusion through a controlled delamination process are analysed for maximum cohesive strength. An interfacial crack-bridging axial-toughening mechanism

is maintained for interface delamination of composites. The methods of micromechanical measurement of interface strength and modifications of interfaces through reinforcement surface treatment are outlined. The results on other systems are presented which include interface synthesis in PACVD amorphous SiC-coated P-55 fibers in an Al matrix, SCS-6 CVD SiC monofilament in Ti- 6Al- 4V and Si sub 3 N sub 4 matrices. Graphs, Photomicrographs. 17 ref.

(83) Hunt, M, **Epic Proportions in Metal-Matrix Composites,** Materials Engineering (Cleveland) 108, (3), Mar. 1991, 24-27.

Abstract: Metal macrocomposites are engineered materials consisting of large-scale combinations of metals with other materials. Macrocomposites include metal sheets bonded to cores of resin, ceramic, metal, honeycomb or foam; cast metals with large-scale reinforcements; components with two or more different monolithic metals bonded to each other; and combinations of monolithic materials and reinforced metals. These macrocomposites improve strength and stiffness of metals while reducing weight and keeping costs lower than conventional metal-matrix composites. A review of macrocomposites covers composite HIP, honeycomb, honeycomb for CATs, resin cores, acoustic materials, sound damping steel, and a cast composite brake drum. Materials mentioned are Ti- 15Al- 3V, Ti- 6Al- 4V, Inconel 718; Al5052, 6061, 2024, 7075, and 7475.

(84) McMeeking, R M ; Evans, A G, **Matrix Fatigue Cracking in Fiber Composites,** University of California (Santa Barbara), Mechanics of Materials 9, (3), 19 Nov. 1990, p. 217-227.

Abstract: A model is developed for fatigue growth of matrix cracks in metals (e.g. Ti- 6Al- 4V) reinforced with aligned continuous elastic fibers (e.g. SiC). The mechanics of elastic cracks bridged by frictionally constrained fibers is used to develop the model, which provides estimates of the tip value of the stress intensity factor amplitude, Delta K sub TIP. It is found that, when the applied load amplitude is held fixed during fatigue crack growth, Delta K sub TIP , and thus the rate of growth approach an asymptotic value independent of crack length. The residual strength after fatigue crack growth is also discussed. In some cases, the residual strength is unaffected by prior fatigue growth. But, in another regime, the matrix crack length allows fibers to begin breaking before the matrix crack grows. The strength is then inversely proportional to the square root of fatigue crack length. Graphs. 19 ref.- AA

(85) Molliex, L ; Favre, J P ; Vassel, A, **Micromechanical Approach of Tensile Properties in Titanium-Based Composites,** ONERA, Conference: Titanium 1990: Products and Applications. Vol. 1, Lake Buena Vista, Florida, USA, 30 Sept.-3 Oct. 1990, p. 180-188.

Abstract: The fragmentation test, where a single Si fiber (SCS-6) embedded in a tensile specimen of Ti-6-4 matrix breaks into short fragments, was applied to determine quantitatively the ability of the interface to transfer stresses between fiber and matrix up to 900 deg C. The interface parameter was then introduced into a model of stochastic fracture of the SCS-6/Ti-6-4 unidirectional composite. The evolution of the tensile strength as a function of temperature was predicted and agrees very well with the experimental tensile test data. Graphs, Photomicrographs. 12 ref.

(86) Bain, K R ; Gambone, M L, **Fatigue Crack Growth of SCS-6/Ti-64 Metal Matrix Composite.Materials Behavior Research,** General Motors, Conference: Fundamental Relationships Between Microstructures and Mechanical Properties of Metal Matrix Composites, Indianapolis, Indiana, USA, 1-5 Oct. 1989, p. 459-469.

Abstract: The longitudinal fatigue crack growth behavior (growth across the fibers) of continuous reinforced SCS-6/Ti-64 composite was tested at 600 deg F (316 deg C) . Several specimen designs were evaluated, and a procedure for precracking the specimens was developed . The fatigue crack growth was measured in a range of stress intensity from 20-60 ksi root in. and a range of crack growth rate from 10 exp - 9 in./cycle to 3 x 10 exp - 7 in/cycle . The effect of frequency was examined between cycling at 20 Hz down to 0.2 cycles/min . Reducing the frequency did not increase the rate of crack growth between 20 Hz and 20 cpm . However, the crack growth rate did increase when the cycle frequency was decreased to 0.2 cycles/min . This may be due to the effect of the environment on either the matrix or the fiber matrix interface . The cracks were found to grow normal to the load and across the fibers at low stress intensities but vertical crack growth was found in all specimen geometries at high initial cyclic stress intensities. Fractography of the failed specimens indicated that the matrix and the fibers did not fail on the same plane. Crack growth is planar through the matrix. The fibers are "pulled out" of the matrix and fracture out of the plane of the matrix. Graphs, Photomicrographs. 2 ref.

(87) Sensmeier, M D ; Wright, P K, **The Effect of Fiber Bridging on Fatigue Crack Growth in Titanium Matrix Composites,** GE Aircraft Engines, Conference: Fundamental Relationships Between Microstructures and

Mechanical Properties of Metal Matrix Composites, Indianapolis, Indiana, 1-5 Oct. 1989, p. 441-457.

Abstract: The model analysis and experimental results show that fiber bridging of fatigue cracks can occur in Ti matrix composites (Ti- 6Al- 4V/SiC) under conditions of practical interest. This fiber bridging can have a profound effect on the fatigue crack growth rates measured for the matrix cracks. The extent of fiber bridging is found to depend on fiber/matrix interfacial shear strength, applied stress, and fiber strength. For optimum crack growth resistance in the composite system, the right balance of interfacial strength and fiber bridging must be obtained. If the interface is too strong, the degree of fiber bridging is lessened and the crack grows fairly quickly. However, if the interface is too weak, there is much more bridging yet less closure force is achieved. If the correct interface stress range is achieved, a successful balance between the bridging zone size and bridging closure force will be obtained. For the composite system studied, it was found that decreasing the applied stress range increases the interface stress range over which substantial increases in crack growth life can be obtained. Also, increasing the strength of the fiber should result in a similar increase in this range. Graphs, Photomicrographs. 2 ref.

(88) Bakuckas, J. G. ; Johnson, W. S., **Application of Fiber Bridging Models to Fatigue Crack Growth in Unidirectional Titanium Matrix Composites,** National Aeronautics and Space Administration, Hampton, VA. Langley Research Center. Corp., Report No.: NAS 1.15:107588; NASA-TM-107588, Jul 92, p. 54.

Abstract: Several fiber bridging models were reviewed and applied to study the matrix fatigue crack growth behavior in center notched (0)(sub 8) SCS-6/Ti-15-3 and (0)(sub 4) SCS-6/Ti-6Al-4V laminates. Observations revealed that fatigue damage consisted primarily of matrix cracks and fiber matrix interfacial failure in the (0)(sub 8) SCS-6/Ti-15-3 laminates. Fiber-matrix interface failure included fracture of the brittle reaction zone and cracking between the two carbon rich fiber coatings. Intact fibers in the wake of the matrix cracks reduce the stress intensity factor range. Thus, an applied stress intensity factor range is inappropriate to characterize matrix crack growth behavior. Fiber bridging models were used to determine the matrix stress intensity factor range in titanium metal matrix composites. In these models, the fibers in the wake of the crack are idealized as a closure pressure. An unknown constant frictional shear stress is assumed to act along the debond or slip length of the bridging fibers. The frictional shear stress was used as a curve fitting parameter to available data (crack growth data, crack opening displacement data, and debond length data). Large variations in the frictional

shear stress required to fit the experimental data indicate that the fiber bridging models in their present form lack predictive capabilities. However, these models provide an efficient and relatively simple engineering method for conducting parametric studies of the matrix growth behavior based on constituent properties.

(89) Lamathe, G.; Kagawa, Y. (Tokyo Univ., Japan); OKURA, A. (Inst. of Space, Sagamihara, Japan) **Influence of the reaction zone on the interfacial shear stress in SiC/titanium alloy composite, and Astronautical Science,** In: Advanced composite materials II (A93-32976 12-24). Paris, SIRPE and Les Techniques de l'Ingenieur, 1991, p. 266-268.

Abstract: An investigation is conducted of the influence of the reaction-zone thickness on the shear properties of SiC fiber-reinforced Ti-6Al-4V is presently conducted by means of the shear-lag model for determination of interfacial shear debonding stress and frictional sliding shear stress during indentation tests. Three concentric-cylinder models are used to study the behavior of the complex interface between fiber and matrix.

(90) UPADHYA, KAMLESHWAR, ED., **Developments in ceramic and metal-matrix composites**; Proceedings of the Symposium, TMS Annual Meeting, San Diego, CA, Mar. 1-5, 1992, p. 397

Abstract: The present volume on aerospace applications of advanced composites discusses test environment and temperature changes on the tensile behavior of SiC/SiC, the foil-fiber-foil hot-pressing fabrication of fiber-reinforced Ti6Al4V, the fabrication of NB3Al in situ composite microstructures, fiber/matrix interface reactions in SiC-reinforced Ti alloys, and X-ray computed tomography for advanced materials and processes. Also discussed are the damping behavior characterization of graphite particulate-reinforced Al composites, the numerical modeling of residual stresses in graded ceramic/metal materials, the growth rate of thermally-induced microcracks in metal-matrix composites, laminated metal composites, Fe/sapphire interfaces, and the flow behavior of constrained ductile phases.

(91) ONZAWA, TADAO; SUZUMURA, AKIO; KIM, JONG H., **Influence of reaction zone thickness on tensile strength for titanium-matrix composites reinforced with SiC fiber IN: Composites;** Proceedings of the 8th International Conference on Composite Materials (ICCM/8), Honolulu, HI, July 15-19, 1991. Section 12-21, p. 19-J-1 to 19-J-10.

Abstract: The effect of the reaction-zone thickness on the tensile strength of SiC-fiber-reinforced composites with various Ti-containing matrices including

a commercially pure Ti (CPTi), Ti-6Al-4V, and Ti-21V-4Al, was investigated. The major reaction products in the fiber-matrix interface were TiC and Ti5Si3. Results of SEM and TEM observations showed that the growth rate of the reaction zone in the composite with Ti-21V-4Al matrix was lower than in composites with CPTi and Ti-6Al-4V matrices. The tensile strength of composites decreased with increasing reaction-zone thickness, but only after the reaction zone thickness reached the value of 1 micron. (I.S.).

(92) JAMES, N. A.; LOVETT, D. J.; WARWICK, C. M., **Mechanical behaviour of a continuous fibre reinforced titanium matrix composite,** Proceedings of the 8th International Conference on Composite Materials (ICCM/8), Honolulu, HI, July 15-19, 1991. Section 12-21, p. 19-I-1 to 19-I-10.

Abstract: C/TiB2-coated SiC monofilament has been consolidated in a Ti-6Al-4V matrix. The composite shows strength greater than 1700 MPa and a stiffness of 210 GPa. Exposure to 865 C in vacuum leads to little strength loss after 3.25 hours. The strength of the composite after longer exposure at this temperature also has been studied and related to fracture behavior.

(93) NAKAJO, Y., WANG, S. S. (Illinois, University, Urbana), **High-temperature fatigue crack growth of SCS6/Ti-6Al-4V metal-matrix composite,** Proceedings of the 5th Japan-U.S. Conference on Composite Materials, Tokyo, Japan, June 24-27, 1990, p. 329-336.

Abstract: Fatigue crack growth experiments were conducted on double edge notch specimen of SCS6/Ti-6Al-4V unidirectional metal-matrix composite both at room temperature and at 316 C along with experiments for monotonic fracture toughness. The results clearly depict the high-temperature effects on basic material service and design. For transverse fatigue crack growth, commonly used DeltaJ-da/dN data reduction is successfully conducted, but for longitudinal fatigue crack growth, the same DeltaJ-da/dN data reduction is found to be invalid because it cannot account for perpendicular cracking, fiber debonding, or developing plastic zone which are undertaking during the longitudinal fatigue crack growth.

(94) GAMBONE, M. L., **Fatigue and fracture of titanium aluminides,** volume 2 Final Report, 1 Jul. 1985 - 31 Jul. 1989, Detroit Diesel Allison, Indianapolis, IN., Publication Date: Feb. 1990 235P., Report No.: AD-A227353; ALLISON-EDR-14249-VOL-2; WRDC-TR-89-4145-VOL-2, Contract No.: F33615-85-C-5111; AF PROJ. 2420

Abstract: Titanium aluminide composites hold great promise for application in the later stages of advanced compressor systems. This conclusion is based on the assumption that Ti3Al composites can achieve the fatigue strength levels projected from data for the SiC/Ti 6Al-4V composite system yet remain stable to 650 C or higher temperatures. In the limited results to date, Ti3Al composite specimens have exhibited a minimum of fiber/matrix interaction, good strength stiffness, and significantly better fatigue strength than monolithic Ti3Al. The good fatigue and high stiffness are essential for application to the high temperature compressor spacers in the minimum-weight rotor configuration being developed. The key material design parameters for titanium aluminides and titanium aluminide composites must be identified and understood. These parameters include the fatigue and fracture behavior (crack initiation and propagation as a function of temperature, frequency, size, and stress ratio), the near threshold stressintensity crack growth rates, and the thermomechanical fatigue behavior.

(95) Barney, C.; Beevers, C. J.; Bowen, P., **Fatigue crack propagation in silicon carbide continuous fiber-reinforced Ti-6Al-4V alloy metal-matrix composites;** Composites, 1993 v. 24, no. 3, Pp. 229-34.

IDENTIFIERS: silicon carbide titanium composite fatigue, fiber silicon carbide titanium fatigue **DESCRIPTORS**: Synthetic fibers,silicon carbide.. composites with titanium alloy, fatigue crack propagation in **CAS REGISTRY NUMBERS**: 12743-70-3 composites with silicon carbide fibers, fatigue crack propagation in 409-21-2 properties, composites with titanium alloy matrix, fatigue crack propagation in,

(96) Hemptenmacher, J.; Leucht, R.; Dudek, H. J., **Metallographic characterization of titanium alloy Ti6Al4V used as a metal matrix in silicon carbide fiber composites;** Inst. Werkstofforsch., Dtsch. Forschungsanst. Luft- und Raumfahrt, Cologne/Porz, Germany, Sonderb. Prakt. Metallogr, 1992 v. 23, no. Metallographie, p. 245-57

IDENTIFIERS: titanium composite silicon carbide microstructure, silicon carbide fiber composite microstructure, **DESCRIPTORS**: Synthetic fibers,silicon carbide... composites with titanium-aluminum-vanadium alloy, microstructure of, **CAS REGISTRY NUMBERS**: 12743-70-3 composites with silicon carbide fibers, microstructure of 409-21-2 uses, fibers, composites with titanium-aluminum-vanadium alloy microstructure of,

APPENDIX B

A Review of Ti-6Al-4V/SCS-6 Composite Characterization Data

LIST OF TABLES

LIST OF FIGURES

LIST OF FIGURES (Cont'd)

LIST OF FIGURES (Cont'd)

LIST OF FIGURES (Cont'd)

LIST OF FIGURES (Cont'd)

LIST OF FIGURES (Cont'd)

Mechanical Properties And Characterization of SCS-6/Ti-6AL-4V Composite

(1) Title : Mechanical and Fracture Properties of Metal Matrix Composites

Author : S. Bandyapadhyay

The paper presents a very brief overview of the mechanical and fracture properties of MMCs with emphasis on discontinuously reinforced aluminium alloys. The composite strength is shown to increases with 30-40% vf but with further reinforcement, the failure is likely at the onset of yield due to loss of ductility. The higher vf, the inability of the matrix to redistribute the stresses results in very high localized fiber stresses. The yield strength of discontinuously reinforced aluminium alloy is noted as ≅ 450 MPa, Ultimate Tensile Strength ≅ 600 MPa and elastic modulus in excess of 120 GPa. The properties for SiC reinforced aluminum Ti-6-4 are shown in Table 1. The stress strain behavior of various Al matrices with 20% vf of SiC is shown in Fig. 1. The effect of variation in the Sic/6061 Al composite is presented in Fig. 2. The paper does not provide data for continuously reinforced composites.

(2) Title : The Influence of the Interface on Mechanical Behavior of Ti-6Al-4V/SCS-6 Composites

Author : P. K. Wright, R. Nimmer, G. Smith, M. Sensmier and M. Brun

The paper provides a detailed experimental and FEM treatment of the nature of fiber/matrix interface for the Ti-6Al-4V/SCS-6 composite. The main thrust of the paper is to provide evidence supporting hypothesis that interface bonding is primarily due to thermal residual stresses. In transverse tensile loading, normal to the fiber direction, the interface separation occurs much earlier than the composite fracture.

The test coupons were made from Ti-6-4/SCS-6 composite panels having 26 to 37% vf, purchased from Textron. The fibers were C-rich coated. The as fabricated structure of the interface is shown in Fig. 3a. Some of the panels were heat treated and thermally cycled. The heat treatment was carried out at 900 C (1650 F) in vacuum for 10 hours and thermal cycling was done 2000 times between 21 C (70 F) and 427 C (800 F), in air. An increase in the reaction zone of the interface was observed for the heat treated material (Fig. 3b), whereas the structure of thermally cycled fiber matrix interface (Fig. 3c) did not show any degradation.

The following tests were carried out :

(1) Transverse tension.
(2) Longitudinal tension.
(3) In-plane shear.
(4) Longitudinal fatigue crack growth.

The composite properties for longitudinal and transverse tests at RT, 316 C (600F) and 427 C (800 F) - for longitudinal tension only are shown in Table 2. The stress strain response of the composite from transverse tensile test is plotted in Fig. 4. The *knee* in the plot is attributed to separation of fiber/matrix interface which occurs at low applied loads. The finite element analysis result is also given in Fig. 4 which shows close agreement with the observations. The interface separation occurs when the residual stresses (45 ksi/310 MPa) are overcome by the applied load. The composite has weak strength under transverse tensile loading. The results from the longitudinal tensile tests are shown in Fig. 5 for the as fabricated, heat treated and thermally cycled specimens. Any degradation of UTS for the thermally treated samples is not clearly evident. Also, the interface separation does not play major role during the longitudinal tensile loading. At post-test examination, the fiber pullout lengths were measured to be less than 0.01-0.015 inch (0.25-0.40 mm) for all types of tests.

The in-plane shear tests were done using Iosipescu and ± 45 tension/compression methods. No yielding occurred till buckling for compressive tests whereas prominent yielding was observed for tensile tests. The test results are shown in Fig. 6. The interfacial shear strengths of Ti-64/SCS-6 as found from the fiber indentation tests are given in Table 3. The tests concluded that interface friction coefficient is between 0.75 and 1. The interface shear strength was observed to be about half the matrix yield strength, i.e., 66 ksi (450 MPa).

(3) Title : <u>The Relationship between Interfacial Reaction and Tensile Strength of SiC Filament Reinforced Ti Alloy Composites</u>

Author : Yoshio Imai, Yoshikazu Shinohara, Susumu Ikeno and Ichiro Shiota

The influence of reaction zone of SCS-6 and Ti/Ti-8Mo/Ti-6-4 composites on their tensile strength were analyzed at microscopic level. The materials were heat treated at 1023 K for 32.4 ks, at 1073 K for 126 ks and at 1123 K for 360 ks. The composites did not show noticeable degradation except those treated at 1123 K for 360 ks. The reaction

product growth was minimum for SCS-6/Ti-6-4. The thickness δ of the reaction products is calculated as follows :

$$\delta = (2A\,t)^{\frac{1}{2}}$$

where A is reaction rate constant and t is heating time. The parameter A is expressed as

$$A = A_0 \exp(-Q/kT)$$

where A_0 is constant, Q is activation energy and k is Boltzmann constant. The value of A_0 for Ti-6-4 matrix is given as 1.24E-05. cm^2/sec.

Fig. 7 shows reaction zone view of Ti-6-4/SCS-6 composite after heat treatment and Fig. 8 gives the thickness of the reaction zone versus square root of the heating time. The growth rate of reaction zone thickness for SCS-6/Ti-6-4 was minimum among the tested composites. The relationships between tensile strength and heating time, and effect of reaction products on composite tensile strength are shown in Figs. 9 and 10, respectively. All composites, heat treated at 1123 K for 360 ks, show an abrupt drop of strength with an increase of reaction zone thickness. For Ti-6-4/SCS-6, the strength was 60% of ROM. As the constituents individually do not lose their strength to such extent, the drop in strength is attributed to faults in the reaction zone.

(4) Title : Shear Creep Deformation of SCS6/Ti-6Al-4V Metal Matrix Composite at Elevated Temperatures

Author : A. Miyase and S. S. Wang

The article provides experimental results of monotonic shear and shear creep tests for the SCS-6/Ti-6-4 composite at 600 F and room temperatures. The tests were conducted on 8 layer specimens processed at 1700 F under 15 ksi for 2 hours. Both 0 and 90 degree specimens were tested.

The monotonic shear stress strain curves for the composite and matrix are shown in Fig. 11 for RT and in Fig. 12 for 600 F. For 90 degree, abrupt failure occurs at the onset of plasticity. The predicted composite shear moduli are 10.0 and 8.7 Msi at room temperature and 600 F, respectively, using Halpin-Tsai equation. These values are approximately 10% higher than given by the experimental data. The results at 600 F for shear creep tests of unidirectional SCS-6/Ti-6-4 for

various stress levels are shown in Fig. 13. The shear creep for both 0 and 90 degree specimens is well behaved. Because the fiber creep at this temperature is negligible, the shear mode is dominated by the fiber/matrix interface deformation.

The failure modes are also examined under monotonic and shear creep loading. The 90 degree specimen were loaded at τ = 27 ksi and 0 degree specimen at τ = 40 ksi. The photographic evidence from the tests is shown in Figs. 14-21. For both monotonic shear and shear creep, the failure modes are similar. The cause of failures is the debonding of the interface, primarily between SCS-6 and the matrix. The authors have also noted that in case of monotonic shear loading for 90 degree orientation, the failure appears at a single fracture plane, whereas for 0 degree the failure occurs by developing multiple shear bands along the fiber direction. For 0 degree test, the damaged fibers were aligned in the thickness direction. For 90 degree test, SiC fiber and SCS6 coating interphase was also damaged.

(5) Title : Fracture mechanisms of fiber-reinforced titanium alloy matrix composites. Part II: Tensile behavior

Author : S. M. Jeng, J.-M., Yang, C. J. Yang

Along with other MMC materials, tensile and fracture tests were carried out on SCS-6/Ti-6-4 of 36% vf, unidirectional composite. The samples were heat treated in vacuum at 800 C for 50 and 100 hrs before the test. The experiment was conducted at RT. The paper emphasizes that the MMC behavior is dependent upon mechanical properties of the constituents, fiber/matrix interface and geometrical conditions. Above 700 C, the chemical reaction at the interface severely degrades the fiber strength. The stress strain curve for SCS-6/Ti-6-4 composite is shown in Fig. 22. The tensile properties for as fabricated and thermally exposed composite are given in Table 4. The pre-test thermal treatment did not degrade the material properties of SCS-6/Ti-6-4.

The post-test examination revealed a flat fracture surface, interface debond, matrix plastic deformation and multiple cracking of the interfacial reaction zone. The interface between carbon layer and reaction zone, however, was intact. The tensile strength, cracking length and the reaction zone Weibull modulus values are given in Table 5. Fig. 23 shows the tensile strength of the interfacial region for SCS-6/Ti-6-4 (also for SCS-6/Ti-15-3) as a function of the reaction zone thickness.

(6) Title : Ultimate strengths of fiber-reinforced ceramics and metals

Author : W. A. Curtin

A theory for predicting ultimate tensile strength of fiber reinforced ceramics is discussed which is then applied, in modified form, to predict MMC strength. The assumption is that a small pre-existing matrix crack propagates at the critical stress σ_{mx} in a plane perpendicular to the fiber. The crack does not propagate across the fiber, instead, the fiber matrix interface debonds and the stress is transferred to the matrix through shear over a length defined as a function of critical stress and the internal shear. Once the matrix cracks are sufficiently closed space, all applied loads are carried by the fibers alone. The situation is depicted in Fig. 24. The global load sharing theory allows that the average stress per unbroken fiber is σv_f. If some fibers are broken in a chosen plane then other fibers near the plane must carry load $T>\sigma v_f$. It is assumed that no fibers are broken within a *sliding length* $\pm l_f$ of the chosen plane, as shown in Fig. 25. The broken fibers within $\pm l_f$ carry reduced load of $2\tau Lr$ where L and r are the average distance of broken fibers from the plane and fiber radius, respectively.

The matrix cracking phenomenon is modified for the case of MMC materials. It is now assumed that beyond true matrix stress σ_y, the matrix can not carry additional load. The debonding of the fiber/matrix interface still occurs upon fiber fracture. The modified theory to predict the ultimate MMC tensile strength is as under :

$$\sigma_u = f[(\frac{2}{m+2})^{\frac{1}{m+1}} (\frac{m+1}{m+2})] \sigma_c + (1-f) \sigma_y$$

$$\sigma_c = [\frac{\sigma_0^m \tau L_0}{r}]^{1/m+1}$$

m = Weibull modulus.
τ = sliding resistance (shear).
f = fiber volume fraction.

The mechanical properties of SCS-6 and predicted strength of SCS-6/Ti-6-4 are shown in Table 6. The Table also lists results predicted by the Rule of Mixtures (ROM) and Bundle Rule of Mixture theories (BROM). The predictions are within acceptable agreement of experimental data.

(7) Title : Tensile and Compressive Properties of Metal Matrix Composites

Author : R. J. Arsenault

The chapter analyzes the elastic characteristics of continuous and discontinuous MMCs by applying the ROM and other analytical expressions to predict the material properties. Restricting discussion to CMMCs (Continuous Metal Matrix Composites) only, the equations reproduced here are in general applicable to all types of composites. Considering that the MMC operating environment are likely to be at high temperatures with significant non-linearities, the information available in the current article is of limited value.

Using ROM, the longitudinal and transverse modulus of elasticity for a unidirectional composite are given by :

$$E_{11} = E_f V_f + E_m V_m \qquad \text{(longitudinal)}$$

$$\frac{1}{E_{22}} = \frac{V_m}{E_m} + \frac{V_f}{E_f} \qquad \text{(transverse)}$$

The elastic moduli and stress strain relationships for a transversely isotropic composite (Fig. 26) having 5 independent elastic constants are listed in Table 7. The elastic longitudinal, transverse and shear modulus and Poisson ratios are shown in Table 8, defined in micromechanics modelling approach. The Halpin-Tsai equations are also useful in approximating the elastic composite behavior. For unidirectionally loaded fibers, the moduli is given by :

$$\frac{p}{p_m} = \frac{1 + \xi\eta V_f}{1 + \eta V_f}$$

$$\eta = \frac{p_f/p_m - 1}{p_f/p_m + \xi}$$

where p and p_m denote the composite and corresponding matrix moduli The values for empirical constant ξ are given in Table 9.

The stress state of an axially loaded unit cell (cylinder-within-cylinder) is shown in Fig. 27. where the inner cylinder represents a fiber. The UTS provided by the model for two MMCs, i.e., SiC/Ti-6-4 and SCS-6/Ti-6-4) are given in Table 10.

(8) Title : Interfacial Properties Measurement For SiC Fiber-Reinforced Titanium Alloy Composites

Author : C. J. Yang, S. M. Jeng, and J.-M., Yang

The interfacial properties for SCS-6/Ti-6-4 and other MMC were measured by indentation technique using Vickers microhardness indenter. The SCS-6/Ti-6-4 composite was tested as fabricated and also after annealing at 800 C for 50 and 100 hrs. The samples were 1 to 5 times the fiber diameter and load was increased form 0.1 to 3.6 kg in 0.1 kg increments till fiber/matrix sliding was initiated. Then the pushed out fiber was indented in the reverse direction The test arrangement and a pushed out fiber are shown in Figs. 28 and 29, respectively. On the average, 15 tests were carried out from one sample. The shear stress was calculated from

$$\tau_{rf} = P/2\pi rt$$

$$\tau_{rf} = P/2\pi r\,(t-\alpha) \qquad \text{(corrected)}$$

assuming that frictional and debonding stresses were constant along the fiber length. In the above equation P is the debonding load, r is the fiber radius, t is the specimen thickness and α is a correction constant for free edge effect.

The interfacial debond strength and frictional stress for SCS-6/Ti-6-4 are shown in Table 11. The annealed specimen show some increase in debond and frictional stresses. The interface between the two carbon coatings, outer carbon coating, reaction zone and matrix were all debonded (Fig. 30). It was noticed that the reaction primarily occurred between C-rich layer and the matrix, therefor, preserving fiber characteristics.

(9) Title : <u>The Tensioned Pushout Test for Fiber-Matrix Interface Characterization Under Mixed Mode Loading</u>

Author : M. C. Watson and T. W. Clyne

A 5 mm^2, 2 mm thick specimen was cut form 35% vf laminate with fibers parallel to the thickness. The specimen was then diffusion bonded into a large matrix panel to facilitate gripping for transverse loading. Before diffusion, the specimen edges were chamfered to 45 deg angle. It was then placed on six alloy foils, each 20 mm^2 and 500 μm thick. A constant stress of 150 MPa was maintained at 850 C for 30 mins. The diffusion scheme is shown in Fig. 31. The specimen was then cut, grounded and thinned by careful metallographic polishing to a foil of 110 μm thickness.

The test method is illustrated in Fig. 32. To compensate for any specimen curvature incurred during preparation, handling and loading, strain gauges were attached both at the top and bottom of the specimen. These were then adjusted to ensure proper biaxial loading. The in-plane stress was applied by screw arrangement on half of each pair of grips. The axial load was applied via indenter till the pushout was achieved.

The total in-plane load includes the applied load plus the residual stress, which can be obtained using an analytical model. The shear stress was calculated from

$$\tau_{rf} = \frac{\sigma_{po}}{4s}$$

where σ_{po} is the pushout stress, s is the ratio of fiber depth to diameter. The approximation to the radial stress was done using the following equations :

$$\sigma_1 = \frac{E_m \varepsilon_s}{(1-\nu_m)}$$

and $$\sigma_r = 1.25\, \sigma_1$$

In the above, ε_s is the strain gauge reading, E_m and ν_m are the matrix Young's modulus and Poisson's ratios, respectively. The fiber/matrix interface stress is approximated at 25% higher than the far field in-plane stress σ_1. The fiber and matrix properties used in calculations are given in Table 12. The experimental interfacial shear and radial stresses for SiC/Ti-6-4 are plotted in Fig. 33. The data is considered preliminary but the test technique can be used effectively to get further data for biaxial loading.

(10) Title : Micromechanical Modeling of Fiber/Matrix Interface Effects in Transversely Loaded SiC/Ti-6-4 Metal Matrix Composites

Author : Ronald P. Nimmer, R. J. Banker, Edward S. Russell, Gary A. Smith and Kennard Wright.

Residual Stresses

A detailed 3-D unit cell finite element analysis of SCS-6/Ti-6-4 was carried out under the assumptions of perfect and weak fiber/matrix bond. Also, the accumulation of residual stresses was calculated and

compared with measurements. The composite was fabricated by HIP process with vf of 0.35. A typical composite microstructure is shown in Fig. 34 and model geometry is given in Fig. 35. The Ti-6-4 properties used in the analysis are shown in Table 13. The fiber SCS-6 was assumed to be isotropic and homogeneous. The time independent, linear elastic properties supplied by the supplier were as follows:

$$E = 414 \text{ GPa}$$
$$\nu = 0.3$$
$$\alpha = 4.86 \times 10^{-6} / C$$
$$T_{ref} = 900 \text{ C}$$

where α is the coefficient of thermal expansion.

The residual stresses in matrix at location M1 (shown in the figure) as a function of temperature are plotted in Fig. 36. The matrix residual stresses are maximum at the indicated location, i.e., M1. The plot shows that the matrix is below but close to yield, using von Mises criterion. The y direction fiber and matrix stress contours are shown in Fig. 37. At z = 0 plane, these stresses are equal to the radial stress and in x-z plane, the y direction stresses are equivalent to the residual hoop stress. The radial stresses are compressive whereas the circumferential stresses change sign across the fiber-matrix interface. The large positive hoop stress in the matrix tends to develop radial direction crack in the matrix. The effective stress in the matrix is plotted in Fig. 38. The fiber effective stress (465 to 475 MPa and uniform) is not shown. The maximum tensile values occur close to the interface along y and z axis and minimum stress occurs along the unit cell diagonal.

The authors point out effect of significant variations in reported values of coefficient of thermal expansion. If a large α value is used in the analysis then matrix may yield between 400 and 500 C during cool down. It was further shown that when time dependent matrix properties were used in power law model, the prediction of effective stress fell by 16% and no yielding was indicated (Fig. 39). A cooling rate of 2300 C/hr was assumed for the above analysis. Using X-ray diffraction, the average tensile residual stresses were measured as 275-345 MPa (axial) and 175-200 MPa (transverse). Therefore, the finite element calculations predicted 21% and 35% higher residual stresses in the axial and radial directions, respectively. However, predictions by using time dependent matrix properties are closer to the measurements.

Fiber/Matrix Interface

Finite Element analysis was conducted using perfect and weak interface geometrical models for the unit composite cell of 35% vf. The weak interface assumes 0 transverse tensile strength of the interface and in compression, the materials can not inter-penetrate. The average stress strain curves for the two cases are plotted in Fig. 40. The analysis included the effect of residual stresses and time independent material properties. The interface coefficient of friction was assumed to be 0.3. The contours of y direction stress at 175 MPa, 250 MPa and effective stress at 470 MPa are shown in Figs. 41 to 43. The comparison of weak bond analysis and experimental stress strain data at RT, 315 and 427 C is provided in Figs. 44 to 46. The parameter R in the plots is the b to c ratio (Fig. 36).

The prominent feature of the experimental data and weak interface is the occurrence of *knee* which corresponds to the separation of fiber matrix interface. The photograph in Fig. 47 shows the state of the interface at 138 and 276 MPa, respectively. A separation is clearly visible for the latter case, which is at the stress level above the *knee*.

(11) Title : The Effect of The Matrix Constitutive Model On Residual Thermal Stresses in MMC.

Author : James B. Brayshaw and Marek-Jerzy Pindera

The paper presents a comparison of residual stresses using micromechanic method of cells (Aboudi), Bodner-Partom unified theory of viscoplasticity and finite element results of Nimmer et. al [10]. The properties used for SiC fibers and Ti-6-4 are given in Tables 14 to 17.

Temperature dependent response of Ti-6-4 is shown in Fig. 48. Fig. 49 shows comparison of σ_r, σ_θ, and σ_{axial} from Aboudi's and finite element models (Nimmer et. al. (10) above) using time-independent matrix properties. The method of cells provides average stress values over a number of finite elements between the two adjacent fibers. The finite element results shown are for a matrix element next to the fiber/matrix interface toward the nearest neighboring fiber. A comparison of residual effective stress using both models is also shown in Fig. 50, both for time dependent and time independent matrix properties.

In addition to finite element method, the residual stresses were also compared using method of cells for Bodner-Partom and Power-law creep models using the higher set of α values from Table 14. The residual effective stresses at four cooling rates using the two models are plotted in Fig. 51. Further, comparison of residual stress σ_r, σ_θ, and σ_{axial} using the above two models is shown in Fig. 52. The plots indicate that using the Power-law model, the stresses are proportional to the cooling rate. The accumulation effect is greater above 500 C. It is suggested that for Bodner-Partom model, the stresses are not high enough to initiate significant time dependent behavior, therefor the stresses are same at all cooling rates.

(12) Title : Mechanical Characterization of SCS-6/Ti-6-4 Metal Matrix Composite

Author : C. T. Sun, J. L. Chen, G. T. Sha and W. E. Koop

This paper provides detailed results from off axis SCS-6/Ti-6-4 tensile tests conducted at RT with 40% vf. The test data are co-related with an orthotropic plasticity model. The fiber/matrix interface damage (weak bond) and residual stresses due to thermal coefficient mismatch have also been investigated.

The off axis tensile test results are shown in Table 18 and the corresponding stress strain curves are plotted in Fig. 53. Also in Figs. 54 and 55, loading and unloading behavior of 45 and 90 deg specimens is shown. The pseudo plasticity observed in the figures is not predicted by continuum plasticity. The hysteresis is attributed to slippage and damage of the fiber/matrix interface.

Elastic Model

To calculate the off axis properties, the coordinate system is aligned with the principle material axis, x1 and x2. Then by using generalized Hooke's Law for the orthotropic elastic model :

$$E_\theta = \left[\frac{\cos^4\theta}{E_1} + \left(\frac{1}{G_{12}} - 2\frac{\nu_{12}}{E_1}\right)\cos^2\theta \sin^2\theta + \frac{\sin^4\theta}{E_2} \right]^{-1}$$

$$\nu_{xy} = E_x \left[\frac{\nu_{12}}{E_1}(\sin^4\theta + \cos^4\theta) - \left(\frac{1}{E_1} + \frac{1}{E_2} - \frac{1}{G_{12}}\right)\sin^2\theta + \cos^2\theta \right]$$

The values for G_{12} were found by choosing a value such that E_θ agrees well with the experiment. The predicted values of Young's moduli and Poisson's ratio are compared with the test data in Figs. 56 and 57.

Plasticity Model

To characterize the plastic behavior of composite, authors introduced a *one-parameter plastic model.* The model is based on a plastic potential function as under :

$$f = \frac{1}{2}(\sigma_{22}^2 + 2a_{66}\,\sigma_{12}^2)$$

The model assumes that the composite is linearly elastic in the fiber direction, i.e., $d\varepsilon_{11}^p = 0$. The other incremental plastic strains are calculated from :

$$d\varepsilon_{ij}^p = d\lambda \frac{\partial f}{\partial \sigma_{ij}}, \; ij = 11, 22, 12$$

$$dW^p = \sigma_{ij}\, d\varepsilon_{ij}^p = 2f\, d\lambda \quad \text{(plastic work increment)}$$

$$\bar{\sigma} = \sqrt{3f} = \sigma_x\, h(\theta) \quad \text{(effective stress)}$$

$$d\bar{\varepsilon}^p = \frac{dW^p}{\bar{\sigma}} = d\varepsilon_x^p / h(\theta) \quad \text{(effective plastic strain)}$$

$$h(\theta) = \left[\frac{3}{2}(\text{Sin}^4\theta + 2\,a_{66}\,\text{Sin}^2\theta\,\text{Cos}^2\theta)\right]^{1/2}$$

$$d\lambda = 3/2 \frac{1}{h^2(\theta)} \frac{d\varepsilon_x^p}{d\sigma_x} \frac{d\sigma_x}{\sigma_x} \quad \text{(proportionality constant)}$$

and

The total plastic strain for off axis loading (Fig. 58) is obtained from :

$$\varepsilon_x = \frac{\sigma_x}{E_\theta} + \varepsilon_x^p$$

Yield Criterion

The authors also propose an off-axis yield criterion obtained from the potential plastic flow function using equation :

$$\sigma_{22}^2 + 2a_{66}\sigma_{12}^2 = k_y^2$$

where k_y is the yield stress for the 90 deg specimen. The yield plot using $a_{66} = 0.85$ and $a_{66} = 0.5$ is shown in Fig. 59.

Failure Criterion

Two failure criteria are derived for SCS-6/Ti-6-4 (Fig. 60). The first criterion assumes independent modes of failure for the fiber and matrix. The equations based on the longitudinal and transverse composite strength are :

$$\sigma_{22}^2 + 2b_{66}\sigma_{12}^2 = Y^2 \text{ (matrix failure)}$$

$$\sigma_{11} = X \text{ (fiber failure)}$$

from test results

$$X = 1.793 \text{ GPa, } Y = 313.8 \text{ GPa and } b_{66} = 0.85$$

The second failure criterion uses a quadratic stress function of the form:

$$b_{11}\,\sigma_{11}^2 + \sigma_{22}^2 + 2\,b_{12}\,\sigma_{11}\,\sigma_{12} + 2\,b_{66}\,\sigma_{12}^2 = Y^2$$

where, from the test data $b_{11} = 0.03$, $b_{12} = -0.03$ and $b_{66} = 0.85$

Residual Stresses

The authors also derive expression for residual stresses using a micromechanics model based on one dimensional strength of material approach. The fiber and matrix both are modeled as square regions as shown in Fig. 61. The residual stress is considered only between regions AF and AM. They also investigate the complete interface separation post behavior for transverse loading by assuming a *hole* in place of the fiber. The prediction of off-axis stress strain with the test data is compared in Fig. 62.

The article may be useful as it provides off axis data of SCS-6/Ti-6-4.

(13) Title : Modeling the Transverse Creep of Titanium-Based Metal Matrix Composite

Author : M. R. Eggleston and E. Krempl

The creep test data and and finite element results are compared for SCS-6/Ti-6-4 composite. The specimen micrograph and geometry are shown in Figs. 63 and 64, respectively. The material was fabricated at GE using an rf-plasma spray system with 4 layers of SCS-6. The tests and analysis were conducted for 28% nominal vf material at 480 C (900 F) in air. The transverse creep strain and creep rate are plotted in Fig. 65 and creep rates for the composite and matrix are compared in Fig. 66.

For the finite element analysis, matrix was modelled using unified viscoplasticity theory based on overstress (VBO). The governing equations of the VBO model are reproduced in Fig. 67 for the sake of completeness. The growth laws for the state variables allow high temperature creep modeling by interaction of hardening and static recovery. The values for the constants are found by curve fitting the test data and are shown in Table 19. The authors conclude that the VBO theory is not reliable for matrix modelling at low stress levels, i.e, below 240 MPa. At higher stress levels, the results are accurate for creep strain of up to 5%. The creep strain rate data and VBO modeling for Ti-6-4 are compared in Figs. 68 and 69 for 340 MPa and 140 MPa, respectively.

Finite element analyses was performed using ABAQUS. The fiber matrix interfaces was modeled assuming a perfect bond and as a sliding surface with no strength in the normal direction. The mesh is shown in Fig. 70. Comparison of SCS-6/Ti-6-4 creep rate from the tests and F.E. analysis is shown in Fig. 71. The composite creep behaviors, for perfect and weak interfaces are compared in Figs. 72 and 73 at 170 MPa and 340 MPa, respectively. In these figures, solid lines indicate the test data. It is observed that F.E. model results assuming weak interface and sliding surface are in better agreement with test data.

(14) Title : Creep Behavior of SCS-6/Ti-6AL-4V unidirectional Composites

Author : S. W. Schwenker, I. Roman and D. Eylon

Longitudinal Creep test data is compared with an analytical model at elevated temperatures in which the fiber and matrix are constrained to deform at the same rate. The deformation in the fiber is elastic whereas the matrix undergoes elastic-secondary creep. On relaxation, the stress in the matrix is redistributed to the fibers. The model equations are given below where subscripts f, m and c denote fiber, matrix and composite, respectively.

$$\dot{\varepsilon} = \frac{1}{E_f}\frac{d\sigma_f}{dt} \quad \text{(elstic fiber deformation)}$$

$$\dot{\varepsilon} = \frac{1}{E_m}\frac{d\sigma_m}{dt} + B_m \sigma_m^n \quad \text{(matrix deformation)}$$

$$\sigma_c = \sigma_f v_f + \sigma_m v_m \quad \text{(rule of mixtures)}$$

$$\dot{\varepsilon} = \alpha B_m \sigma_m^n \left(1 - \frac{E_f v_f}{\sigma_c}\varepsilon\right)^n \quad \text{(Composite creep rate)}$$

where $$\alpha = \left[\frac{E_m v_m}{E_m v_m + E_f v_f}\right] v_m^n$$

also $\varepsilon_0 = \sigma_c/(\sigma_f V_f + \sigma_m V_m)$ was taken as the initial condition.

The material tested was 8 ply SCS-6/Ti-6-4 composite of vf approximately 35%. The longitudinal creep test results at 427 C and 538 C at strain rate of $10^{-4}s^{-1}$ at various stress levels are shown in Figs. 74 and 75, respectively. Tests were also carried out for the matrix neat material to obtain data for the above defined analytical model. The matrix material properties and constants obtained from the test results are shown in Table 20. The fiber moduli was taken as 374 GPa and 354 GPa at 427 C and 538 C, respectively. The predicted creep results for the composite and test data at 4 stress levels are compared in Figs. 76-79. As observed, the model shows lower creep than the test data. It is also noted that the model does not include the effect of residual stresses. Also, the predictive accuracy further decreases with increasing load levels.

(15) Title : <u>On Time Dependent Deformation Modeling of Metal Matrix Composites</u>

Author : J. Ahmad, U. Santhosh and I. U. Haq

This article presents two micromechanical models which improve co-relation of predicted and creep test data (Schwenker et. al. -14 above). The first model adds the effect of residual stresses in the matrix creep and the second model considers fiber breaks as a damage mechanism at higher loads.

Creep Model

In the subsequent equations subscripts f, m, c and T denote fiber and matrix, composite and thermal contributions, respectively. The model incorporating the effect of residual stresses for uniaxial creep is given below :

$$\dot{\varepsilon}_m = B_m \sigma_m^n \quad \text{(matrix strain rate)}$$

$$\dot{\varepsilon} = B_u \sigma_m^n \quad \text{(composite strain rate)}$$

where

$$B_u = \left[\frac{B_m E_m v_m}{E_c}\right]$$

$$E_c = E_f v_f + E_m v_m \quad \text{(rule of mixtures)}$$

$$\sigma_m = \frac{\sigma_c}{v_m}\left(1 - \frac{E_f v_f}{\sigma_c}\varepsilon\right) + \sigma_m^T \quad \text{(matrix stress)}$$

By integrating matrix strain rate, the time dependence portion of composite strain is expressed as under :

$$\varepsilon_c = \frac{P - y(t)}{Q} - \frac{\sigma_c}{E_c}$$

in the above equation

$$P = \left[\frac{B_m E_m v_m}{E_c}\right]^{1/n} \left(\frac{\sigma_c}{v_m} + \sigma_m^T\right)$$

$$Q = \left[\frac{B_m E_m v_m}{E_c}\right]^{1/n} \frac{E_f v_f}{v_m}$$

$$y(t) = \left[(n-1)\,Qt + \frac{1}{y_0^{n-1}}\right]^{-1/n-1}$$

and

$$y_0 = P - \left(Q \frac{\sigma_c}{E_c}\right)$$

The α_f and α_m were taken as 3.9 and 9.77 (μm/m/C) at 538 C. The predictions using the creep model and finite element (unit cell) analysis are compared with the creep test data, with and without the effect of residual stresses. The comparison is done for 538 C and constant stress levels of 655 and 965 MPa and vf of 33%. The results from the creep model and F.E. analysis agree well with the experiment at lower stress levels (Figs. 80 and 81). At higher loads, the test data show increasing creep whereas the analysis shows creep saturation. A closer agreement with the test data is obtained by assuming fiber damage.

Fiber Damage Model

Consider a unidirectional laminate of length $2l$ and width 2W, a symmetric half of which is schematically depicted in Fig.82. Consider that at each edge of the panel there is a region B of width W_B in which all the fibers have fractured along the symmetry line. The remaining width of the panel (2 W_U) has no broken fibers. The panel is subjected to uniform applied displacement d_c at each end, such that the global composite strain is d_c/l.

Fig. 83 depicts the cross-section of a unit cell within the region B. It consists of a region B_1, in which the composite behaves as in the unbroken fiber region U, and a region B_2 which contains the fiber fracture location and its associated fiber-matrix split of length 2a. Ahead of each tip of the fiber-matrix split is a distance 2s over which some load transfer occurs by shear. That is, 2s is a shear lag distance. The shear stress varies from some high value at the tip of the split to zero at a distance 2s from the tip in some fashion. Assuming this variation to be linear, one can say that the fiber carries no normal stress over a distance d on each side of the fiber fracture location, where d is the sum of a and s. Thus, in the region B_2, the matrix material supports the entire applied load on region B.

Denoting stress rate by $\dot{\sigma}$, with subscripts U, B, B_1 and B_2 indicating the regions shown in Fig. 82 and 83, we have

$$\dot{\sigma}_{B_1} = \frac{W}{W_B}\left(\dot{\sigma}_c - \frac{W_u}{W}\dot{\sigma}_u\right)$$

$$\text{and} \qquad \dot{\varepsilon} = \dot{\varepsilon}_B = \dot{\varepsilon}_u$$

form equilibrium and compatibility considerations.

For the region U with no broken fibers, the creep model from the previous section can be used to write.

$$\dot{\varepsilon}_u = \frac{\dot{\sigma}_u}{E_c} + B_u \sigma_{mu}^n$$

where σ_{mu} denotes matrix stress in the region U. For region B,

$$\dot{\varepsilon}_B = \frac{\dot{\sigma}_{B_1}}{E_B} + \frac{l-d}{l} B_u \sigma_{mB_1}^n + \frac{d}{l} B_m \left(\frac{\sigma_{B_1}}{1-V_f}\right)^n$$

where σ_{mB_1} denotes matrix stress in the region B_1 and

$$E_B = \frac{lV_m E_m E_c}{dE_c + (l-d)E_m V_m}$$

With the assumption that the fibers remain elastic, the following expression for the composite's global strain rate ($\dot{\varepsilon}$):

$$\left(1 + \frac{W_u E_c}{W_B E_B}\right) \dot{\varepsilon} = \frac{W_u E_c}{W_B W_B} B_u \left[\frac{\sigma_u}{V_m} \varepsilon + \sigma_m^T\right]^n$$

$$+\left(1-\frac{d}{l}\right) B_u \sigma_{mB_1}^n + \frac{d}{l}\left[\frac{B_u W}{W_B V_m} \cdot \left(\sigma_c - \frac{W_u \sigma_u}{W}\right)^n\right]$$

where,

$$\sigma_{mB_1} = \frac{W}{W_B V_m}\left(\sigma_o - \frac{W_u}{W}\sigma_u\right) - \frac{E_f V_f}{V_m}\left(\frac{1}{1-d}\right)\left(\varepsilon - \frac{d}{l}\varepsilon_{B_2}\right) + \sigma_M^T$$

and s_u and ε_{B_2} can be found by integrating the following expressions:

$$\dot{\sigma}_u = E_c\left[\dot{\varepsilon} - B_u\left(\frac{\sigma_u}{V_m} - \frac{E_f V_f}{V_m}\varepsilon + \sigma_m^T\right)^n\right]$$

$$\dot{\varepsilon}_{B_2} = B_m\left[\frac{W}{W_B V_m}\left(\sigma_o - \frac{W_u}{W}\sigma_u\right)\right]^n$$

The initial conditions to be used in evaluating s_u and ε_{B_2} are:

$$\sigma_u(t=0) = \left(\frac{W}{W_u} - \frac{W_B E_B}{W_u E_o}\right)\sigma_c$$

and $$\varepsilon_{B_2}(t=0) = \frac{\sigma_c E_B}{V_m E_m E_o}$$

where $$E_o = E_c \frac{W_u}{W} + E_B \frac{W_B}{W}$$

The total strain in the composite panel is found by numerical integration. The initial elastic strain of the panel can be expressed as:

$$\varepsilon(t=0) = \sigma_c/E_o$$

Fig. 84 shows the predicted time dependent or "creep" strain in the composite panel for W_B/W of 0.1 and various d/l ratios. The results correspond to 538°C and applied stress of 965 MPa. It is seen that creep strain changes by less than ten percent for four orders of magnitude change in d/l. Thus, the solution is not very sensitive to the choice of d/l.

In Fig. 85, results are presented for d/l = 0.1 percent and the width of the region with broken fibers ranging from 0.1 to 30 percent of the total width of the panel. Comparing with the experimental curve in Fig. 85 the theoretical curve agrees with the former for the case W_B/W = 0.25, corresponding to approximately three rows of broken fibers at each specimen edge. This is in qualitative agreement with experimental observations reported by Schwenker et. al. for tests at 538°C.

(16) Title : Strain-Controlled Fatigue Testing

Author : Sami M. El-Soudani and Mary L. Gambone

Strain controlled fatigue testing of 40% vf, unidirectional SCS-6/Ti-6-4 of was conducted at RT and 600 F. The tested material properties are given in Table 21 at these temperatures. Both, longitudinal and transverse fatigue tests were performed. The test was conducted at 20 cycles/min at a strain R-ratio of 0.1. The initial load-displacement trace was given particular attention in order to study the onset of damage. A typical initial load-displacement trace is shown in Fig. 86 for specimen

L9, where L indicates longitudinal loading. Fig. 87 shows the trace of a typical initial transverse load-displacement (the specimen number T9 denotes transverse loading). Also, the test data for the two orientations are compared in Fig. 88. The test results are summarized below :

(1). The fatigue curves are well defined for longitudinal and transverse testing at RT and 600 F.

(2). With few exceptions, the longitudinal tests exhibited only elastic load-displacement trace over the entire specimen life.

(3). The majority of transversely loaded specimen showed hysteresis which indicates early onset of damage.

(4) The longitudinal fatigue life is several orders of magnitude higher than the transverse fatigue life for comparable total strain levels.

(5) In longitudinal testing, a well defined knee occurs as the strain amplitude attains a value nearing 85% of the monotonic fracture strain.

The authors provide the following observations after analyzing the tested specimens by electron microscopy (Figs. 89 and 90) :

(1) For longitudinally loaded specimens, fatigue cracks were primarily initiated at edges and corners where the fibers were exposed during fabrication. Cracks were also noted at the surface.

(2) In the transverse specimens, fatigue cracks initiate at fiber/matrix interface and propagate into the matrix.

Based on test results and photographic evidence, the layout of a model for fatigue damage accumulation is illustrated in Fig. 91. The model is based on load displacement behavior of three components: (1) the undamaged or virgin fiber (2) Composite with initial fiber volume fraction vf and $vf' < vf$ and (3) virgin matrix material. The lowest curve depicts 100% debonding, i.e., matrix with holes.

The conclusion is drawn that there are three distinct regions of composite longitudinal fatigue life for SCS-6/Ti-6-4 described as under :

(1) The first region is controlled by the fiber properties. In this region, the high stresses and strain approach the fiber strength.

(2) In the second, intermediate fatigue life region, matrix microcracking is the dominant factor. The stress and strain values are not sufficient to cause fiber damage.

(2) In the third region, stresses and strains are below those needed for matrix fatigue crack initiation.

Also, the damage under transverse loading was initiated during the first few cycles. The brittle nature of the fiber/matrix interface was held mainly responsible for the low transverse strength of SCS-6/Ti-6-4 composite.

Table 1. unidirectional fibre reinforced MMCs mechanical properties

Composite (density g/cm³)	Direction	V,%	σ_{max} MPa	E GPa
SiC/Ti.6Al.4V (3.86)	0°	35	1750	300
	90°	35	410	-

Table 2 - Tensile Properties of Ti-6Al-4V/SCS-6 as a Function of Thermal Treatment

Orientation	Temperature °C (°F)	Thermal Treatment		
		As Fabricated MPa (ksi)	900C/10 hr MPa (ksi)	Thermal Cycled MPa (ksi)
Longitudinal	RT	1500 (217.0)	1280 (185.3)	1675 (242.7)
		1770 (257.0)		
	316 (600F)	1120 (162.6)	1390 (201.4)	1440 (208.9)
		1385 (199.5)		
	427 (800F)	1082 (156.9)	947 (137.3)	1400 (202.8)
		1360 (197.3)		
Transverse	RT	592 (85.8)	584 (84.7)	-
	316 (600F)	321 (46.5)	479 (69.4)	-

Table 3 - Fiber Indentation Results

Material Condition	Interfacial Shear Strength MPa (ksi)
As-fabricated (panel 1)	276 ± 10 (40.0 ± 1.5)
As-fabricated (panel 2)	190 ± 3 (27.6 ± 0.5)
Aged (900C/1650F, 10 hrs.)	358 ± 23 (51.9 ± 3.4)
2000 cycles, 21-427C (70-800F)	208 ± 22 (30.2 ± 3.2)

TABLE 4

Tensile properties of SCS-6/Ti-6-4 composite

Condition	Young's modulus (GPa)	Ultimate strength (MPa)	Strain-to-failure (%)	Matrix tensile strength (MPa)
As fabricated	213 ± 1	1634 ± 117	1.1 ± 0.12	1024
800 °C/50 h	207 ± 7	1724 ± 103	1 ± 0.1	1027
800 °C/100 h	222 ± 5	1662 ± 21	0.79 ± 0.11	1003

TABLE 5

Multiple cracking length and strength of interfacial reaction layer in SCS-6/Ti alloy matrix composites

Composite	Condition	Cracking length (μm)	Strength (MPa)	Weibull modulus (m)
SCS-6/Ti-6-4	As fabricated	8.37 ± 3.6	768 ± 326	2.2
	800 °C/50 h	7.4 ± 3.0	506 ± 208	2.5
	800 °C/100 h	6.9 ± 2.8	361 ± 144	2.9

Table 6. **Measured and predicted strengths (in MPa) for CMCs and MMCs**

Ref.	Fibre	Matrix	f	Fibre strength (MPa)	m	r (μm)	τ (MPa)	σ_y (MPa)
$\bar{\sigma}$ at L_o = 25.4 mm (1 in)								
13	SCS-6	Ti–6–4	Variable	3650	9	70	40[a]	896

Fibre	Matrix	Expt	Theory	ROM	BROM
SCS-6	Ti–6–4				
	f = 0.27	1556	1566	1654	1368
	f = 0.34	1670	1726	1832	1480
	f = 0.34	1490	1726	1832	1480
	f = 0.43	1900	1944	2080	1633

TABLE 7

Elastic Moduli of a Transversely Isotropic Fibrous Composite

$E = C_{11} - \frac{2C_{12}^2}{C_{22} + C_{23}}$	$K_{23} = \frac{1}{2}(C_{22} + C_{23})$
$G = G_{12} = G_{13} = C_{44}$	$G_{23} = \frac{1}{2}(C_{22} - C_{23})$
$\nu = \nu_{13} = \nu_{31} = \frac{1}{2}\left(\frac{C_{11} - E}{K_{23}}\right)^{1/2}$	$\nu_{23} = \frac{K_{23} - \phi G_{23}}{K_{23} + \phi G_{23}}$
$E_2 = E_3 = \frac{4G_{23}K_{23}}{E_{23} + \phi\Gamma_{23}}$	$\phi = 1 + \frac{4K_{23}\nu^2}{E}$

Stress–Strain Relationships

$\varepsilon_{11} = (1/E_1)[\sigma_{11} - \nu(\sigma_{22} + \sigma_{33})]$	$\varepsilon_{22} = \varepsilon_{33} = (1/E_2)(\sigma_{22} - \nu\sigma_{33}) - (\nu/E)\sigma_{11}$
$\gamma_{12} = \gamma_{13} = (1/G)\sigma_{12}$	$\gamma_{23} = \frac{2(1 + \nu_{23})}{E_2}\sigma_{23}$

TABLE 8
ELASTIC CONSTANTS OF A TRANSVERSELY ISOTROPIC COMPOSITE IN TERMS OF COMPONENT CONSTANTS (MATRIX ISOTROPIC, FIBER ANISTROPIC)

Longitudinal modulus	$E_{11} = E_{f1}V_f + E_m V_m$
Transverse modulus	$E_{22} = E_{33} = \dfrac{E_m}{1 - (V_f)^{1/2}(1 - E_m/E_{f2})}$
Shear modulus	$G_{12} = G_{13} = \dfrac{G_m}{1 - (V_f)^{1/2}(1 - G_m/G_{f12})}$
Shear modulus	$G_{23} = \dfrac{G_m}{1 - (V_f)^{1/2}(1 - G_m/G_{f23})}$
Poisson ratio	$\nu_{12} = \nu_{13} = \nu_{f12}V_f + \nu_m V_m$
Poisson ratio	$\nu_{23} = \dfrac{E_{22}}{2G_{23}} - 1$

TABLE 9
VALUES OF ξ FOR SOME UNIAXIAL COMPOSITES

Modulus	ξ
E_{11}	$2(l/d)$
E_{22}	0.5
G_{12}	1.0
G_{21}	0.5
K	0

Source: Adapted with permission from Springer-Verlag, New York, K. K. Chawla, "Composite Materials," 1987.

TABLE 10
COMPOSITE TENSILE ROOM TEMPERATURE PROPERTIES[a]

System	Ultimate tensile strength		Modulus[b]
	Longitudinal MPa	Transverse MPa	longitudinal GPa
SiC/Ti–6Al–4V[b]	820	380	225
SCS–6/Ti–6Al–4V[b]	1,455	340	240

[a] Four-ply, undirectionally reinforced, 35 to 40 vol-%.
[b] After fabrication and low temperature, 1,96°C for 512 hours exposure.

Table11 Interfacial debond strength and frictional stress of SCS-6/Ti alloy matrix composites

matrix	conditions	debond stress (MPa)	corrected debond stress (MPa)	frictional stress (MPa)	Test Method
Ti-6-4	as-fabricated	138.3	155.9	87.5	indentation
	as-fabricated	—	180.0	—	fragmentation [12]
	800 °C/50 h	151.1	164.5	90.2	indentation
	800 °C/100 h	153.5	167.1	90.2	indentation

TABLE 12 Thermophysical data

Property	Fibre (SiC)	Composite (Ti-35%SiC)	Matrix (Ti-6Al-4V)
Axial E (GPa)	450	232	115
Trans. E (GPa)	450	155	115
Axial ν	0.2	0.3	0.35
Trans. ν	0.2	0.25	0.35
Axial α (10^{-6} K^{-1})	4.0	5.0	8.0
Trans. α (10^{-6} K^{-1})	4.0	7.0	8.0

TABLE 13–*Ti-6Al-4V properties.*

Temperature, °C	Young's Modulus, GPa	ν	Yield Stress, MPa	Flow Modulus, GPa	α (Ref. = 900°C) (10^{-6}) (°C)$^{-1}$
21	113.7	0.3	900	4.6	9.44
149	107.5	0.3	730	4.7	9.62
315	97.9	0.3	517	5.4	9.78
482	81.3	0.3	482	4.8	9.83
649	49.6	0.3	303	1.7	9.72
900	20.7	0.3	35	1.2	9.81

Creep law: $\dot{\epsilon}_c = a_0(\sigma^{a_1})(t^{a_2})e^{-\left[\frac{a_3}{T+274}\right]}$

$a_0 = 3.6 \times 10^6$ (MPa)$^{-3.403}$ (h)$^{-0.9251}$,
$a_1 = 3.403$,
$a_2 = 0.9251$, and
$a_3 = 3.6 \times 10^4$ (°C).

Temperature (°C)	E (GPa)	ν	α_{low} (10^{-6}/°C)	α_{high} (10^{-6}/°C)	σ_Y (MPa)	E_{flow} (GPa)
21	113.7	0.3	9.44	11.0	900	4.6
149	107.5	0.3	9.62	11.3	730	4.7
315	97.9	0.3	9.78	11.7	517	5.4
482	81.3	0.3	9.83	12.0	482	4.8
649	49.6	0.3	9.72	12.2	303	1.7
900	20.7	0.3	9.81	12.4	35	1.2

Table 14 Material constants of the titanium alloy Ti-6Al-4V

Fiber	E_A (GPa)	ν_A	E_T (GPa)	ν_T	G_A (GPa)	α (10^{-6}/°C)
SiC	414	0.3	414	0.3	159.2	4.86

Table 15 Material properties of the SiC fibers

a_0 (10^9) (MPa)$^{-3.403}$ (hr.)$^{-0.9251}$	a_1	a_2	a_3 (10^4) (°C)
3.6	3.403	0.9251	3.6

Table 16 Power-law creep coefficients of the titanium alloy Ti-6Al-4V

Temperature (°C)	D_0^{-1} (s)	Z_0 (MPa)	Z_1 (MPa)	m	n
21	10^{-4}	1060	1500	12.7	10.0
149	10^{-4}	890	1500	11.68	8.42
315	10^{-4}	800	1500	19.2	3.6
482	10^{-4}	1140	1500	121	1.71
649	10^{-4}	1160	1500	85.6	1.038
900	10^{-4}	580	1500	340	0.396

Table 17 Bodner-Partom parameters of the titanium alloy Ti-6Al-4V

Table 18 Off-axis tension test results.

θ	Specimen	Th x Wd (mm x mm)	E_x (GPa)	σ_1 (MPa)	σ_u (MPa)
	1	2.49 x 18.9	231	/	1963
0°	2	2.49 x 18.9	230	/	1618
	3	2.46 x 19.2	229	/	1812
	Average		230	/	1798
	1	2.44 x 18.7	235	/	1832
5°	2	2.44 x 18.7	235	/	1464
	3	2.44 x 18.7	231	/	/
	Average		234	/	1648
	1	2.44 x 18.7	230	/	1511
10°	2	2.44 x 18.7	228	/	1539
	Average		229	/	1525
	1	2.49 x 18.9	205	834	1026
	2	2.49 x 18.7	205	876	1006
15°	3	2.39 x 19.1	208	828	978
	4	2.49 x 18.5	217	862	952
	5	2.49 x 18.8	221	/	931
	Average		211	850	979
	1	2.49 x 18.6	162	425	544
	2	2.49 x 18.6	161	399	566
	3	2.39 x 19.1	172	341	524
30°	4	2.39 x 19.1	168	423	535
	5	2.49 x 18.4	181	455	517
	6	2.49 x 18.8	188	448	544
	Average		172	415	538
	1	2.49 x 18.8	135	290	381
	2	2.49 x 19.2	141	255	387
45°	3	2.39 x 19.1	155	270	405
	4	2.49 x 19.5	162	290	386
	5	2.49 x 18.9	167	283	390
	Average		152	278	390
60°	1	2.49 x 18.1	159	241	369
	2	2.49 x 18.9	162	184	303
	Average		161	213	336
	1	2.49 x 18.9	146	177	301
	2	2.49 x 18.6	130	169	319
	3	2.39 x 19.1	143	192	310
90°	4	2.39 x 19.1	155	200	341
	5	2.49 x 18.8	160	172	300
	6	2.49 x 18.8	167	184	270
	Average		150	182	307

Variable	Value	Units
K_1	2.5	Hours
K_2	8270.	MPa
K_3	2.0	---
K_4	0.0	MPa
K_5	0.0160	1/MPa
C_1	26200.	MPa
C_{2e}	79200.	MPa
C_3	0.0508	1/MPa
C_4	4.79	1/MPa
R_{s3}	0.0	1/Hours
R_{c1}	0.0	---
R_{c2}	0.00002	---
R_{c3}	1.0	1/Hours
h	1.0	---
G_1	200.	MPa
A_e	169.	MPa
B	162.	MPa
E	91600.	MPa
E_1	2070.	MPa
υ	0.30	---

Table 19 VBO Material Coefficients for Ti-6Al-4V at 480°C

TABLE 20 Tension and Creep Properties of Ti-6Al-4V Neat Panels

	Tension Properties*			Power-Law Creep Constants	
Temp (°C)	E_m (GPa)	σ_{ys} (MPa)	σ_{uts} (MPa)	n	B_m ($MPa^{-n}s^{-1}$)
427	85	502	618	8	2.58×10^{-29}
538	69	443	478	7	2.12×10^{-23}

*reported values represent the average of triplicate tests

Table 21 - Tensile Test Results for SCS-6/Ti-6Al-4V Metal Matrix Composite

Test Specimen No.	Test Orientation	Test Temperature [°F]	Yield Stress [ksi]	Ultimate Strength [ksi]	Elastic Modulus [Msi]	Elongation Percent	Poisson's Ratio
1	Longitudinal	RT	--*	252.4	33.5	0.815	0.258
2	Longitudinal	RT	--*	246.0	31.2	0.810	0.254
3	Transverse	RT	--*	30.2	24.2	0.146	0.195
4	Transverse	RT	--*	20.6	22.0	0.096	0.189
5	Longitudinal	600	200.10	224.81	34.68	0.70	0.280
6	Longitudinal	600	205.03	205.03	31.81	0.66	0.270
7	Longitudinal	600	180.48	180.48	33.13	0.56	0.270
8	Transverse	600	22.55	33.81	17.93	0.71	0.150

* quasielastic values

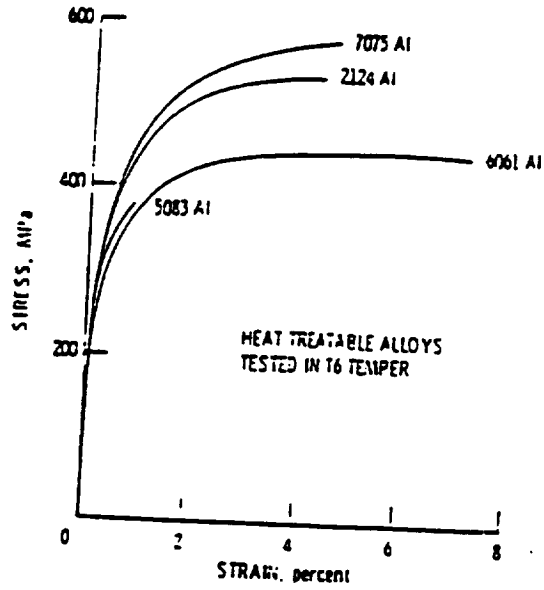

Figure 1. Effect of Al matrix alloy on stress-strain behavior of composites with 20 vol pct SiC_p reinforcement

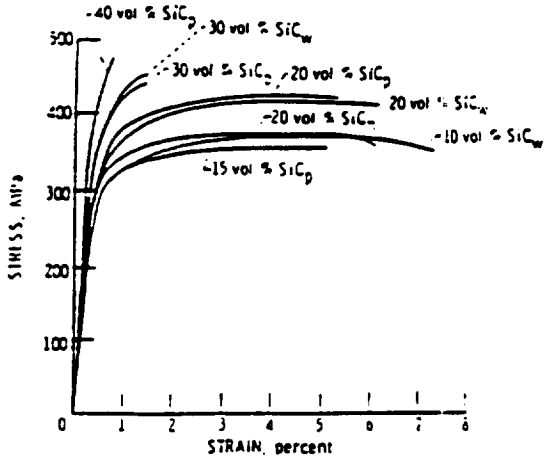

Figure 2. Stress-strain curves of SiC/6061 Al composites (T6-temper, tested in longitudinal direction) [4].

a) As Fabricated

b) 1650°F/10 hours

c) Thermal cycled 2000 times from RT to 800°F

Figure 3 - Interface Microstructure as Influenced by Thermal Treatments

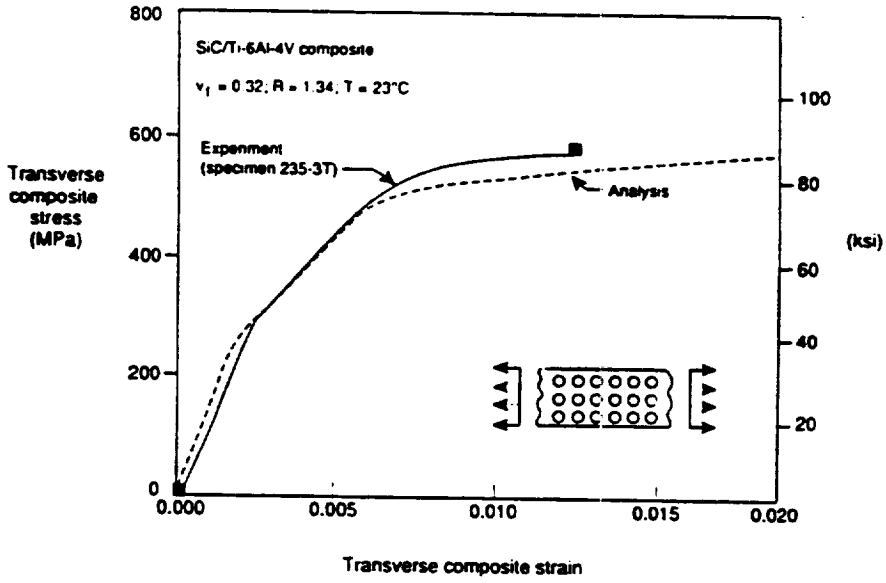

Figure 4 - Transverse Stress-Strain Behavior of Ti-6Al-4V/SCS-6 at Room Temperature Comparing Experimental and Analytical Curves

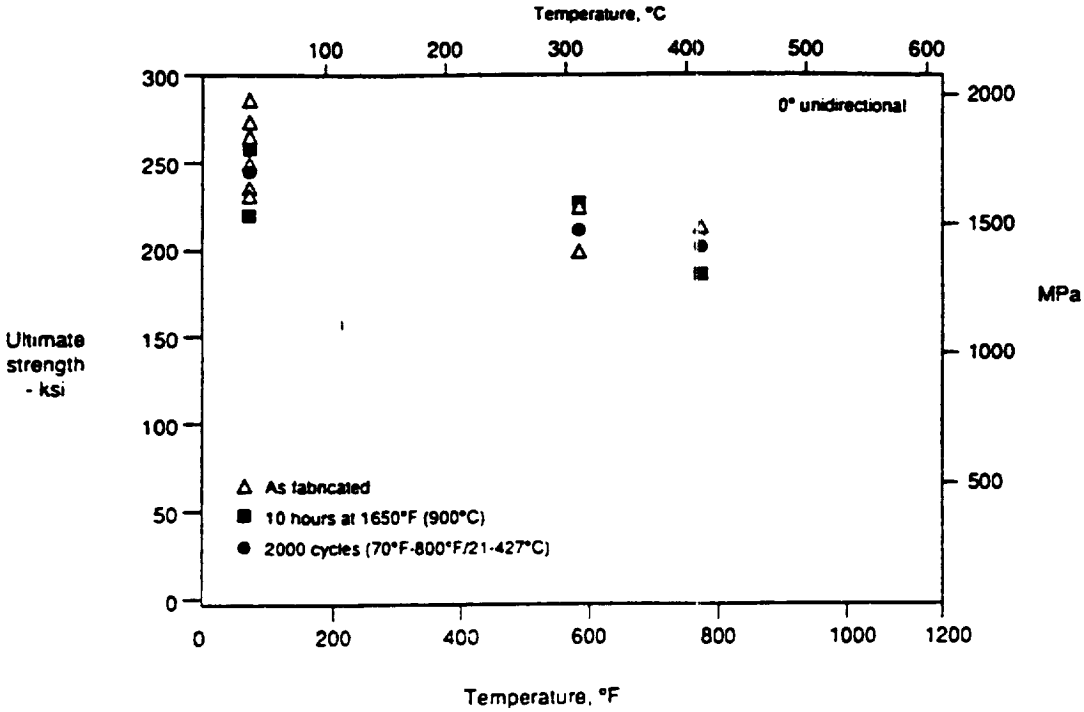

Figure 5 - Thermal Treatment Effects on Longitudinal Tensile Strength of Ti-6Al-4V/SCS-6 (Adjusted to 35% V_f)

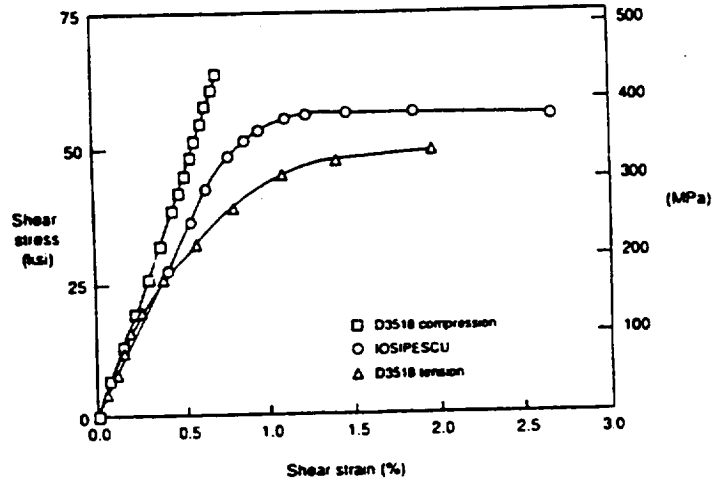

Figure 6 - In-Plane Shear Stress-Strain Behavior for Ti-6Al-4V/SCS-6 from: Compression Test of $\pm 45^{\circ}$ Laminate; Iosipescu Test; and Tension Test of $\pm 45^{\circ}$ Laminate

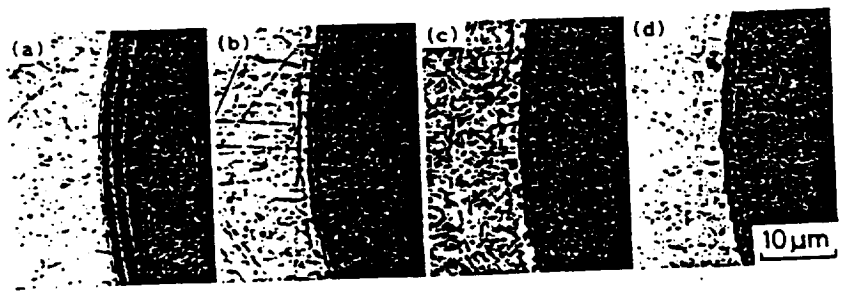

Fig.7 Optical micrographs of reaction products in SCS-6/Ti-6Al-4V heat-treated at 1123K for 0(a), 32.4(b), 126(c) and 360ks(d)

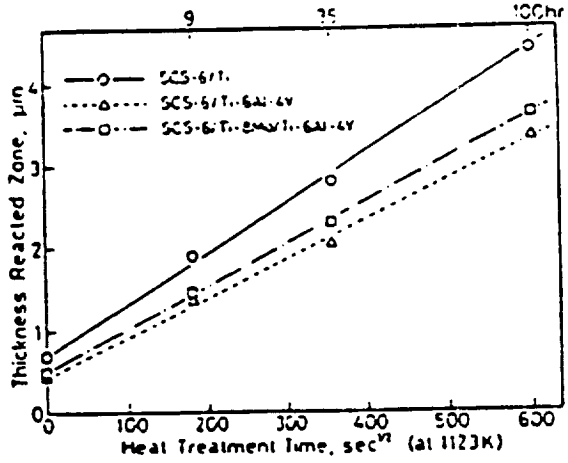

Fig.8 Relationships between thickness of reaction products and root of heating time at 1123K

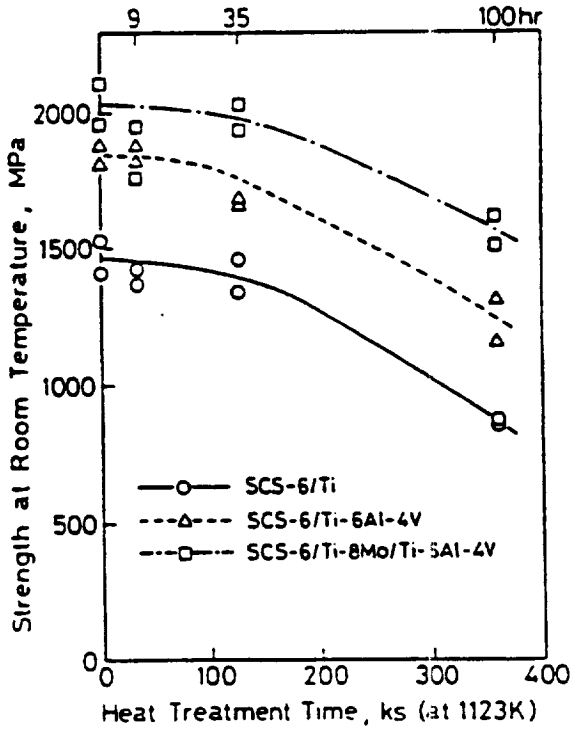

Fig.9 Relationships between tensile strength and heating time

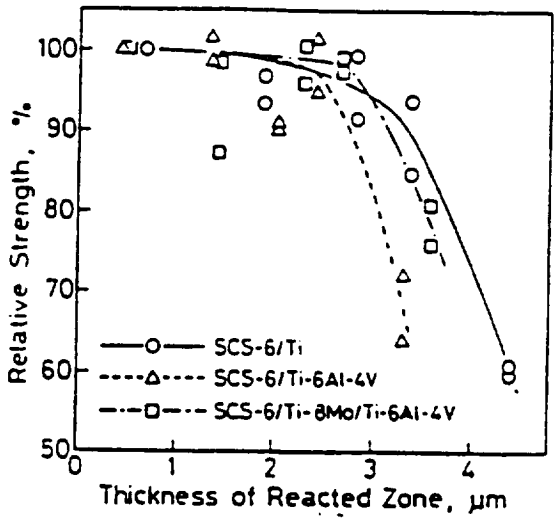

Fig.10 Effect of reaction products on tensile strength of composites

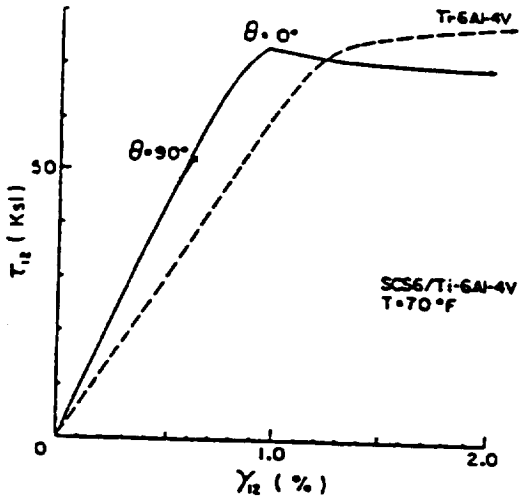

Fig. 11. Monotonic Shear Stress Strain Curves of Unidirectional SCS6/Ti-6Al-4V MMC at Room Temperature.

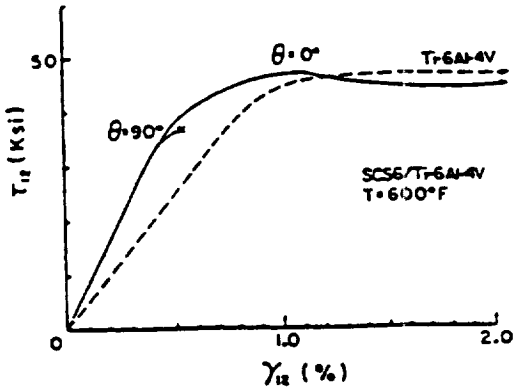

Fig. 12. Monotonic Shear Stress Strain Curves of Unidirectional SCS6/Ti-6Al-4V MMC at 600°F.

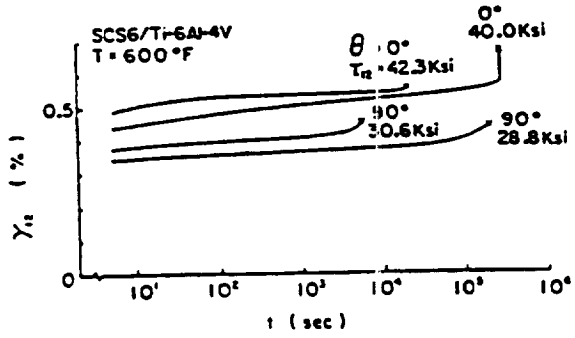

Fig. 13. Shear Creep Curves of Unidirectional SCS6/Ti-6Al-4V MMC at 600°F under Various Shear Stress Levels.

Fig.14. Monotonic Shear Failure Modes of Unidirectional SCS6/Ti-6Al-4V MMC at 600°F. (a) θ = 90 deg. and (b) θ = 0 deg..

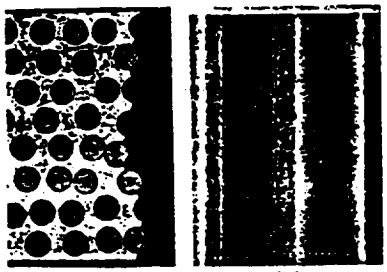

(a) (b)

Fig.15. (a)Photomicrographs of Fracture Surface Cross Section and (b)SEM Fractographs of SCS6/Ti-6Al-4V MMC θ = 90 deg. Specimen Failed under Monotonic Shear Loading at 600°F.

(a) (b)

Fig.16. (a)Photomicrographs of Fracture Surface Cross Section and (b)SEM Photographs of SCS6/Ti-6Al-4V MMC θ = 0 deg. Specimen Failed under Monotonic Shear Loading at 600°F.

(a) (b)

Fig.17. Shear Creep Failure Modes of SCS6/Ti-6Al-4V MMC at 600°F. (a) θ = 90 deg. and (b) θ = 0 deg..

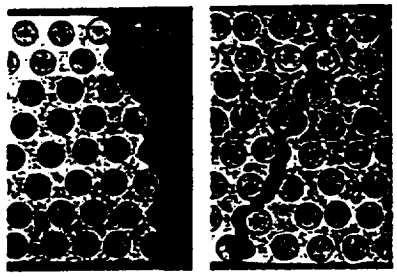

(a) (b)

Fig.18. Photomicrographs of Fracture Surface Cross Section of Shear Creep Ruptured SCS6/Ti-6Al-4V MMC at 600°F (a) θ = 90 deg., τ_{12} = 27.0 Ksi and (b) θ = 0 deg., τ_{12} = 40.0 Ksi.

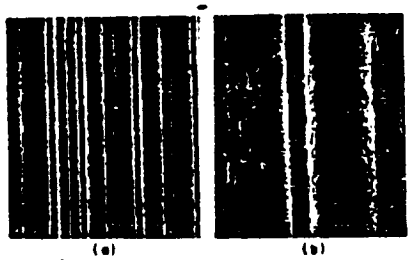

(a) (b)

Fig.19. SEM Fractographs of Shear Creep Ruptured θ = 90 deg. SCS6/Ti-6Al-4V MMC at 600°F under τ_{12} = 27.0 Ksi.

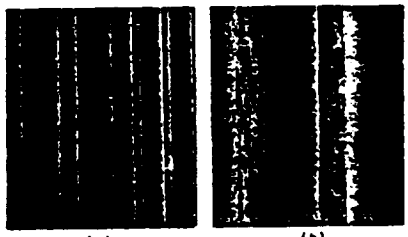

(a) (b)

Fig.20. SEM Fractographs of Shear Creep Ruptured θ = 90 deg. SCS6/Ti-6Al-4V MMC at 600°F under τ_{12} = 30.6 Ksi.

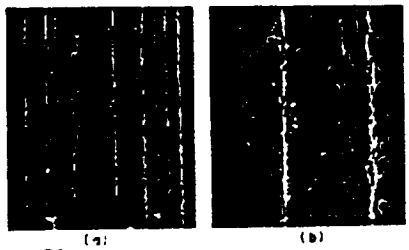

(a) (b)

Fig.21. SEM Fractographs of Shear Creep Ruptured θ = 0 deg. SCS6/Ti-6Al-4V MMC at 600°F under τ_{12} = 42.3 Ksi.

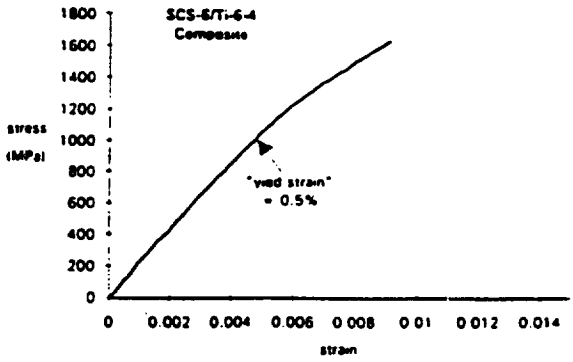

Fig. 22 Typical stress-strain curve of SCS-6/Ti-6-4 composite.

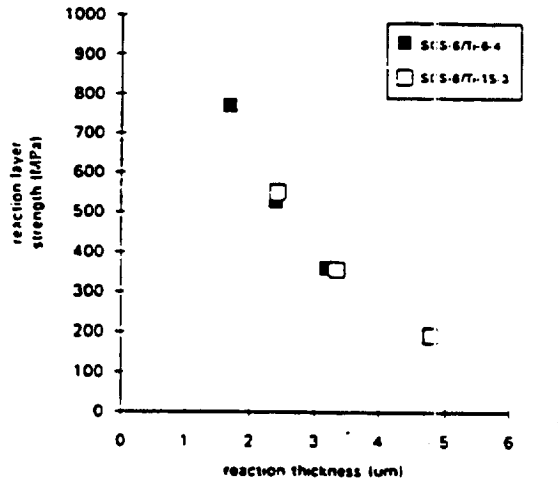

Fig. 23. Variation of tensile strength of interfacial reaction zone as a function of reaction zone thickness of SCS-6/Ti alloy matrix composite.

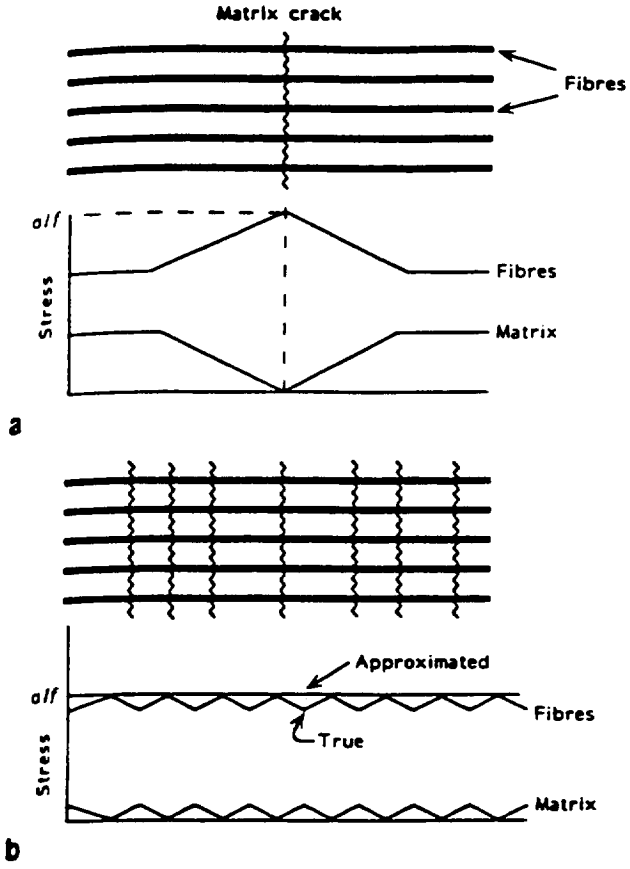

Fig 24 Matrix and fibre stresses after first matrix cracking: (b) stresses after saturated multiple matrix cracking (not to same scale as (a))

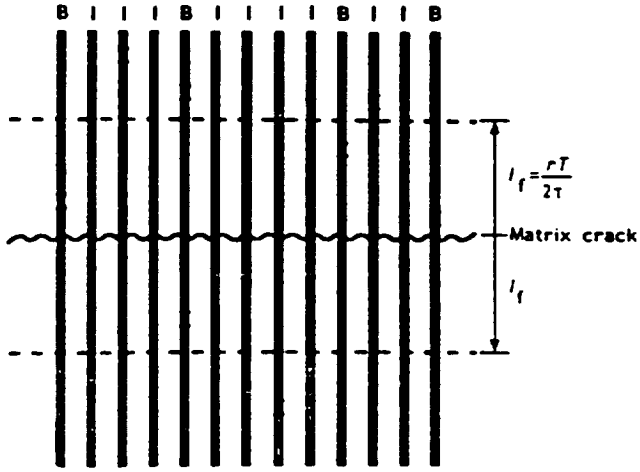

Fig 25 Schematic of composite focusing on one matrix crack. Fibres with no breaks within $\pm l_f = \pm rT/2\tau$ are intact (I) and carry load T; fibres with breaks in $\pm l_f$ are broken (B) and carry reduced loads at the matrix crack plane. Intact fibres can have breaks further than $\pm l_f$ from the matrix crack plane

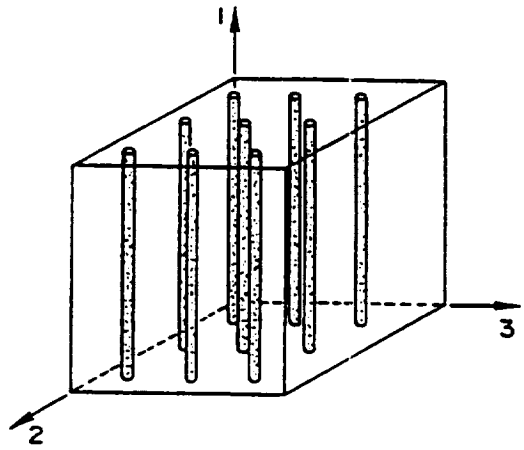

FIG. 26. A transversely isotropic fiber composite: Plane transverse to fibers (2–3 plane) is isotropic.

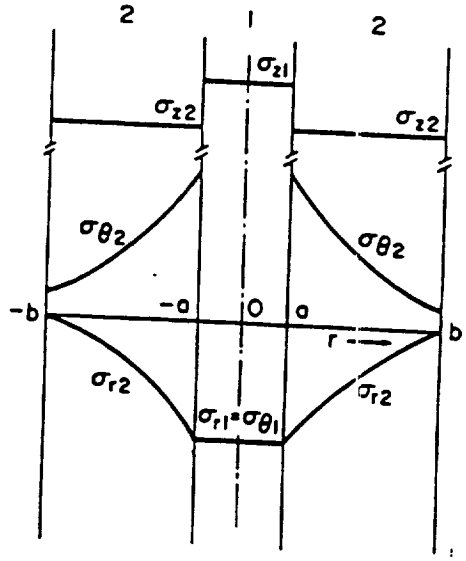

FIG. 27. Three-dimensional stress distribution (schematic) in unit composite shown in Fig. 12. Transverse stresses (σ_r and σ_θ) result from the differences in the Poisson ratios of fiber and matrix.

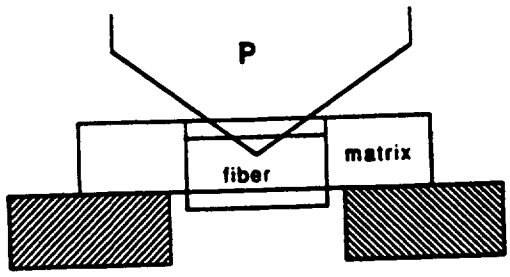

Fig. 28 The geometry of the indentation test.

Fig.29 The SEM photograph of a pushout SCS-6 fiber.

Fig.30 The origin of fiber/matrix debonding in an as-fabricated SCS-6/Ti-6-4 composite.

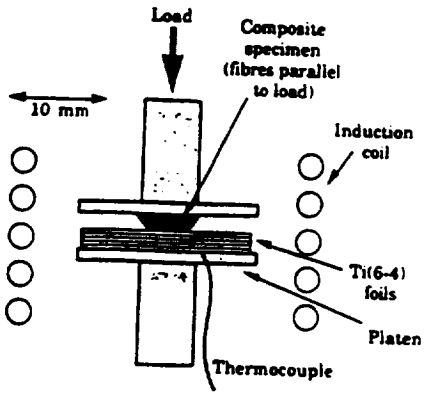

Fig. 31 Schematic illustration of the diffusion bonding set-up used to produce specimens for the test.

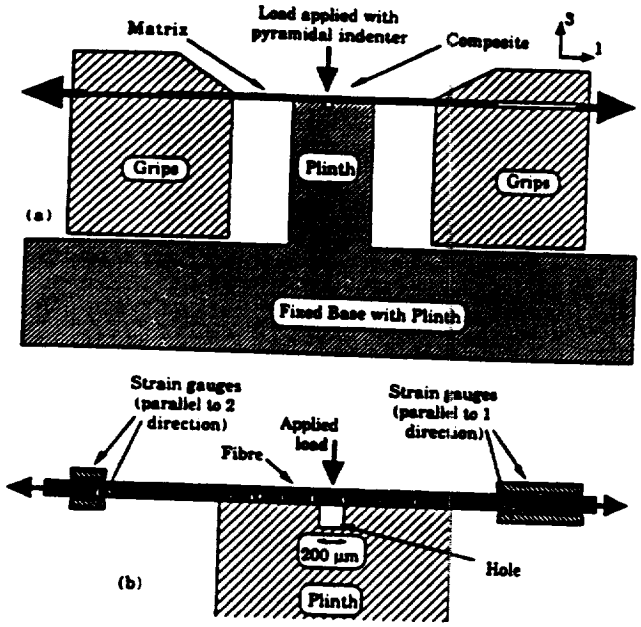

Fig. 32 Schematic illustration of the loading set-up.

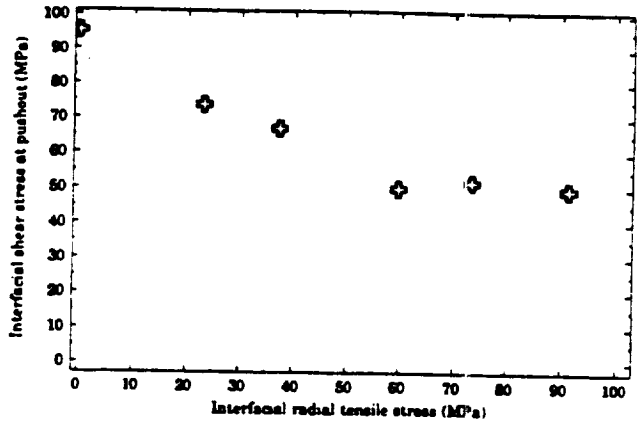

Fig. 33 Tensile pushout test data for SCS-6/Ti-6-4 (35%v_f)

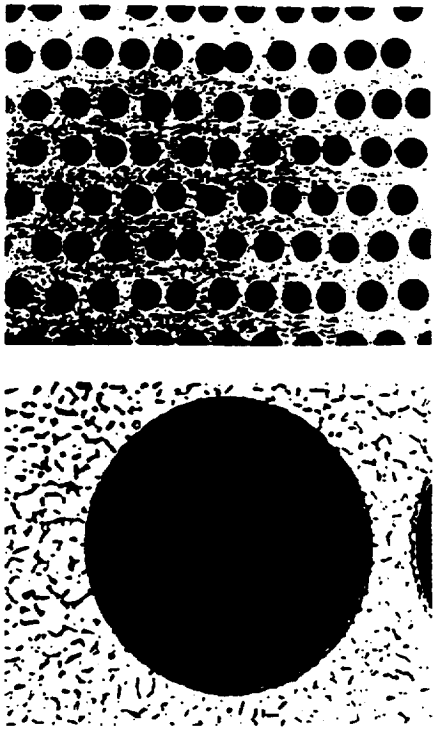

FIG. 34-*Composite microstructure:* (top) *general fiber dispersion and* (bottom) *closeup of matrix microstructure near a fiber.*

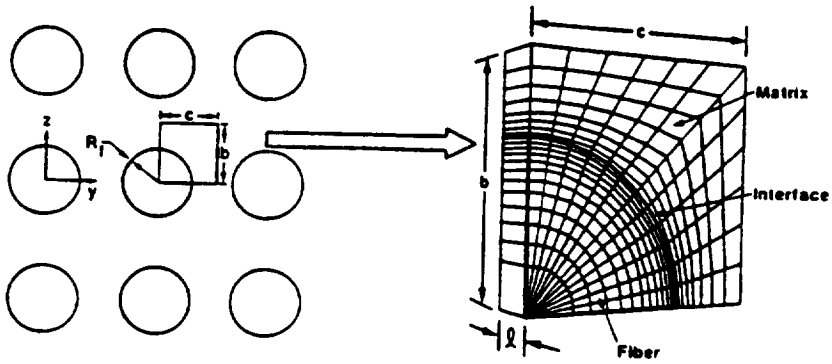

FIG. 35-*Infinite square array of fibers and finite element idealization of a unit cell.*

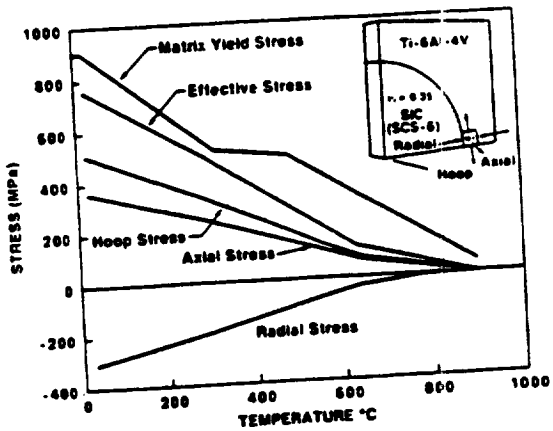

FIG.36–*Stress in the titanium matrix at Location* M1 *as a function of temperature (properties reported by the supplier and from Table 1).*

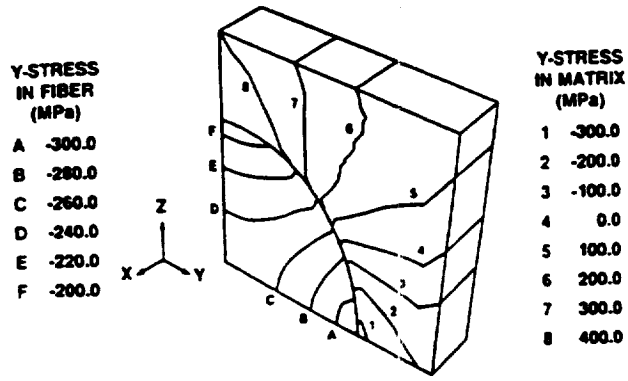

FIG.37–*y-direction stress in fiber and matrix at room temperature after cooling from 900°C.*

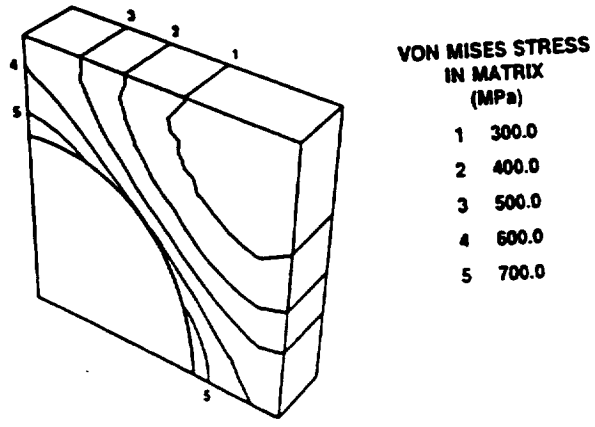

FIG.38–*Effective (von Mises) stress in the matrix at room temperature after cooling from 900°C.*

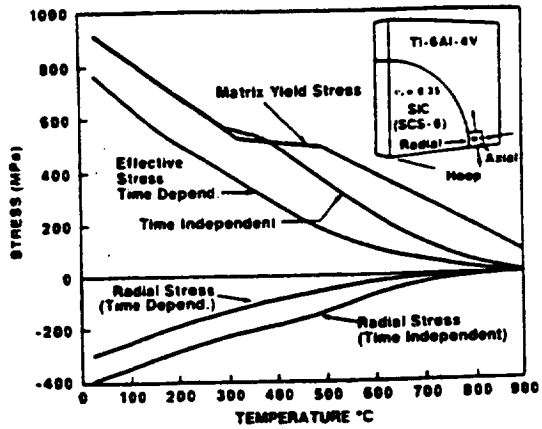

FIG. 39—*Comparison of time-dependent and time-independent predictions of effective and radial stresses in the titanium matrix at Location* M1 *as a function of temperature; high values of expansion coefficients*

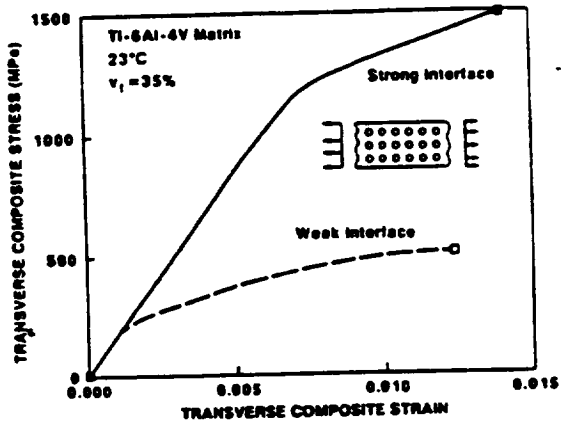

FIG. 40—*Comparison of average transverse stress-strain response of an SiC/Ti-6Al-4V composite under the assumptions of strong and weak interface conditions.*

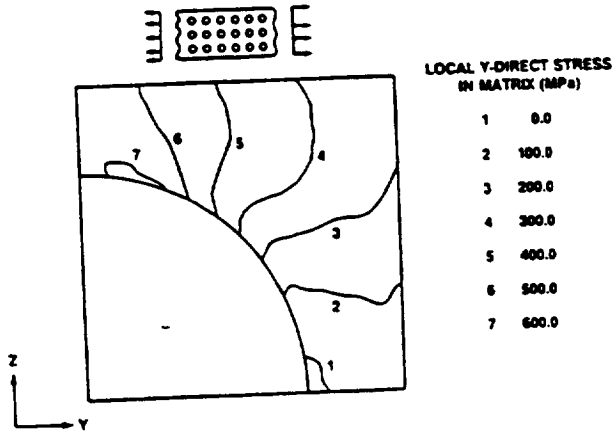

FIG. 41—*Local y-direction stress component in composite cell at an average transverse stress of 175 MPa (weak interface).*

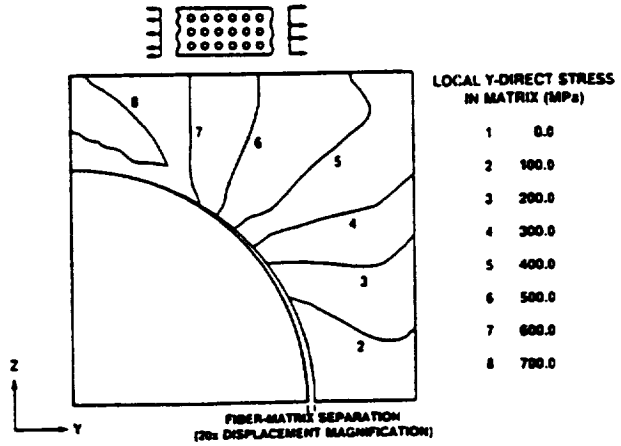

FIG. 42—*Local y-direction stress component in composite cell at an average transverse stress of 250 MPa (weak interface).*

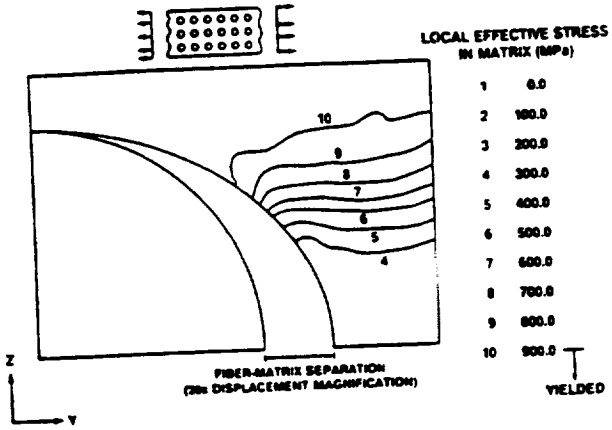

FIG 43—*Local effective stresses in the Ti-6Al-4V matrix at an average transverse stress of 470 MPa (weak interface).*

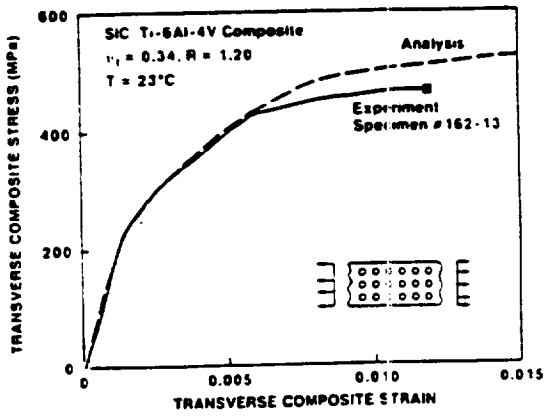

FIG. 44—*Comparison of predicted and measured transverse stress-strain behavior, room temperature, ν_f = 0.34, R = 1.20.*

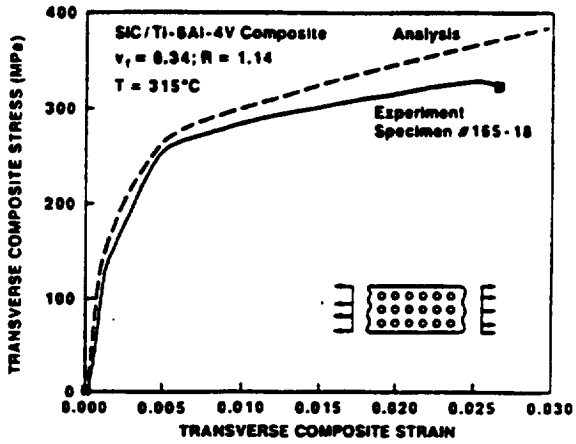

FIG. 45—*Comparison of predicted and measured transverse stress-strain behavior; 315°C (600°F), v_f = 0.35, R = 1.13.*

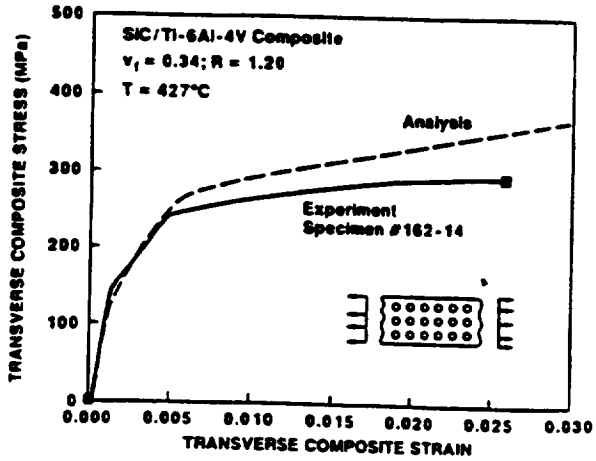

FIG. 46—*Comparison of predicted and measured transverse stress-strain behavior; 427°C (800°F), v_f = 0.34, R = 1.20.*

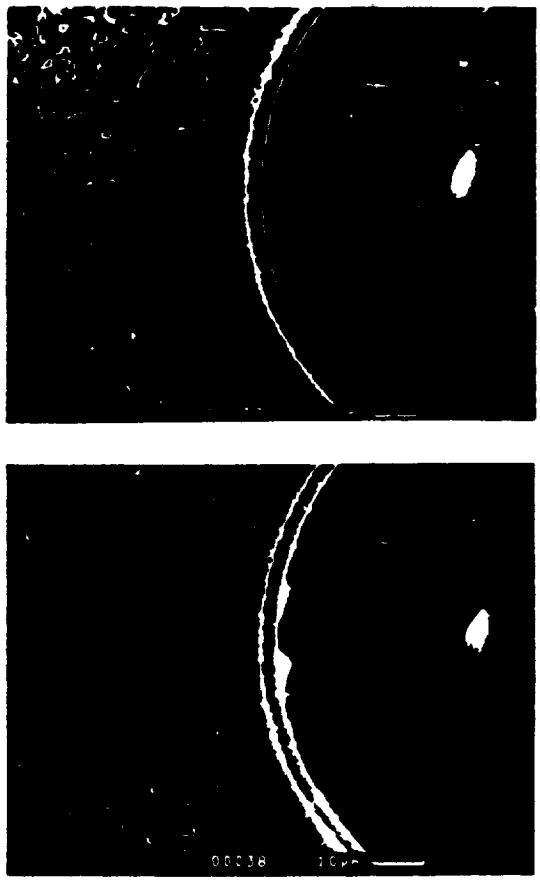

FIG. 47—*Observed interface deformation before* (a) *and after* (b) *"knee" in a transverse stress-strain curve.*

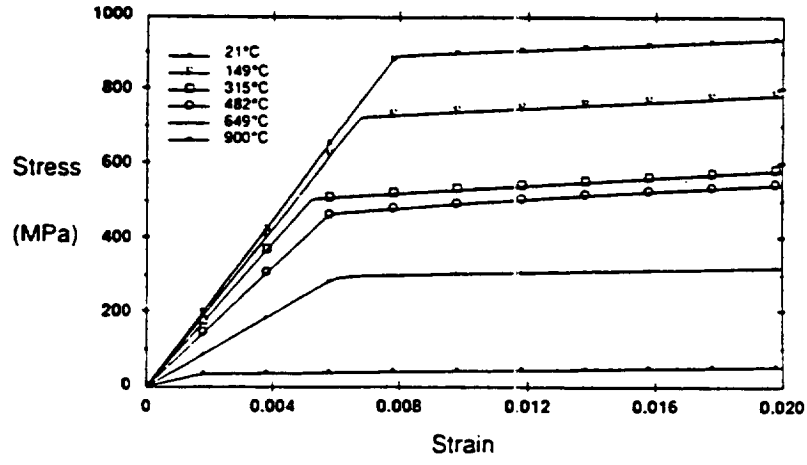

Figure 48- Temperature-dependent response of titanium Ti-6Al-4V based on data of Nimmer et al [8].

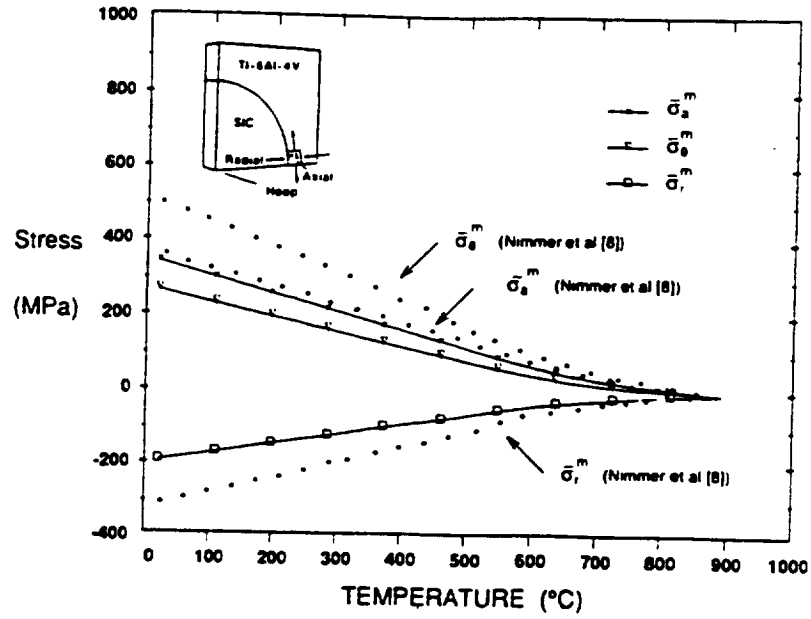

Figure49- Evolution of residual axial, hoop and radial stresses in the matrix during the cooling process for the time-independent matrix response. Comparison between method of cells and finite-element analysis.

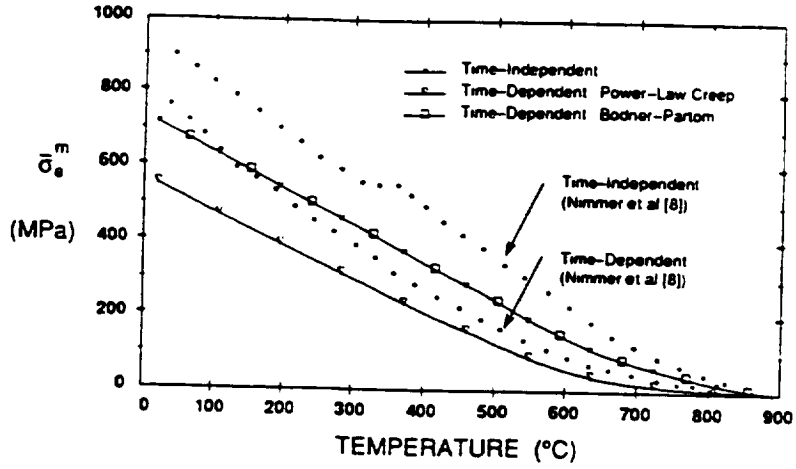

Figure 50- Evolution of residual effective stress in the matrix during the cooling process for both time-independent and time-dependent matrix response. Comparison between the method of cells and finite-element analysis.

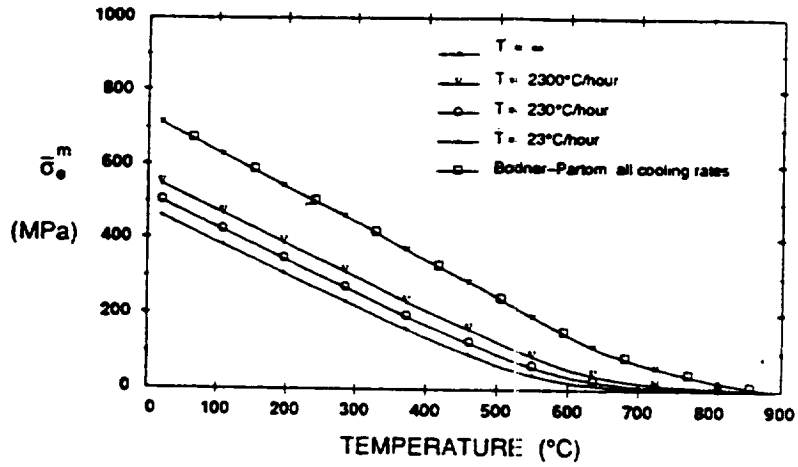

Figure 51 - The effect of cooling rate on the evolution of residual effective stress in the matrix predicted by the method of cells for the Bodner-Partom and power-law creep models.

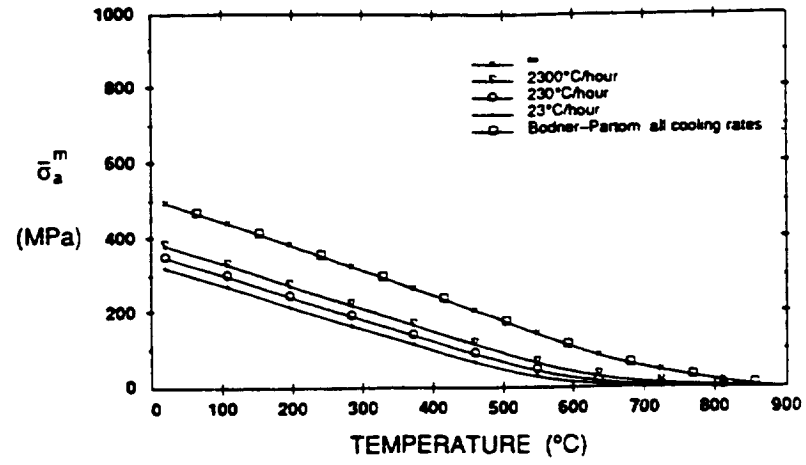

A

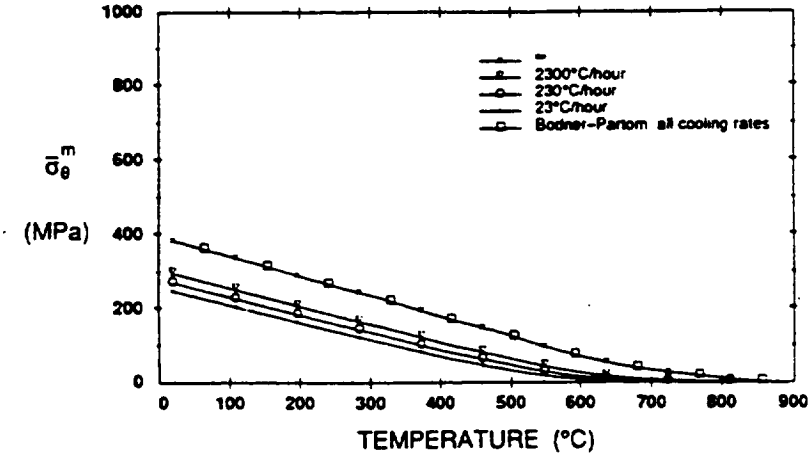

B

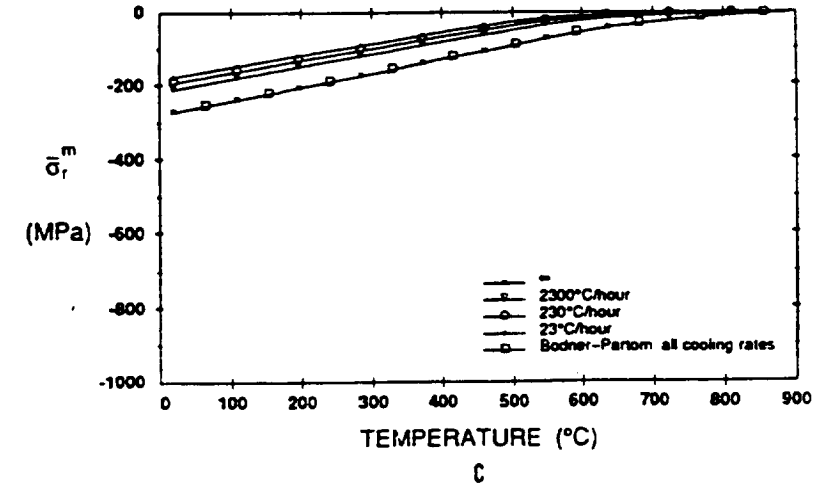

C

Figure 52- The effect of cooling rate on the evolution of residual axial (a), hoop (b), and radial (c) stress in the matrix predicted by the method of cells for the Bodner-Partom and power-law creep models.

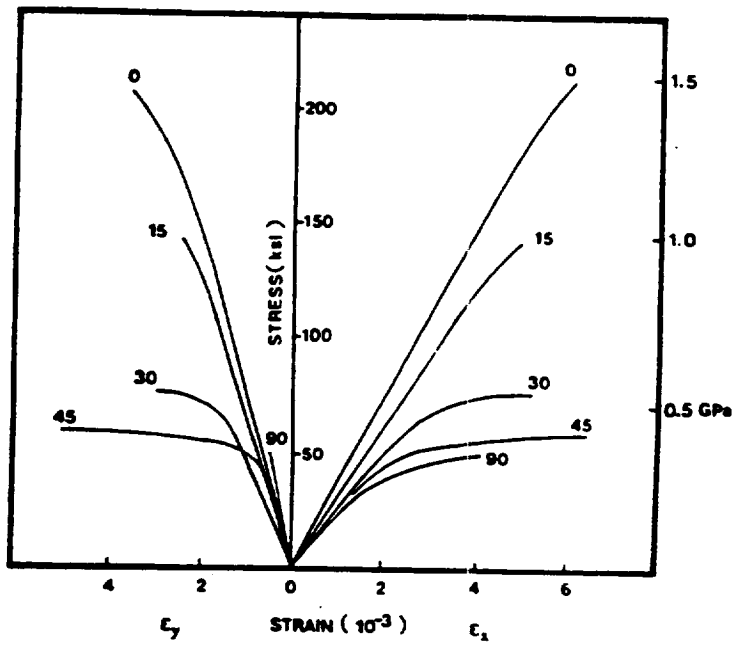

Figure 53 Typical off-axis stress-strain curves.

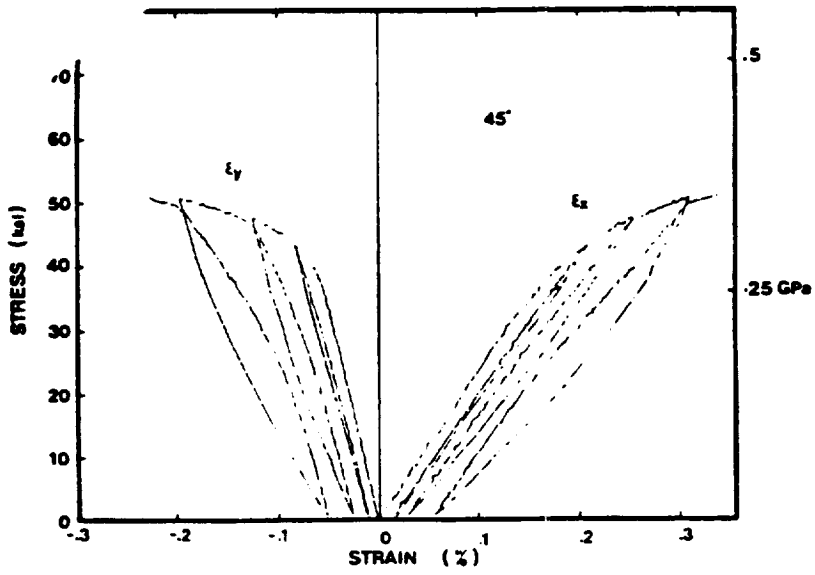

Figure54 Loading-unloading curves for the 45°-specimen.

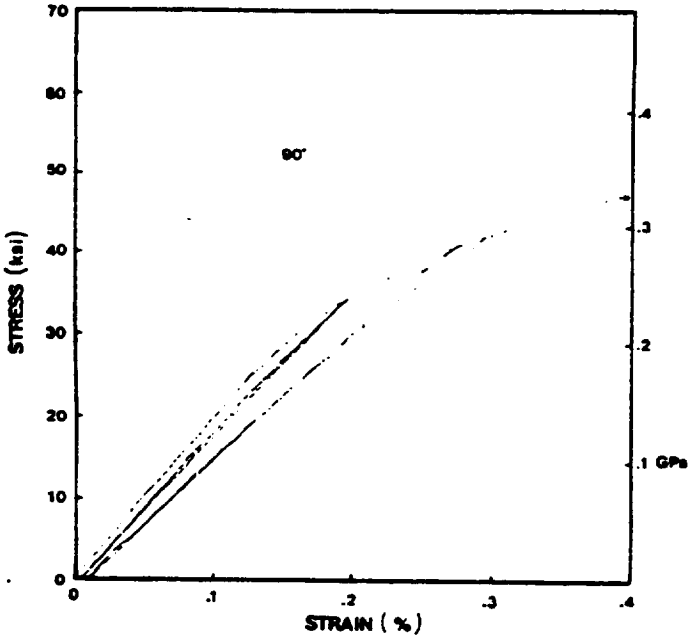

Figure 55 Loading-unloading curves for the 90°-specimen.

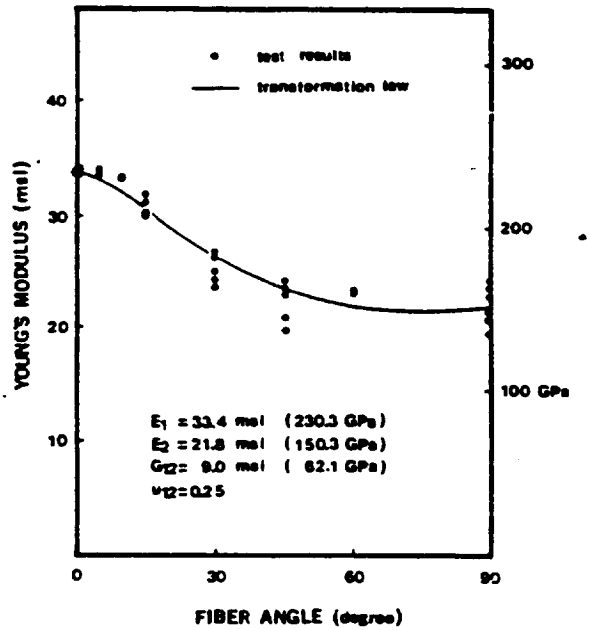

Figure 56 Comparison of measured apparent Young's moduli and Equation (4).

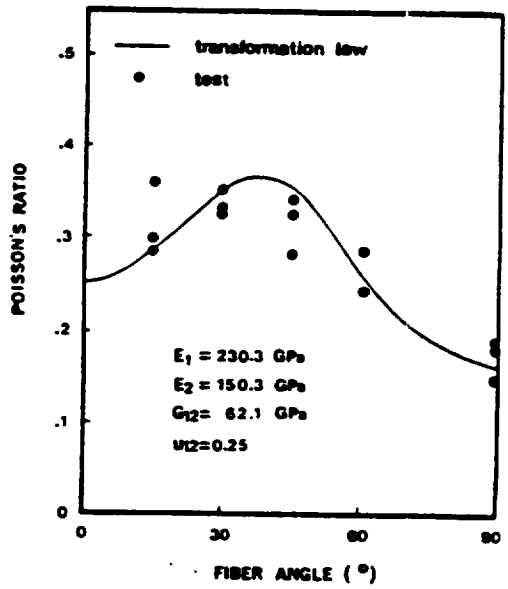

Figure 57 Comparison of elastic Poisson's ratio from test with transformation law.

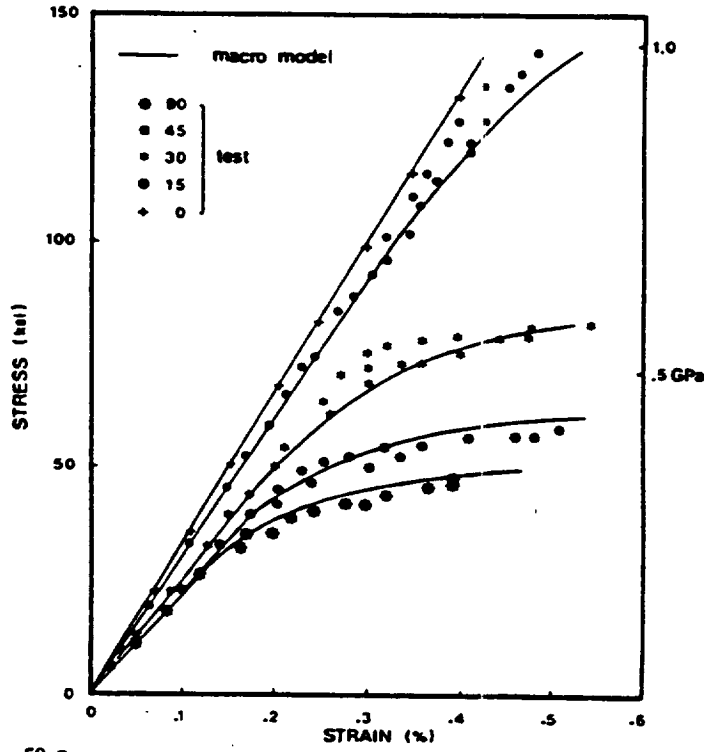

Figure 58 Comparison of the predicted and experimental off-axis stress-strain curves.

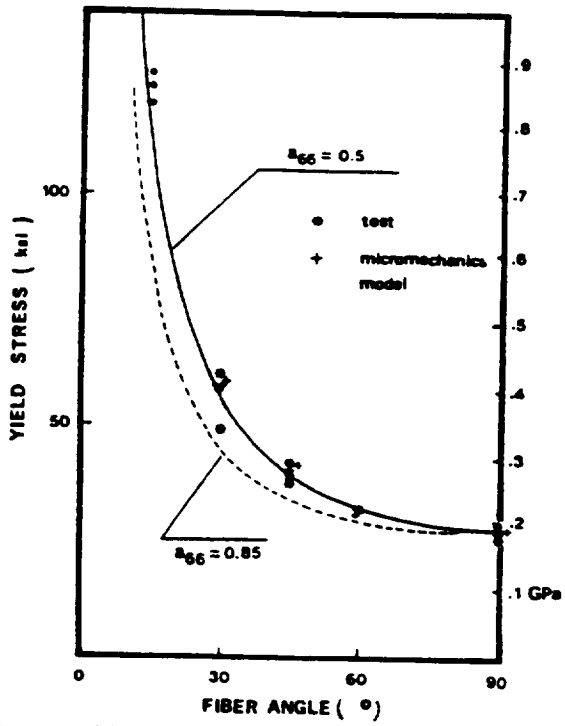

Figure 59. Apparent yield stresses for off-axis specimens. The prediction of micro-mechanical model is for fiber/matrix separation.

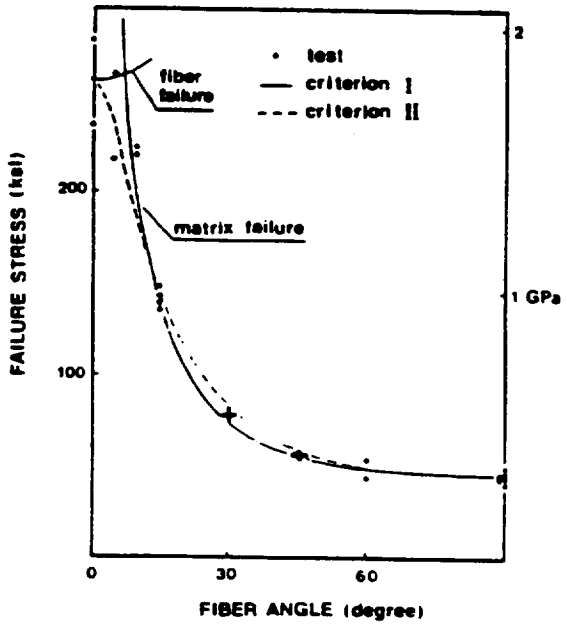

Figure 60. Experimental and predicted failure stresses for off-axis specimens.

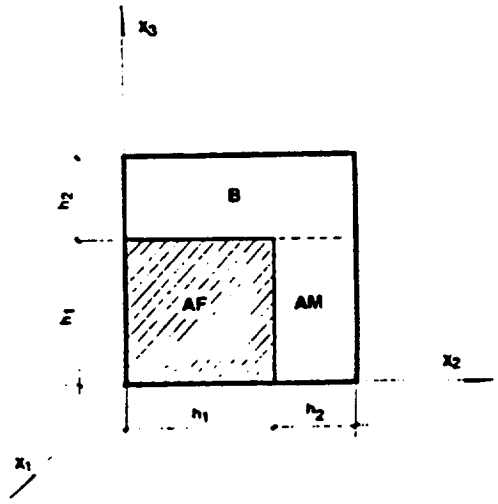

Figure 61. A quadrant of the simplified representative unit cell of the fiber composite.

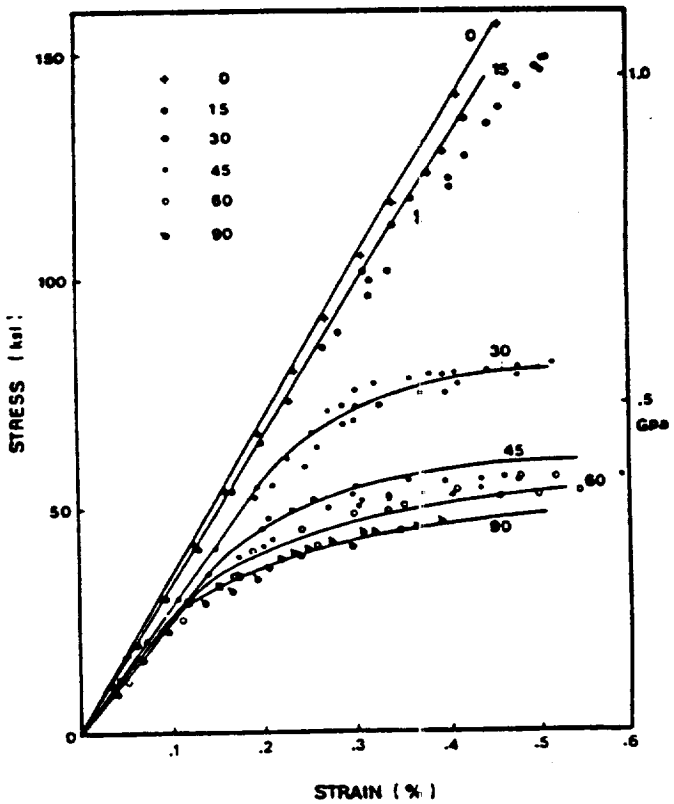

Figure 62. Off-axis stress-strain curves predicted using continuous damage model with modified yielding stress for matrix material.

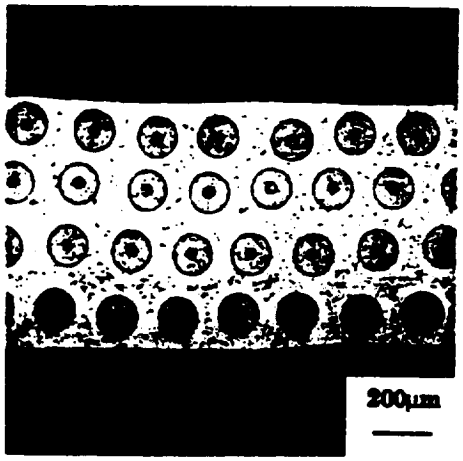

Figure 63 Micrograph of SCS-6/Ti-6Al-4V Consolidated Composite

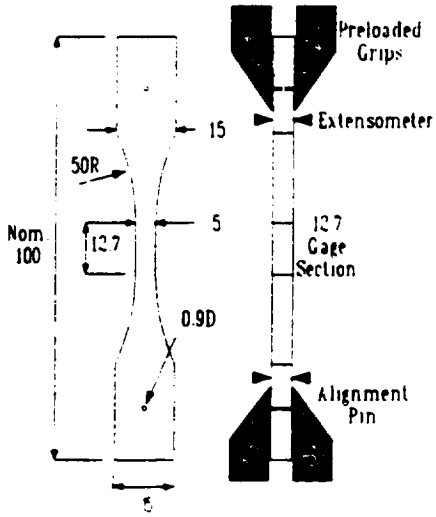

Figure 64 MMC Creep Specimen Geometry (dimensions in mm, fiber direction is ↔)

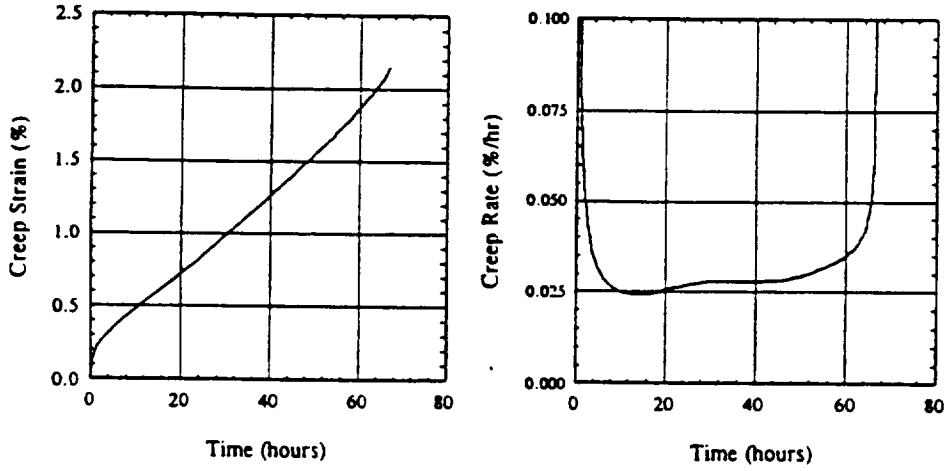

Figure 65 Typical Creep Result for SCS-6/Ti-6Al-4V Tested at 480°C in Air (transverse Series 50 specimen tested at 240 MPa)

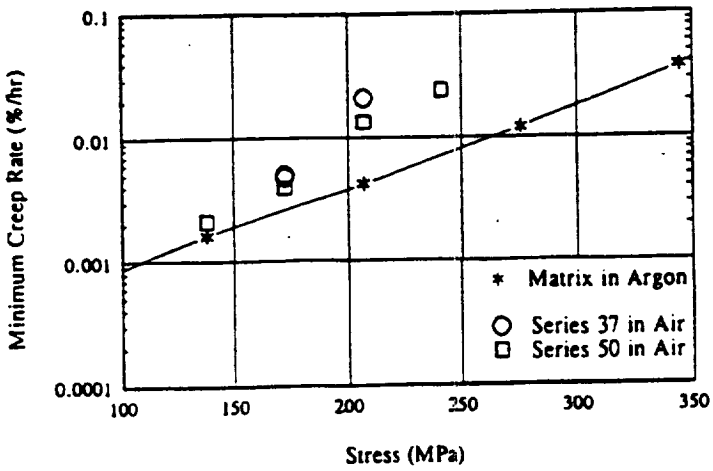

Figure 66 Comparison of SCS-6/Ti-6Al-4V Composite Creep Rates (all tests performed at 480°C)

VBO model

FLOW LAW $\dot{\epsilon}_{ij} = \dot{\epsilon}^{el}_{ij} + \dot{\epsilon}^{in}_{ij} = \frac{1+\nu}{E}\dot{s}_{ij} + \frac{3}{2Ek}(s_{ij} - g_{ij})$ and $\dot{\epsilon}_{ii} = \frac{1}{3K}\dot{\sigma}_{ii}$

STATE VARIABLES

EQUILIBRIUM STRESS $\dot{g}_{ij} = \Psi\left[\frac{1}{1+\nu}\dot{\epsilon}^{el}_{ij} + \frac{2}{3}\dot{\epsilon}^{in}_{ij}\right] - \frac{2(g_{ij}-f_{ij})}{3b}\dot{p} - gR_g[g_{ij}]$

KINEMATIC STRESS $\dot{f}_{ij} = \frac{2E_t\dot{\epsilon}^{in}_{ij}}{3}\left[\frac{A-B}{A_o-B}\right]$

ISOTROPIC STRESS $A = B + \frac{A_o - B}{1+G_1\lambda}$ and $b = \frac{A}{\Psi - E_t}\left(\frac{E-E_t}{E}\right)$

FUNCTIONS AND RELATIONS

SHAPE FUNCTION $\Psi = C_1 + (C_2 - C_1)\exp(-C_3\Gamma)$

where $C_2 = E\left[\frac{A_o(E/C_{20}-1)}{A\exp(C_4(A-A_o))}+1\right]^{-1}$

VISCOSITY FUNCTION $$k = K_1\left[1 + \frac{\Gamma}{K_2}\right]^{-K_3(1 + \exp(K_3(\Gamma - K_4)))}$$

RECOVERY FUNCTION $$R_\xi[\xi] = \frac{R_{\xi 3}}{2}\left[\tanh(U_\xi) + \tanh(V_\xi)\right]$$

where $$U_\xi = -3 + 6\left[\frac{\xi - R_{\xi 1}}{R_{\xi 2} - R_{\xi 1}}\right] \quad \textit{and} \quad V_\xi = 3 + 6\left[\frac{\xi + R_{\xi 1}}{R_{\xi 2} - R_{\xi 1}}\right]$$

and $$\lambda = hp - \eta, \quad \dot{\eta} = h\dot{p} - \eta \cdot R_\eta[\eta], \quad \dot{p} = \sqrt{\frac{2}{3}\dot{e}_{ij}^{in}\dot{e}_{ij}^{in}}, \quad \Gamma = \sqrt{\frac{3}{2}(s_{ij} - g_{ij})(s_{ij} - g_{ij})}$$

where

σ is the stress,
s is the deviatoric stress,
ϵ is the strain,
e is the deviatoric strain,
g is the equilibrium (back) stress (deviatoric),
f is the kinematic hardening variable (deviatoric),
A is the isotropic hardening variable,
Ψ is the shape function, which controls the quasi-elastic to inelastic region transition,
and k is the viscosity function, which controls the model's rate dependence.

Figure 67 VBO Model.

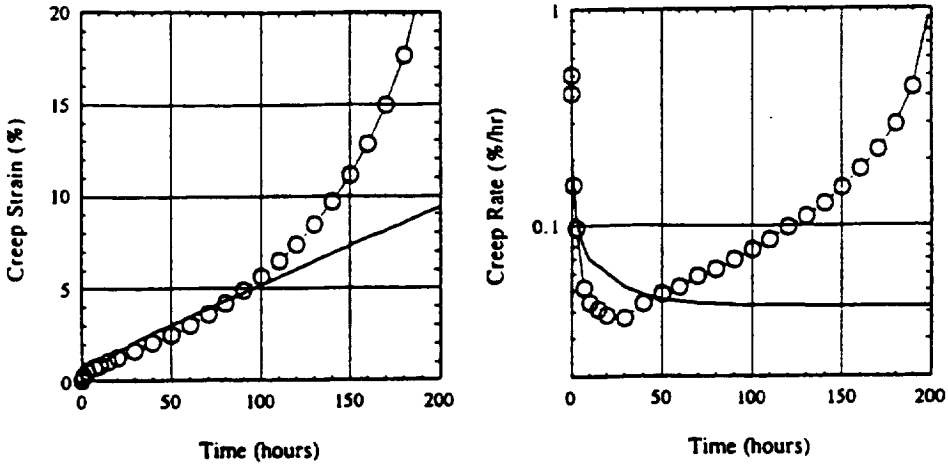

Figure 68 Comparison of VBO Model with Ti-6Al-4V Creep Data at 480°C and 340 MPa
(lines represent VBO model and O represent data)

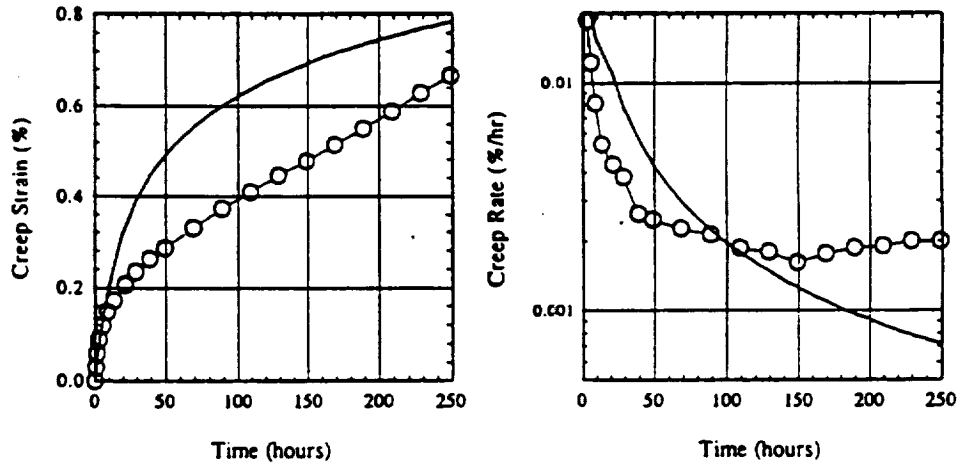

Figure 69 Comparison of VBO Model with Ti-6Al-4V Creep Data at 480°C and 140 MPa
(lines represent VBO model and O represent data)

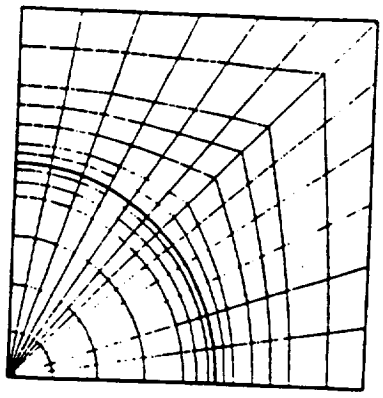

Figure 70 Finite Element Model for the Transverse MMC Composite

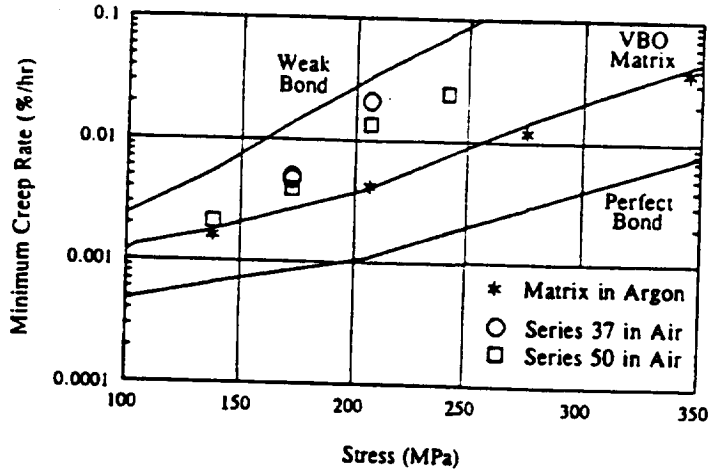

Figure 71: Comparison of SCS-6/Ti-6Al-4V Minimum Creep Rates at 480°C in Air with Finite Element VBO Model Predictions (shown as lines)

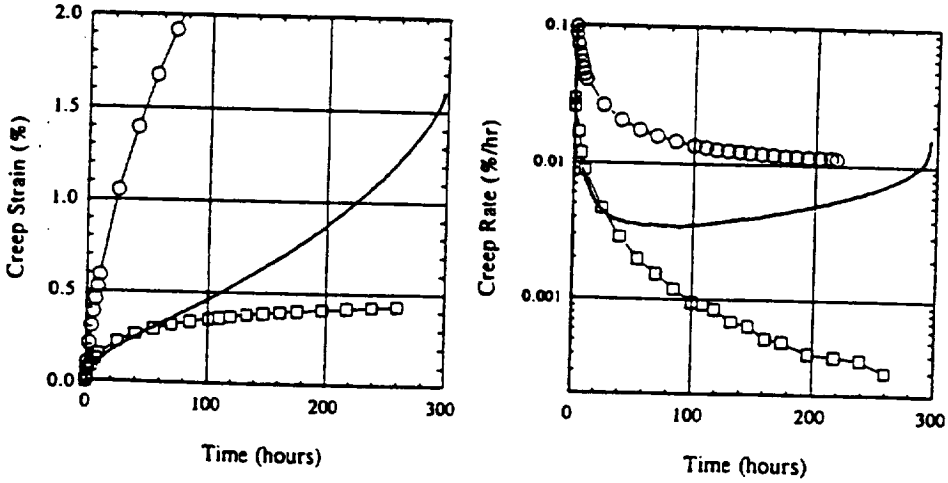

Figure 72: Comparison of SCS-6/Ti-6Al-4V Creep Behavior at 480°C and 170 MPa in Air with FEM-VBO Model Predictions for (□) Perfect and (O) Weak Interface Bonding

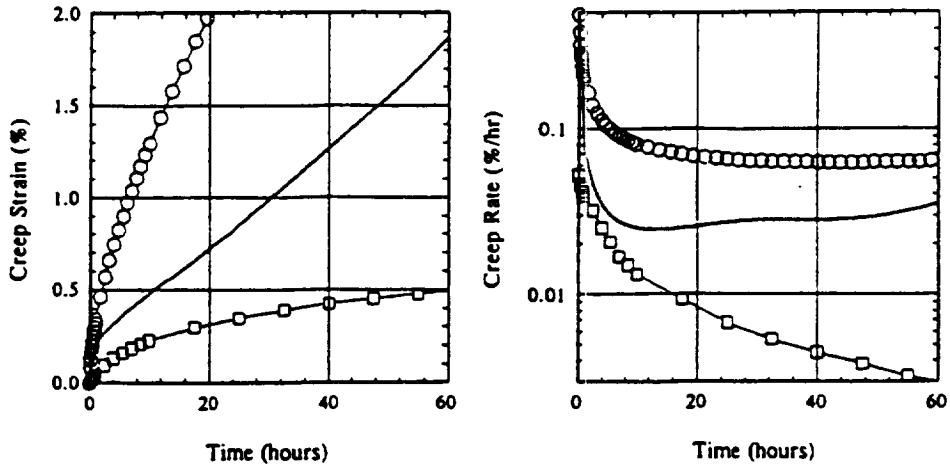

Figure 73. Comparison of SCS-6/Ti-6Al-4V Creep Behavior at 480°C and 240 MPa in Air with FEM-VBO Model Predictions for (□) Perfect and (○) Weak Interface Bonding

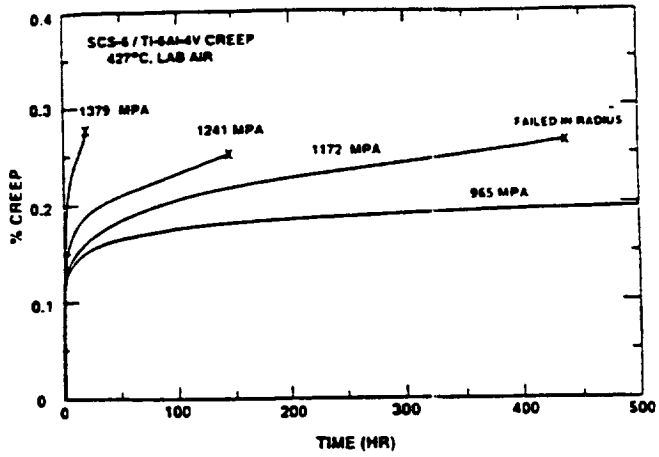

FIGURE 74 Longitudinal creep curves for SCS-6/Ti-6Al-4V at 427°C and stresses from 965 MPa to 1379 MPa. Unless otherwise indicated, tests were unloaded after 500 hours if failure did not occur.

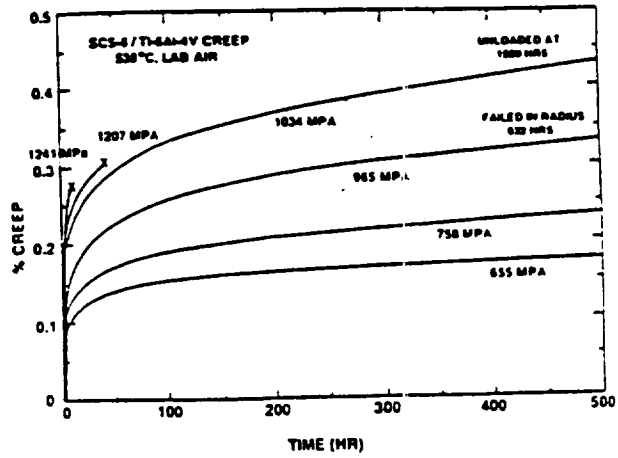

FIGURE 75 Longitudinal creep curves for SCS-6/Ti-6Al-4V at 538°C and stresses from 655 MPa to 1241 MPa. Unless otherwise indicated, tests were unloaded after 500 hours if failure did not occur.

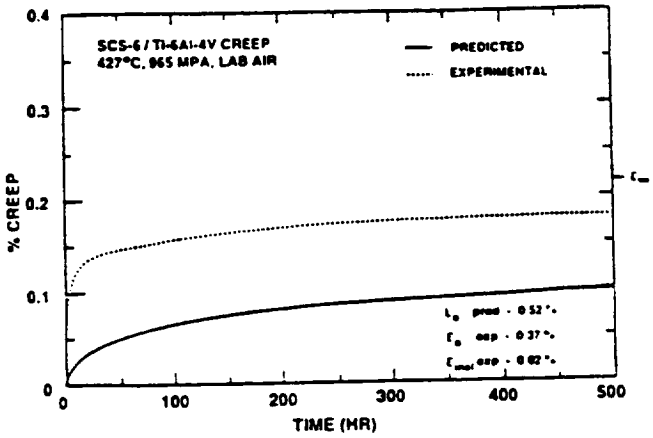

FIGURE 76 Comparison of experimental and predicted longitudinal creep behavior of SCS-6/Ti-6Al-4V MMC at 427°C and 965 MPa.

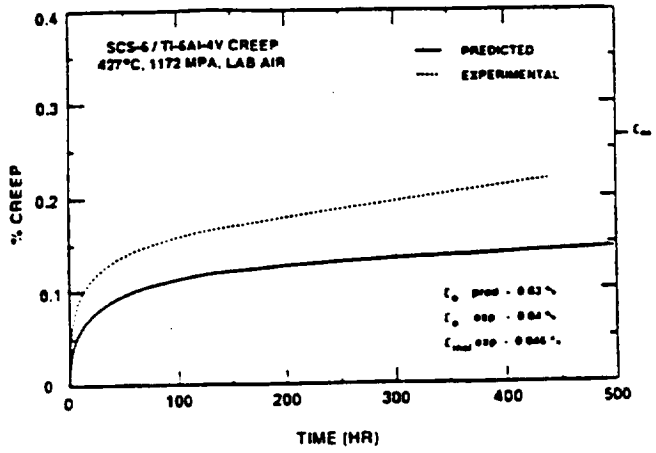

FIGURE 77 Comparison of experimental and predicted longitudinal creep behavior of SCS-6/Ti-6Al-4V MMC at 427°C and 1172 MPa.

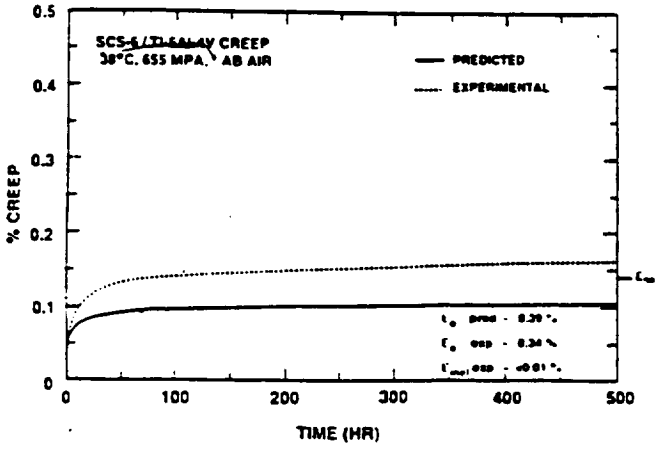

FIGURE 78 Comparison of experimental and predicted longitudinal creep behavior of SCS-6/Ti-6Al-4V MMC at 538°C and 655 MPa.

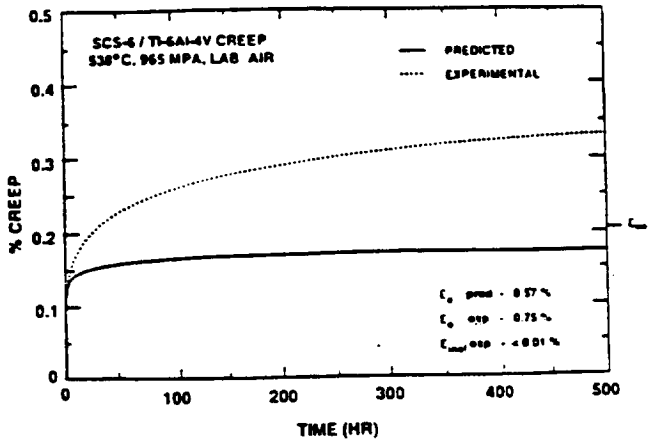

FIGURE 79 Comparison of experimental and predicted longitudinal creep behavior of SCS-6/Ti-6Al-4V MMC at 538°C and 965 MPa.

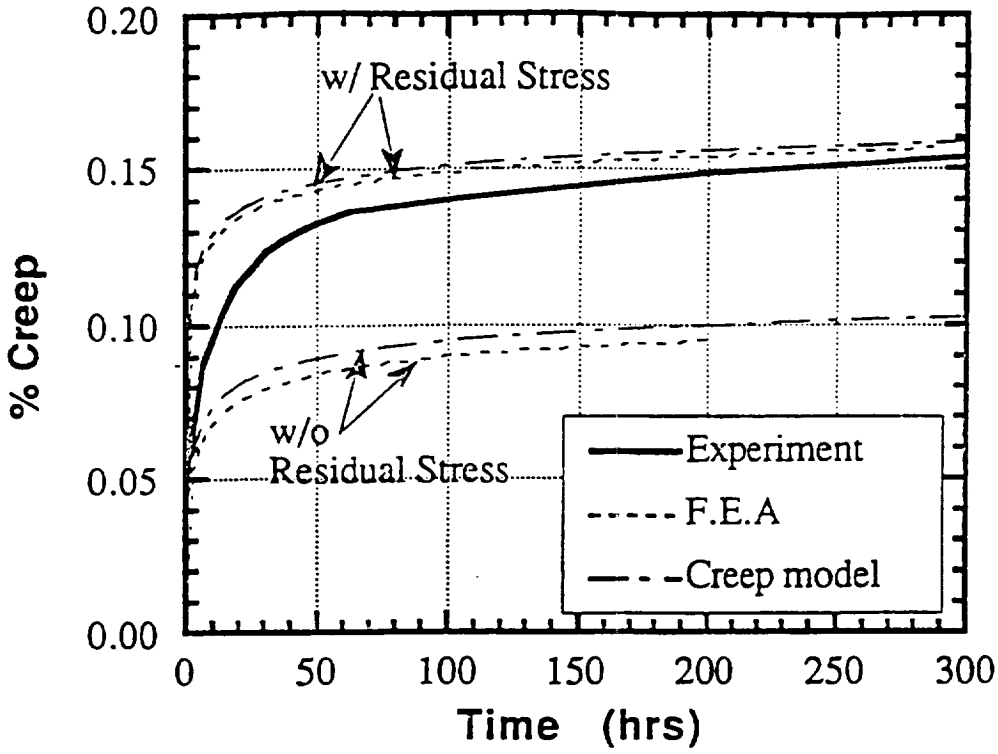

Figure-80 Creep of 33% SCS-6/Ti-6-4 lamina at 538°C and 655 MPa

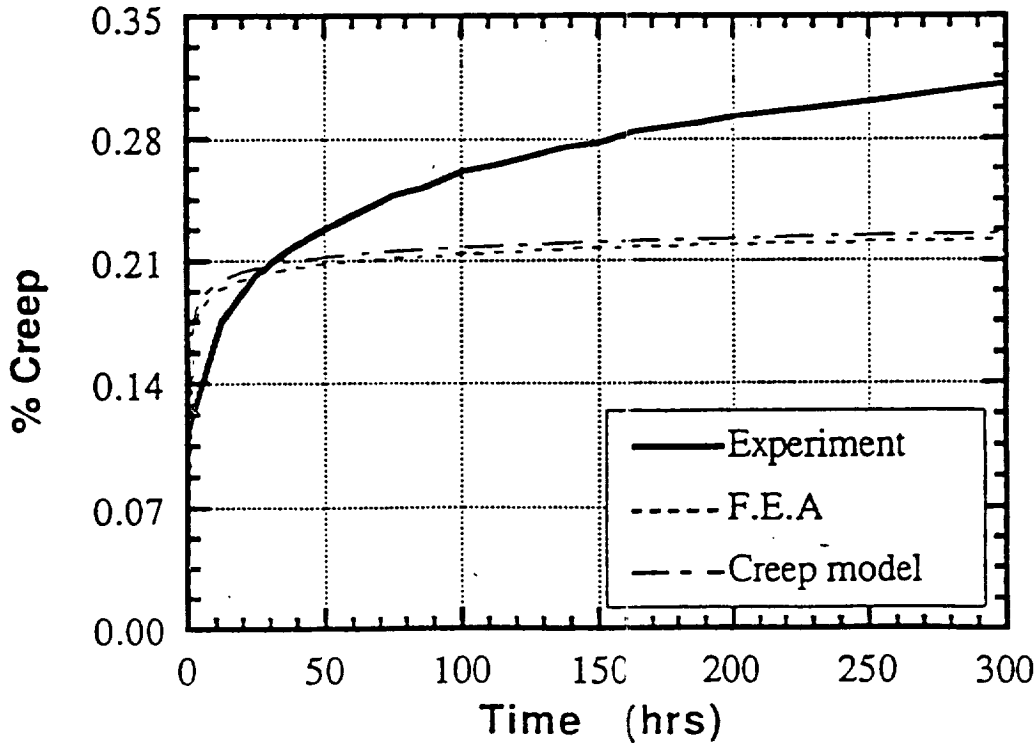

Figure-81 Creep of 33% SCS-6/Ti-6-4 lamina at 538°C and 965 MPa

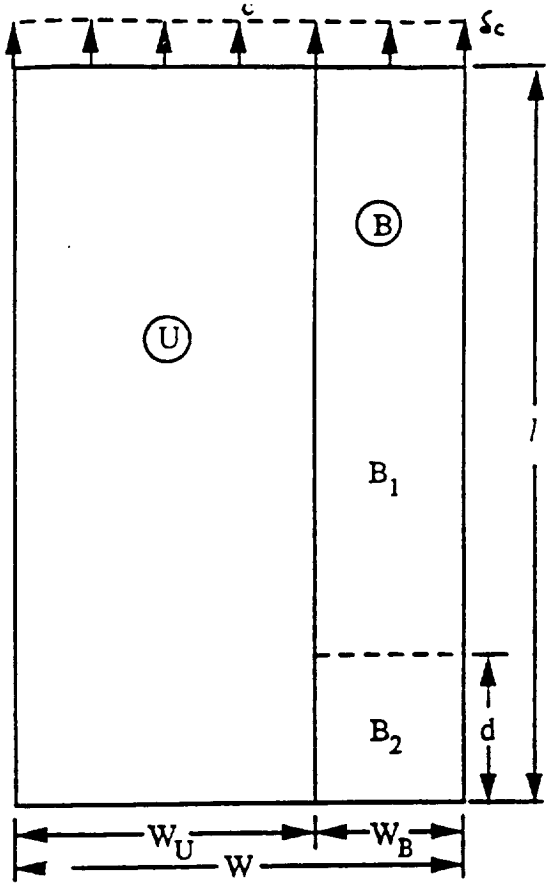

Figure-82 Upper symmetric half of a composite panel with broken fibers in region b

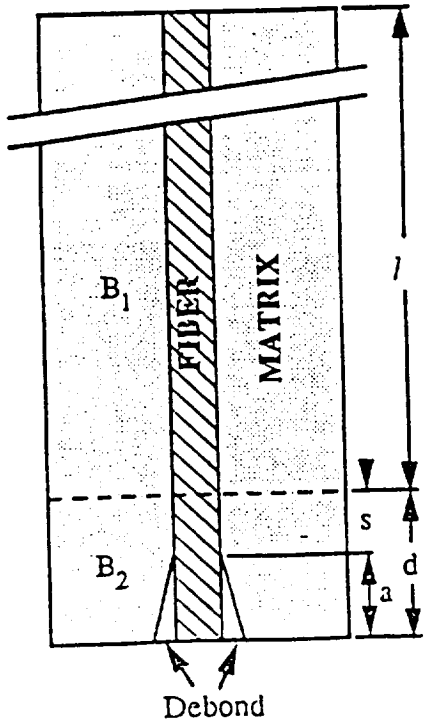

Figure-83 Cross-section of a unit cell within the broken region B

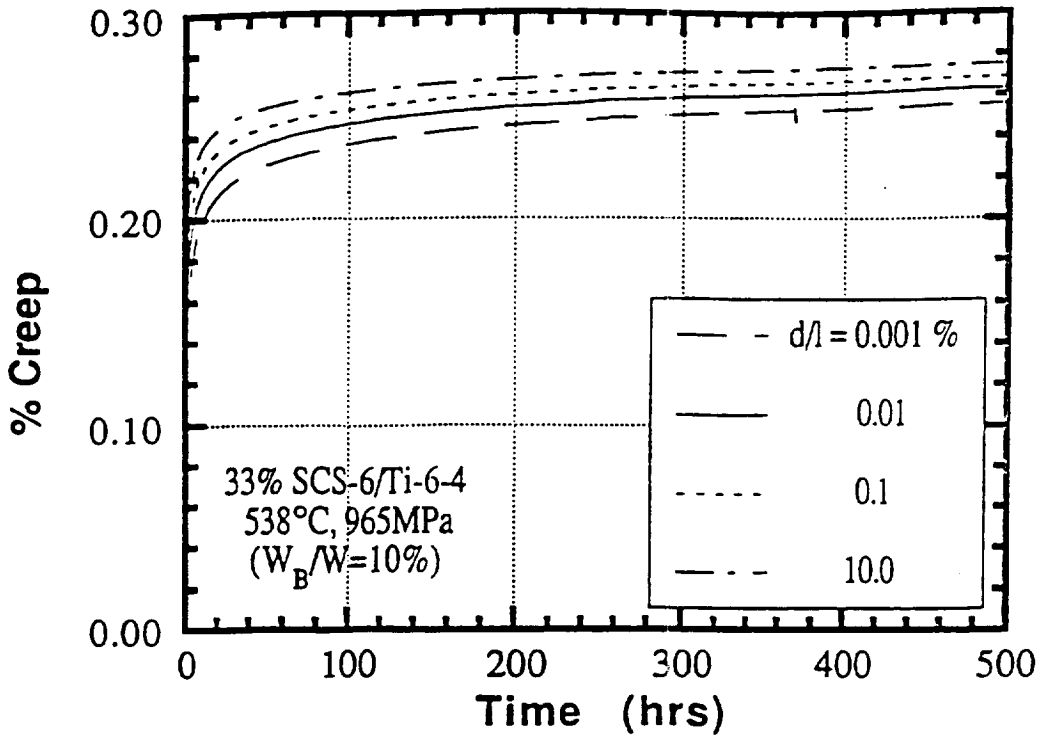

Figure-84 Effect of fiber debond length on composite creep

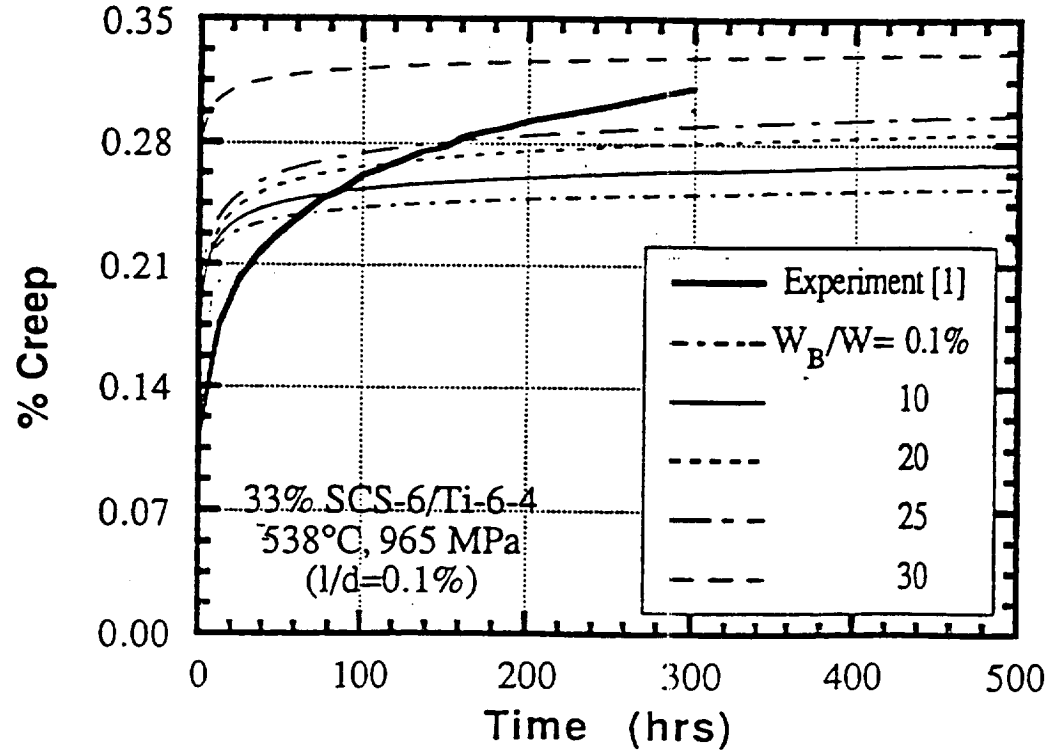

Figure-85 Effect of volume of broken fibers on composite creep

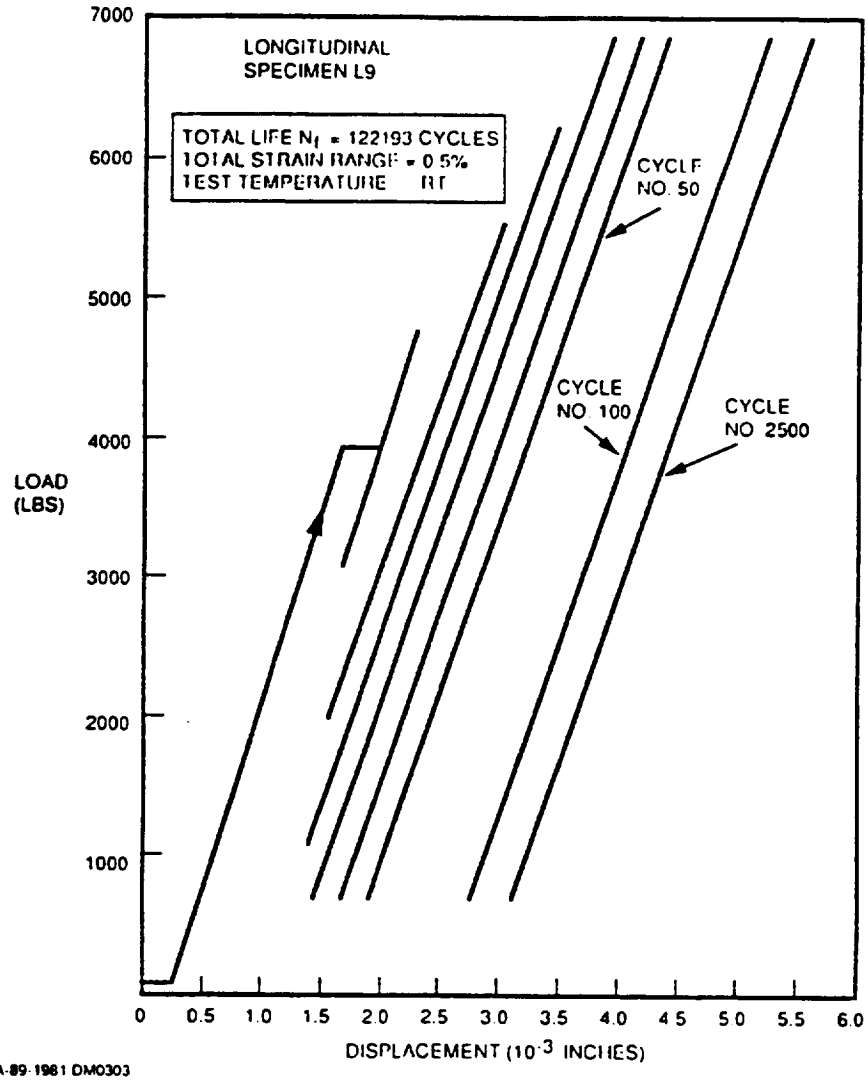

Figure 86 Typical High-Cycle Fatigue Load-Displacement Diagrams during Initial Fatigue Loading at Room Temperature of a Longitudinal Test Specimen (L9) of SCS6/Ti-6Al-4V Metal-Matrix Composite

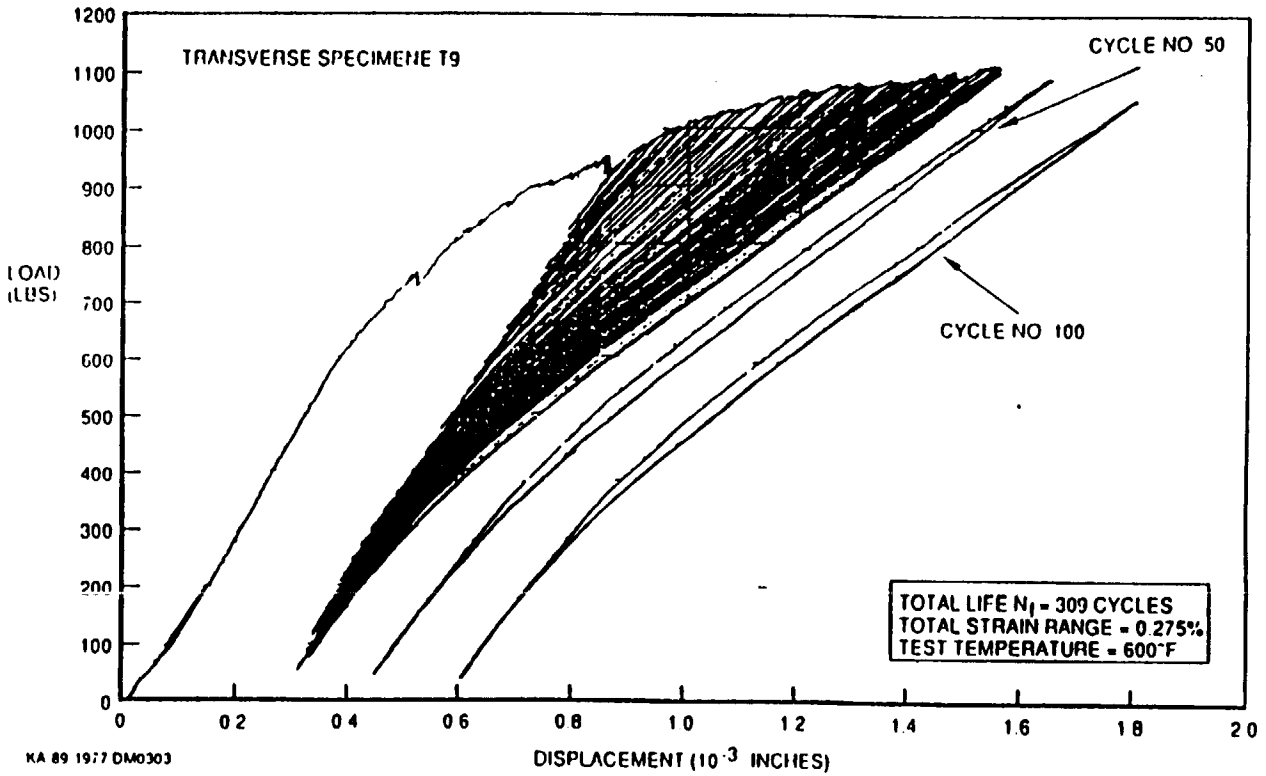

Figure 87. Typical Elevated-Temperature Low-Cycle Fatigue Hysteresis Loops Obtained During Initial Fatigue Loading of a Transverse Test Specimen (T9) of SCS6/Ti-6Al-4V Metal-Matrix Composite

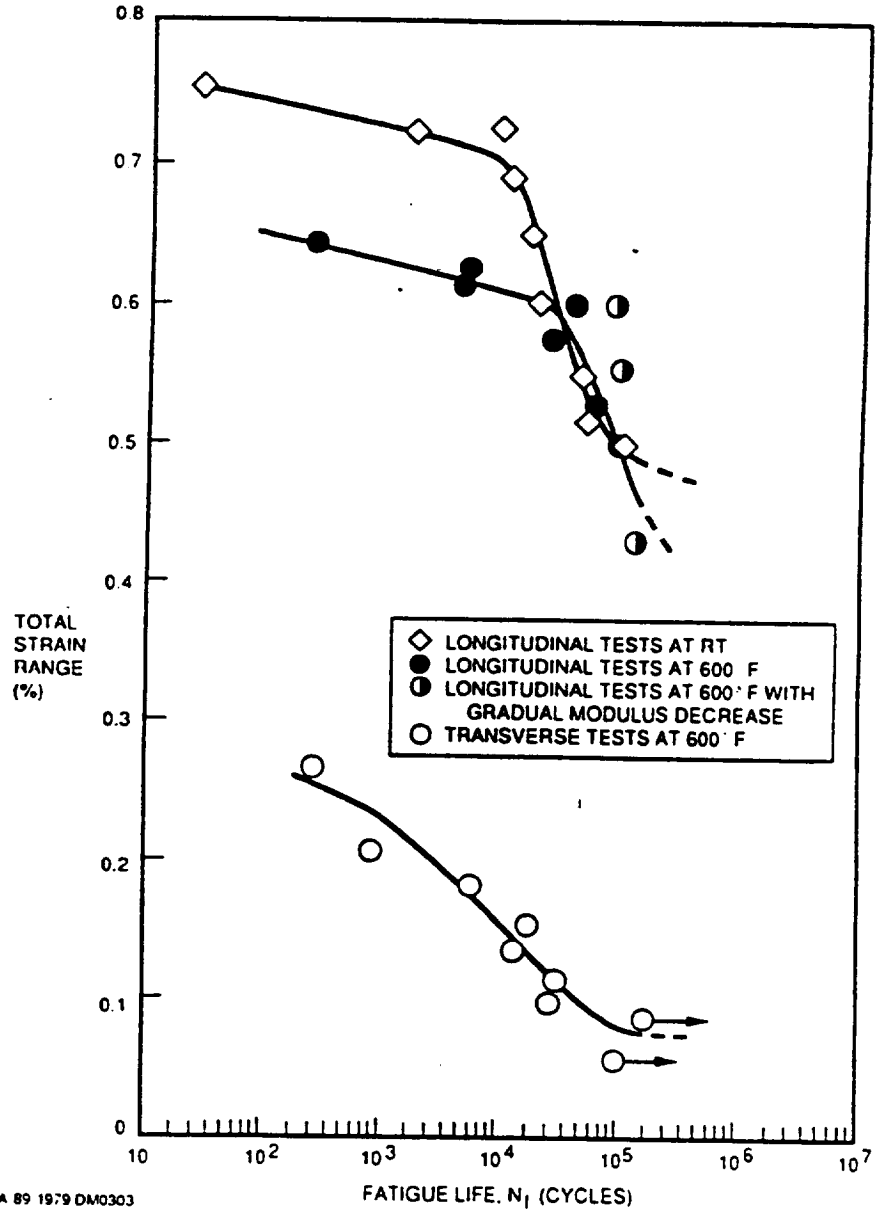

Figure 88. Comparison of Fatigue Behavior of the Longitudinal and Transverse Orientations at Room and Elevated Temperature for SCS6/Ti-6Al-4V Metal-Matrix Composite

a

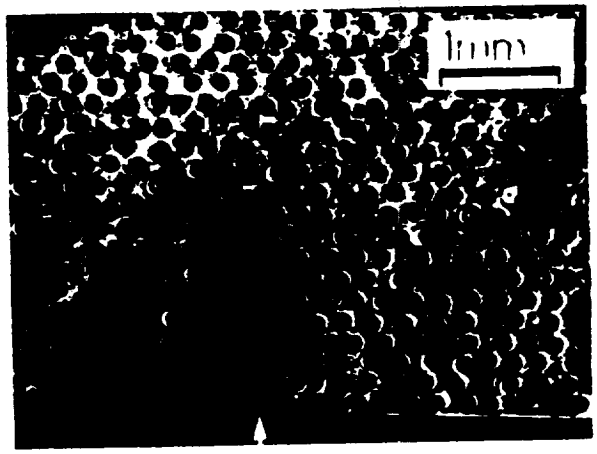

b

Figure 89. Typical Fatigue Fractures of Longitudinal SCS6/Ti-6Al-4V Specimens Showing (a) a Corner Initiation and (b) a Face Initiation Marked by Arrows

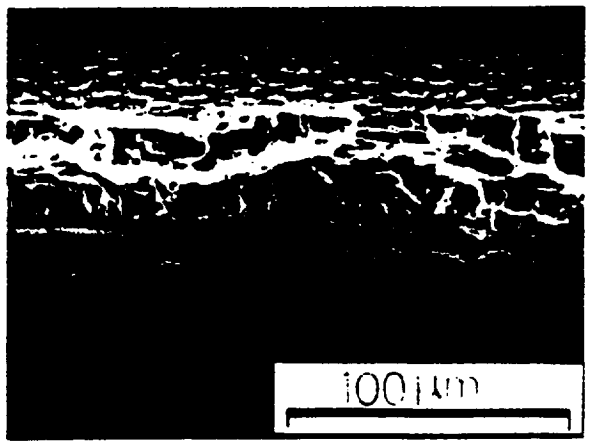

a

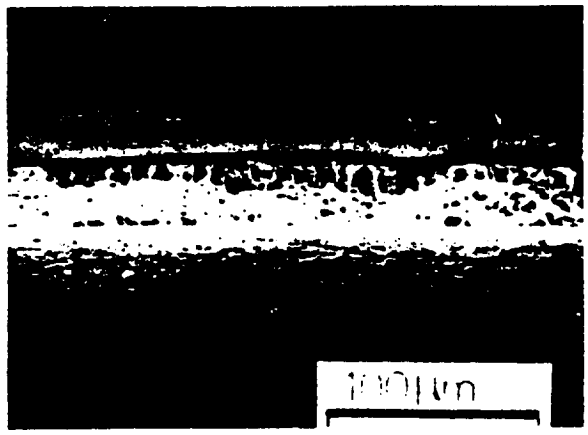

b

Figure 90. Typical Transverse Fatigue Fractures of SCS6/Ti-6Al-4V. In (a) Two Fatigue Cracks Propagate Toward Each Other, and in (b) a Single Crack Initiates at the Interface (Arrow)

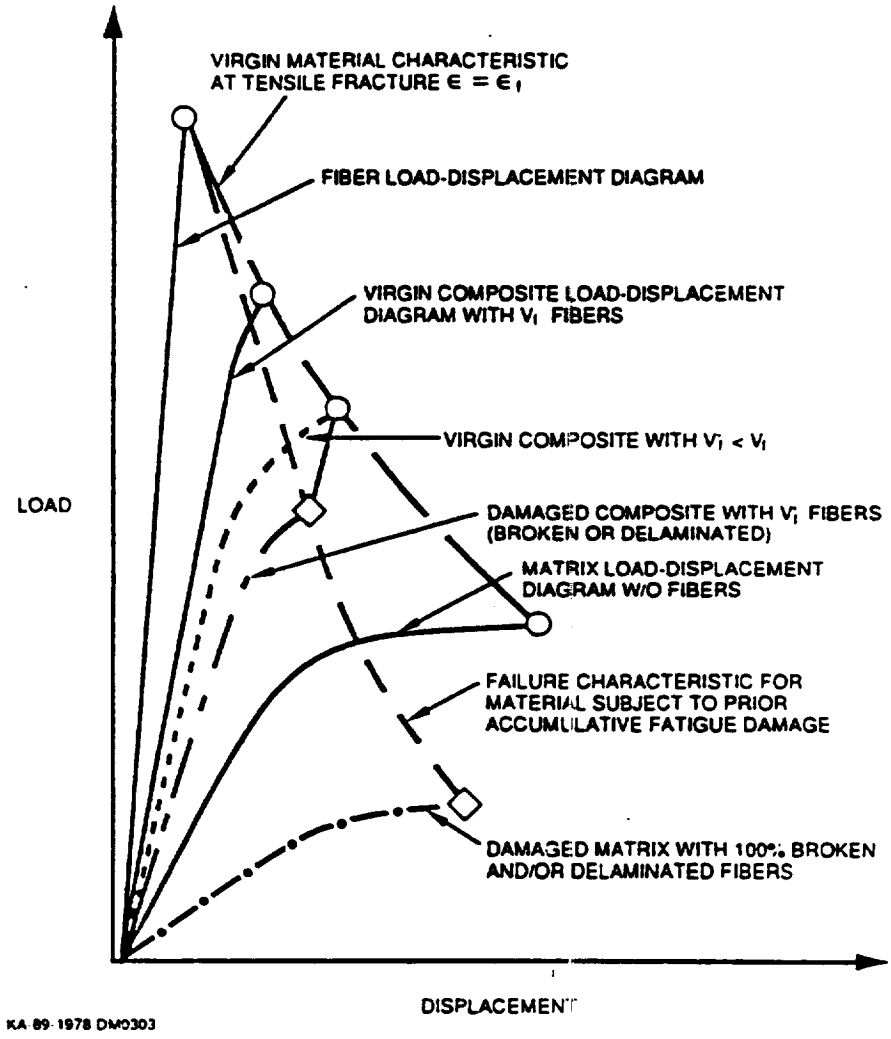

Figure 91. Illustration of Model for Fatigue Damage Accumulation in SCS6/Ti-6Al-4V Unidirectional Metal Matrix Composite System

APPENDIX C

METAL MATRIX COMPOSITE RESPONSE UNDER BIAXIAL LOADING

U. Santhosh & J. Ahmad

AdTech Systems Research, Inc.
1342 N. Fairfield Rd.
Dayton, OH 45433-2698
Tele: (513) 426-3329

To be presented at the 1992 ASME WAM,
November, Anaheim, CA

ABSTRACT

The investigation is aimed at assessing the effect of biaxial loading on monotonic stress-strain response of metal matrix composites for high temperature applications. A micromechanics approach is used. The approach is implemented by a nonlinear finite element analysis method, and validated by comparing predicted behavior against available data under uniaxial loading. Predicted behavior under biaxial loading shows smaller strain values at apparent yield of the composite in both the longitudinal and transverse directions compared to uniaxial loading. Also, longitudinal stress at apparent yield is lower under biaxial loading than in uniaxial loading. The results suggest the need for experimental investigations of biaxial loading effects.

1. INTRODUCTION

Continuous fiber metal matrix composites (MMCs) are being considered by the aerospace industry for use in certain engine and airframe components of supersonic and hypersonic vehicles [1]. For example, an important application in engines is the use of MMC ring inserts in rotating components made of titanium (Ti) alloys or intermetallic compounds. Typically, the inserts have a Ti-based matrix with continuous circumferentially oriented silicon carbide fibers. The purpose of the inserts is to alleviate the relatively high hoop stress close to the bore of the component (caused by centrifugal forces) without increasing the weight of the component. In airframe applications MMC cross-ply laminates are being considered for the skin.

Significant amount of research is being done aimed at characterizing and understanding the behavior of MMCs under a variety mechanical, thermal and thermomechanical load conditions [1]. A review of open literature on the subject reveals that the focus of this research is almost exclusively on MMC behavior under unidirectional loading. The study of MMC response under biaxial and multiaxial loading has remained largely unexplored. This is despite the fact that in many applications, including the ones cited in the previous paragraph, MMC components are subjected to multiaxial loading.

Common methods of biaxial testing, such as using cruciform specimens [2], require specimen sizes much larger than used in uniaxial testing. The current lack of ready availability and high cost of most MMCs precludes a study which would involve many tests. However, mathematical modelling techniques can be used to explore the effect of biaxial loading. This is the rationale for the work reported in the present paper. The approach is to (a) select a modeling technique which allows the consideration of multiaxial loading, (b) validate the technique using available data on MMCs under uniaxial loading, and (c) predict stress-strain response of MMCs under biaxial loading.

A nonlinear finite element based micromechanics model is used. The reason is that only at the micromechanics level reasonable assumptions regarding material behavior of the constituents (the

matrix and fiber materials) under multiaxial loading can be made. The model includes consideration of MMC consolidation process induced residual stresses and damage in the form of fiber-matrix debonding. A description of the model is given in the next section. Following that, micromechanics model predictions are compared with experimental data on some titanium (Ti) alloy matrix composites with silicon carbide fibers under uniaxial loading. Finally, predictions under biaxial loading conditions are presented and discussed.

2. MODEL DESCRIPTION

Prediction of stress-strain response of composites is made using a variety of models. Broadly, these models can be categorized as (a) laminate level models, (b) lamina/ply level models, and (c) micromechanics models. These three categories respectively require laminate, lamina/ply and constituent stress-strain data as part of the input under thermal, environmental and mechanical conditions of interest. Under biaxial loading, none of these data are readily available for Ti alloy matrix composites. However, it seems reasonable to assume that the matrix material stress-strain response under biaxial loading can be adequately well predicted by using well established methods of plasticity theory.

We assume that the fiber behaves linear-elastically and is isotropic. While the linear elastic response assumption may be reasonable for most fibers in use with Ti alloy matrices, the isotropicity assumption may not. For example, see a schematic drawing of the Textron Specialty Materials' (TSM's) SCS-6 fiber cross-section in Figure 1 from reference [3]. While no data can be found on radially loaded fibers, composition of the fiber suggests that it is unlikely to be the same as under axial loading. Nevertheless, due to lack of data, we assume the fiber to be isotropic. The error introduced by this assumption will contribute to any difference between predicted and measured stress-strain response of unidirectional composites loaded transverse (90 degrees) to the fiber direction. This is discussed in the next section.

We also assume that if there is a "reaction zone" between the fiber and the matrix, its dimensions and properties are such that one can assume a step change in material properties from fiber to matrix. This amounts to assuming the reaction zone width being much smaller compared to the characteristic length and/or reaction zone properties being approximately the same as the matrix. The characteristic length in this context is smaller of the fiber radius and half the fiber spacing.

Based on data and analyses on some Ti-alloy/SCS-6 composites (for example, see references [4] and [5]) it also seems reasonable to assume that there is either no chemical or diffusion bond or a very weak bond between the fiber and the matrix. Then, the fibers and the matrix are held together only by the consolidation process induced residual stresses. Relative sliding and opening between a fiber and matrix become possible when the interface shear and radial stresses caused by applied mechanical or thermal stress loading nullify the residual shear and radial stresses, respectively. The assumptions of small or no reaction zone and small or no bond strength also avoid the need for experimentally measured reaction zone properties and bond strength which are generally unavailable anyway.

With the above main assumptions, we consider a unidirectional composite to be made up of a large number of identical unit cells of the configuration shown in Figure 2, repeated in directions marked X_1, X_2 and X_3. L_2 and L_3 represent fiber spacing in the two directions such that the fiber volume fraction (V_f) is equal to $\pi r_f^2/4L_2L_3$. Reflective symmetry about the X_2 and X_3 axes allows consideration of only one quarter of the cell with the prescription of boundary displacements (u_i) such that $u_2=0$ on $0\le x_3\le L_3$ and $u_3=0$ on $0\le X_2\le L_2$.

We allow the composite to be subjected to straining in the three directions by uniform displacements δ_1, δ_2 and δ_3 applied to the three planes. Thus the model allows for all stress components (σ_{ij}) to be non-zero except σ_{12} and σ_{13} shear components which are assumed to be zero. Also the strain component ε_{11} is assumed to be a constant. Thus, the problem is one of generalized plane strain. Note that even when δ_2 and/or δ_3 are zero, the corresponding plane is constrained such that it displaces parallel to itself. Thus, the unit cell is meant to represent the behavior in the interior of the composite at a distance (away from all free surfaces) which is large compared to the largest cell dimension.

To model possible fiber-matrix debonding, we also impose the constraint that at $r=r_f$, the radial displacement component (u_r) in the matrix and the fiber are such that $(u_r)_m - (u_r)_f \le 0$. The subscripts m and f denote matrix and fiber, respectively. The condition is implemented in a nonlinear contact algorithm which allows for opening between the fiber and the matrix and restricts interpenetration of one material region into another.

The above boundary conditions, together with the equilibrium and compatibility equations and stress-strain relations for the fiber and the matrix materials constitute a nonlinear boundary value

problem which we solve numerically by the finite element method. The fiber stress-strain behavior is represented by the Hooke's law for isotropic materials with appropriate adjustment for free thermal expansion. The matrix material is modeled as elastic-plastic using von Mises yield condition, associated flow rule, and isotropic hardening. Stress-strain relations as well as the coefficients of thermal expansion for both the fiber and matrix materials are considered to be temperature dependent.

The finite element discretization is done using the isoparametric formulation with biquadratic basis functions for displacements. The eight node general quadrilateral elements have 17 degrees of freedom: u_2 and u_3 at each node, plus a u_1 degree of freedom common to all nodes for enforcing the generalized plane strain condition. The problem is solved incrementally using the Modified Newton Raphson technique within each increment.

3. MODEL VERIFICATION

The micromechanics model described in the previous section involves several assumptions regarding behavior of the constituent materials, topographical structure of the composite, interface strength etc. Also, the boundary value problem is solved using a numerical technique which also involves several assumptions. It is infeasible to evaluate the effect of each individual assumption on the accuracy of model predictions. However, their synergistic effect on solution accuracy can be assessed by comparing model predictions with measured stress-strain data. For this purpose, we consider the following three MMCs:

(A) Ti-24Al-11Nb matrix with 35 percent volume fraction of SCS-6 fiber,

(B) Ti-15-3 matrix with 34 percent volume fraction of SCS-6 fiber,

and (C) another β phase Ti alloy with 33 percent volume fraction of SCS-6 fiber.

Figures 3 (a, b and c) show the uniaxial stress-strain test data on matrix materials for the three MMCs. The temperature dependent Young's modulus (E), Poisson's ratio (ν) and coefficients of thermal expansion (α) for the three matrix materials are given in Table 1. The SCS-6 fiber properties are given in Table 2. The matrix material data were obtained from references [6-10]. Not all data on each material could be found from a single source. For example, Ti-15-3 stress-strain curves at various temperatures (Figure 3b) were obtained from references [7], [8] and [9] because no single reference contained all the data within the temperature range of interest. Consequently, as discussed in reference [9], the data were obtained not only using different lots of material but also using materials subjected to somewhat different heat treatments prior to testing.

Figures 4 and 5 show the predicted and experimentally obtained stress-strain curves under 0 degree loading for the three MMCs at room temperature and at elevated temperature, respectively. No fiber-matrix debonding was predicted in any of the composites. All predicted as well as measured stress-strain curves show deviation from linear elastic response at strain levels lower than the corresponding matrix material strain at yield. This is the consequence of consolidation process induced residual stresses which produce a tensile initial strain in parts of the matrix material. If there were no residual stresses and the fiber and matrix were held together purely by a chemical or physical bond, the deviation from linearity would occur at exactly the matrix material strain at yield. Figure 6 for the material system (C) shows that this is the case when the model is used without the consideration of residual stresses. The post yield stress-strain behavior under 0 degree loading can be expressed as:

$$(d\sigma/d\varepsilon)_{0\ degree} = E_c - [\ \gamma_m\ (1 - v_f) + \ \gamma_f\ v_f] \tag{1}$$

where

$$E_c = E_f\, v_f + E_m(1-v_f), \tag{2}$$

$$\gamma_{m,f} = \frac{E_{m,f}^2\, \lambda_{m,f}}{1+E_{m,f}\, \lambda_{m,f}}\ , \tag{3}$$

and

$$d\varepsilon^i_{m,f} = \lambda_{m,f}\, d\sigma_{m,f} \tag{4}$$

In the above, $d\varepsilon^i$ and $d\sigma$ represent inelastic strain and stress increments, respectively. The subscripts f, m and c indicate the fiber, matrix and composite respectively. Assuming the fiber to be elastic, λ_f=0 and assuming matrix to have constant strain hardening with tangent modulus E^P_m, one gets for the 0 degree composite:

$$(d\sigma/d\varepsilon)_{0\ degree} = v_f\, E_f + (1 - v_f)\, E^P_m \tag{5}$$

The result shown in Figure 6 compare well with Equation (5). Equations (1) to (4) can be used to predict 0 degree response of composites for other matrix material constitutive models.

In the presence of residual stresses, an estimate of the 0 degree composite yield stress (σ_y) is as follows:

$$(\sigma_y)_{0\ degree} = \frac{E_c}{E_m}\sigma_{ym} + E_f\, v_f\, (\bar{\alpha}_m - \bar{\alpha}_f)\, (T_t - T_c)\,, \qquad (6)$$

where σ_{ym} is the matrix yield stress, T_t is the test temperature and T_c is the (stress free) composite consolidation temperature. The coefficients of thermal expansion $\bar{\alpha}_m$ and $\bar{\alpha}_f$ for the matrix and the fiber materials represent average values over the temperature range $T_t \leq T \leq T_c$. The result shown in Figure 6 compares well with the estimate given by Equation (6). This estimate is not expected to be very accurate if the residual stresses in significantly large portions of the matrix exceed matrix yield stress.

Under 90 degree loading, the predicted and experimentally obtained stress-strain curves for MMCs (A), (B) and (C) are shown in Figure 7 for room temperature and in Figure 8 for elevated temperature. In contrast to the 0 degree loading, transverse loading was found to cause large enough tensile radial stress at a portion of the fiber-matrix boundary to nullify the compressive interfacial residual stresses prior to matrix yielding. Thus, the model predicted fiber-matrix separation in all cases.

In Figure 7, the first inflection in the predicted stress-strain behavior is a manifestation of fiber-matrix separation. For MMC (B), Figure 9(a) shows the progression of fiber-matrix separation as predicted by the model. It shows that the first inflection in the predicted Figure 7 curve for (b) occurs at an applied strain level which corresponds to the onset of separation.

Figures 9 (a and b) also show the extent of matrix yielding with increasing applied strain for MMC (B) at room temperature and at 538°C. The extent of matrix yielding is presented as percent of yielded matrix volume. Comparing Figures 9 (a and b) with Figures 7 and 8, it is seen that the second inflections in the predicted stress strain curves approximately correspond to the onset of matrix yielding.

Comparing the predicted and measured stress-strain responses shown in Figures 7 and 8, it is seen that while the model is able to capture the character of the curves, there are differences. The tendency of the model is typically to overestimate the stress at a given strain.

In the elastic range prior to separation, the measured response is typically more compliant than predicted by both the present finite element model and by the rule of mixtures applied to constituent compliance values (sometimes referred to as "inverse" rule of mixtures). The discrepancy between predicted and measured initial elastic response may be at least partly attributable to the way transverse strain of the composite is defined. In the model, the strain is simply the applied (uniform) displacement at $x_2 = L_2$ (see Figure 2) divided by L_2. This implies that the displacement u_2 varies linearly with x_2. This of course is not the case. An alternative definition of strain may indeed bring the predicted initial elastic response closer to that found experimentally.

Stress at which fiber-matrix separation is predicted is typically lower than at the first inflection in the measured stress-strain response. This may be due to an underestimate of consolidation process induced residual stresses by the model or (for some composites) due to possibly erroneous assumption in the model that there is no chemical or physical bond between the matrix and the fiber materials. Additionally, possible inaccuracies in the matrix and fiber properties used as input to the model may have contributed to the discrepancy between predicted and experimentally obtained stress strain curves.

Notwithstanding some discrepancies between the predicted and measured 0 degree and 90 degree composite stress-strain behavior, we considered model predictions accurate enough to allow at least a preliminary investigation which involves simultaneous 0 and 90 degree loading of the unit cell. This investigation is discussed in the next selection.

4. BIAXIAL LOADING EFFECTS

Employing the same unit cell model as described in the previous section, computations were performed on composites (A), (B), and (C) with simultaneous application of uniform strains ε_L and ε_T in directions X_1 and X_2, respectively. Solutions were obtained for each composite under seven different applied $\varepsilon_T/\varepsilon_L$ ratios ranging from purely longitudinal ($\varepsilon_T/\varepsilon_L=0$) to purely transverse ($\varepsilon_T/\varepsilon_L=\infty$) strains. The results are shown in Figures 10, 11 and 12.

Figures 10a, 11a, and 12a show the predicted fiber direction stress-strain response for composites A, B, and C, respectively. In each case, computation was terminated if complete debonding between the fiber and the matrix was predicted. As expected, the predicted initial elastic response is stiffer under biaxial loading than that under purely longitudinal loading. This trend

would be expected to continue in the inelastic region if there was no damage. To study the effect of biaxiality in the presence of damage on the longitudinal and transverse stress-strain responses, consider the curves for composite A corresponding to two biaxiality ratios ($\varepsilon_T/\varepsilon_L$): 0.2 and 5.0 respectively. As discussed in the previous section, the first inflection (knee) in the transverse stress-strain curve is a manifestation of damage occuring at the fiber-matrix interface. This inflexion is apparent in the transverse stress-strain curves under biaxial loading shown in Figures 10b, 11b, and 12b. Figure 10 shows that the first inflection in the transverse stress strain curves at the above mentioned two biaxiality ratios occurs at ε_T values of approximately 0.09 and 0.15 percent, respectively. At these ε_T values, the corresponding longitudinal strains (ε_L) are 0.45 percent and 0.03 percent. Figure 10a (and more clearly Figure 13, which presents a magnified view of the two specific curves being considered) shows that the longitudinal stress-strain curves deviate from linearity at these approximate strain values of 0.45 and 0.03 percent. But there is no "knee" in the longitudinal curve.

The absence of a sharp knee in the longitudinal stress strain curves is a consequence of the uniform displacement (δ_1) boundary condition imposed at all node points of the unit cell, and maintained even after fiber-matrix debond occurs. In essence, this boundary condition precludes any possible change in longitudinal elastic modulus (E_L) of the composite due to debonding. Thus, the knee is absent from longitudinal stress-strain curves. Debonding does however cause stress redistribution and localized matrix yielding at debond termini as shown schematically in Figure 14. This localized yielding causes the premature deviation from linearity, apparent in Figure 13, at longitudinal strains smaller than the strain at apparent yield in the purely longitudinal loading case.

Overall, the computational results suggest that the effects of biaxial loading on longitudinal (0 degree) stress-strain of the composites are in the form of increased apparent stiffness (E_L) in the linear range and reduced strain at apparent yield (ε_{Ly}) of the composite. The apparent yield stress, σ_{Ly} (= $E_L\varepsilon_{Ly}$) is less under biaxial loading than under uniaxial loading. The post yield behavior depends on the hardening characteristics of the matrix as well as on the growth behavior of the debond length. While the extent of these effects are of course material dependent, as seen by comparing Figures 10a, 11a, and 12a, the qualitative features are the same.

The effects of biaxial loading on transverse stress-strain behavior are similar to those for the longitudinal case but somewhat more pronounced. Biaxial loading causes an increase in the apparent elastic stiffness (E_T) and decrease in the strain (ε_{Ty}) at which deviation from elastic behavior occurs (see Figures 10b, 11b, and 12b). As discussed earlier, fiber-matrix debond damage causes a knee in the stress strain curves which is most pronounced in the purely transverse loading case ($\varepsilon_T/\varepsilon_L=\infty$). The curves become more plasticity dominated than damage dominated with decreasing $\varepsilon_T/\varepsilon_L$ ratio. In contrast to the longitudinal behavior, the apparent transverse yield stress (σ_{Ty}) is larger under biaxial loading than under purely transverse loading. However, in the large strain regime the apparent transverse hardening modulii for the biaxial cases are less than for the purely transverse loading case.

5. CONCLUSION

The objective of the present work was to assess the effect of biaxial loading on the stress-strain response of Ti-based matrix composites with continuous silicon carbide (SCS-6) fibers. Three different matrix material properties were used. For all three composites, existing experimental evidence indicated weak fiber-matrix interfaces.

A micromechanics approach was adopted to predict MMC response under biaxial loading. The approach was implemented using a generalized plane strain nonlinear finite element analysis procedure which included an algorithm for modeling fiber matrix debonding. It was demonstrated that the approach provided a reasonably good prediction of (at least) the key features of the composite stress-strain behavior under uniaxial loading. The predicted stress-strain curves under biaxial loading (for which no experimental data could be found) should be viewed in the same vein, that is, while the predicted trends and features are believed to be representative of what would happen in a test, specific values of key parameters (such as apparent yield stresses and strains) may not be precise.

For the MMCs considered, the expected increase in both longitudinal and transverse apparent modulii (E_L and E_T) was observed under biaxial loading. It was found that the fiber-matrix debond caused by transverse loads has the effect of lowering the apparent longitudinal stress (and strain) at yield. Depending upon the biaxiality ratio, this decrease in yield strength and strain may be significant enough to deserve consideration as a design parameter.

The effect of biaxial loading on transverse stress-strain behavior was also found to be significant, especially for applied $\varepsilon_T/\varepsilon_L < 1.0$. An interesting feature (in the range of practical interest) is the cross over of transverse stress-strain curves (see Figures 10b, 11b, and 12b). Depending upon the transverse stress (σ_T) level, the transverse strain (ε_T) under biaxial loading can be less or more than under purely transverse loading.

REFERENCES

[1] Smith, P.R. and Revelos, W.C., Titanium Matrix Composites, WL-TR-92-4035, Wright-Patterson Air Force Base, OH, April 1992.

[2] Whitney, J.M., Daniel, I.M. and Pipes, R.B., Experimental Mechanics of Fiber Reinforced Composite Materials, SESA Monograph No. 4, Society for Experimental Stress Analysis, Prentice-Hall, pp 215-222, 1982.

[3] Das, G., "Microstructural Characterization of Ceramic Reinforcements for Composites", Titanium Aluminide Composites, WL-TR-91-4020, Smith, P.R., Balsone, S.J. and Nicholas, T. eds, Wright-Patterson Air Force Base, OH, pp 20-58, February 1991.

[4] Majumdar, B.S. and Newaz, G.M., "Inelastic Deformation of Metal Matrix Composites: Plasticity and Damage Mechanisms", to appear in *the Philosophical Magazine*, 1992.

[5] Sohi, M., Adams, J. and Mahapatra, R., "Transverse Constitutive Response of Titanium Aluminide Metal matrix Composites", Titanium Aluminide Composites, WL-TR-91-4020, Smith, P.R., Balsone, S.J. and Nicholas, T. eds, Wright-Patterson Air Force Base, OH, pp 20-58, February 1991.

[6] Kroupa, J.L., "Elastic-Plastic Finite Element Analysis of MMC Subjected to Thermomechanical Fatigue", Titanium Aluminide Composites, WL-TR-91-4020, Smith, P.R., Balsone, S.J. and Nicholas, T. eds, Wright-Patterson Air Force Base, OH, pp 20-58, February 1991.

[7] Mirdamadi, M., Johnson, W.S., Bahei-El-Din, Y.A., and Castelli, M.G., "Analysis of Thermomechanical Fatigue of Unidirectional Titanium Metal Matrix composites," NASA Technical Memorandum 104105, 1991.

[8] Newaz, G.M., and Majumdar, B.S., "A Comparison of Mechanical Response of MMC at Room and Elevated Temperatures," submitted to *Composites Science and Technology*, 1992.

[9] Santhosh, U., Ahmad, J. and Nagar, A., "Non-Linear Micromechanics Analysis Prediction of the Behavior of Titanium-Alloy Matrix Composites", Session on Fracture & Damage-Modeling and Analysis II, 1992 ASME Winter Annual Meeting, Symposium on High Temperature Materials and Structures (to appear in proceedings), November 1992.

[10] Ahmad, J. and Haq, I., "A Compilation of Test Data on β 21S Matrix Material for Metal matrix Composites", AdTech Systems Research Inc. Report to NASP Institute for the Mechanics and Life of High Temperature Composites (NIC), 1992.

Table-1: Mechanical Properties of MMC Matrix

Temperature (°C)	Tensile Modulus (GPa)	Poisson's Ratio	Yield Strength (MPa)	Tangent Modulus (GPa)	CTE (µm/m/°C)
Ti-24-11					
21	84.1	0.30	1140	0.9	9.27
168	86.3	0.30	680	2.1	9.86
315	88.4	0.30	410	3.3	10.45
649	48.1	0.30	257	4.1	11.79
760	36.1	0.30	172	3.7	12.24
1010	11.3	0.30	54	4.2	13.25
Ti-15-3					
25	86.3	0.36	763	3.2	8.48
482	72.2	0.36	577	3.5	9.71
538	77.8	0.36	447	2.6	9.87
566	64.4	0.36	287	2.3	9.98
650	53.0	0.36	198	1.1	10.26
B alloy					
21	117.0	0.34	1050	3.8	8.34
316	101.0	0.34	775	5.4	9.35
482	95.4	0.34	690	6.4	9.97
566	78.1	0.34	470	17.0	10.30
621	73.2	0.34	289	14.7	10.53

Table-2: Mechanical Properties of SCS-6 Fiber

Temperature (°C)	Tensile Modulus (GPa)	Poisson's Ratio	CTE (µm/m/°C)
25	393	0.25	3.56
482	376	0.25	3.99
538	374	0.25	4.07
566	373	0.25	4.12
650	370	0.25	4.27

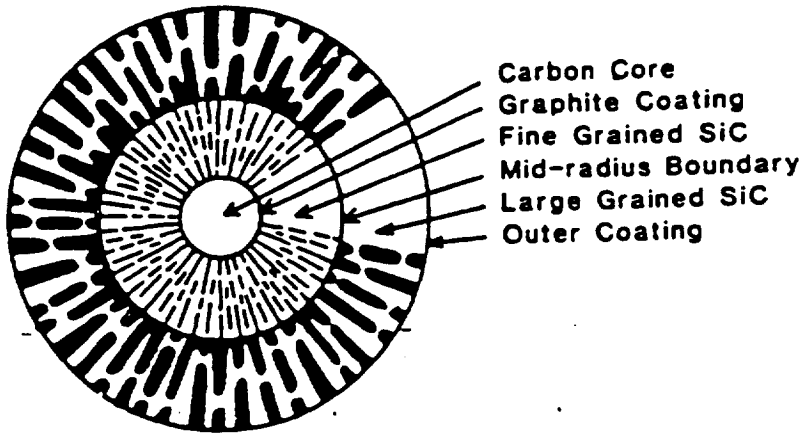

Figure 1: A schematic diagram of a cross-section of an SCS-6 fiber.

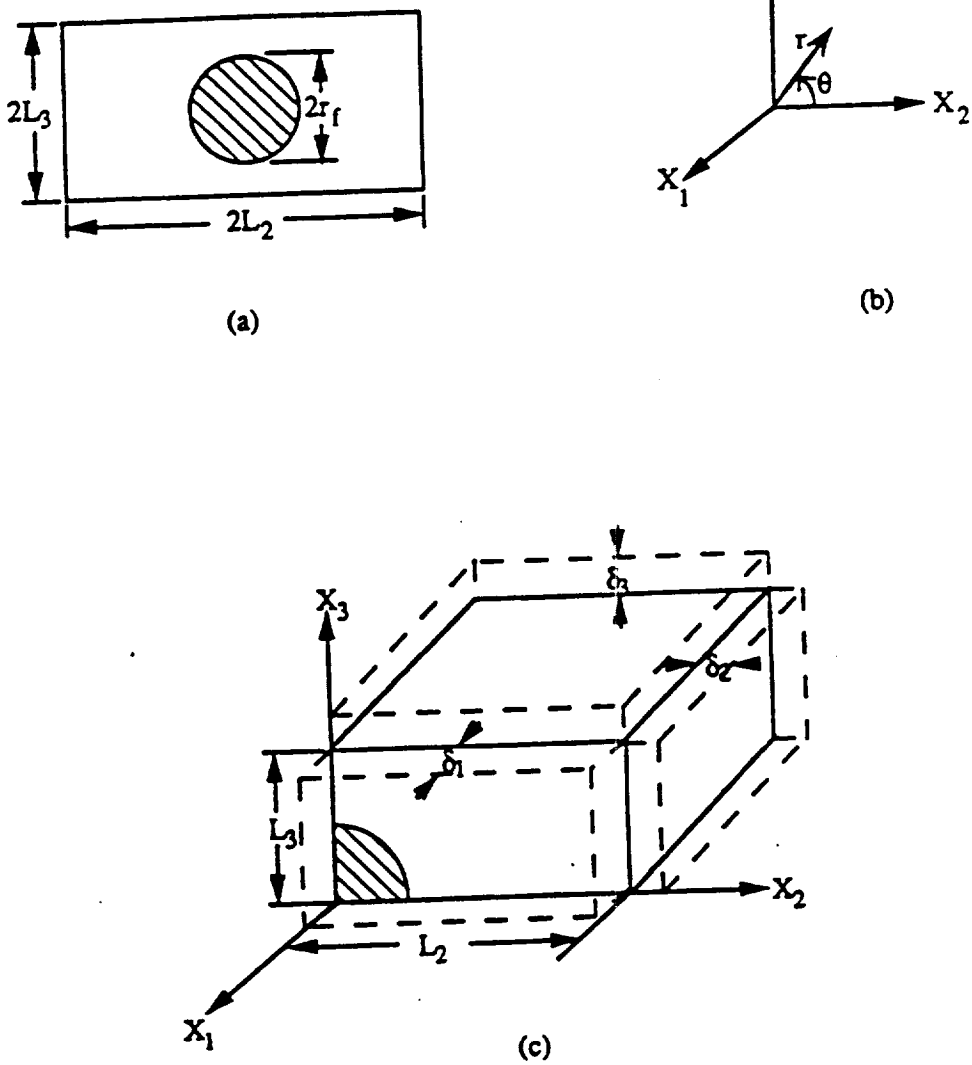

Fig. 2 Micromechanics model of MMC.

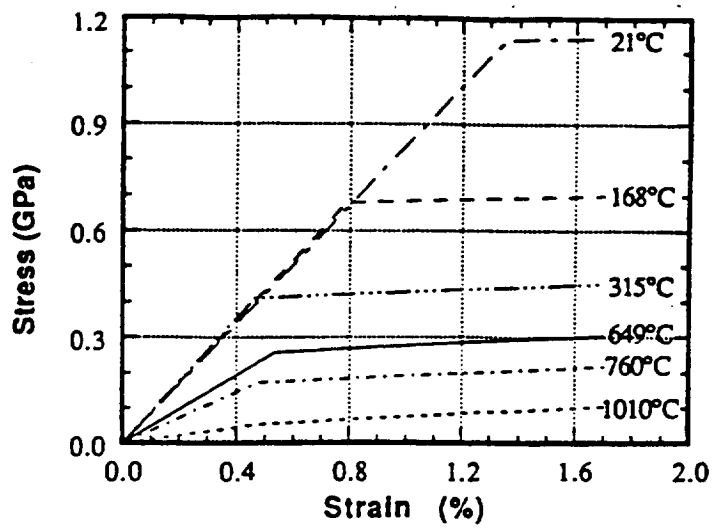

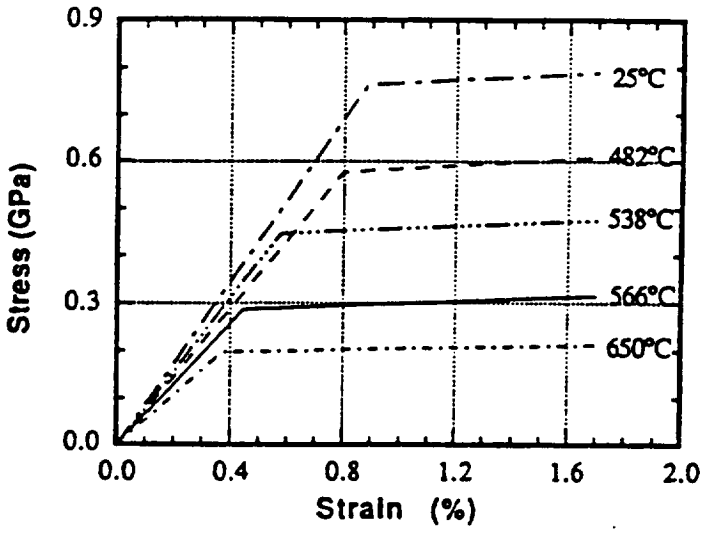

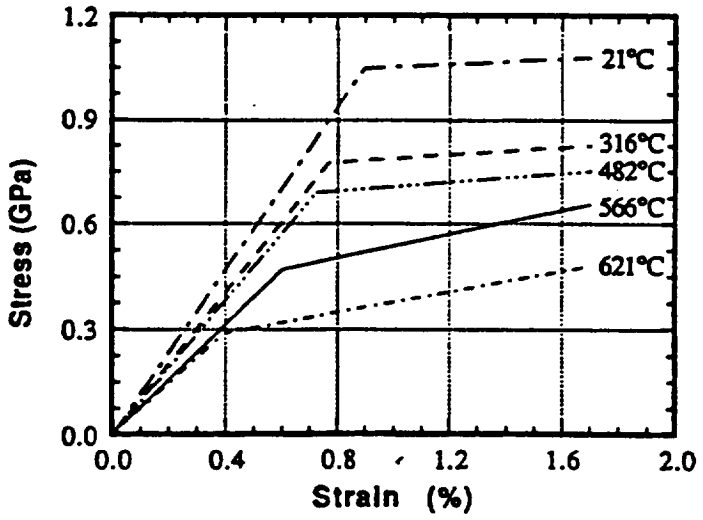

Fig. 3 Temperature dependent uniaxial stress-strain behavior in tension of the MMC matrix materials:
(a) Matrix material of composite A.
(b) Matrix material of composite B.
(c) Matrix material of composite C.

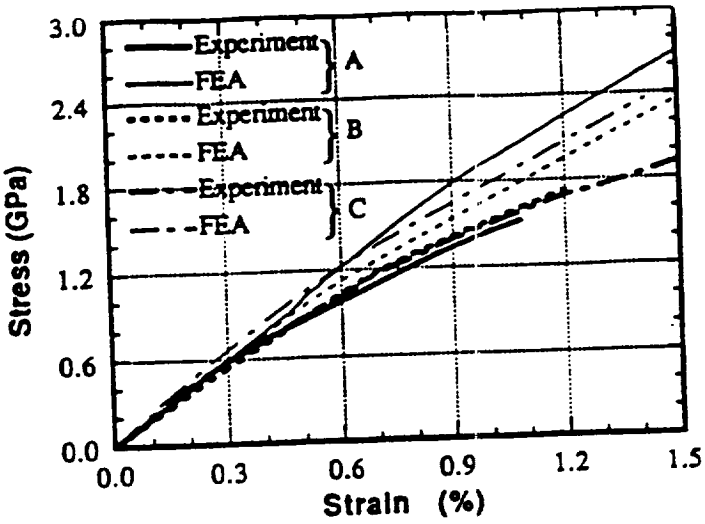

Fig. 4 Predicted and experimental 0° stress-strain response at room temperature for MMCs A, B and C.

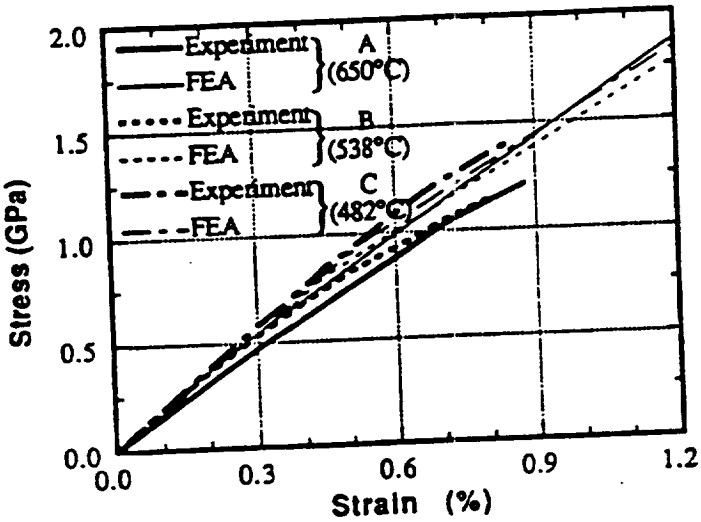

Fig. 5 Predicted and experimental 0° stress-strain response at elevated temperature for MMCs A, B and C.

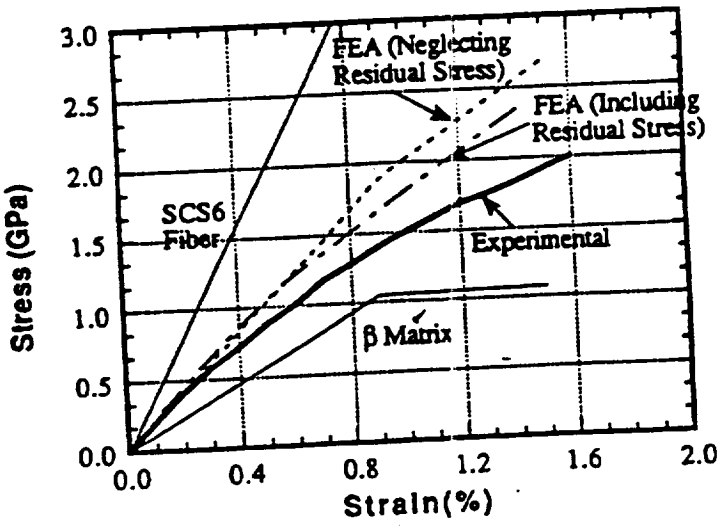

Fig. 6 0° stress-strain response of MMC C at room temperature showing the effect of residual stresses on the composite's yield stress.

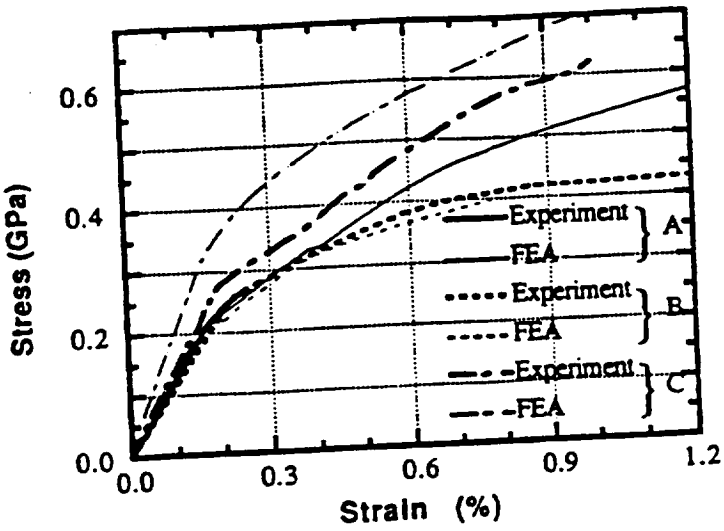

Fig. 7 Predicted and experimental 90° stress-strain response at room temperature for MMCs A, B and C.

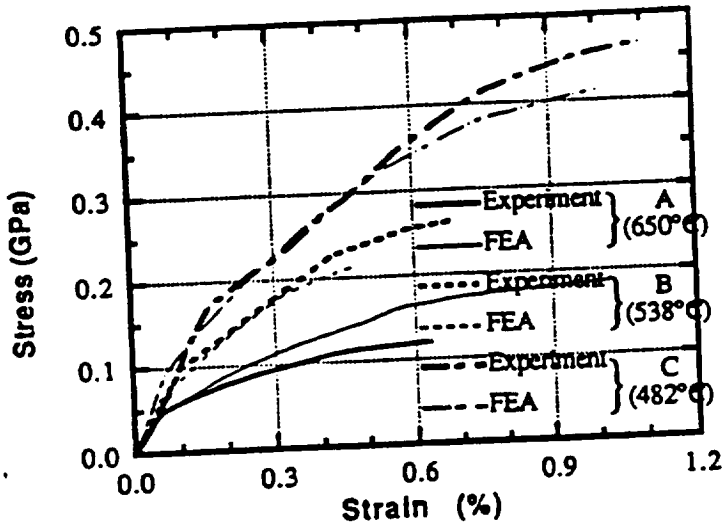

Fig. 8 Predicted and experimental 90° stress-strain response at elevated temperature for MMCs A, B and C.

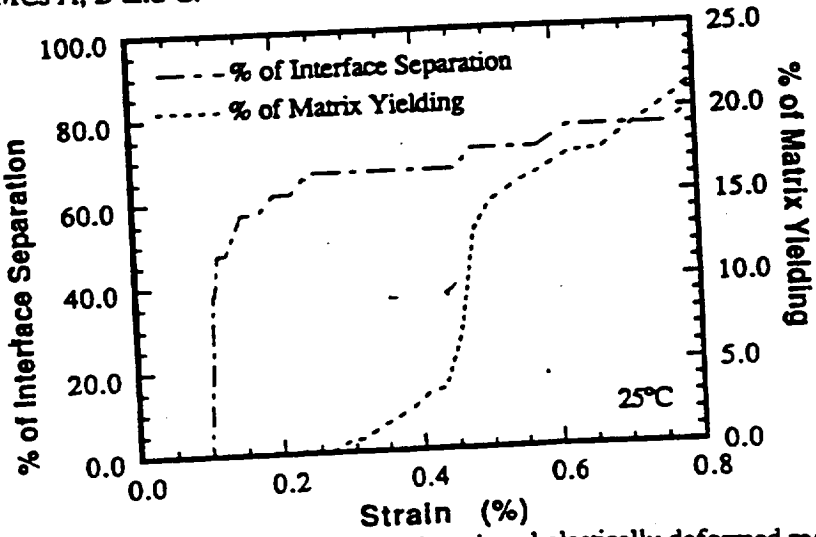

Fig. 9(a) Predicted development of debond length and plastically deformed region in MMC B subjected to transverse loading at room temperature.

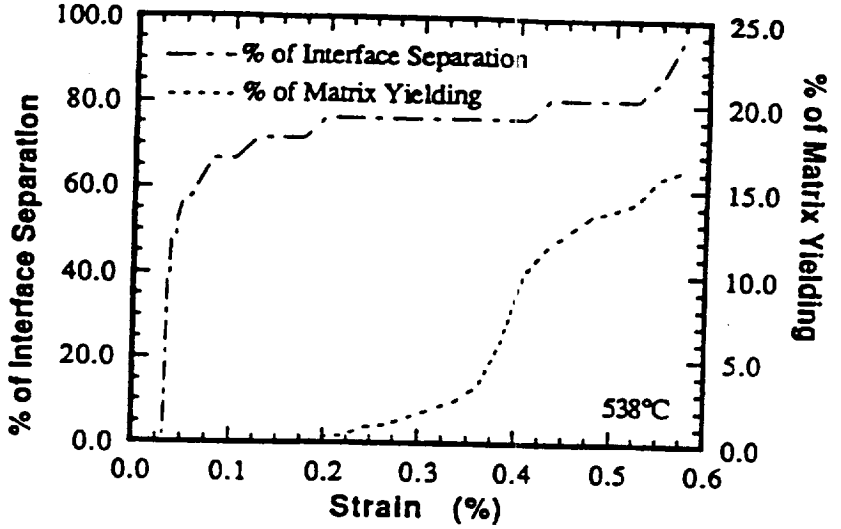

Fig. 9(b) Predicted development of debond length and plastically deformed region in MMC B subjected to transverse loading at elevated temperature.

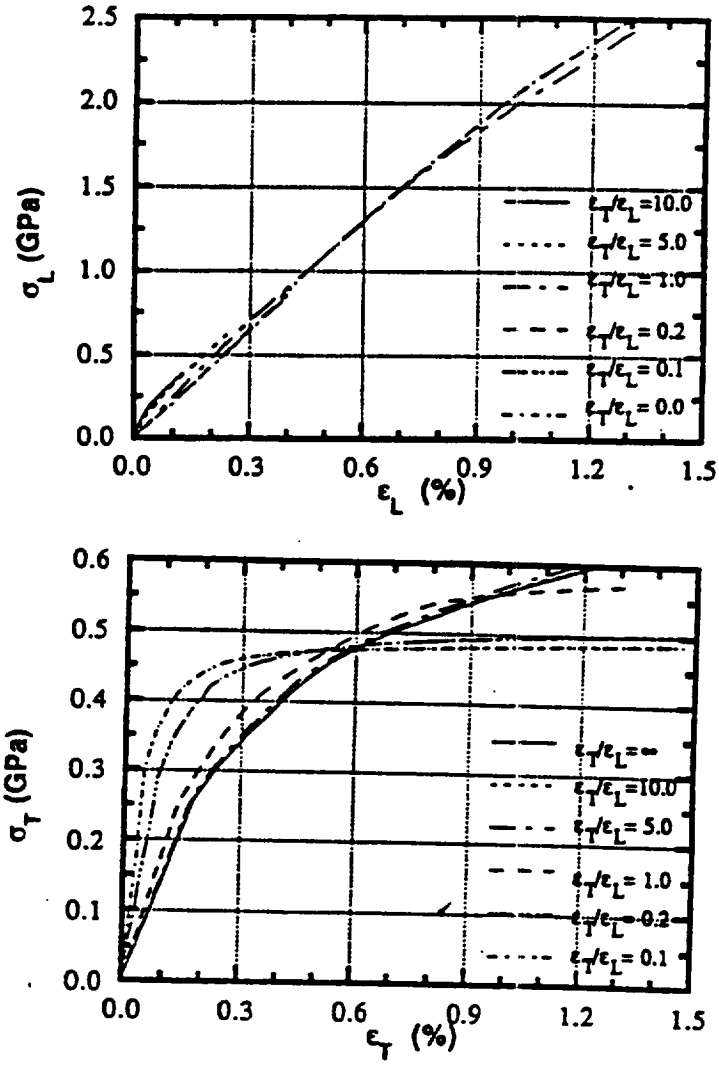

Fig. 10 Biaxial Behavior of MMC A:
(a) Longitudinal stress-strain response.
(b) Transverse stress-strain response.

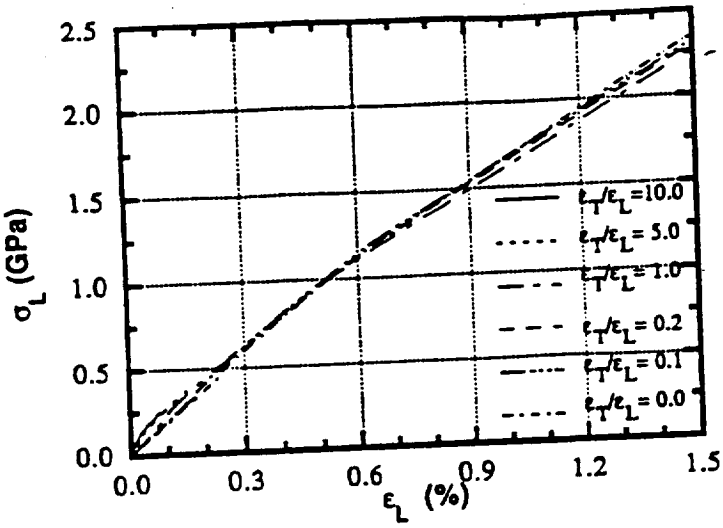

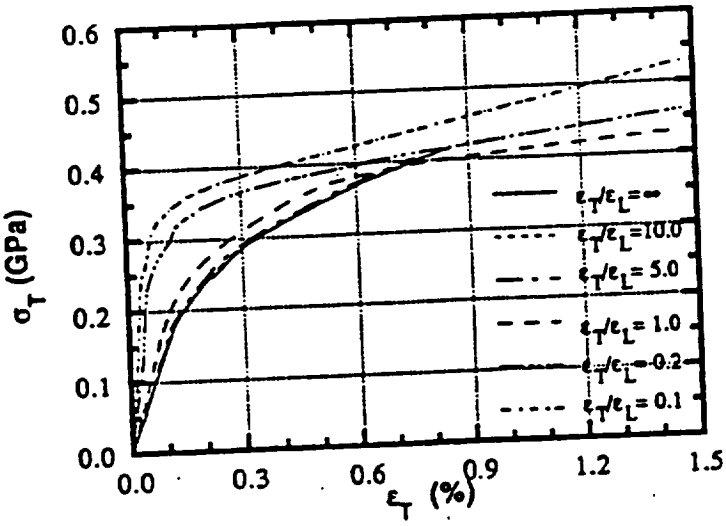

Fig. 11 Biaxial Behavior of MMC B:
(a) Longitudinal stress-strain response
(b) Transverse stress-strain response

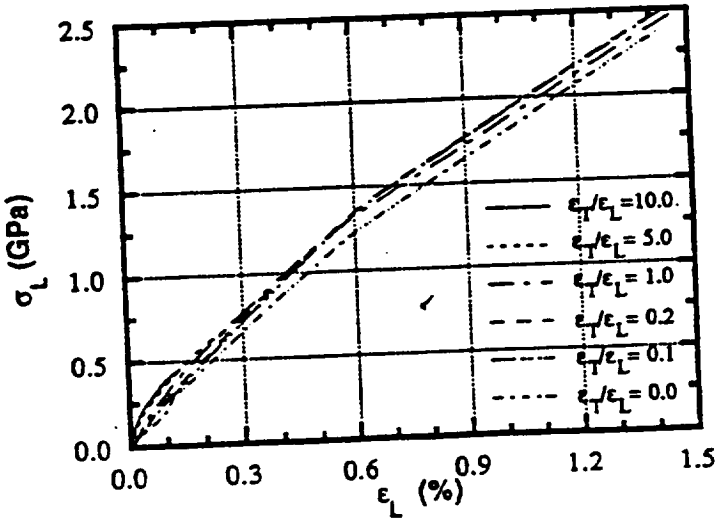

Fig. 12(a) Biaxial Behavior of MMC C: Longitudinal stress-strain response.

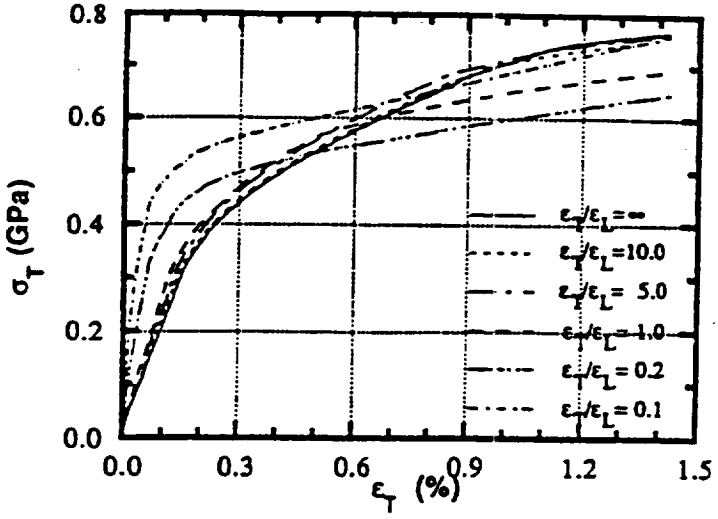

Fig. 12(b) Biaxial Behavior of MMC C: Transverse stress-strain response.

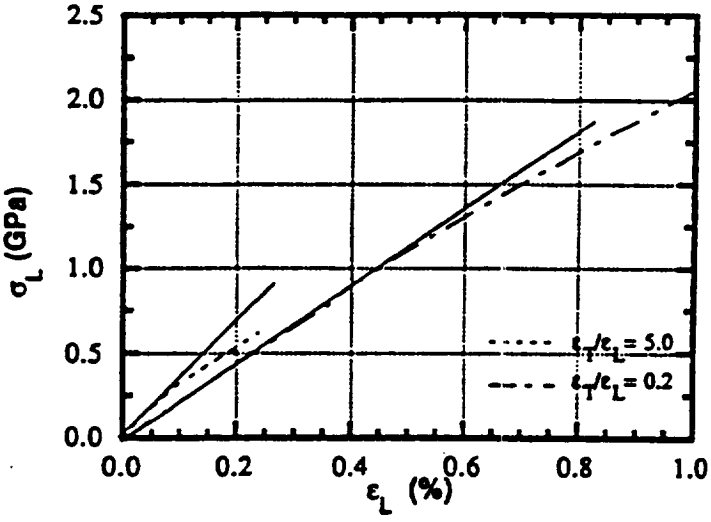

Fig. 13 Longitudinal stress-strain response of MMC A for $\varepsilon_T=0.2\varepsilon_L$ and $\varepsilon_T=5.0\varepsilon_L$, showing onset of premature yielding.

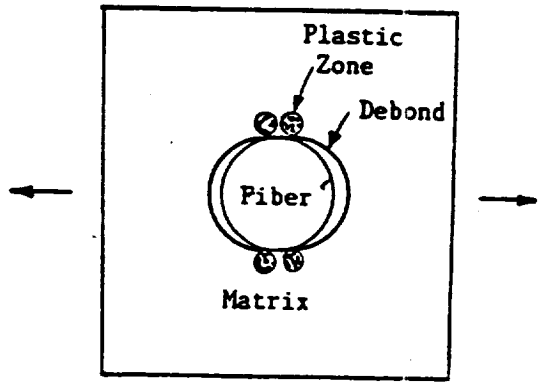

Fig. 14 Plastic deformation zones at debond termini causing premature nonlinearity in longitudinal stress-strain response under biaxial loading.

REPORT DOCUMENTATION PAGE

Form Approved
OMB No. 0704-0188

1. AGENCY USE ONLY (*Leave blank*)	2. REPORT DATE	3. REPORT TYPE AND DATES COVERED
	September 1998	Final Contractor Report

4. TITLE AND SUBTITLE

TMC Behavior Modeling and Life Prediction Under Multiaxial Stresses

5. FUNDING NUMBERS

WU–523–21–13–00
NAS3–27027

6. AUTHOR(S)

H.F. Merrick, S.Z. Aksoy, M. Costen, and J. Ahmad

7. PERFORMING ORGANIZATION NAME(S) AND ADDRESS(ES)

AlliedSignal Engines
111 S. 34th Street
P.O. Box 52180
Phoenix, Arizona 85072–2180

8. PERFORMING ORGANIZATION REPORT NUMBER

E–11188

9. SPONSORING/MONITORING AGENCY NAME(S) AND ADDRESS(ES)

National Aeronautics and Space Administration
Lewis Research Center
Cleveland, Ohio 44135–3191

10. SPONSORING/MONITORING AGENCY REPORT NUMBER

NASA CR—1998-207928
AlliedSignal Engines 21–9835

11. SUPPLEMENTARY NOTES

H.F. Merrick, AlliedSignal Engines, 111 S. 34th Street, P.O. Box 52180, Phoenix, Arizona 85072–2180; S.Z. Aksoy and M. Costen, Aerospace Structural Research Corp., 252 Depot Road, Suite 2C, Milford, Connecticut 06460; and J. Ahmad, Research Applications, Inc., 11772 Sorrento Valley Road, Suite 145, San Diego, California 92121–1085 . Project Manager, Steven M. Arnold, Structures and Acoustics Division, NASA Lewis Research Center, organization code 5920, (216) 433–3334.

12a. DISTRIBUTION/AVAILABILITY STATEMENT

Unclassified - Unlimited
Subject Categories: 24 and 39 Distribution: Nonstandard

This publication is available from the NASA Center for AeroSpace Information, (301) 621–0390.

12b. DISTRIBUTION CODE

13. ABSTRACT (*Maximum 200 words*)

The goal of this program was to manufacture and burst test small diameter SCS–6/Ti–6Al–4V composite rings for use in the design of an advanced titanium matrix composite (TMC) impeller. The Textron Specialty Metals grooved foil-fiber process was successfully used to make high quality TMC rings. A novel spin test arbor with "soft touch" fingers to retain the TMC ring was designed and manufactured. The design of the arbor took into account its use for cyclic experiments as well as ring burst tests. Spin testing of the instrumented ring was performed at ambient, 149C (300F), and 316C (600F) temperatures. Assembly vibration was encountered during spin testing but this was overcome through simple modification of the arbor. A spin-to-burst test was successfully completed at 316C (600F). The rotational speed of the TMC ring at burst was close to that predicted. In addition to the spin test program, a number of SCS-6/Ti-6Al-4V test panels were made. Neat Ti-6Al-4V panels also were made.

14. SUBJECT TERMS	15. NUMBER OF PAGES
Advanced impeller; Titanium matrix composites; Experimentation; Analysis; Life prediction; Disks; High temperature	206
	16. PRICE CODE: A10

17. SECURITY CLASSIFICATION OF REPORT	18. SECURITY CLASSIFICATION OF THIS PAGE	19. SECURITY CLASSIFICATION OF ABSTRACT	20. LIMITATION OF ABSTRACT
Unclassified	Unclassified	Unclassified	